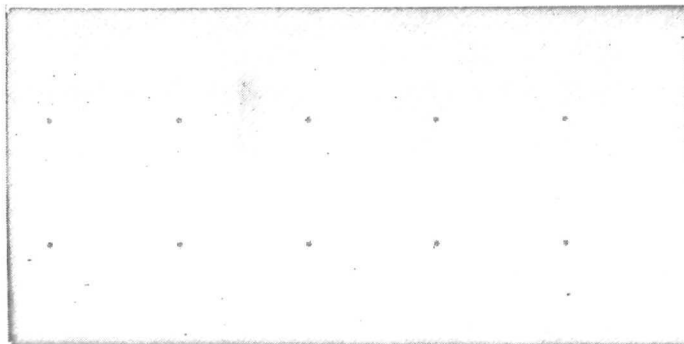


N72-25465

**CASE FILE  
COPY**



*Lockheed*

HUNTSVILLE RESEARCH & ENGINEERING CENTER

LOCKHEED MISSILES & SPACE COMPANY, INC.  
A SUBSIDIARY OF LOCKHEED AIRCRAFT CORPORATION

HUNTSVILLE, ALABAMA

LOCKHEED MISSILES & SPACE COMPANY  
HUNTSVILLE RESEARCH & ENGINEERING CENTER  
HUNTSVILLE RESEARCH PARK  
4800 BRADFORD DRIVE, HUNTSVILLE, ALABAMA

LOAD RELIEF AND GUST  
ALLEVIATION CONTROL  
STUDY

FINAL REPORT

April 1972

Contract NAS8-27009

Prepared for National Aeronautics and Space Administration  
Marshall Space Flight Center, Alabama 35812

by  
R. R. Vieweg

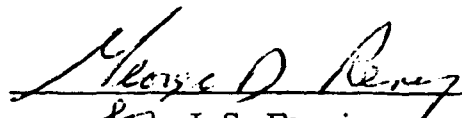
APPROVED:



W. Trautwein, Supervisor  
Vehicle Dynamics & Control Section



T. R. Beal, Manager  
Dynamics & Guidance Department



J. S. Farrior  
Resident Director

## FOREWORD

This report presents the results of work performed during the period April 1971 to March 1972 by Lockheed's Huntsville Research & Engineering Center while under contract to the National Aeronautics and Space Administration for the Aero-Astrodynamic Laboratory of Marshall Space Flight Center (MSFC), Contract NAS8-27009.

The report documents the work performed on "Load Relief and Gust Alleviation," an advanced control system study applied to INT-21 launch vehicle with a 141-foot payload. This vehicle is a Saturn V derivative.

Mr. J. M. Livingston of NASA-MSFC, Aero-Astrodynamic Laboratory, S&E-AERO-DF, was the MSFC Contracting Officer's Representative. Mr. R. R. Vieweg was the project engineer at Lockheed. Major contributors were Dr. W. Trautwein, who provided technical advice, and Mr. A. Hansing, who performed all of the hybrid computer work. Dr. G. C. Feng developed the equations of motion and assembled the original raw mass, aerodynamic, propulsion, structural dynamics, and trajectory data. Mr. C. L. Connor brought the INT-21 digital computer check simulation to an operational status.

## SUMMARY

This report presents the results of a study in which Lockheed's computerized optimal control technique was applied to the synthesis of a load relief control system for an advanced Saturn V derivative launch vehicle (INT-21). This technique included selection of a load relief control law and then computerized optimization of the controller gain schedules for a set of pre-selected adverse synthetic wind speed profiles. The gain optimization was effected using Lockheed's Hybrid Optimizer Program to minimize (optimize) a direct performance functional which specified the design goal (load relief) in meaningful engineering terms (explicit representation of maximum bending moments).

When evaluated under similar conditions, the Lockheed load relief controller produced significantly smaller peak bending moments than those obtained in other recent studies.

The effectiveness of Lockheed's load relief controller was verified by "flying" the analog simulated vehicle through a large number of measured wind speed profiles, prerecorded on magnetic tape. Statistical parameters were evaluated in the digital computer portion of the hybrid computer and are included.

## CONTENTS

Section		Page
	FOREWORD	ii
	SUMMARY	iii
1	INTRODUCTION	1-1
2	DIRECT HYBRID COMPUTER OPTIMIZATION TECHNIQUE	2-1
	2.1 Basic Scheme	2-1
	2.2 Performance Evaluation	2-1
	2.3 Continuous Straight Line Segment Control System Gain Schedules	2-3
	2.4 Optimization ("Look-Ahead") Interval and Update Sequencing	2-5
	2.5 Systematic Optimization Search	2-9
	2.6 Reducing the Sensitivity to Adverse Condition Uncertainty	2-11
3	DETAILED STATEMENT OF THE PROBLEM	3-1
	3.1 Description of Vehicle Dynamics	3-1
	3.2 System Disturbances	3-4
	3.3 Design Objectives	3-7
4	SELECTION OF LOAD RELIEF PERFORMANCE CRITERION	4-1
5	CONTROLLER DESIGN AND OPTIMIZATION	5-1
	5.1 Selection of Controller	5-1
	5.2 Selection of Design Disturbances	5-5
	5.3 Optimization Results for Synthetic Winds	5-7

CONTENTS (Continued)

Section		Page
6	PERFORMANCE VERIFICATION	6-1
7	CONCLUSIONS AND RECOMMENDATIONS	7-1
	7.1 Controller Design and Optimization	7-1
	7.2 Performance Verification	7-4
8	REFERENCES	8-1
Appendix		
A	INT-21 RAW DATA PACKAGE AND EOM TIME-VARYING COEFFICIENTS (TVC's)	A-1
B	SYNTHETIC WIND MODELS	B-1
C	ANALOG COMPUTER SIMULATION DIAGRAMS	C-1
D	DIGITAL SIMULATION CHECK SOLUTIONS	D-1

Section 1  
INTRODUCTION

The relief of structural loads by advanced control system design is a critical factor in the Saturn system's potential to economically launch a variety of different Space Station/Base payload configurations. Although similar in total vehicle height to the Saturn V, the Space Station/Base payloads are of larger diameter and may have docking port fairings and solar panel housings protruding from the cylinder shape, making these vehicles more vulnerable to aerodynamic disturbances which interact with structural and liquid propellant modes.

The primary objective of this study is to define an advanced control system which will provide load relief and structural modal suppression for the INT-21 launch vehicle with a 141-foot payload. A Lockheed-developed optimization method implemented on a hybrid computer utilizes a systematic design approach to minimize peak structural loads for a specified range of flight conditions. This approach combines systematic grid search of control-parameter space (global optimization) with minimum-seeking gradient techniques (local optimization) to minimize a direct (peak structural loads defined explicitly) performance functional. A detailed description is presented in Section 2.

As implied above, the primary design goal of this project was to devise a controller for INT-21 such that bending loads due to wind forces are minimized. In the past, the principal mechanism for attaining such load relief has been to control the vehicle in such a manner that it "turns into the wind," thus reducing the relative wind angle of attack. While aerodynamically stable vehicles tend in this direction (weathercocking) without any additional controls applied, INT-21 is aerodynamically unstable; this implies the need to sense the

relative wind angle and then use this information to gimbal the main engine in such a way that the angle of attack is reduced.

In the area of gust alleviation, results from recent gust penetration load investigations were evaluated and assessed concerning their implications on the INT-21. Contrary to earlier expectations, the maximum gust penetration loads for large Saturn-class launch vehicles are encountered after full penetration into the gust (Ref. 10). The transient response during gust penetration does not produce the highest loads. An efficient load relief controller can therefore be expected to alleviate significantly the maximum gust penetration loads. Another finding was that sophisticated mathematical models of launch vehicle aerodynamics including flow separation effects, time-lag effects during gust penetration and accelerated flow produce maximum gust induced bending loads which are no more than 1.24% of the loads resulting from the worst design wind profiles used in this study.

A unified design approach was therefore chosen in which gust induced load effects were included throughout the controller design. Load relief and gust alleviation were considered to be design objectives that must be simultaneously satisfied.

The specific major objective of this control study, then, was to define and optimize the main engine (thrust vector) controller for INT-21 ascent so as to achieve the following goals:

- Critical peak structural loads during the ascent flight be minimized.
- Control system sensitivity to off-nominal environmental characteristics be minimized.
- To obtain desirable stability and terminal drift characteristics.
- Statistical evaluation of INT-21 performance which shows desirable characteristics in response to a large number of measured tape winds.



This study was performed in the following steps:

- Derivation of INT-21 ascent equations of motion (EOM).
- Assembly of mass, aerodynamic propulsion, structural dynamics, and trajectory data for INT-21 with 141-foot payload.
- Development of a digital computer program capable of calculating, printing, and plotting the following three items:
  1. Time-varying coefficients (TVC's) of EOM for internal use in the digital simulation and outside use in the analog simulation.
  2. Up to ten different synthetic wind speed curves, including gusts (converts wind speed versus altitude to wind angle versus time for a given nominal flight profile), for use both in the digital and analog simulations.
  3. Solution of the INT-21 ascent EOM to provide a means for verifying analog simulation.
- Programming and checkout of the analog computer simulation of INT-21 ascent dynamics (includes EOM, TVC's, synthetic winds, and baseline attitude control system).
- Definition of control system requirements.
- Development and analog simulation of a performance criterion (possibly direct) reflecting design goals (minimum peak bending loads at critical vehicle stations).
- Synthesis of a controller capable of achieving the load relief and gust alleviation design goals.
- Hybrid computer high speed optimization of controller gain schedules. Includes:
  1. Implementation (and minor reprogramming) of Lockheed's Hybrid Optimizer Digital program.
  2. Selection of two most appropriate adverse synthetic winds for controller gain optimization.
  3. Hybrid optimization runs and analysis of results based on the above design objectives.
- Performance verification of resultant controller and gain schedules through statistical evaluation of response to a large number of measured tape winds.

## Section 2

## DIRECT HYBRID COMPUTER OPTIMIZATION TECHNIQUE

## 2.1 BASIC SCHEME

The Direct Hybrid Computer Optimization Technique, hereafter referred to as the Hybrid Optimizer (or the optimizer) utilizes a systematic design approach to minimize a direct scalar performance measure,  $J$ , which may be expressed directly in meaningful engineering terms (rather than indirectly, as is frequently the case with quadratic form integrand, time-integral performance functionals).

A math model of system dynamics is implemented on the analog portion of the hybrid computer. The digital side of the hybrid computer directs a systematic search throughout control-parameter space to determine time-varying control parameter gain scheduling (control policy) which minimizes the direct scalar performance measure,  $J$ . The optimal (minimum)  $J$ , ( $J^0$ ), is determined sequentially for each of many successive time intervals so that control parameter gain schedules are actually optimized only with respect to each particular time interval over which  $J$  is evaluated, not the total problem solution time (see Sections 2.3 and 2.4).

## 2.2 PERFORMANCE EVALUATION

The Hybrid Optimizer is dependent on some performance measure,  $J$ , to guide the Performance Analyzer section of the digital program (see Fig. 2-1). The performance measure,  $J$ , might contain more than one term, each term being appropriately weighted (as directed by the engineering emphasis).

Constituent terms of  $J$  may be either of a direct or indirect nature. Physical examples of direct terms would include aircraft and missile bending

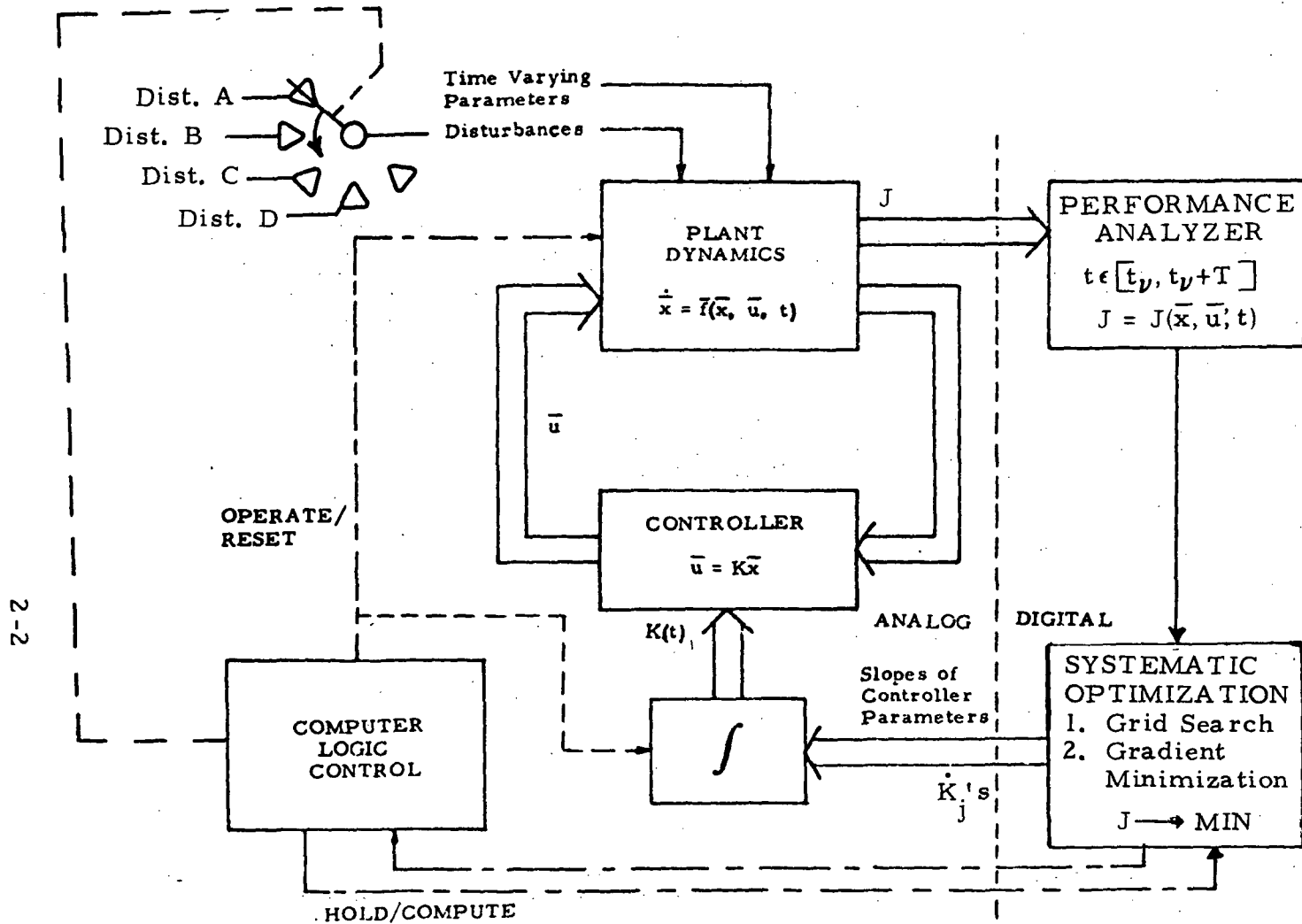


Fig. 2-1 - Basic Control System Optimization Scheme. Complete plant and control system dynamics are simulated repetitively on analog console of hybrid computer. Performance is analyzed after simulation by digital computer and optimized through iterative changes in slopes of controller gain schedules to determine gain schedule slopes yielding  $J \rightarrow \text{Min}$ .

moments, critical engine temperatures, sound intensities, etc. Examples of indirect terms would include time-integral functionals whose integrands contain quadratic functions of the system state and control vector components.

The one feature that makes the Hybrid Optimizer a unique and practical optimization tool is its ability to specify design goals in the most direct manner with virtually no mathematical constraints concerning its functional form. This "free-form" ability gives the Hybrid Optimizer a definite edge in handling problems of the minimax species. It is specifically due to this particular minimax capability that the Hybrid Optimizer has achieved excellent results in optimizing load relief type control laws applied to launch vehicles. In this type of optimization, maximum bending moments at critical launch vehicle locations are directly introduced as constituent terms of the performance measure,  $J$  (with suitable weighting coefficients).

As will be detailed in the following sections, the Hybrid Optimizer accomplishes its objectives through a stepwise, forward integration procedure. It yields excellent results for many types of optimization problems, but generally it is not an appropriate tool for solving optimal control problems wherein the terminal manifold (transversality, or end, condition) has been "tightly" prespecified.

### 2.3 CONTINUOUS STRAIGHT LINE SEGMENT CONTROL SYSTEM GAIN SCHEDULES

The end product generated by the Hybrid Optimizer is a set of time-varying control system gain schedules in polygonal (continuous straight line segment) form. One such gain schedule,  $a_0(t)$ , is pictorially represented in Fig. 2-2.

These continuous piecewise linear gain schedules represent a realistic compromise between the two extremes:

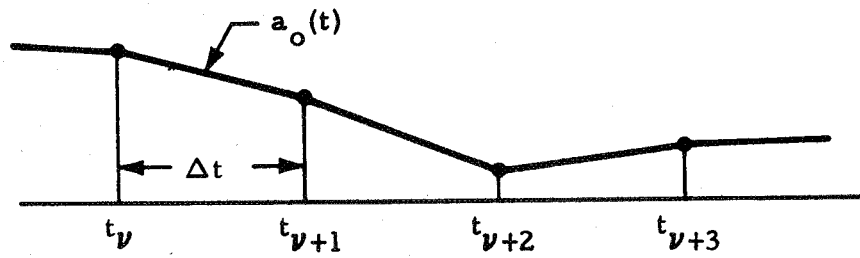


Fig. 2-2 - Polygonal Form of Optimal Controller Gain Schedules

1. Carrying many terms of Taylor Series representations of control system gain schedules (with the large computational load that would be required in figuring several Taylor terms for each gain schedule), and
2. Using piecewise constant gain schedules, which are relatively easy to calculate but not so practical to use because of the unacceptable transients resulting from the undesirable gain schedule step-type discontinuities.

Furthermore, the continuous piecewise linear gain schedules provided by the Hybrid Optimizer are relatively easy to implement in real control system hardware.

### 2.3.1 Update Interval

Refer again to Fig. 2-2. Control system gain slope  $\dot{a}_0(t)$  experiences a stepwise change every  $\Delta t$  seconds — at times  $t_{\nu}$ ,  $t_{\nu+1}$ ,  $t_{\nu+2}$ , etc.  $\Delta t$  is called the update interval and was experimentally set at 5 seconds for the INT-21 Load Relief and Gust Alleviation optimization. The update interval  $\Delta t$  is generally made as long as possible in order to minimize the computational requirements and the number of straight line segments needed to generate the time-varying gain schedules. However,  $\Delta t$  must still be short enough so that the resulting polygonal gain schedules satisfactorily represent the smooth optimal gain schedules which would be the exact optimal solution. Successive optimization ("look-ahead") intervals are always started at the end (finish) of the last update interval (see next section for complete description of the optimize-update sequencing). Note: control system gain schedule slopes  $\dot{a}_0(t)$ ,  $\dot{a}_1(t)$  of Figs. 2-2, 2-3, 2-4 and 2-5 correspond to the  $\dot{K}_j$ 's of Fig. 2-1 and  $\dot{K}$  of Fig. 2-6.

## 2.4 OPTIMIZATION ("Look-Ahead") INTERVAL AND UPDATE SEQUENCING

In early attempts to solve minimax type problems, it was discovered that evaluation of the performance measure,  $J$ , over the total solution time of the particular minimax problem at hand usually led to undesirable results,

in an engineering (practical) sense. While this early approach would, in fact, locate control system gain slopes that minimized the performance measure,  $J$ , the results were of academic interest only because the optimizer selected just one straight line segment to cover the total time of flight.

The optimization algorithm currently implemented by the Hybrid Optimizer provides more acceptable minimax results; it is described in the remainder of this section.

Refer to Fig. 2-3. The total solution (mission) time of interest is the time interval  $[t^0, t^1]$ . Update times are designated  $t_1, t_2, \dots$ , etc. Optimization ("look-ahead") time is  $T$ .

At the  $\nu^{\text{th}}$  update time,  $t_\nu$ , the Hybrid Optimizer performs a series of fast-time forward integrations on the analog console, each starting at  $t_\nu$ . At the start of each fast-time run (at  $t_\nu$ ), the same "initial conditions" are always impressed. Between runs, the optimizer iteratively adjusts the controller gain slopes in order to find the gain slopes which minimize  $J$  on the optimization interval  $[t_\nu, t_\nu + T]$ . (See Fig. 2-4 for further clarification of this point.) Once these optimal gain slopes have been determined, the system equations are integrated (updated) in real time, using the optimal slopes, from time ( $t_\nu$ ) to ( $t_{\nu+1}$ ). Then, the procedure is repeated all over again, starting at  $t_{\nu+1}$ , and the next "look-ahead" interval becomes  $[t_{\nu+1}, t_{\nu+1} + T]$ . In this manner, an optimized polygonal gain schedule is generated for each time-varying control system gain being optimized.

Selection of the "look-ahead" time interval,  $T$ , is a compromise procedure. It must be short enough to emphasize the effects of current update interval  $[t_\nu, t_{\nu+1}]$  on  $J$ ; however, it is usually desirable to make  $T$  longer than the update interval (see Fig. 2-3b) and "look-ahead" to the future and have the gain slopes "trending" in the appropriate direction so that the resulting gains will be able to "cope" with these future, anticipated conditions as they unfold.  $T$  is usually determined experimentally. For the Load Relief and Gust Alleviation Control Study, a 15-second "look-ahead" (optimization) interval was used.

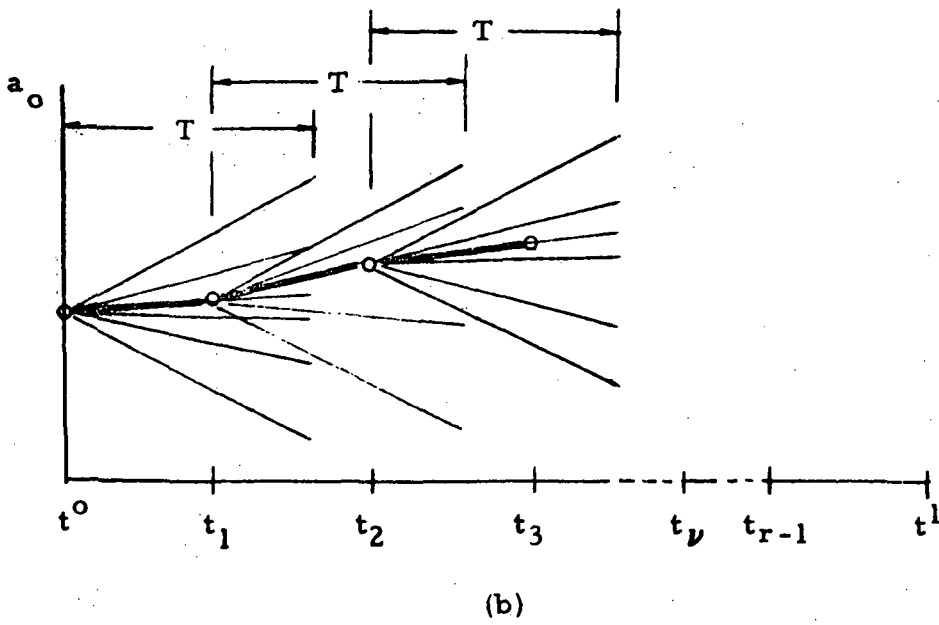
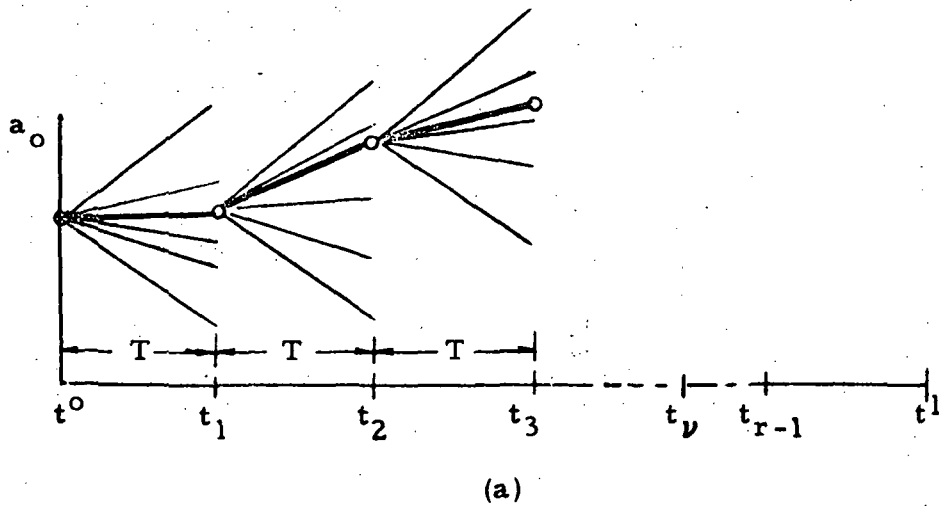


Fig. 2-3 - Total Missile Time ( $t^0, t^1$ ) Broken Down into Finite Number  $r$  of updating Intervals  $(t^0, t_1), (t_1, t_2), \dots, (t_\nu, t_{\nu+1}), (t_{r-1}, t^1)$ . Optimization Intervals  $(t_\nu, t_\nu+T)$  are identical to updating intervals  $(t_\nu, t_{\nu+1})$  as in Fig. 2-3(a) or are longer than updating intervals (Fig. 2-3(b)).



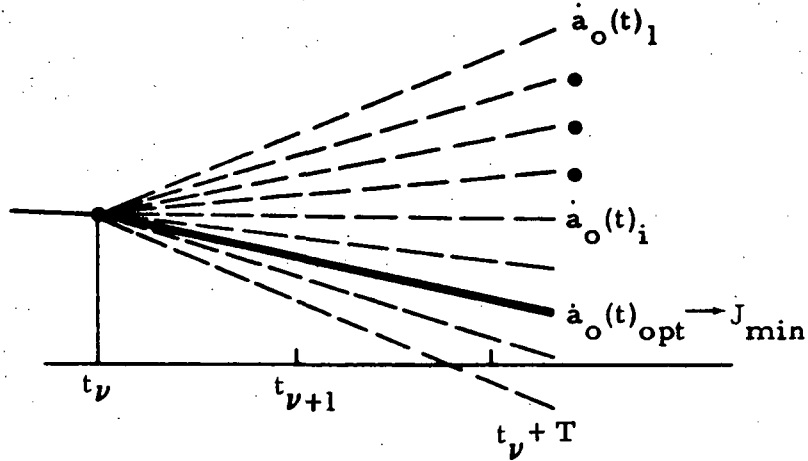


Fig. 2-4 - During Optimization Cycle Starting at Time  $t_\nu$ , a Large Number of Linear Controller Gain Schedules Having Different Slopes are Evaluated for their Optimality

## 2.5 SYSTEMATIC OPTIMIZATION SEARCH

When the system forcing function is known, a priori, the Hybrid Optimizer proceeds in a systematic manner, as described in the following and pictorially represented in the two-dimensional parameter space optimization example of Fig. 2-5. On any optimization ("look-ahead") interval  $[t_\nu, t_\nu+T]$ , the performance measure,  $J$ , is first coarsely evaluated (grid search) throughout a wide range of control system parameter space to locate the most likely general area for a global minimum. Then, proceeding from the grid point of minimum  $J$ , a gradient search refinement locates the true global minimum. These two steps are further detailed below in the interests of clarity

- Grid Search

$J$  is evaluated over "look-ahead" interval  $[t_\nu, t_\nu+T]$  for all possible parameter combinations within a grid space of specified fineness and limits. This coarse survey of parameter space locates the most probable area of the global minimum of  $J$ .

- Gradient Search Refinement

A powerful gradient minimization scheme based on the method of conjugate gradients (Ref. 2) starts at the grid search minimum and uses a modern method of steepest descent to more precisely determine the control parameter space location for which  $J$  is a minimum.

Figure 2-5 depicts the systematic optimization search for a two-dimensional grid, where  $J(\dot{a}_0, \dot{a}_1)$  evaluated on  $[t_\nu, t_\nu+T]$  is a two-dimensional surface and the "lowest point" is sought. Lockheed's Hybrid Optimizer has been used for a three-dimensional control parameter grid space and, digital storage capacity permitting plus analog run time accepted, the Hybrid Optimizer could be used for an  $n$ -dimensional control parameter grid search space (with its associated  $n$ -dimensional  $J$  hypersurface).

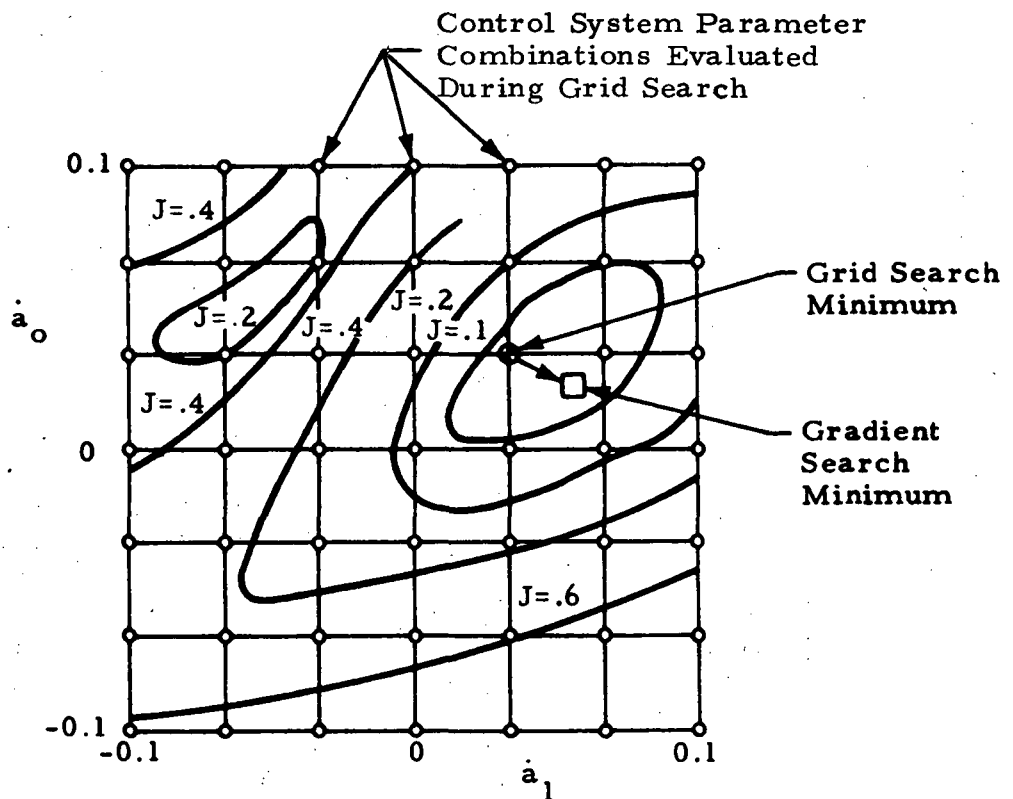


Fig. 2-5 - Control System Parameter Optimization Over "Look-Ahead" Interval  $[t_p, t + T]$  Performed in Two Phases: (1) Systematic Grid Search (o) for Coarse Survey of Parameter Space; Grid Point of Minimum  $J$  (●) Serves as Starting Point for (2) Gradient Search Which Locates the Minimum More Precisely (□). From grid search contour plots (lines of  $J = \text{const}$ ) can be drawn for better insight into  $J$ -topology.

## 2.6 REDUCING THE SENSITIVITY TO ADVERSE CONDITION UNCERTAINTY

The preceding section explained the basic Systematic Optimization Search algorithm used when the system forcing function is prespecified. Unfortunately, this is not always the case. For example, in the case of launch vehicle control systems, it is desirable to minimize peak bending moments assuming that the launch vehicle may encounter any one of several different adverse environmental or failure conditions.

Lockheed's Hybrid Optimizer includes the capability of optimizing with respect to several different adverse conditions — resulting in the highly desirable optimal desensitized control system gain schedules. The remainder of this section includes a brief explanation of the Hybrid Optimizer mechanism for achieving desensitization for two adverse condition uncertainties.

Refer to Fig. 2-6 for clarification of the desensitization procedure when it is uncertain which of just two different adverse conditions, A or B, might occur. Instead of optimizing over "look-ahead" interval  $[t_\nu, t_\nu+T]$  for just one adverse condition, the optimizer is modified to use two adverse conditions (A and B) at each point throughout grid search space. The two resulting J curves,  $J_A(\dot{K})$  and  $J_B(\dot{K})$  then have the upper bound curve  $\tilde{J}(\dot{K})$ . Both adverse conditions are simulated over time interval  $[t_\nu, t_\nu+T]$  in fast time (requiring twice as many fast-time runs), and the optimization (minimization) is performed with respect to the upper bound,  $\tilde{J}(\dot{K})$ , curve. The objective is to locate the "least upper bound" of the two J curves,  $J_A(\dot{K})$  and  $J_B(\dot{K})$  in Fig. 2-6. The gradient search is handled in the same manner as when only one adverse condition was considered, except that gradients are computed by perturbing controller gain slopes and using the changes effected in  $\tilde{J}(\dot{K})$ .

This method of desensitizing for two different adverse conditions can be seen as solving a minimax problem on yet another parameter space: that of

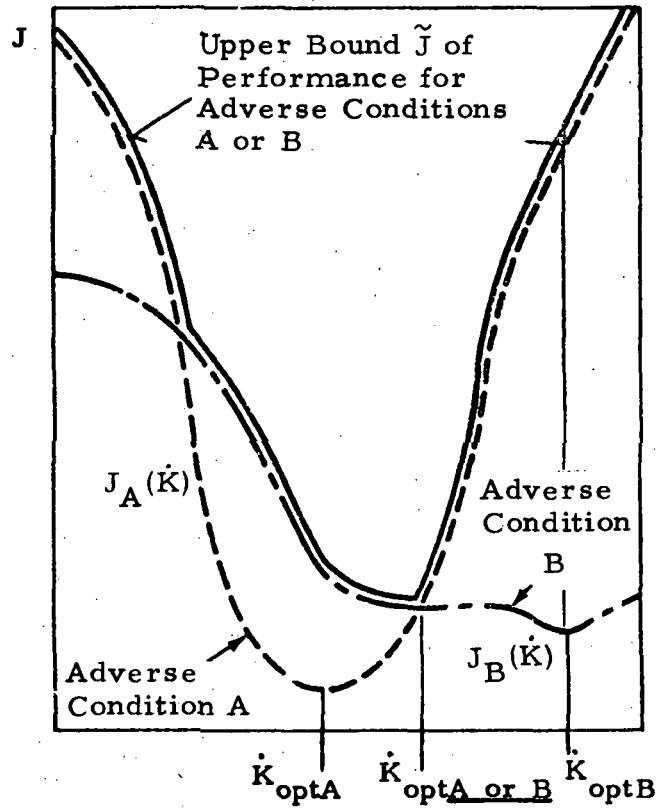


Fig. 2-6 - Optimum Adjustment of Scalar Control Parameter  $\dot{K}$  Over Time Interval  $[t_\nu, t_\nu+T]$  Considering Possible Occurrence of Adverse Conditions A or B

adverse condition uncertainty. This is expected-worst-case design, in a sense, because one of the worst situations that could occur is to be optimized for A (or B) and then have adverse condition B (or A) occur in an actual launch (flight). By mechanizing the desensitization procedure described in this section, Lockheed's Hybrid Optimizer determines the best compromise.

Conceptually, more than two adverse condition uncertainties could be included during the uncertainty optimization. The cost of increasing this dimension beyond two would be in digital memory requirements and analog run time (more fast-time runs required).

## Section 3

## DETAILED STATEMENT OF THE PROBLEM

A detailed description of the "Load Relief and Gust Alleviation Control Study" problem may be broken down into three main areas: INT-21 Vehicle Dynamics, Systems Disturbances, and Design Objectives. These three areas are covered in the remainder of Section 3.

## 3.1 DESCRIPTION OF VEHICLE DYNAMICS

The vehicle dynamics are best described by a statement of the system equations of motion, presented in conjunction with a diagram showing all of the pertinent problem variables and their relation to each other. The pictorial situation is presented in Fig. 3-1. The equations of motion, presented below, are of perturbation form with respect to the boost ascent trajectory. The three INT-21 structural modes were furnished by a Boeing report (Attachment to Memo 5-9406-INT-21-27, July 1970) and were computed under the assumptions of frozen propellant and no axial acceleration affects. Most of the EOM coefficients listed below are functions of flight time.

System Equations of Motion:

## ● Translation

$$\ddot{z} = K_1 \phi + K_2 \alpha + K_3 \beta + \sum_{i=1}^3 G_{t_i} \eta_i + B_E \ddot{\beta}$$

$$K_1 = \frac{F - D}{m}$$

$$G_{t_i} = (F/m) Y_i'(x_E)$$

$$K_2 = \frac{q S_A C_{N\alpha}}{m}$$

$$B_E = \frac{4m_E l_E}{m}$$

$$K_3 = \frac{F_c}{m}$$

where  $\ddot{z}$  is the linear acceleration normal to the guidance reference direction specified by  $\chi_c(t)$ , the "tilt" program.

● Rotation

$$\ddot{\phi} = -c_1\alpha - c_2\beta + \sum_{i=1}^3 G_{r_i} \eta_i + C_E \ddot{\beta}$$

$$c_1 = qS_A C_{N_A} (x_{CG} - x_{CP}) / I_{yy} \quad G_{r_i} = -F \left[ Y_i(x_E) + (x_{CG} - x_E) Y_i'(x_E) \right] / I_{yy}$$

$$c_2 = F_c (x_{CG} - x_E) / I_{yy} \quad c_E = -4 \left[ I_E + m_E \ell_E (x_{CG} - x_E) \right] / I_{yy}$$

where  $\phi$  is the perturbation attitude angle, measured with respect to the reference direction  $\chi_c(t)$ .

● Angle of Attack

$$\alpha = \alpha'_w + \phi, \quad \alpha'_w = \alpha_w - \frac{\dot{z}}{V}$$

where, for  $|\dot{z}| \ll |V|$ ,  $\lambda \cong \chi_c$  and  $V_T \cong V$ . Therefore,

$$\alpha'_w \cong \tan^{-1} (V_w \cos \chi_c) / (V - V_w \sin \chi_c)$$

where  $\alpha$  is the angle from vehicle rigid body centerline over to the effective wind direction (relative wind vector,  $\vec{V}_r$ ). Note that  $\alpha_w$  locates  $\vec{V}_r$  with respect to  $\vec{V}_T$ , the total velocity of the vehicle and  $\alpha'_w$  locates  $\vec{V}_r$  with respect to the direction specified by  $\chi_c(t)$ , the guidance commanded flight direction.

● System Bending Modes (i = 1, 2, 3)

$$\ddot{\eta}_i = -\bar{G}_{b_i} \eta_i - G_{b_i} \eta_i + B_{b_i} \beta + D_{E_i} \ddot{\beta} + G_{E_i} \ddot{\phi} + N_i \alpha$$



where

$$\begin{aligned} \bar{G}_{b_i} &= 2\zeta_{b_i} \omega_{b_i}; & G_{b_i} &= \omega_{b_i}^2; & B_{b_i} &= F_c Y_i(x_E) / T_i \\ D_{E_i} &= 4 \left[ m_E \ell_E Y_i(x_E) - I_E Y_i'(x_E) \right] / T_i \\ G_{E_i} &= 4 \left[ m_E (\ell_E + x_{CG} - x_E) Y_i(x_E) - m_E \ell_E (x_{CG} - x_E) Y_i'(x_E) \right] / T_i \\ N_{\dot{\eta}_i} &= (q S_A / T_i) C_{Abl_i} \end{aligned}$$

The bending modes displacements and slopes are contained in the Boeing report previously mentioned in this section. Mode displacements and slopes, as required by the other system equations, were extracted from these data.

● Engine Dynamics

$$\ddot{\beta} = -\bar{N}_E \dot{\beta} - N_E (\beta - \beta_c) - J_E \ddot{\phi} + \sum_{i=1}^3 K_{E_i} \ddot{\eta}_i + L_E \ddot{z} - P_E \phi$$

where

$$\begin{aligned} \bar{N}_E &= 2\zeta_E \omega_E \\ N_E &= \omega_E^2 \\ J_E &= \left[ m_E \ell_E (x_{CG} - x_E) - I_E \right] / I_E \\ K_{E_i} &= \left[ m_E \ell_E Y_i(x_E) - I_E Y_i'(x_E) \right] / I_E \\ L_E &= m_E \ell_E / I_E \\ P_E &= K_1 L_E \end{aligned}$$

where  $\beta$  is the angular engine deflection measured with respect to the flexible body centerline at the engine gimbal location (at the base of the vehicle)

● Bending Moment

$$M_{B_i}(t) = M'_{\alpha_i}(t) \alpha(t) + M'_{\beta_i}(t) \beta(t) + \sum_{j=1}^3 M'_{\ddot{\eta}_{j_i}}(t) \ddot{\eta}_j(t)$$

where  $M_{B_i}(t)$  is the bending moment at station  $i$ .

For this particular study the  $M'_{\ddot{\eta}_{j_i}}$ 's were not available, and therefore not used. However, bending mode contributions to bending moment are relatively small, and therefore their influence can be ignored without too much loss of fidelity.

Therefore, in this study

$$M_{B_i}(t) = M'_{\alpha_i}(t) \alpha(t) + M'_{\beta}(t) \beta(t)$$

The values of the raw data and time-varying coefficients (TVC's) used in actually implementing the above INT-21 ascent simulation may be found in Appendix A: Vehicle Raw Data Package and EOM Time-Varying Coefficients (TVC's).

### 3.2 SYSTEM DISTURBANCES

The only disturbances considered in this study are the horizontal wind speed profiles the vehicle is expected to encounter during actual ascent flights. Figure 3-1 shows, vectorially, the relationship between the horizontal wind speed vector,  $\vec{V}_w$ , the relative wind vector,  $\vec{V}_R$ , and the vehicle total velocity,  $\vec{V}_T$ . As is indicated by Fig. 3-1,

$$\vec{V}_w = \vec{V}_R + \vec{V}_T$$

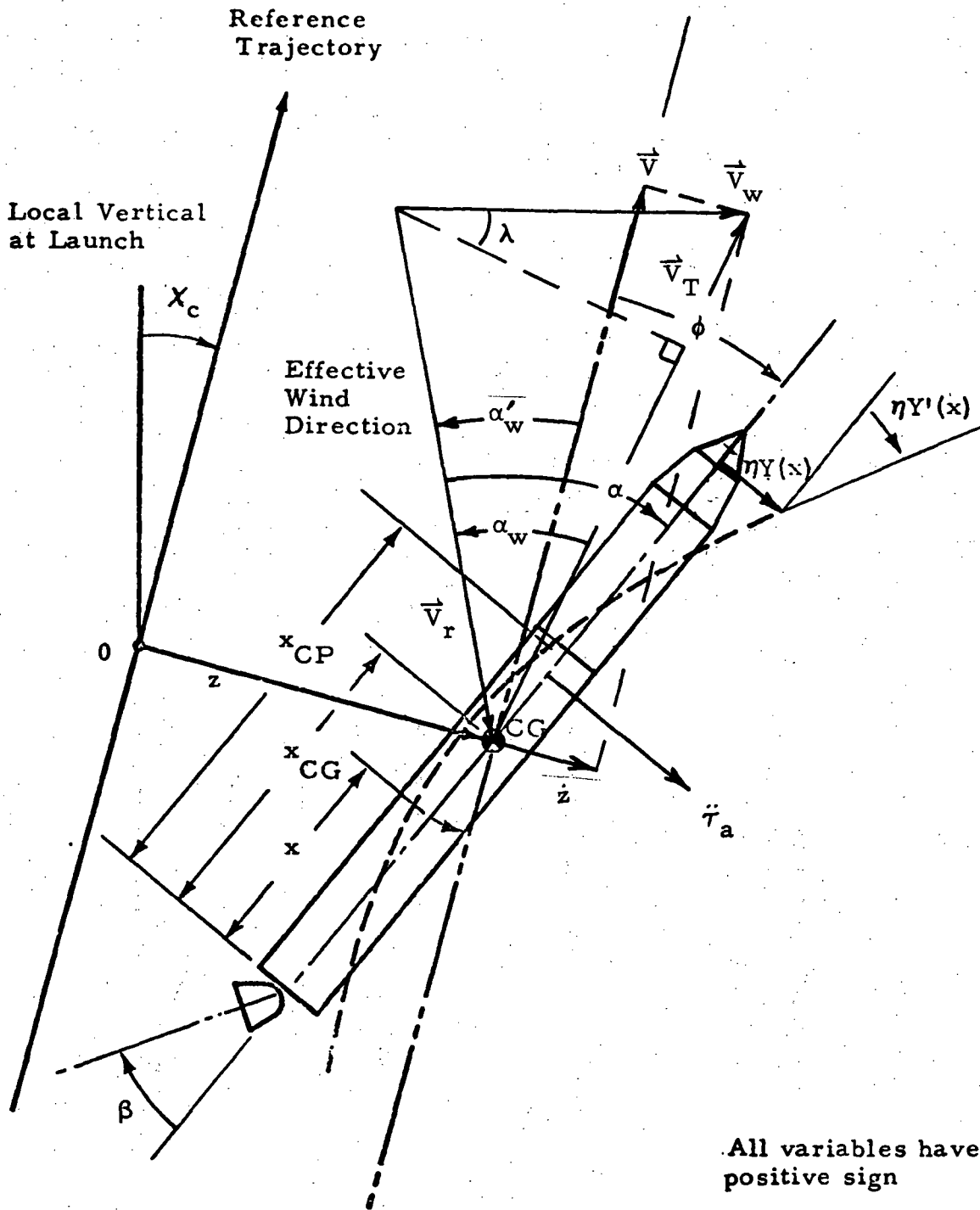


Fig. 3-1 - Coordinate System Employed for INT-21 Ascent Load Relief Control System Optimization

### 3.2.1 Synthetic Winds

During the original analog and digital simulation debug and checkout, and also during the actual controller design process, several synthetic winds were used to "force" the simulations. Using Eastern Test Range wind statistics, six synthetic winds,  $\alpha_w$ 's, tailored specifically to the INT-21 flight profile, were generated. They were developed as an integral part of the digital simulation constructed for INT-21.

These six winds, described below, are presented in Appendix B, Synthetic Wind Models, and were constructed via the procedures established in Ref. 4.

### 3.2.2 Six Synthetic Winds ( $\alpha_w$ 's) for INT-21

- $\alpha_w 1$  = 95 percentile scalar wind speed profile (steady-state) with 85% - reduced 99 percentile shear buildup and superimposed 85% - reduced 99 percentile gust at Mach 1.0.
- $\alpha_w 2$  = 95 percentile scalar wind speed profile (steady-state) with 85% - reduced 99 percentile shear buildup and superimposed 85% - reduced 99 percentile gust at Maximum  $q$ .
- $\alpha_w 3$  = 95 percentile scalar wind speed profile (steady-state) with 99 percentile shear backoff (reverse shear) starting at 10 km.
- $\alpha_w 4$  = 95 percentile scalar wind speed profile (steady-state) with 85% - reduced 99 percentile gust superimposed starting at 10 km and followed by 85% - reduced 99 percentile shear backoff (reverse shear).
- $\alpha_w 5$  = 95 percentile scalar wind speed profile (steady-state) with 85% - reduced 99 percentile shear buildup and superimposed 85% - reduced 99 percentile gust at maximum  $q$ .
- $\alpha_w 6$  = 95 percentile scalar wind speed profile (steady-state) with 85% - reduced 99 percentile shear buildup and superimposed 85% - reduced 99 percentile gust at Mach 2.0.

Two of these winds,  $\alpha_w 2$  and  $\alpha_w 3$ , were duplicated in the analog computer simulation of the system dynamics and were used in the initial control gain schedule optimization. These two winds were also used as

forcing functions in the all-digital simulation. The resulting solution curves were used as "check solutions" to verify the analog computer generated solution curves.

In order to help clarify the procedure for synthetic wind construction, a brief description of  $\alpha_w 2$  (gust at max  $q\alpha$ ) and  $\alpha_w 6$  (gust at Mach 2.0) generation follows.

As shown in Fig. 3-2, wind speed profiles are constructed with altitude the independent variable, using the procedures established in Ref. 4. These functions of altitude are then processed in the digital computer program, using the approximation

$$\alpha_w \cong \tan^{-1} \left( \frac{V_w \cos \chi_c}{V - V_w \sin \chi_c} \right)$$

$\alpha_w 2$  and  $\alpha_w 6$  curves resulting from this processing are shown in Fig. 3-3. All of the synthetic winds are presented in Appendix B, Synthetic Wind Models.

### 3.2.3 Measured Winds

In the performance verification phase of this study (see Section 6), 970 different measured winds were used as input disturbances. These 970 FPS-16/Jimsphere wind profiles had been preprocessed and were in the form  $V_w$  versus flight time including a time speedup factor of 750 when the tape was run at 60 ips. Salient statistical characteristics for these winds are given in Section 6.

## 3.3 DESIGN OBJECTIVES

Results from recent gust penetration load investigations were analyzed to determine gust influences on INT-21 controller design. In Ref. 10, gust penetration loads on Saturn launch vehicles in sinusoidal gusts were investigated.

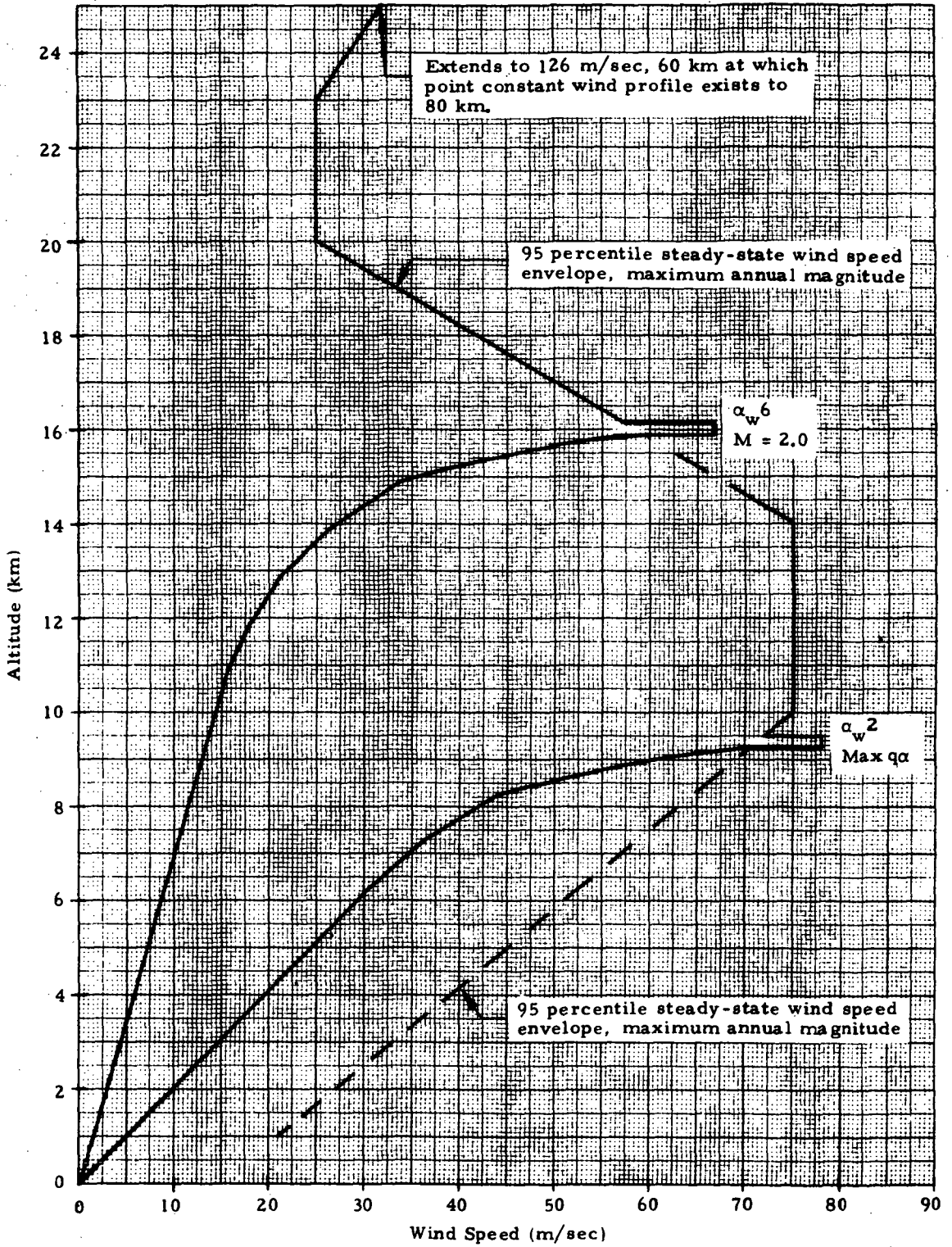


Fig. 3-2 - MSFC Synthetic Wind Profiles for the Eastern Test Range - Maximum Annual Magnitudes. Profiles generated using data and directions contained in Ref. 4 (M = Mach number)

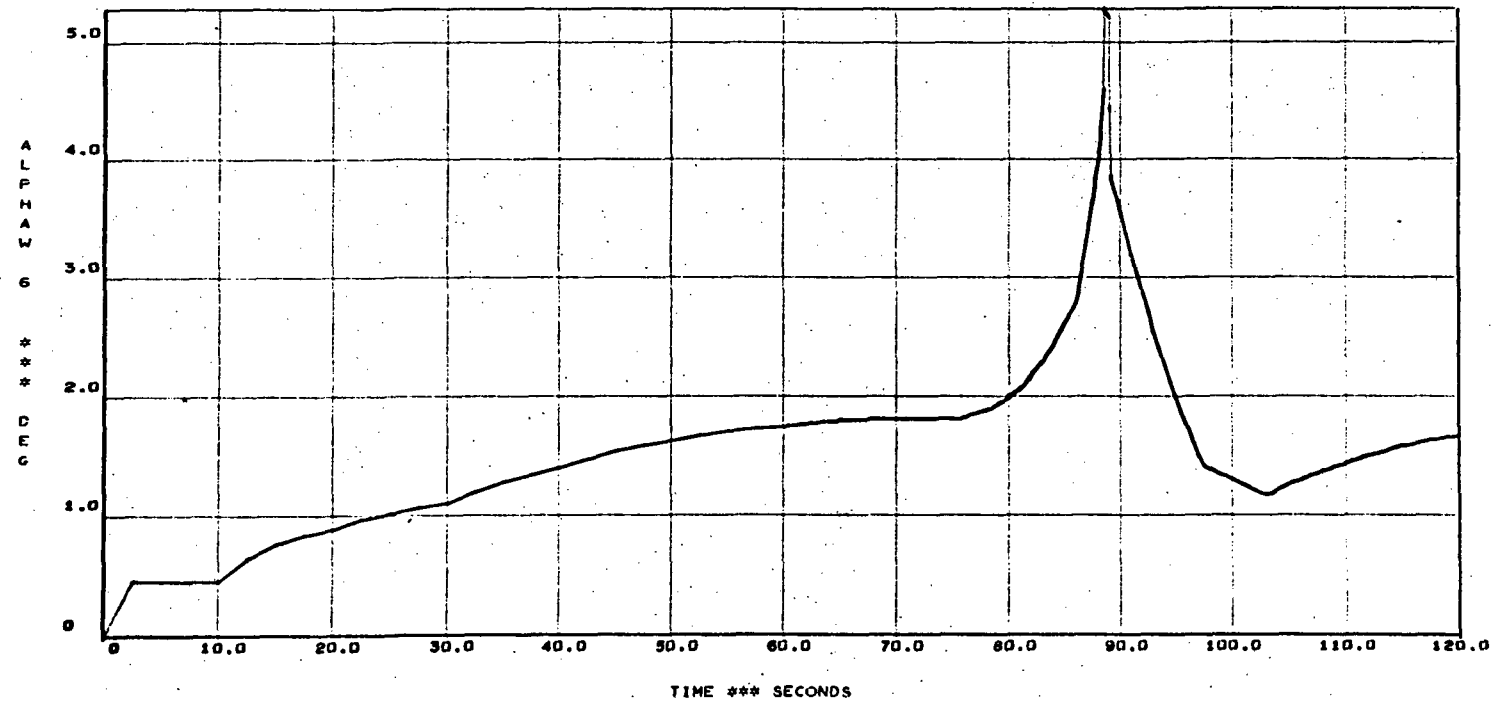
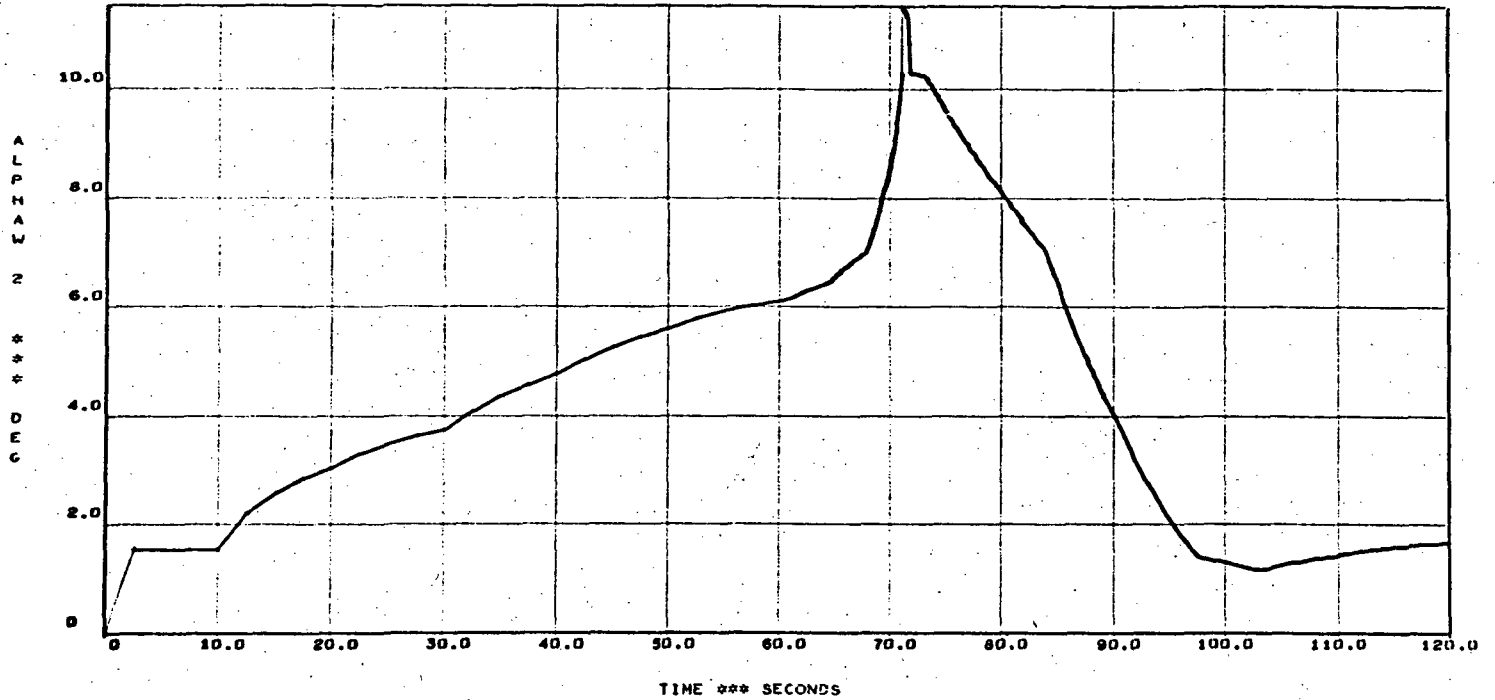


Fig. 3-3 - SC 4020 Plots of  $\alpha_w 2$  and  $\alpha_w 6$  for INT-21 Ascent

$\alpha_w 2$  = 95 Percentile Scalar Wind Speed Profile (steady-state) with 85%-Reduced 99 Percentile Shear Buildup and Superimposed 85%-Reduced 99 Percentile Gust at Maximum  $q\alpha$

$\alpha_w 6$  = 95 Percentile Scalar Wind Speed Profile (steady-state) with 85%-Reduced 99 Percentile Shear Buildup and Superimposed 85%-Reduced 99 Percentile Gust at Mach 2.0

Figure 9, Ref. 10, is reproduced here as Fig. 3-4, and presents Saturn V gust penetration loads as a function of penetration depth into sinusoidal gusts at maximum dynamic pressure ( $M = 1.6$ ). This information is calculated for the worst gust wave length  $L_g = 0.95 L_b$  that was found in this study, where  $L_b$  denotes body length (110 m).

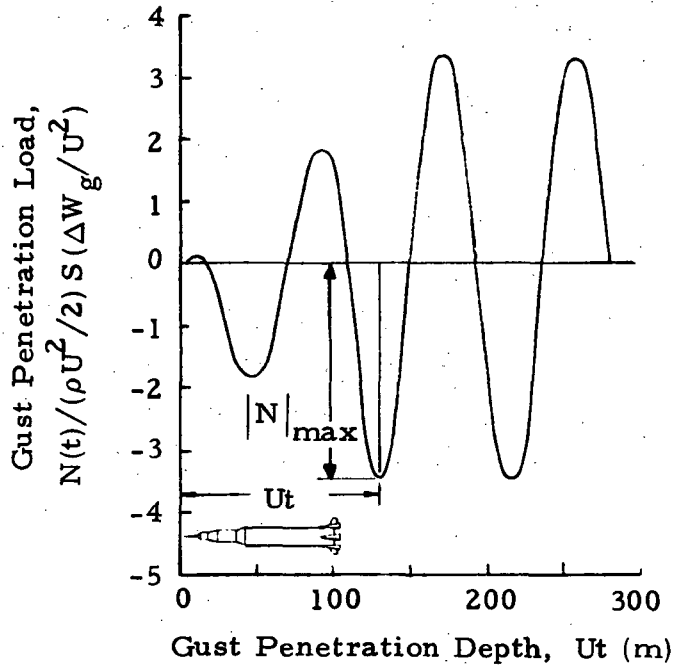


Fig. 3-4 - Saturn V Gust Penetration Loads as a Function of Penetration Depth into Sinusoidal Gust ( $L_b/L_g = 1.05$ ) at Maximum Dynamic Pressure ( $M = 1.6$ )

The normal force corresponding to the unity calibration in Fig. 3-4 is given by

$$\left( \rho \frac{U^2}{2} \right) S \left( \frac{\Delta W_g}{U} \right),$$



where

$$\rho = \text{air density, kg/m}^3$$

$$U = \text{vehicle velocity, m/sec}$$

$$S = \text{reference area, m}^2, S = \pi c^2/4$$

$$c = \text{reference length (maximum body diameter), m}$$

$$\Delta W_g = \text{amplitude of sinusoidal gust velocity normal to vehicle path, m/sec}$$

At the altitude where Saturn V attains a speed of  $M = 1.6$  ( $\approx 12.4$  km), the speed of sound is 295 m/sec. Thus, at this altitude

$$U = 1.6 \times 295 = 472 \text{ m/sec}$$

The dynamic pressure  $q = \rho U^2/2$  at this flight condition is

$$q = q_{\max} = 10,580 \frac{\text{N}}{\text{m}^2} .$$

The reference area for Saturn V is

$$S = 79.36 \text{ m}^2 .$$

Thus,

$$\begin{aligned} \left( \rho \frac{U^2}{2} \right) S &= 10,580 \times 79.36 \text{ N} \\ &= 839,000 \text{ N} \end{aligned}$$

The sinusoidal gusts are defined by  $\Delta W_g \sin 2\pi (U/L_g)t$ , where  $\Delta W_g$  is the sinusoidal peak amplitude. For a worst case sinusoidal gust =  $5 \sin 2\pi (U/L_g)t$  (m/sec),

$$\frac{\Delta W_g}{U} = \frac{5 \text{ m/sec}}{472 \text{ m/sec}} = 0.0106 .$$

Therefore, the normalizing factor in Fig. 3-4 is

$$\begin{aligned} \left(\rho \frac{U^2}{2}\right) S \left(\frac{\Delta W}{U} \frac{g}{g}\right) &= 839,000 \times 0.0106 \text{ N} \\ &= 8,900 \text{ N.} \end{aligned}$$

From Fig. 3-4, the peak normalized gust induced side force is 3.5 which amounts to

$$|N|_{\max} = 3.5 \left(\rho \frac{U^2}{2}\right) S \left(\frac{\Delta W}{U} \frac{g}{g}\right) = 3.5 \times 8,900 \text{ N} = 31,150 \text{ N.} \quad (\text{I})$$

This force may be compared with typical side forces experienced by the Saturn V in the  $M=1.6$  region of ascent flight. For Saturn V, aerodynamic side force,  $F_N$  (normal force), is  $F_N = MK_2\alpha$ .

$$\begin{aligned} MK_2 &= (1.83 \times 10^6 \text{ kg}) \times (7.0 \frac{\text{m}}{\text{sec}^2 \text{-rad}}) \\ &= 12.8 \times 10^6 \frac{\text{N}}{\text{rad}} \end{aligned}$$

Thus, for a 0.1 rad (representative) angle of attack,  $\alpha$ ,

$$F_N = MK_2\alpha = (12.8 \times 10^6 \frac{\text{N}}{\text{rad}}) (0.1 \text{ rad}) = 1.28 \times 10^6 \text{ N} \quad (\text{II})$$

The ratio of these two types of forces (I and II) is

$$\frac{3.115 \times 10^4}{1.28 \times 10^6} = 2.43 \times 10^{-2} = 0.0248.$$

Therefore, worst case side loads due to sinusoidal gusts are rather small compared to typical Saturn V side loads and a similar situation should be obtained for INT-21. Based on this result, it is apparent that no additional control effort is needed to handle gust alleviation requirements. However,

as mentioned in the Introduction, a unified design approach was chosen in which gust induced load effects were included throughout controller design by including gusts with the synthetic design winds.

The overall dominating goal of this study was the relief of structural loads through control system selection and optimization. Specifically, this means minimization of peak structural loads during the INT-21 ascent flight. Further, peak loads should trend in the direction indicated by Fig. 3-5, Bending-Moment Capability During First-Stage Flight for Saturn Voyager.

At the same time that load relief was being achieved, it was necessary to obtain satisfactory stability and terminal drift characteristics. Additionally, control system sensitivity to off-nominal environment characteristics was to be minimized and emphasis placed on reliability, optimality and simplicity.

Finally, the control system final design had to pass an exacting test — system response to the 970 measured winds was to exhibit desirable statistical response characteristics.

NOTE: Data curves computed using data from following references:

- MSFC Memo R-P&VE-SJ-66-132, "Structural Data for Saturn Voyager Studies," 27 June 1966.
- MSFC Memo R-AERO-AD-66-59, "Static Aerodynamic Characteristics ..." 20 December 1966, Figs. 39 thru 43.

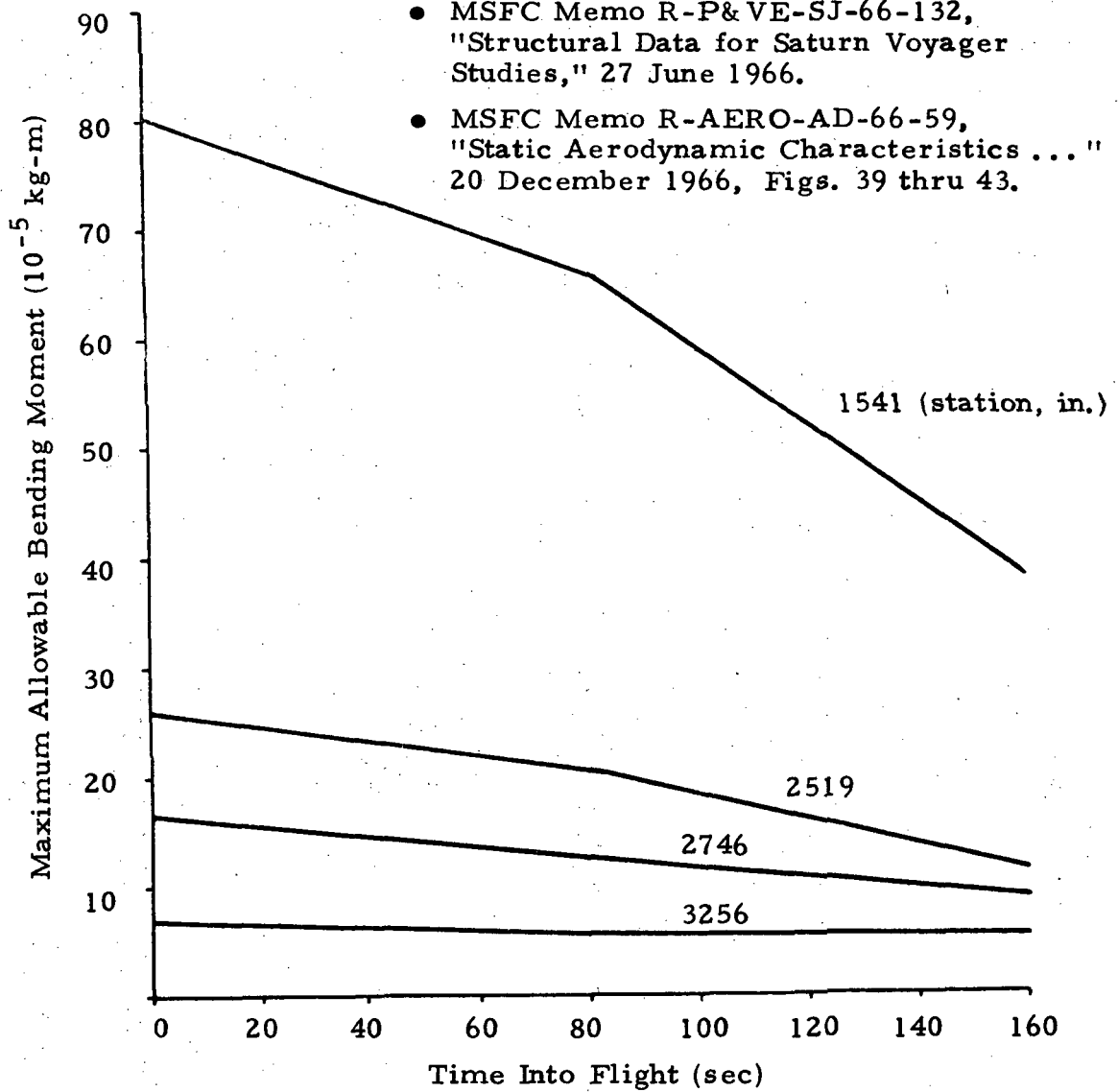


Fig. 3-5 - Bending-Moment Capability During First-Stage Flight for Saturn Voyager

Section 4

SELECTION OF LOAD RELIEF PERFORMANCE CRITERION

Since the earliest stages of this study it was recognized that it would be desirable to represent peak bending moments directly in any performance measure minimization scheme. The availability of Lockheed's Hybrid Optimizer (Section 2) meant that just such a direct representation of design goals could be implemented.

Keeping the above in mind, various formulations of performance criteria were considered. The best performance criterion that was found during this study, and the criterion used in all of the optimization computer runs, is described below.

● Performance Criterion Used During INT-21 Load Relief Optimizations:

Minimize the Performance Measure

$$J [t_{\nu}, t_{\nu+T}] = \max_{j=A, B} \left[ \max_{i=1, 2} \left\{ \left| \frac{M_{B_{ij}}/M'_{\beta_i}}{M_{B_{iME}}/M'_{\beta_i}} \right| \right\} p_i + \frac{q}{T} \int_{t_{\nu}}^{t_{\nu+T}} \left( \frac{\dot{\phi}_{s_j}}{\dot{\phi}_{s_{ME}}} \right)^2 dt \right]$$

where

- a.  $[t_{\nu}, t_{\nu+T}]$  is the "look-ahead interval" over which optimization (J minimization) is to be effected. T was set experimentally at 15 sec.
- b.  $[t_{\nu}, t_{\nu+1}]$  is the "update interval," a 5-sec interval. After optimization has been effected over "look-ahead interval"  $[t_{\nu}, t_{\nu+T}]$ , the next "look-ahead interval" is then  $[t_{\nu+1}, t_{\nu+1} + T]$ , because the "look-ahead interval" starting point has been updated.
- c.  $M_{B_{ij}}$  is the bending moment at critical station i due to wind j. Using the bending moment information available in Fig. 4-6 of Ref. 5 (Fig. 4-2 in this report), 2350 inches was designated as station 1 and 1800 inches as station 2. See Figs. 4-1 and 4-2.

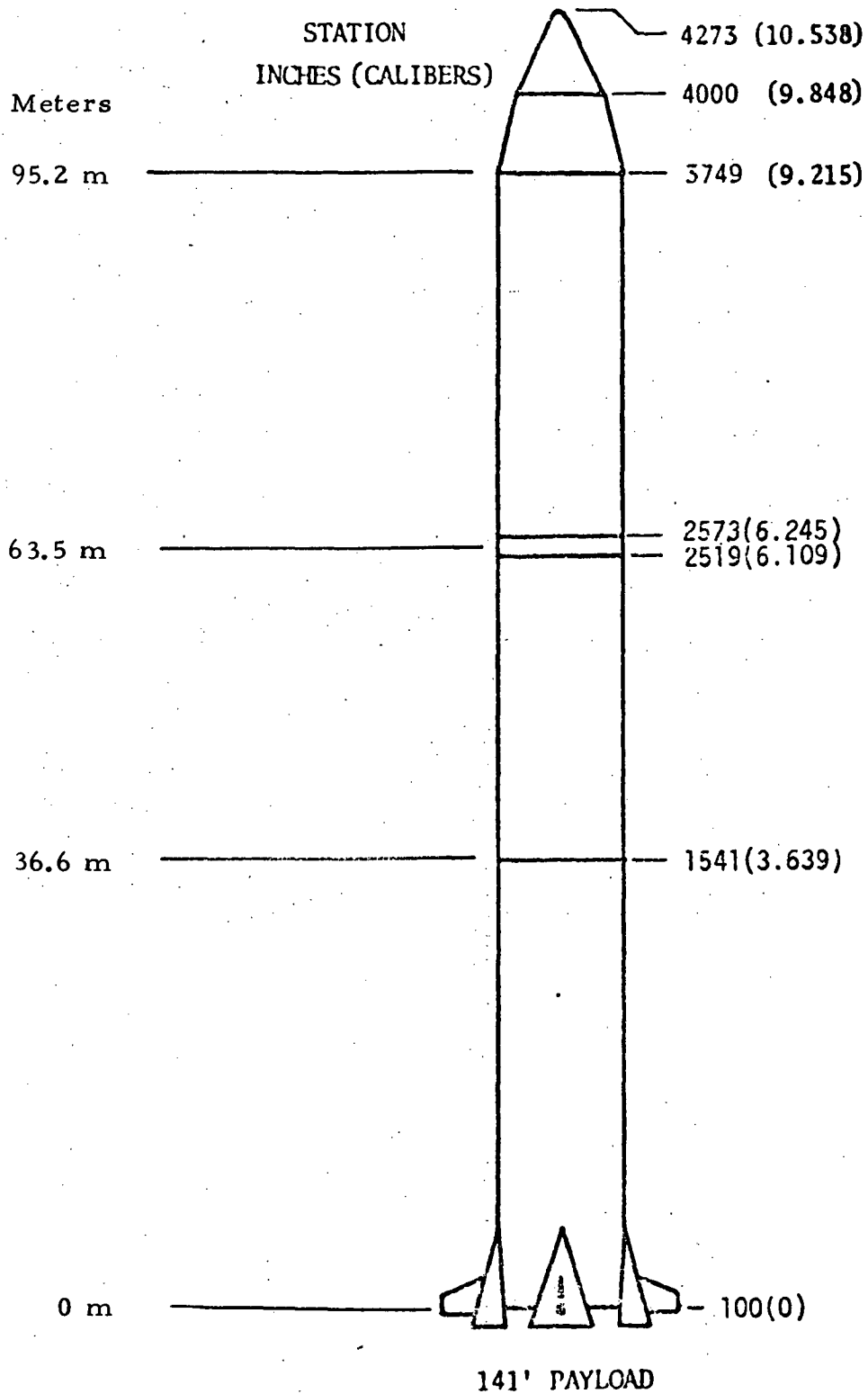
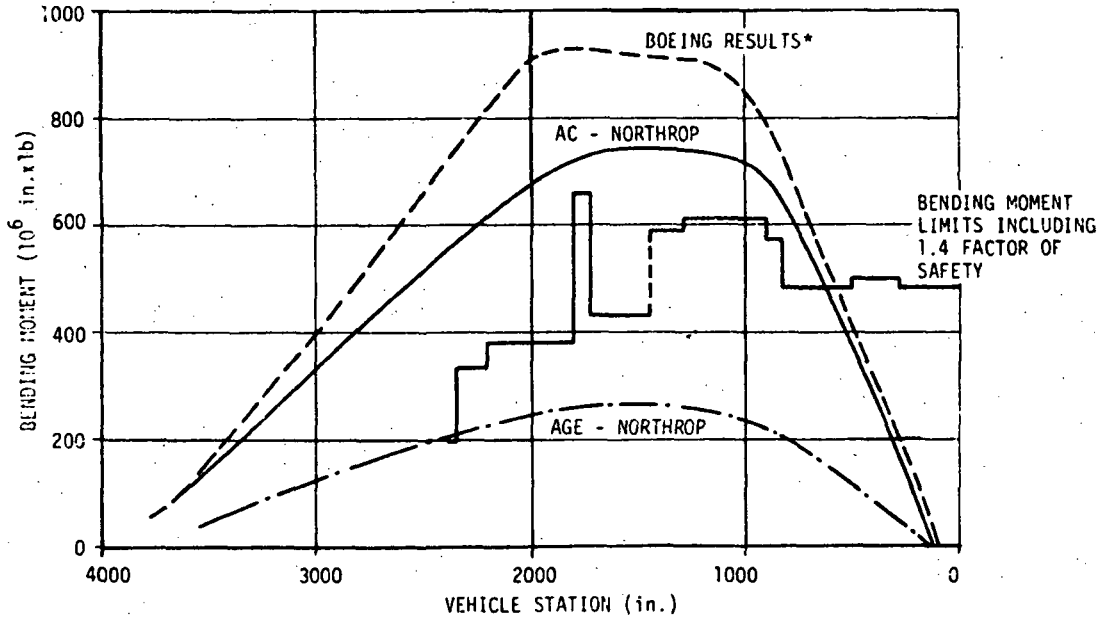


Fig. 4-1 - INT-21 with 141-Foot MDAC Payload:  
Identification of Vehicle Stations



\*DESIGN DATA REPORT INT-21 LAUNCH VEHICLE WITH MDAC 141-FOOT PAYLOAD, ATTACHMENT TO MEMO 5-9406-INT-21-27 (THE BOEING COMPANY)

Fig. 4-2 - Bending Moment Comparisons - 141-Foot Payload

$$\frac{M_{B_i}}{M'_{\beta_i}} = \left( \frac{M'_{\alpha_i}}{M'_{\beta_i}} \right) \alpha + \beta$$

$M_{B_i}_{ME}$  = maximum expected bending moment at station i.

$M_{B1}_{ME} = M_{B2}_{ME} = 10^8$  N-m, and the weighting factors,  $p_i, i=1,2$ , are:  $p_1 = 1.0, p_2 = 0.5$ .  $p_1$  is twice as large as  $p_2$ , reflecting i) the much lower structural limit at station 1, and ii) the desire to penalize forward station bending moment peaks so that a wide range of payload structural characteristics may easily be accommodated.

- d.  $\dot{\phi}_{s_j}$  is the sensed rate of the pitch attitude error due to wind j.  
 $\dot{\phi}_{s_{ME}}$  is the maximum expected value of  $\dot{\phi}_s$ , 5.0 deg/sec.
- e. q is an experimentally set positive number just large enough to guarantee INT-21 stability.

The bending moment critical stations were selected with the aid of the information presented in Fig. 4-2, which shows previously obtained bending moment distributions (versus station) on the same plot with bending moment (structural) limits. These structural limits are known only up to the top of the S-II stage (2nd stage) because the 3rd stage space station module to be carried by INT-21 is not yet well defined.

The structural limits presented in Fig. 4-2 are calculated for  $t_{\max \alpha}$ . They can be expected to change with time as is indicated by the Saturn Voyager information presented in Fig. 3-5.

In load relief controller design the dominant purpose is to minimize the maximum (peak) structural loads. This objective is specified directly in the performance criterion spelled out above.



Section 5  
CONTROLLER DESIGN AND OPTIMIZATION

5.1 SELECTION OF CONTROLLER

Two control laws have figured most prominently in this study. They are:

- Control Law 1

$$\beta_{c_1}(t) = a_0(t) F_{\phi}(s) \phi_s(t) + a_1(t) F_{\dot{\phi}}(s) \dot{\phi}_s(t)$$

- Control Law 2

$$\beta_{c_2}(t) = a_0(t) F_{\phi}(s) \phi_s(t) + a_1(t) F_{\dot{\phi}}(s) \dot{\phi}_s(t) + g_2(t) F_{\ddot{\tau}_a}(s) \ddot{\tau}_{a_s}(t)$$

where subscript s indicates sensor output. Perfect sensors were assumed; therefore, sensor dynamics were not included.

$$\phi_s(t) = \phi(t) + \sum_{i=1}^3 Y'_{i_{x_{pg}}}(t) \eta_i(t); \quad \dot{\phi}_s(t) = \dot{\phi}(t) + \sum_{i=1}^3 Y'_{i_{x_{rg}}}(t) \dot{\eta}_i(t)$$

$$\ddot{\tau}_{a_s}(t) = \ddot{z}_{cg} + (x_a - x_{cg}) \ddot{\phi} + \sum_{i=1}^3 Y_{i_{x_a}}(t) \ddot{\eta}_i(t)$$

where

$$\ddot{z}_{cg} = K_2 \alpha + K_3 \beta + \sum_{i=1}^3 G_{t_i} \eta_i + B_E \ddot{\beta}$$

Refer to Fig. 3-1 for coordinate system that is employed.

Control Law 1, an attitude control system, includes attitude and attitude rate feedback.

Control Law 2, one type of load relief control law, includes attitude, attitude rate, and accelerometer feedback. The accelerometer output is essentially proportional to the lateral acceleration (lateral with respect to the vehicle centerline) of the vehicle center of gravity.

The filters used are described by

$$F_{\phi}(s) = \frac{1 + 10s}{1 + 21.37s + 1.916s^2}$$

$$F_{\dot{\phi}}(s) = \frac{1 + 0.2s + 0.1111s^2}{1 + 0.6071s + 0.2629s^2 + 0.06207s^3}$$

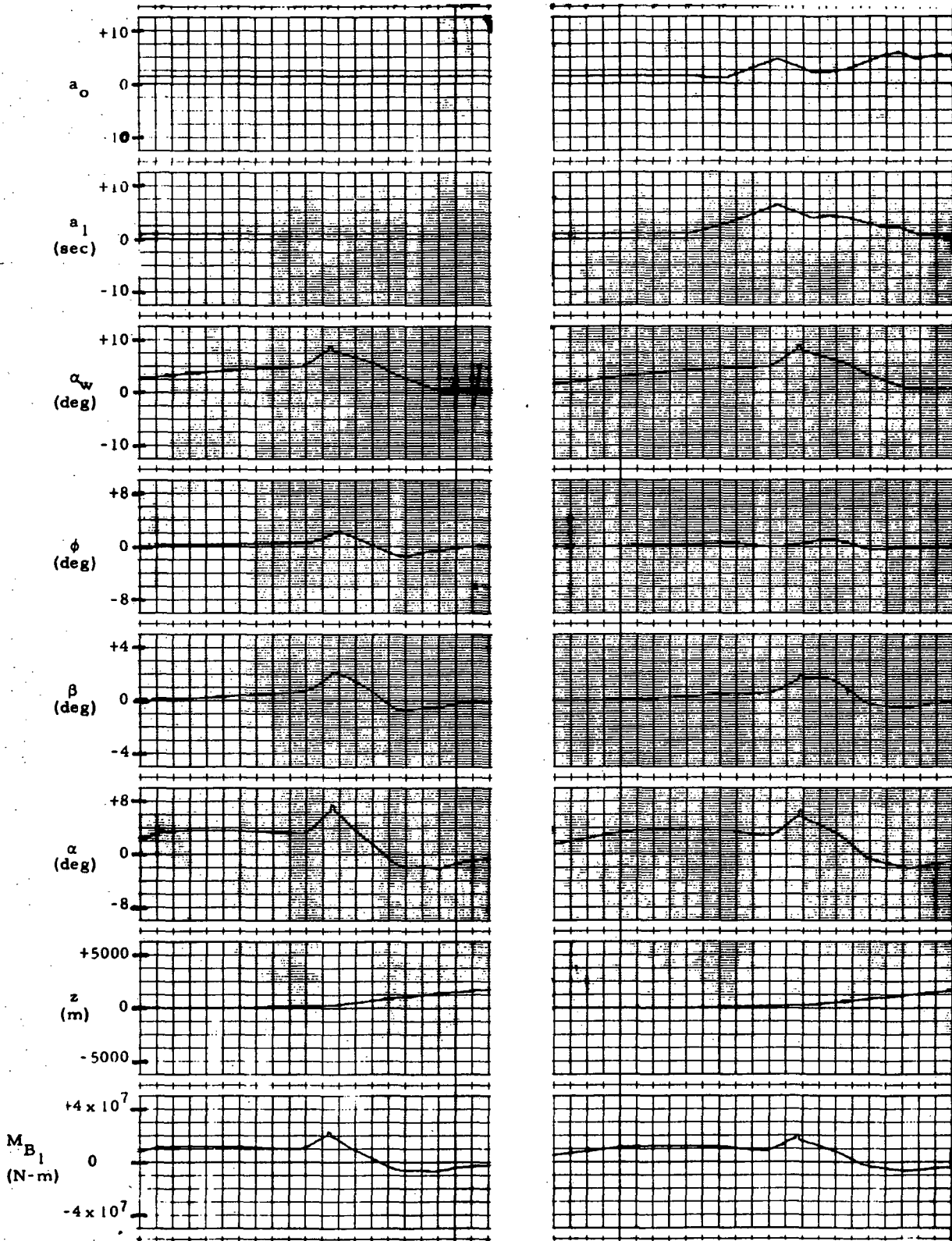
$$F_{\ddot{\tau}_a}(s) = \frac{1}{1 + 2.0s + 0.2778s^2}$$

These filters were extracted from Ref. 5, except that  $F_{\ddot{\tau}_a}(s)$ , presented above, was found to be far more effective in stabilizing the vehicle than the

$$F_{\ddot{z}}(s) = \frac{1}{1 + 0.2s + 0.02778s^2}$$

presented in Table 3-2, p. 3-4, of Ref. 5.

In order to get some feel for INT-21 dynamics and during the initial optimizer checkout, some optimization runs were performed with Control Law 1 implemented in the analog simulation. As is readily apparent in Fig. 5-1, very little load relief may be obtained using a pure attitude control system.



a. Constant Control System Gains:  
 $a_0 = 1.4$ ,  $a_1 = 1.0$  sec,  $g_2 = 0$  deg-sec<sup>2</sup>-m<sup>-1</sup>

b. "Optimized"  $a_0$  and  $a_1$  Control System Gain Schedules;  $g_2 = 0$  deg-sec<sup>2</sup>-m<sup>-1</sup>.

Fig. 5-1 - Analog Computer Solutions of INT-21 System Dynamics

However, these attitude control solution curves do serve to point out the mechanism by which load relief is effected while using a pure attitude control system. As is shown by the optimized gain schedules, load relief is achieved by increasing  $a_0$  and  $a_1$  gains, thereby forcing the vehicle to reduce  $\phi$  and approach the  $X_c(t)$  direction more closely. This routine then provides the maximum "turning into the wind" that is possible using pure attitude control.

The optimized results further serve to demonstrate that the optimizer does find the best way of satisfying the performance criterion once a particular form of control law has been selected.

Intuitively, Control Law 2 seemed to hold out considerable promise as a load relief controller, provided the terminal drift could be kept reasonable. It was expected that  $\ddot{\tau}_a$  would behave very much like  $\alpha$ , and the optimizer could then shape the classical load relief gain schedules for such a controller, reducing  $a_0$  and increasing  $g_2$  during the high  $M'_\alpha(t)$  portions of the flight in order to "head into the wind" (minimize  $\alpha$ ).

Three other control laws were considered in this study. They are listed below without any shaping filters shown.

● Control Law 3

$$\beta_{c_3} = a_0 \phi_s + a_1 \dot{\phi}_s + g_2 \ddot{\tau}_a + e_1 \hat{z}$$

● Control Law 4

$$\beta_{c_4} = a_0 \phi_s + a_1 \dot{\phi}_s + b_0 \hat{\alpha}$$

● Control Law 5

$$\beta_{c_5} = a_0 \phi_s + a_1 \dot{\phi}_s + b_0 \hat{\alpha} + e_1 \hat{z}$$

where

$$\hat{z} = \int_0^t (\ddot{r}_{a_s} + K_1 \phi_s) dt$$

$$\hat{\alpha} = (\ddot{r}_{a_s} - K_3 \beta_s)$$

Control Law 5 was not implemented during this study due to time and other limitations. It is included in this section because it possesses certain features that may well be worth studying in some future load relief project.

Control Law 3 was to be considered in the event that terminal drift became excessive. Control Law 4 could be used in  $\ddot{r}_a$  did not sufficiently correlate with  $\alpha$ ; and Control Law 5 was available in the event that the benefits of both Control Laws 3 and 4 were needed.

It was early observed that Control Law 2 was the simplest and, therefore, the most reliable load relief type control law in the group. Therefore, if none of Control Laws 3, 4 or 5 could provide substantial performance increase (versus Control Law 2), then Control Law 2 would be the best choice.

## 5.2 SELECTION OF DESIGN DISTURBANCES

In selecting meaningful disturbances to use in "forcing" the EOM during the optimization computer runs, four essential factors had to be kept in mind:

- As a general rule,  $\alpha_{\max}$  could be expected to be much larger than  $\beta_{\max}$  (see Figs. 4-1 and 4-2, Ref. 5).
- Comparing Fig. 4-2 (Bending Moment Comparisons) and Fig. 5-2 (Bending Moment Sensitivities vs Station), it is apparent that at the forward, most critical part of the structure, the bending moment is most sensitive to  $\alpha$  due to the fact that  $M'_\alpha$  is much greater than  $M'_\beta$  at the forward stations.
- $M'_\beta(t)$  shows little variation during ascent flight and may be introduced as a constant in the simulation. However,  $M'_\alpha(t)$  varies greatly during ascent flight, and this variation must be included in any complete analysis of the load relief problem.

$$M'_\alpha(t) = M'_{\alpha_{\text{peak}}} M'_{\alpha_{\text{SF}}}(t)$$

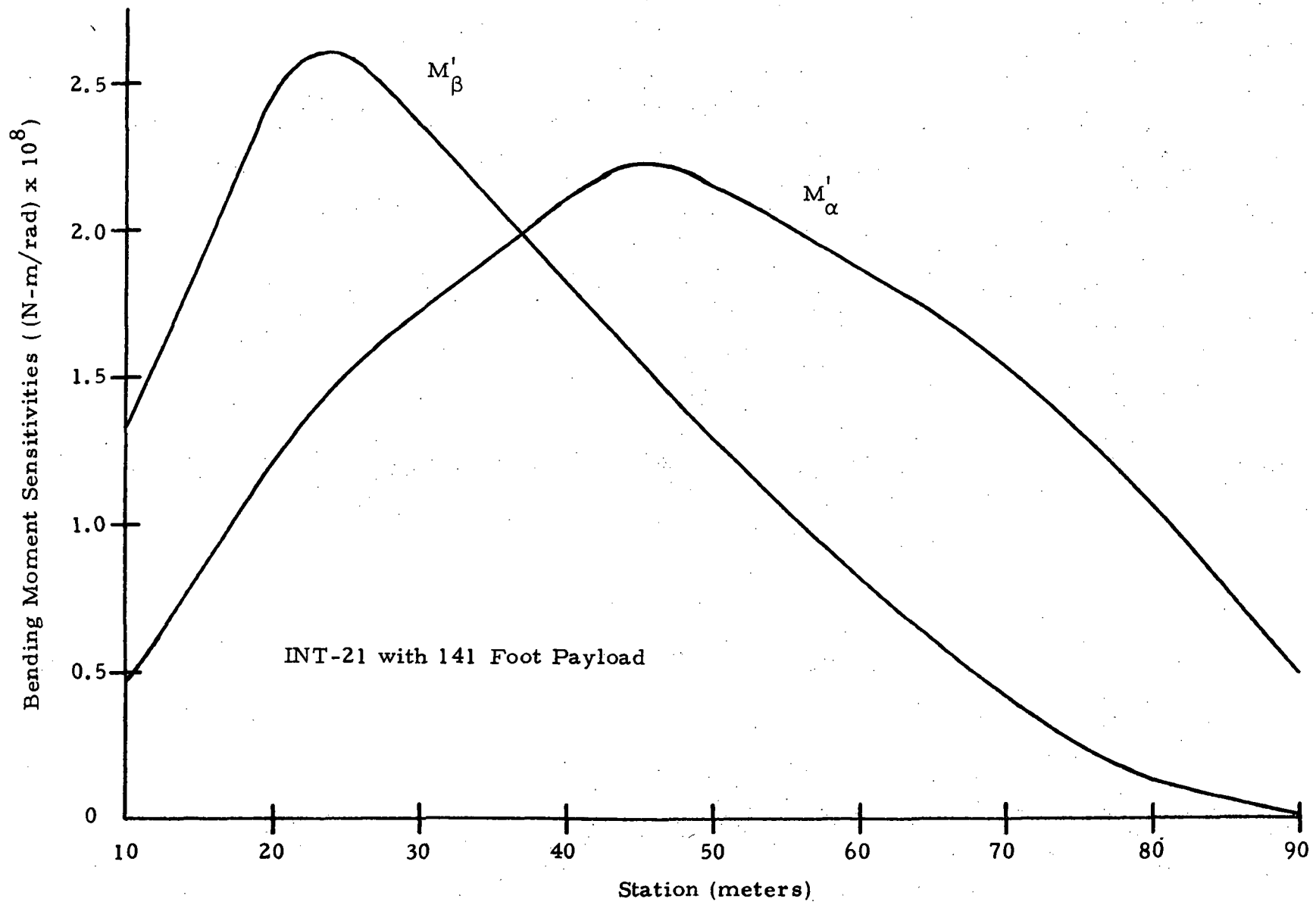


Fig. 5-2 - Bending Moment Sensitivities vs Station

where  $M'_{\alpha_{SF}}(t)$ , the  $M'_\alpha(t)$  shaping function (conservative estimate) is shown in Fig. 5-3. As expected,  $M'_{\alpha_{SF}}(t)$  behaves somewhat like dynamic pressure.

- As per the information covered in Fig. 3-5, bending moment structural limits could be expected to decrease with flight time (as a direct result of the increasing axial loads caused by decreasing vehicle mass and near constant thrust).

The first two factors listed above make it quite clear that the major portion of load relief (bending moment reduction) at critical stations can be had by minimizing  $\alpha$ .

The third point emphasizes that peak bending loads should be expected near  $t_{\max q\alpha}$ . Thus, an adverse synthetic wind gusting at  $\max q\alpha$  would be a useful design disturbance. So,  $\alpha_w2$  could be chosen as the Wind A (adverse condition A) used during optimizer runs. (See Section 2.6).

The last point emphasizes that minimum bending structural limits occur toward the end of ascent flights. Therefore, an adverse synthetic wind gusting in the latter portion of ascent flight would be a useful design disturbance. So,  $\alpha_w5$  could be chosen as the Wind B (adverse condition B) used during optimizer runs.  $\alpha_w6$  would not be an appropriate choice for Wind B because:

1. Its gust peaked at less than 5.4 deg, and
2.  $M'_\alpha(t)$  was already greatly reduced at  $t_{\text{Mach } 2.0}$ .

### 5.3 OPTIMIZATION RESULTS FOR SYNTHETIC WINDS

Before any worthwhile optimization results could be produced, three parameter values peculiar to the Hybrid Optimizer had to be established (see Section 2):

- Update Interval  $[t_\nu, t_{\nu+1}]$
- Look-Ahead Interval  $[t_\nu, t_{\nu+T}]$
- Stability Weighting Factor,  $q$

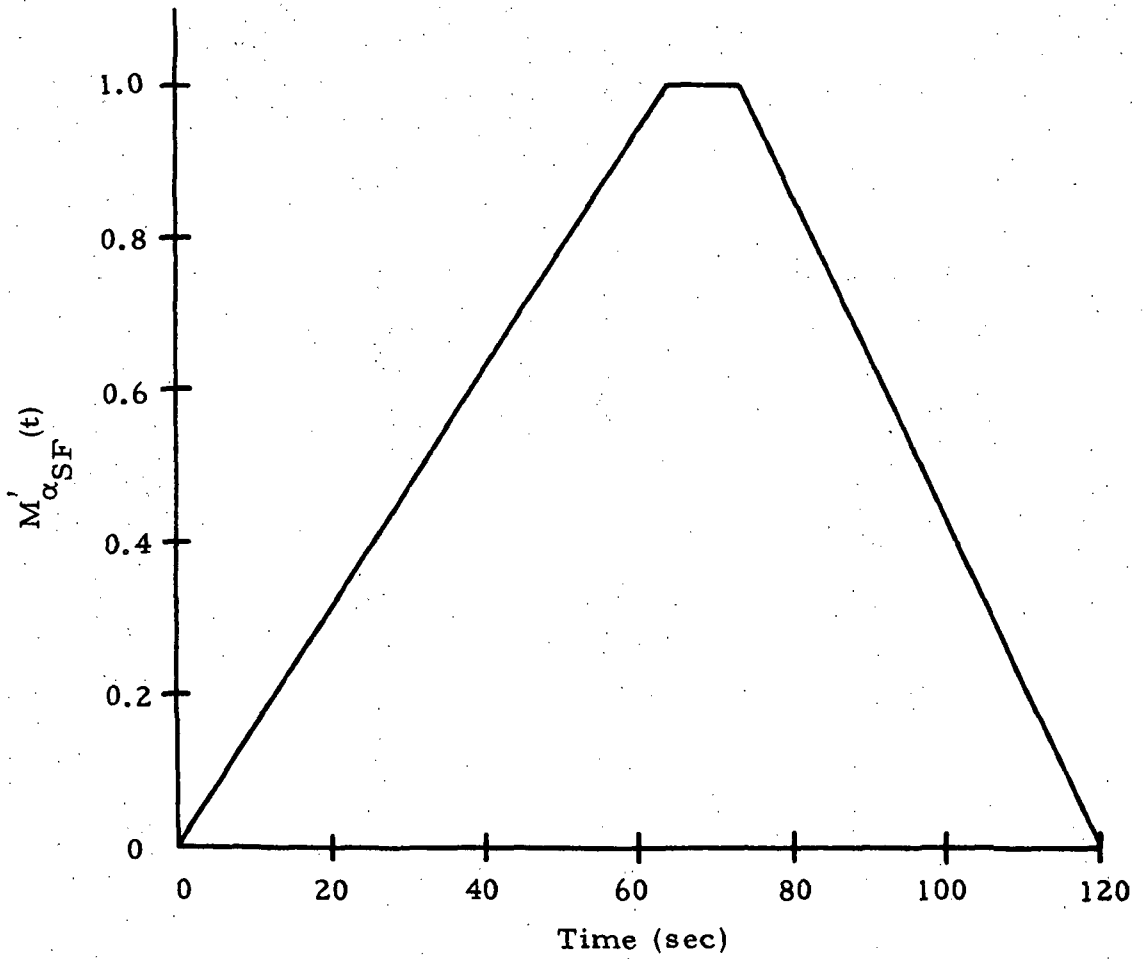


Fig. 5-3 -  $M'_{\alpha_{SF}}(t)$ , The Shaping Function for  $M'_{\alpha}(t)$



Selection of these optimizer parameters was essentially a trial and error process, except that the finalized 5 sec update interval and 15 sec look-ahead interval turned out to be the same as those used in some of the old Saturn V optimization studies.

q was set by first trying a wide range of values to locate the right region with satisfactory response characteristics and then following this rough search by a series of fine changes of q that eventually produced a q value yielding the best tradeoff among bending moment reduction, trajectory stability features, and terminal drift.

$\alpha_w2$  and  $\alpha_w3$  were the two adverse wind conditions (Wind A and Wind B) used as design disturbances in this study. The best early optimization results obtained for these two winds are presented in Figs. 5-4 and 5-5. Figure 5-6 presents an  $\alpha_w2$  digital solution check run.

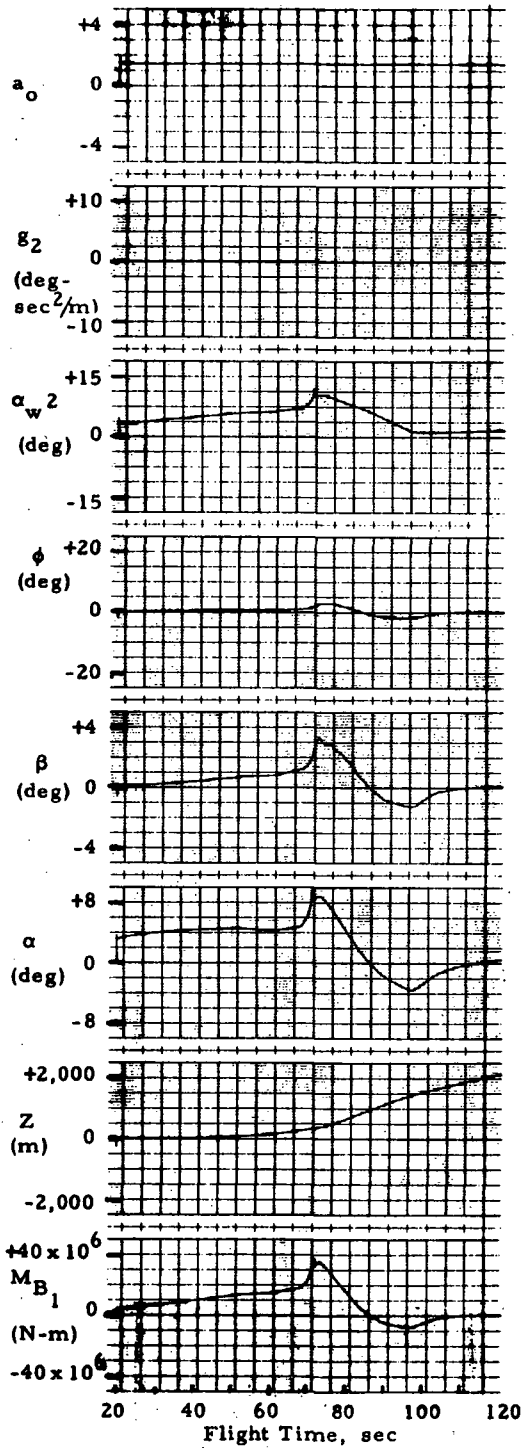
The optimized results yielded several points worth noting. For both  $\alpha_w2$  and  $\alpha_w3$  response,

$$M_{B1_{\max}} = 20.0 \times 10^6 \text{ N-m } (= 177 \times 10^6 \text{ lb}_f\text{-in.})$$

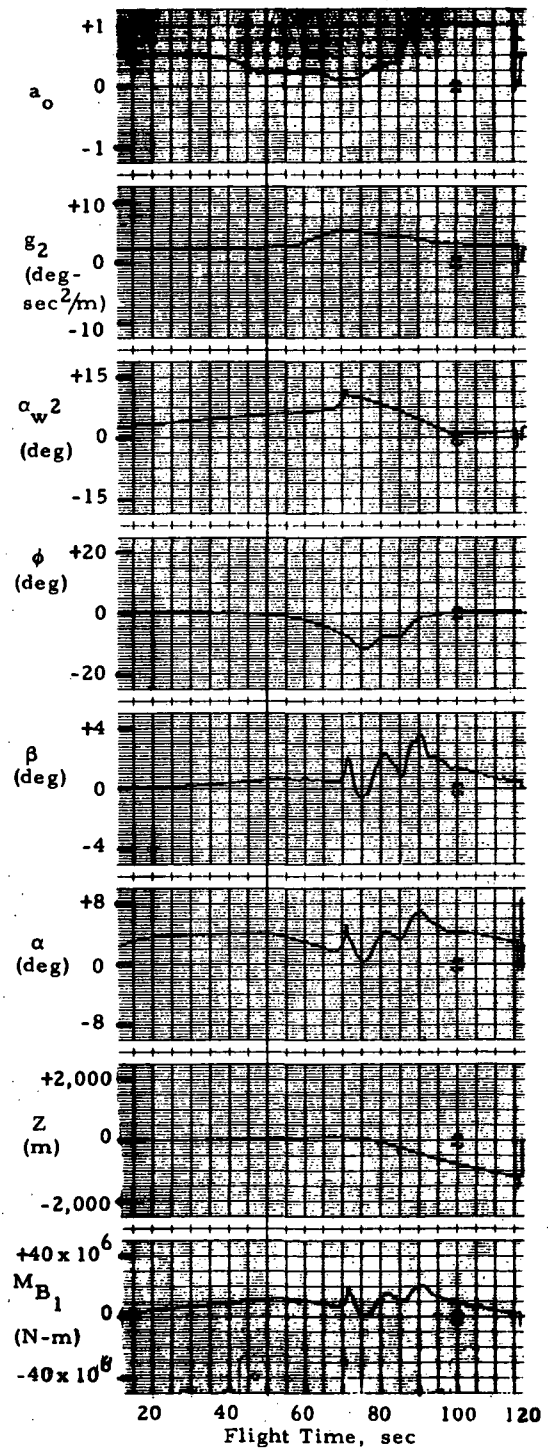
This may be compared with the information presented in Fig. 4-6, p. 4-8, of Ref. 5. This figure is reproduced in this report as Fig. 5-7, with Lockheed results added. Note, particularly, the situation at critical station 2350, with structural limit  $22.0 \times 10^6 \text{ N-m}$  ( $195 \times 10^6 \text{ lb}_f\text{-in.}$ ); best results prior to Lockheed's effort produced  $23.8 \text{ N-m}$  ( $210 \times 10^6 \text{ lb}_f\text{-in.}$ ) which were obtained by using the AGE control law. (See Ref. 5 for a description of AGE and the time-varying gain schedules used with it.)

Several other points worth emphasizing concerning response characteristics generated by Lockheed's optimized control system include:

1. The optimized control system yields strong "turning into the wind" features, resulting in:
  - a.  $\phi_{\max q\alpha} = -7.0 \text{ deg } (\alpha_w2)$  and

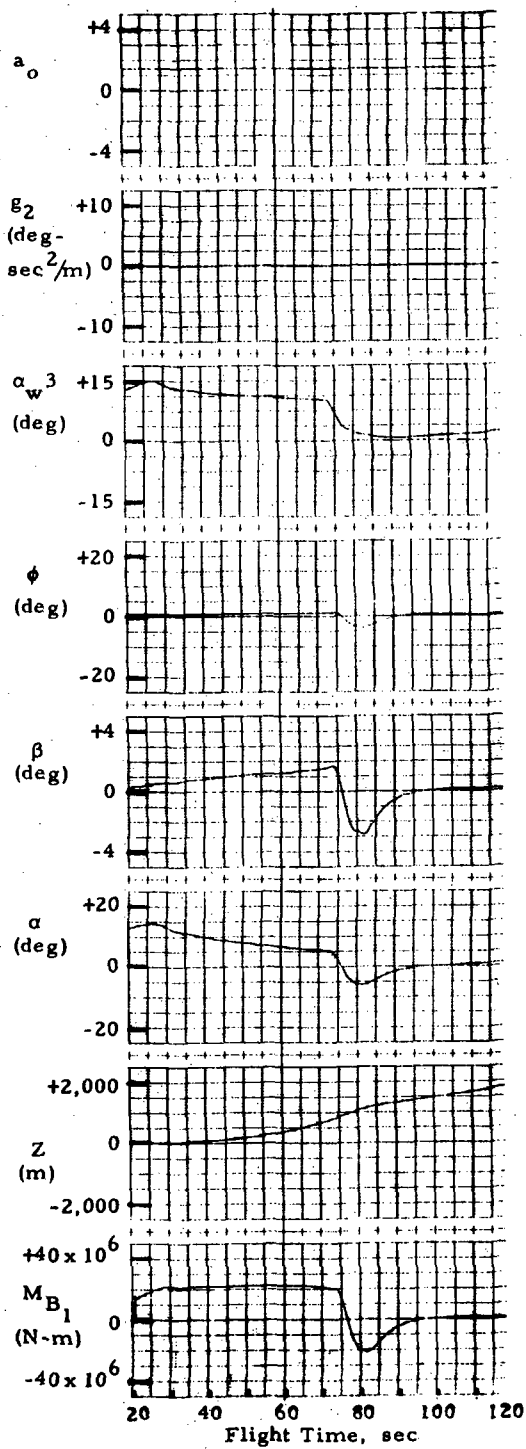


(a) Constant Gain Attitude Control System: Control Law 1 with  $a_o = 1.4$ ,  $a_1 = 1.0$  seconds

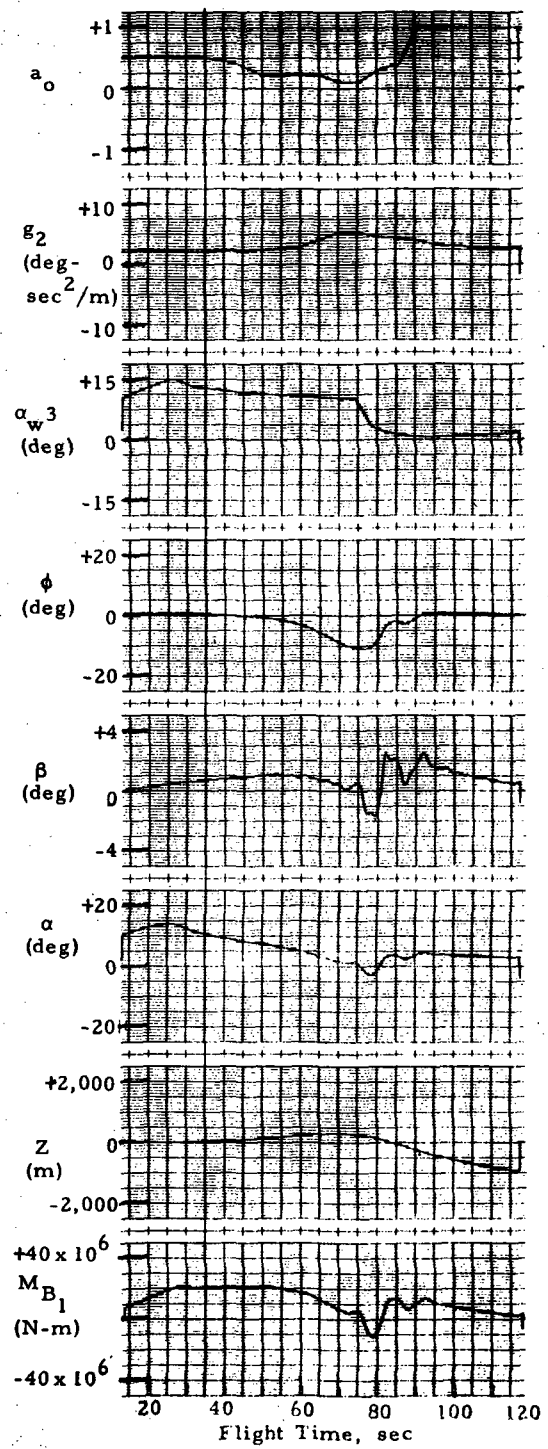


(b) Optimized Time-Varying Gains Load Relief Control System: Control Law 2 Including Optimized  $a_o(t)$ ,  $g_2(t)$  and  $a_1 = 1.5$  seconds

Fig. 5-4 - INT-21 Ascent Simulation Response to  $\alpha_w 2$



(a) Constant Gain Attitude Control System; Control Law 1 with  $a_o = 1.4$ ,  $a_1 = 1.0$  seconds



(b) Optimized Time-Varying Gains Load Relief Control System; Control Law 2 Including Optimized  $a_o(t)$ ,  $g_2(t)$  and  $a_1 = 1.5$  seconds

Fig. 5-5 - INT-21 Ascent Simulation Response to  $\alpha_w^3$

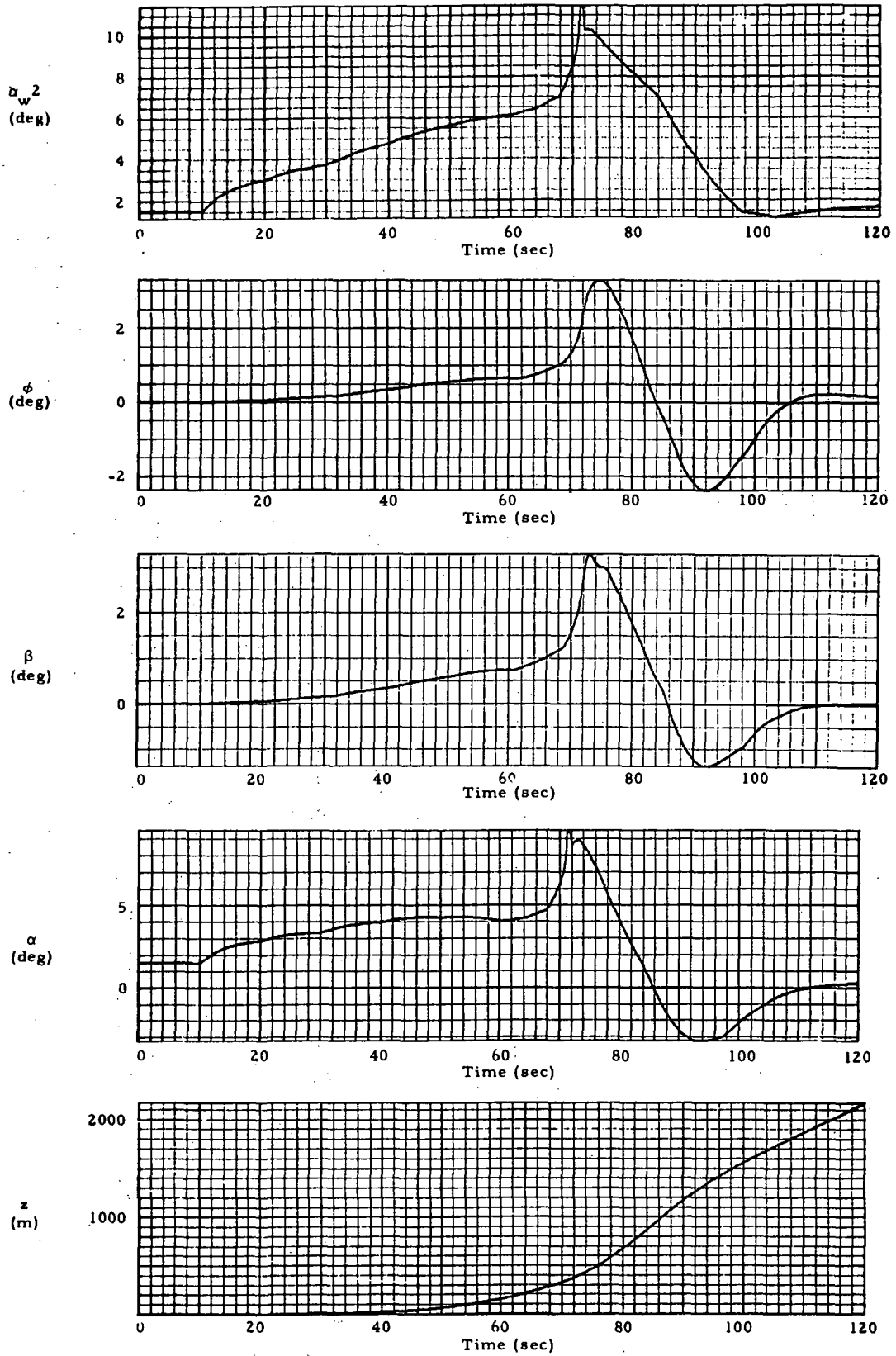
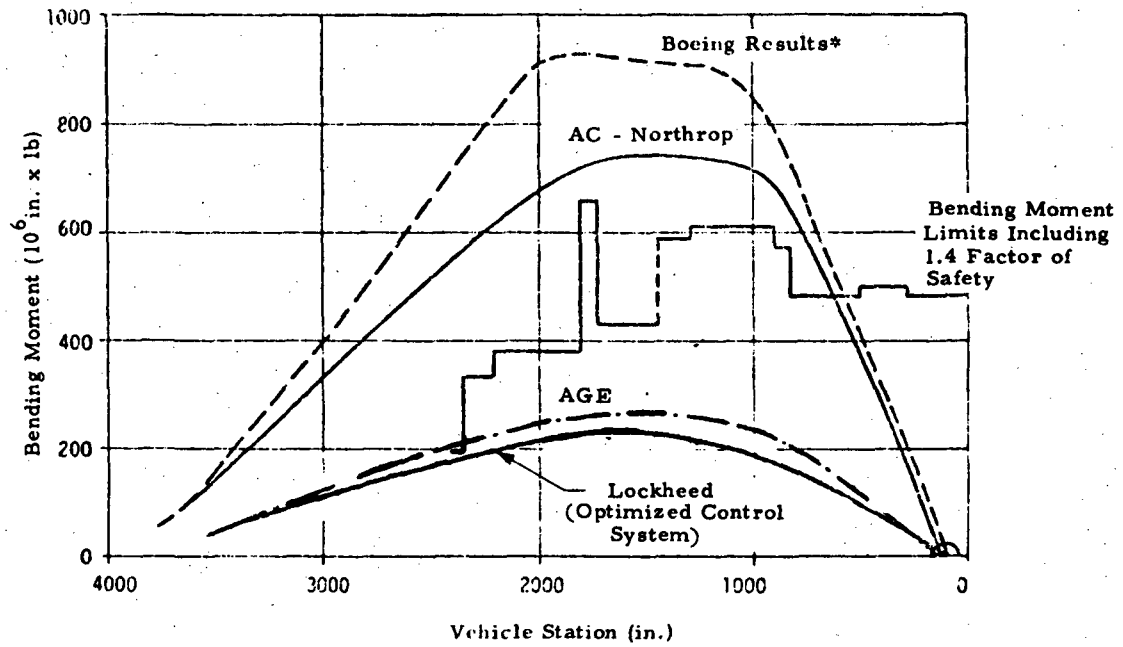


Fig. 5-6 - Digital Computer Solution of INT-21 System Dynamics for Constant Control System Gains:  $a_0 = 1.4$ ,  $a_1 = 1.0$  sec,  $g_2 = 0$  deg-sec<sup>2</sup>-m<sup>-1</sup> ( $\alpha_w 2$  Response)



\*Design data report INT-21 Launch Vehicle with MDAC 141-foot payload, attachment to Memo 5-9406-INT-21-27 (The Boeing Company)

Fig. 5-7 - Bending Moment Comparison Showing Advantage of Lockheed's Optimized Control System

$$\begin{aligned}\phi_{\min} &\cong -12 \text{ deg } (\alpha_w 2) \\ &\cong -11 \text{ deg } (\alpha_w 3)\end{aligned}$$

$$b. \alpha_{\max} q\alpha = +5.2 \text{ deg } (\alpha_w 2)$$

$$\alpha_{\max} = 6.8 \text{ deg } (\alpha_w 2)$$

$$\alpha_{\min} = -3.0 \text{ deg } (\alpha_w 3)$$

$\alpha_{\max} = 14 \text{ deg } (\alpha_w 3)$  occurs very early in the flight and does not cause  $M_{B1}$  to exceed  $20 \times 10^6 \text{ N-m}$  because of the relatively small value of  $M'_\alpha(t)$  at this point in the flight.

2. Engine deflection angle does not exceed 3.6 deg in magnitude and usually remains below 2.5 deg.
3. Terminal drift

$$Z_{\min} \Big|_{t=120 \text{ sec}} = -1,180 \text{ m } (\alpha_w 2) = -940 \text{ m } (\alpha_w 3)$$

After these two-optimized control gains runs were completed and analyzed, it was decided to optimize the third controller gain schedule,  $a_1(t)$ . This optimization effort also used  $\alpha_w 2$  and  $\alpha_w 3$  as the two adverse wind conditions (Wind A and Wind B, respectively) implemented on the analog console.

The results of the three-optimized control gains runs are presented in Figs. 5-8 and 5-9. It should readily be apparent that these final results exhibit the best features of any of the work done up until this time. These gain schedules are presented in Fig. 5-10.

The results shown in Figs. 5-8 and 5-9 exhibit the following additional desirable features:

1. After swinging out to about -10 deg, the attitude angle,  $\phi$ , stays in that vicinity longer, and is a smoother curve, due to the increased damping caused by the  $a_1(t)$  "hat."

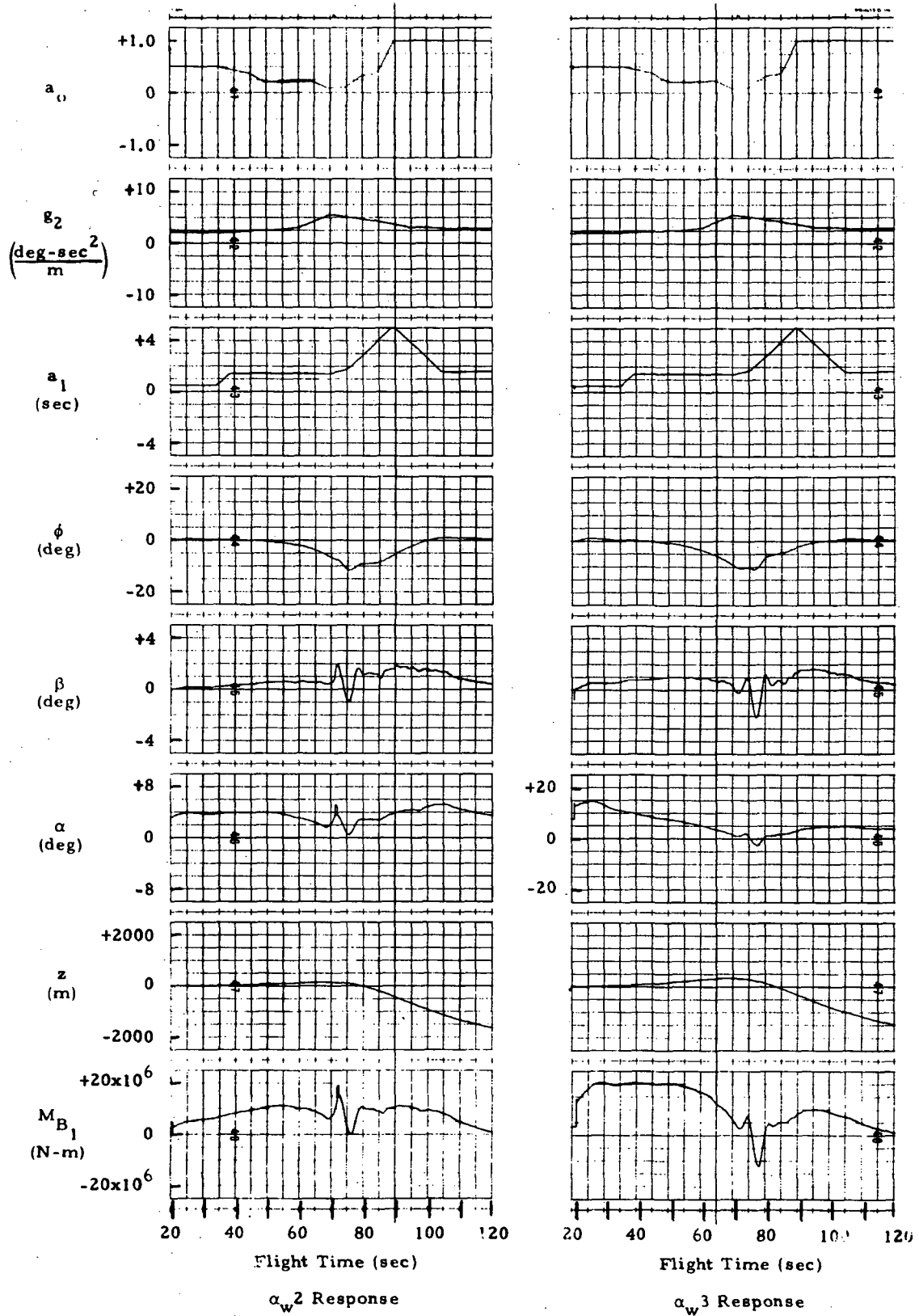


Fig. 5-8 - INT-21 Ascent Simulation Response for Three Optimized Control Gain Schedules: Part I

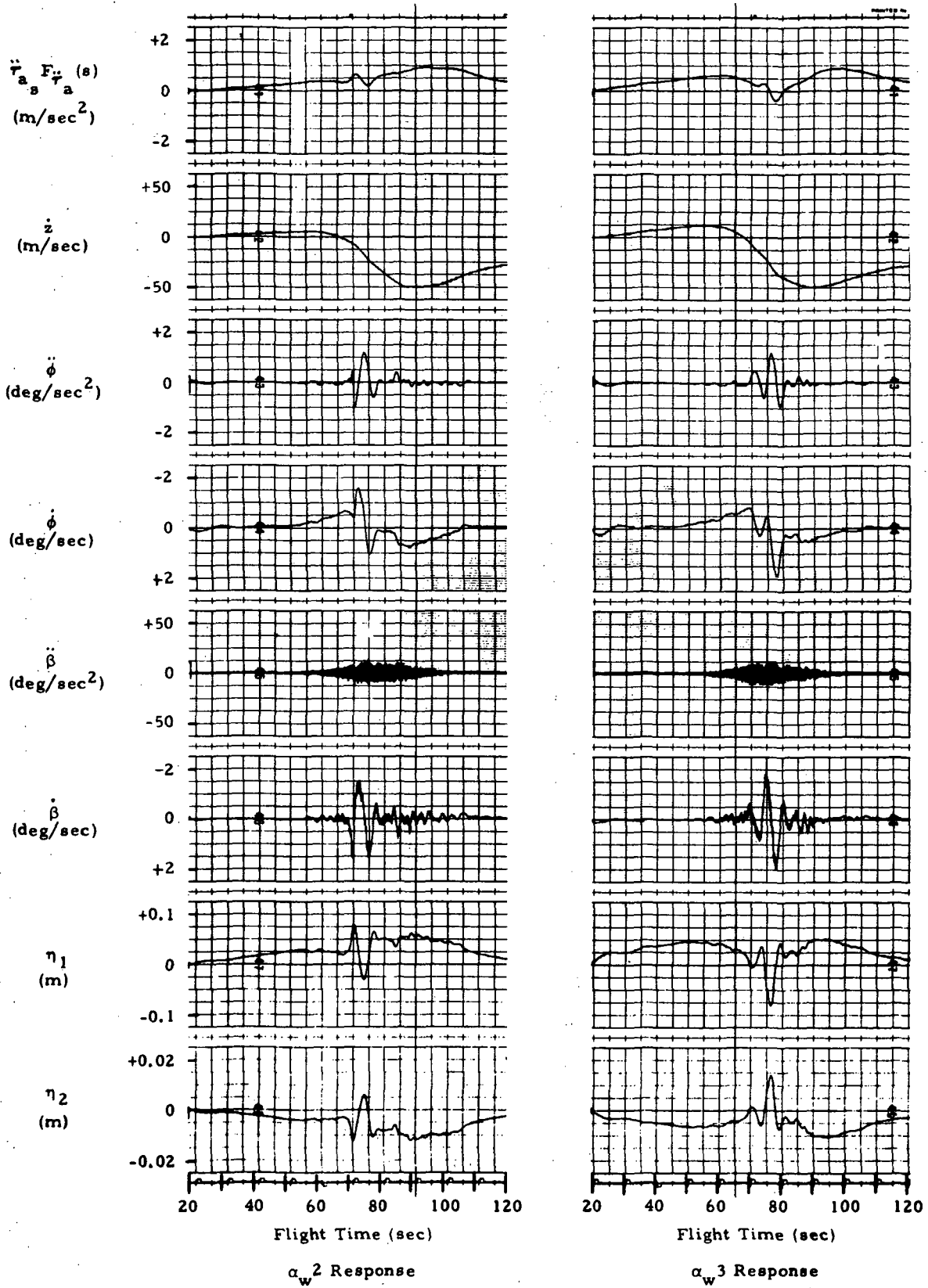


Fig. 5-9 - INT-21 Ascent Simulation Response for Three Optimized Control Gain Schedules: Part II



2. As a direct result of the preceding item,  $\alpha$  remains below 4 deg from  $t_{\max q\alpha}$  to  $t = 90$  sec, a critical region on the  $M'_\alpha(t)$  curve. (See Fig. 5-3.)
3.  $M_{B1}$  remains below  $11.0 \times 10^6$ , N-m after  $t = 73$  sec, and this augurs well with the bending moment capability trends indicated in Fig. 3-5.
4. One of the side benefits of this optimized  $a_1(t)$  response is that  $|\beta|$  remains below 2.0 deg and  $|\dot{\beta}|$  stays below 2.0 deg/sec.
5. Bending mode response compares favorably with the attitude control situation. 1st mode peak values are compared in the following table.

	$\alpha_w^2$	$\alpha_w^3$
Optimized Load Relief Controller	0.08 m	0.08 m
Attitude Control $a_0 = 1.4, a_1 = 1.0$ sec	0.124 m	0.118 m

The attitude control 1st mode responses are presented in Fig. 5-10.

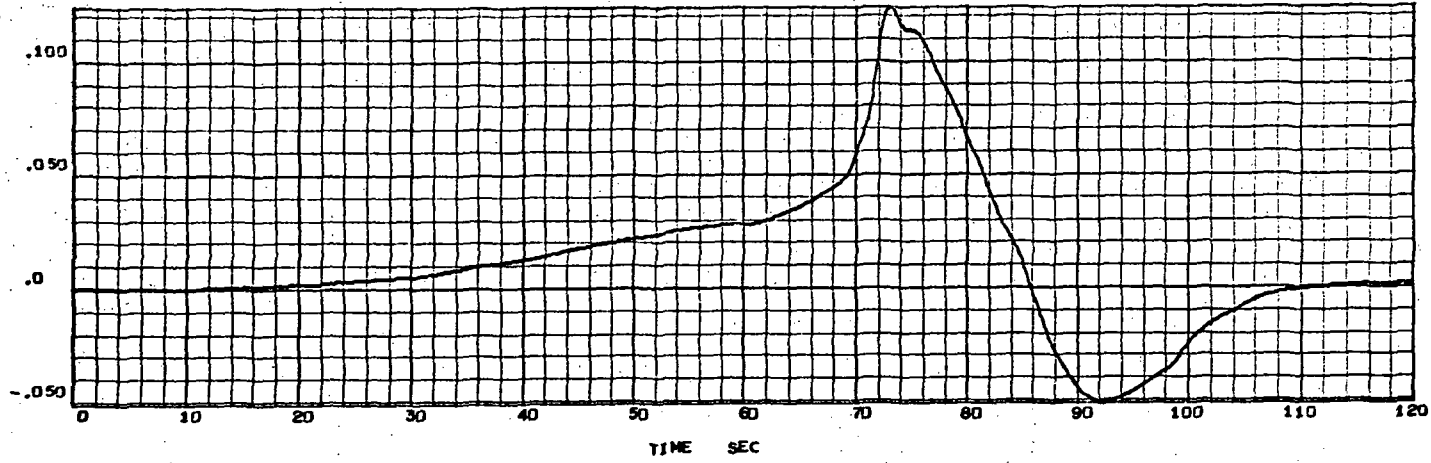
The major "price" paid for these additional load relief and stability features is the slight increase in terminal drift. The terminal drift values shown in Fig. 5-8 are

$$Z_{\min} \Big|_{t=120 \text{ sec}} = -1,600 \text{ m} (\alpha_w^2) = -1,500 \text{ m} (\alpha_w^3)$$

Rather than rerun all of the computer optimization steps using  $\alpha_w^5$  for Wind B as is recommended in Section 5.2, it was decided to use the controller gain schedules of Fig. 5-11 in the performance verification phase of the study. As shown in Fig. 6-1, these gain schedules were modified somewhat after 80 sec flight time in order to provide better load relief characteristics in this later region of ascent flight.

5-18

$\eta_1$   
Response  
to  $\alpha_w 2$   
(m)



$\eta_1$   
Response  
to  $\alpha_w 3$   
(m)

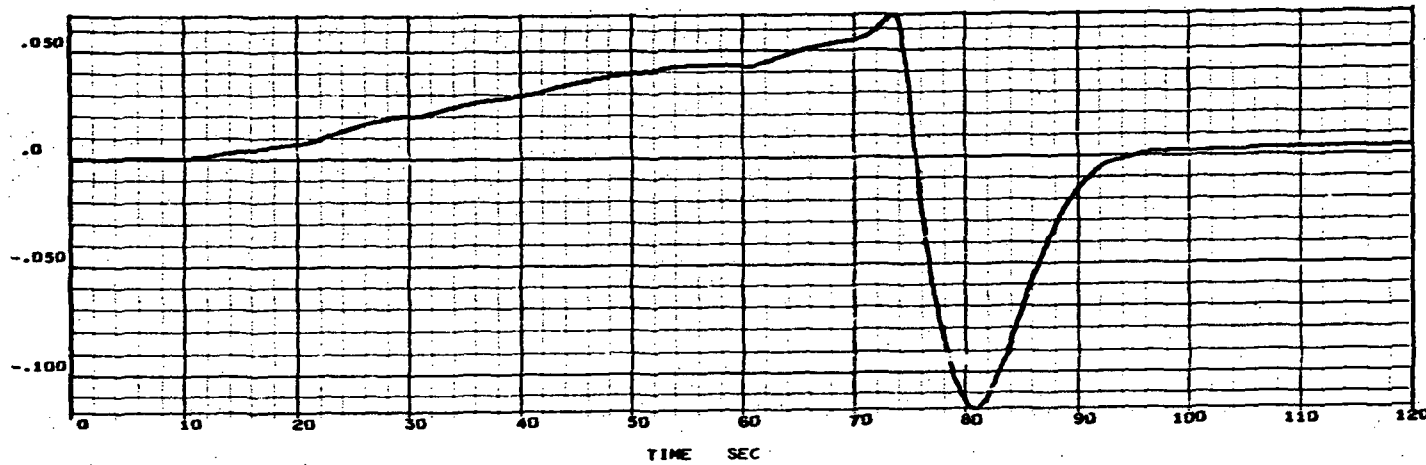


Fig. 5-10 - First Bending Mode Response for Control Law 1  
with  $a_0 = 1.4$  and  $a_1 = 1.0$  sec

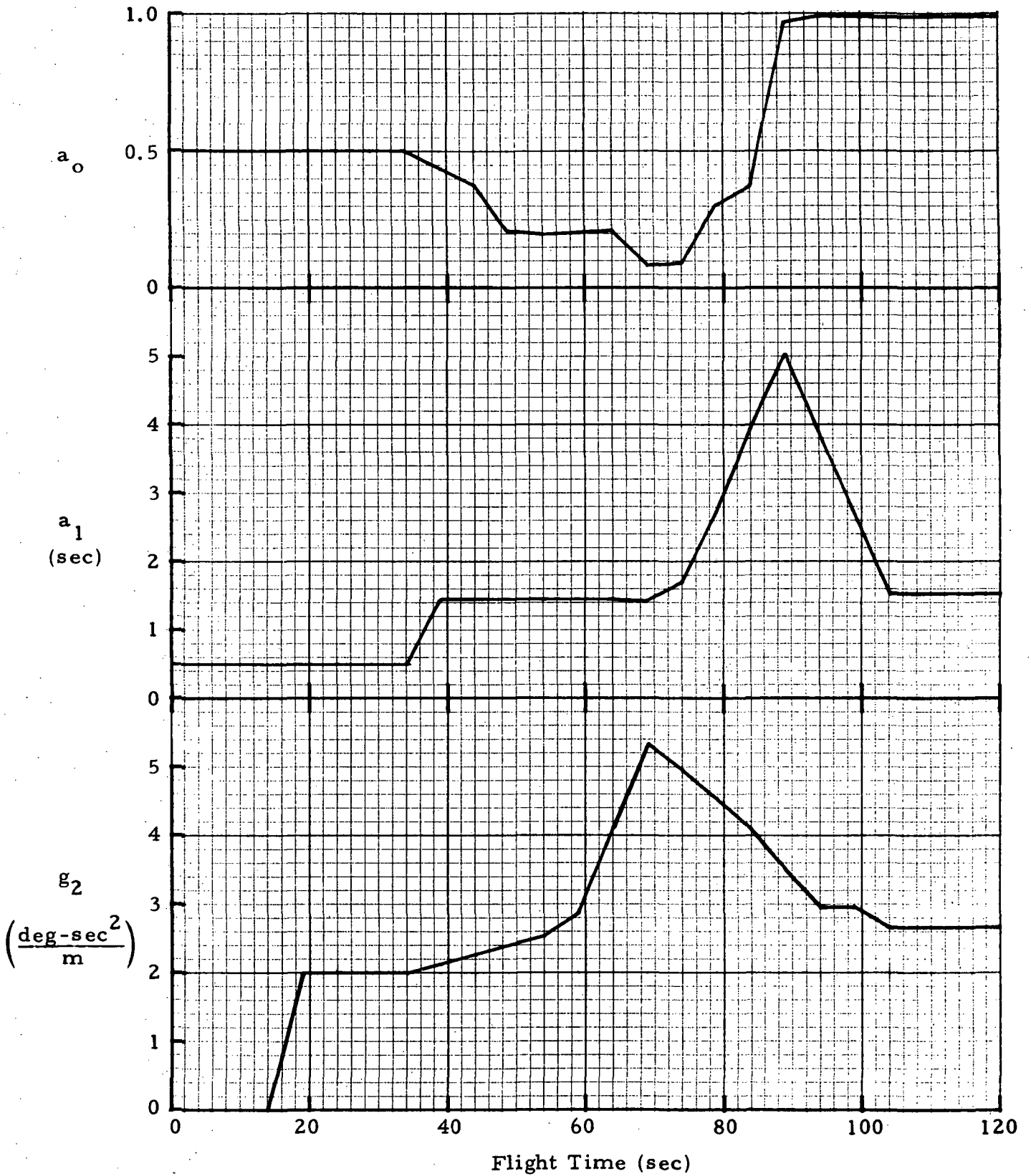


Fig. 5-11 - INT-21 Load Relief Controller Gain Schedules Generated by Lockheed's Hybrid Optimizer

System response characteristics resulting from the optimized controller gain schedules (Fig. 5-11) were quite satisfactory and they were expected to be able to easily pass the statistical evaluation processing discussed in Section 6. If, in fact, system performance was not acceptable as per the performance verification statistical evaluation, then further optimizations would have to be performed using  $\alpha_w 5$  as Wind B.  $\alpha_w 5$  attitude control response is shown in Fig. 5-12.

Control Law 3 was used, briefly, to see if it would help improve drift characteristics without reducing load relief performance overly much. No such success was obtained during the brief time it was tried.

Control Law 4 was introduced to the simulation, but it resulted in unstable solutions being generated. Time did not allow to investigate the source of this instability in depth; this control law may yet turn out to be worth further study efforts.

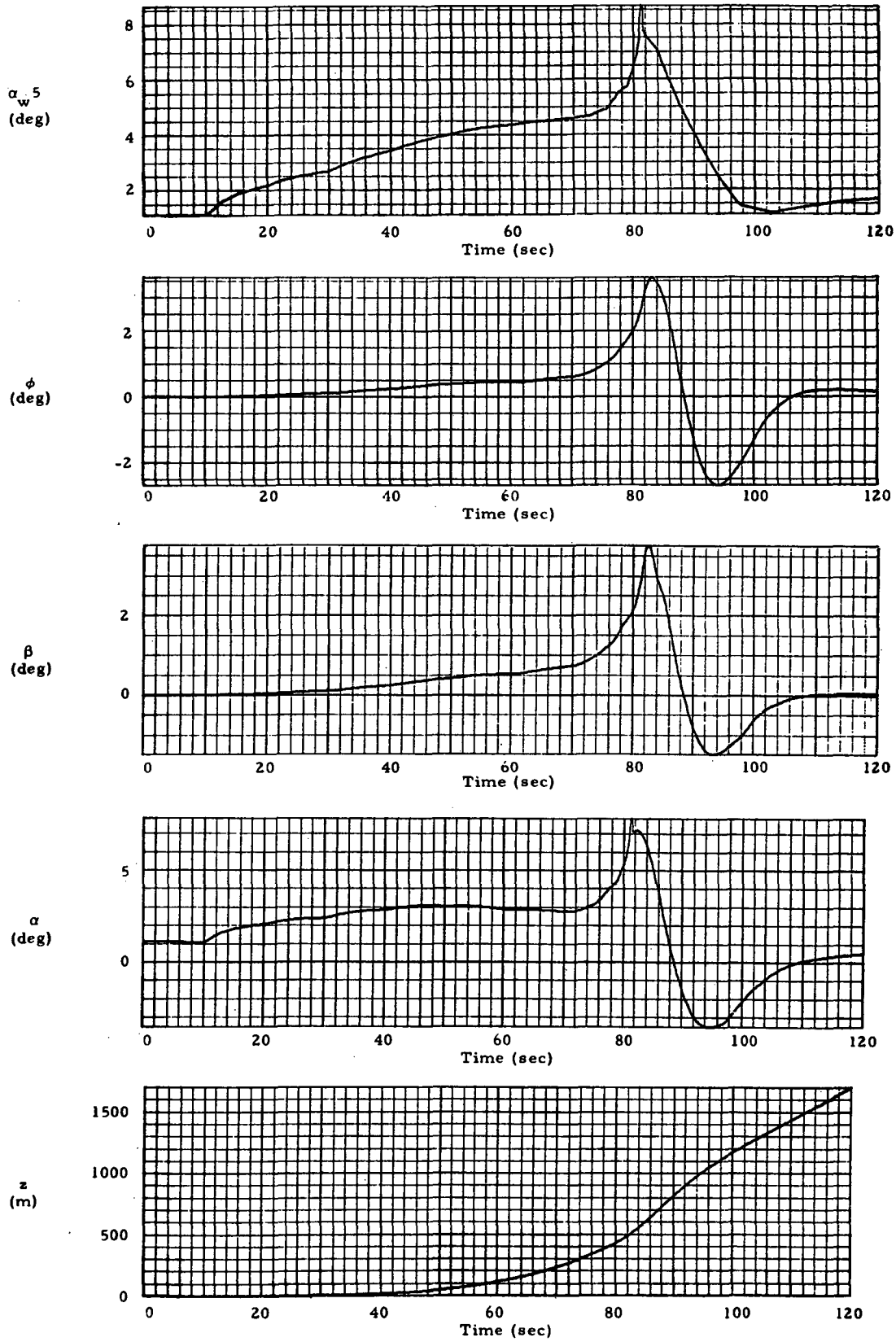


Fig. 5-12 - Digital Computer Solution of INT-21 System Dynamics for Constant Control System Gains:  $a_0 = 1.4$ ,  $a_1 = 1.0$  sec,  $g_2 = 0$  deg-sec<sup>2</sup>-m<sup>-1</sup> ( $\alpha_w 5$  Response)

Section 6  
PERFORMANCE VERIFICATION

As mentioned briefly in Section 1 (Introduction) one of the chief goals of this study was to verify the final design controller by statistically evaluating system response to a large number of measured wind speed profiles. This was to be accomplished by "forcing" the analog simulation sequentially by a large number of measured tape winds and performing a statistical evaluation of critical system parameters over on the digital side of the hybrid computer.

The measured winds used for this phase of the study are 970 preprocessed FPS-16/Jimsphere\* wind profiles that provide  $V_w$  versus flight time for the first 100 seconds of flight. They include a speedup (time-scale) factor of 750 when the tape is run at 60 ips. Time-varying mean ( $\mu_{V_w}$ ) and  $3\sigma$  characteristics of these 970 measured winds are presented in Fig. 6-13.

Some minor reprogramming was required on the analog console in mechanizing the statistical evaluation configuration. Also, a digital program was constructed to evaluate the following critical variable statistical parameters:

- a. Mean value of variable  $x$  at time  $t_i$  =

$$\mu_x(t_i) = \frac{1}{N} \sum_{j=1}^N x_j(t_i)$$

where  $x_j$  is the response of parameter  $x$  to the  $j^{\text{th}}$  taped wind forcing function.

- b. Variance

$$\sigma_x^2(t_i) = \frac{1}{N} \sum_{j=1}^N \left[ x_j(t_i) - \mu_x(t_i) \right]^2$$

---

\* See Ref. 4.

c. Standard Deviation

$$\sigma_x(t_i) = \sqrt{\sigma_x^2(t_i)}$$

- d. Exceedance counts used in establishing the "tail" of the frequency probability density functions for certain critical system variables.

Two minor changes in the control system were effected before the statistical evaluation was performed:

1. Gain schedules, shown in Fig. 6-1, have been modified as follows: After 80 sec flight time, a  $a_0$  gain has been reduced in order to allow the  $\ddot{\theta}_a$  control term to dominate for several seconds beyond this point. This change, in turn, has allowed the  $a_1$  "hat" to be clipped at the 2.0 deg/(deg/sec) level, because that extra bit of damping is no longer required.
2. The  $\phi$  filter has been modified to block out the bending modes more completely. Instead of using

$$F_\phi(s) = \frac{1 + 10s}{1 + 21.37s + 1.916s^2} = \frac{5.22(s + 0.1)}{(s + 0.047)(s + 11.1)}$$

as presented in Section 5,

$$F_\phi(s) = \frac{(s + 0.1)}{(s + 0.04)(s + 2.5)}$$

was used during the statistical evaluation.

$\alpha_w^2$  and  $\alpha_w^6$  synthetic wind response, including the above mentioned control system modifications, is as shown in Figs. 6-2 and 6-3.

Once these control system changes had been effected, the analog computer simulation was fast-timed by 750 in order to correspond to the time scale of the preprocessed wind tape. Also, exceedance sensing additions to the analog program were included.

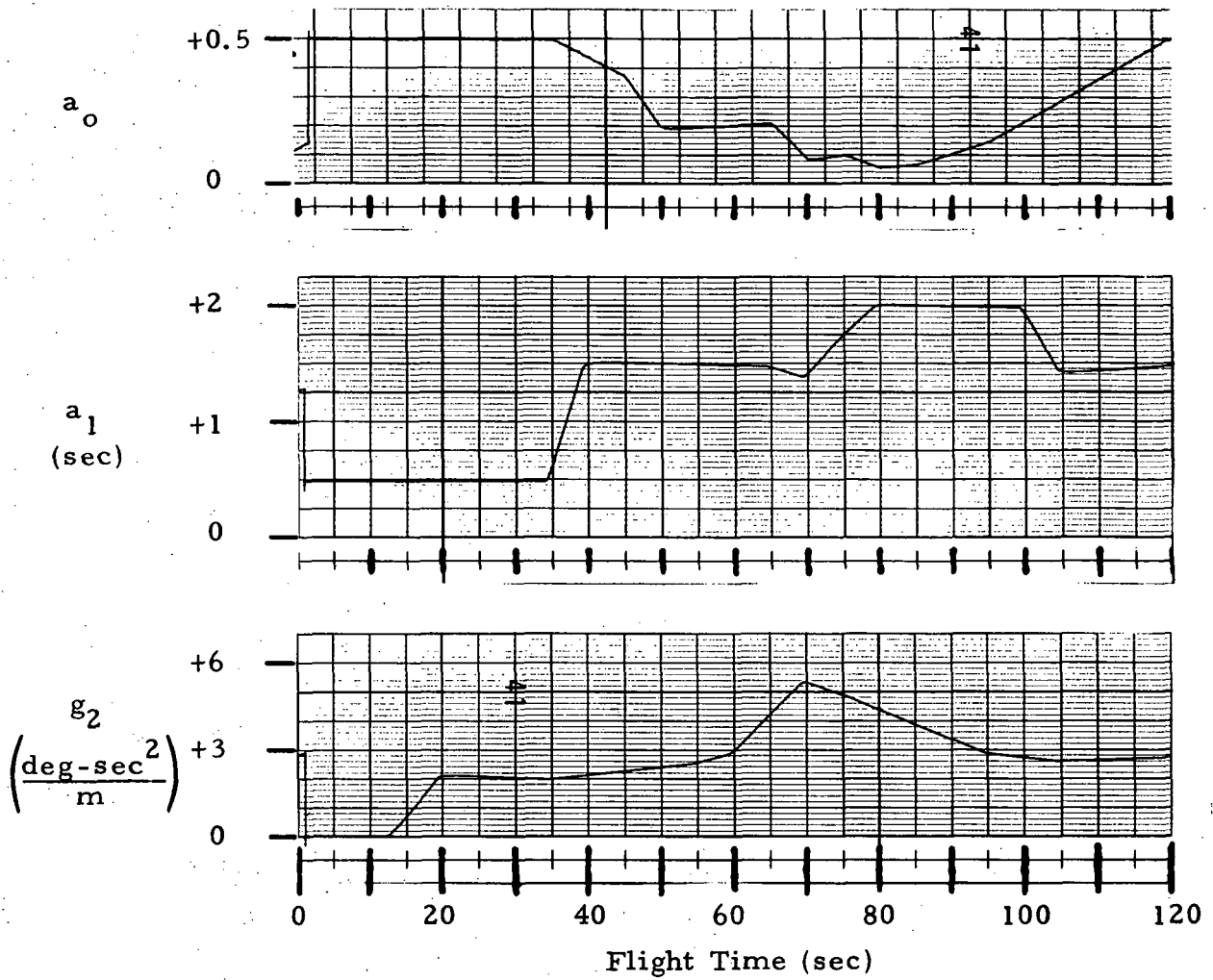


Fig. 6-1 - Controller Gain Schedules Used During Statistical Evaluation



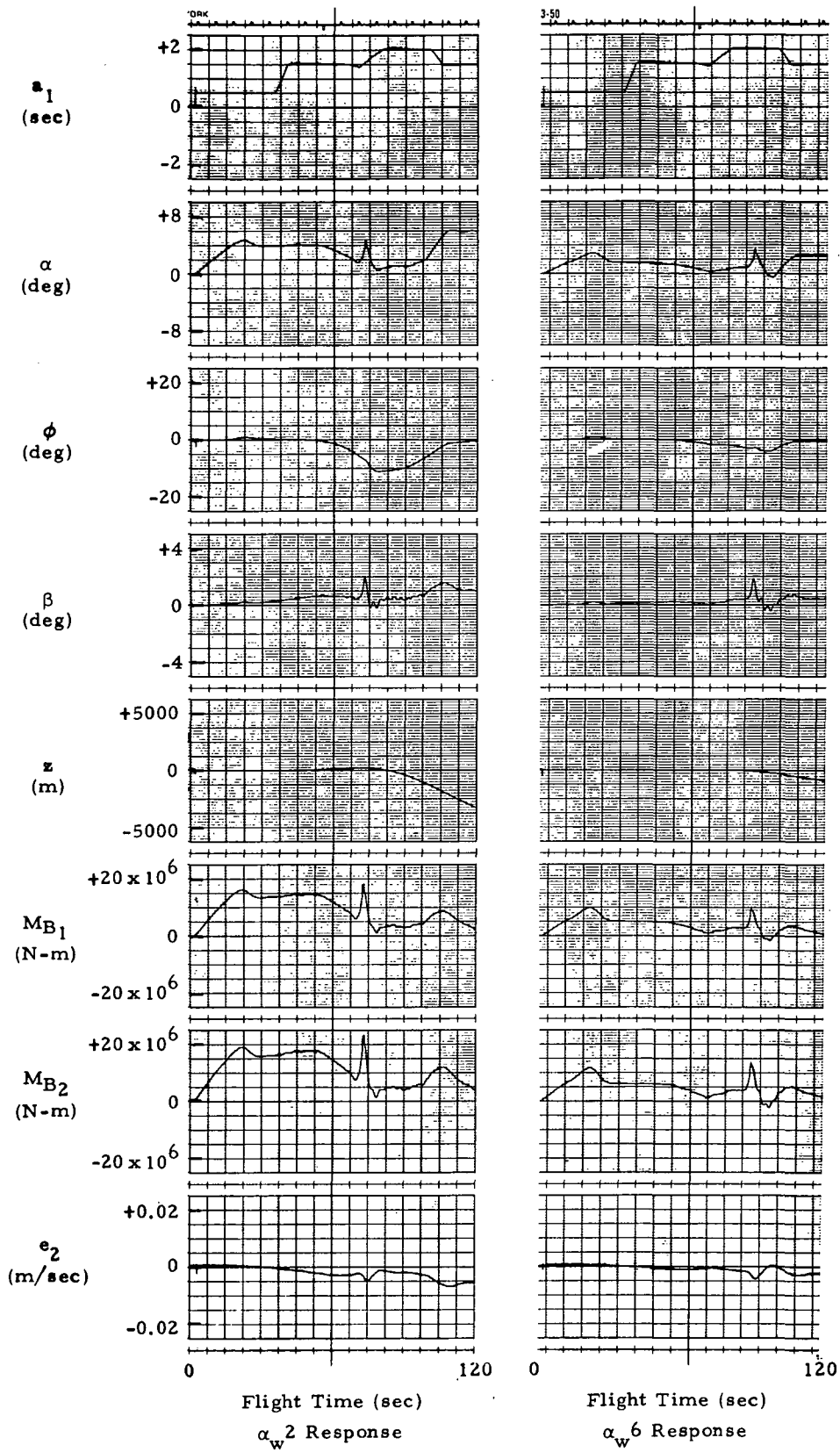


Fig. 6-2 - INT-21 Ascent Simulation Response to Synthetic Winds for the Three Controller Gain Schedules Presented in Fig. 6-1: Part I

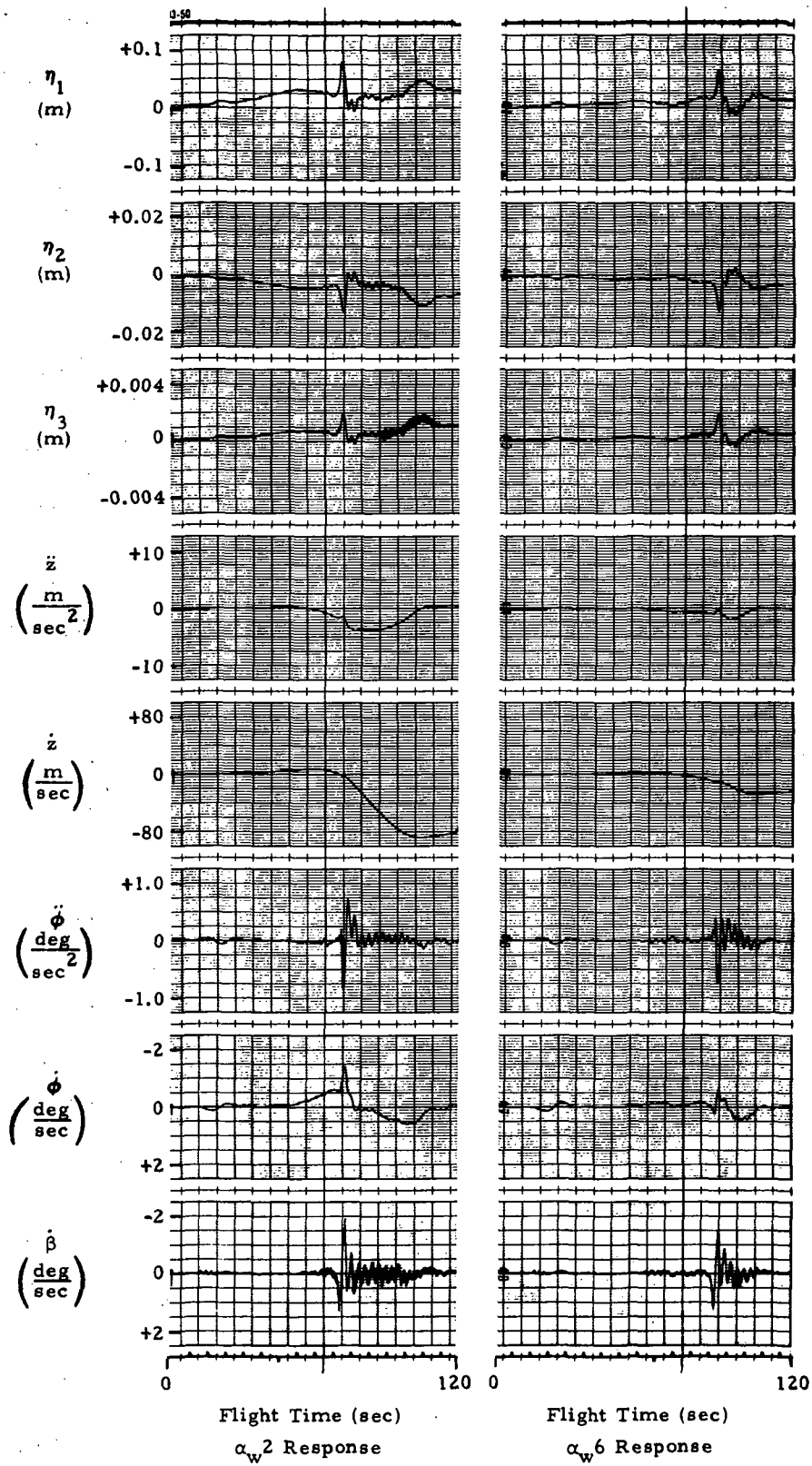


Fig. 6-3 - INT-21 Ascent Simulation Response to Synthetic Winds for the Three Controller Gain Schedules Presented in Fig. 6-1: Part II

System response to several of the measured winds is presented in Fig. 6-4. It should be noted, however, that the higher frequency portions of the system response do not appear in Fig. 6-4 due to the 750 time speedup factor and the limited frequency response range of the electromechanical strip-chart recorder.

Time-varying mean and 3 $\sigma$  curves were calculated for the following variables:  $z, \ddot{z}, \phi, \dot{\phi}, \beta, \dot{\beta}, \alpha, \alpha_w, V_w, M_{B35.6}, M_{B43.2}, M_{B58.5}, \eta_1, \ddot{\eta}_1, \eta_2, \eta_3$ . These results are presented in Figs. 6-5 through 6-20.  $M_{B35.6}, M_{B43.2}$ , and  $M_{B58.5}$  are the bending moments produced at stations 35.6 m, 43.2 m, and 58.5 m, respectively. Analysis of these results brought out several points worth mentioning:

1. The measured winds covered only the first 100 seconds of flight time. Consequently, the drift characteristics are not fully developed in these abbreviated runs.
2.  $3\sigma$  features of  $\beta$  response show the engine gimbal angle rarely (less than 0.3% of these runs) exceeds  $\pm 1.0$  degree.
3. The  $\alpha, M_B,$  and  $\eta_1$  mean values "neck down" in the critical 70-75 second portion of the total flight, thereby demonstrating the load relief effectiveness in this critical (max  $q\alpha$ ) region.
4. Bending moment  $3\sigma$  values stay well below the structural limits for this particular vehicle.
5. Peak bending mode amplitudes are substantially lower than those caused by  $\alpha_w^2$  synthetic wind.
6. In general, measured winds are less severe forcing functions than the  $\alpha_w^2$  synthetic wind.
7. Finally, the overall system response to these 970 measured winds demonstrates clearly that the load relief gain schedules generated by Lockheed's Hybrid Optimizer are very effective in producing desirable load relief system response characteristics.

Two very important conclusions may be reached through examination of the bending moment results (Figs. 6-14 through 6-16):

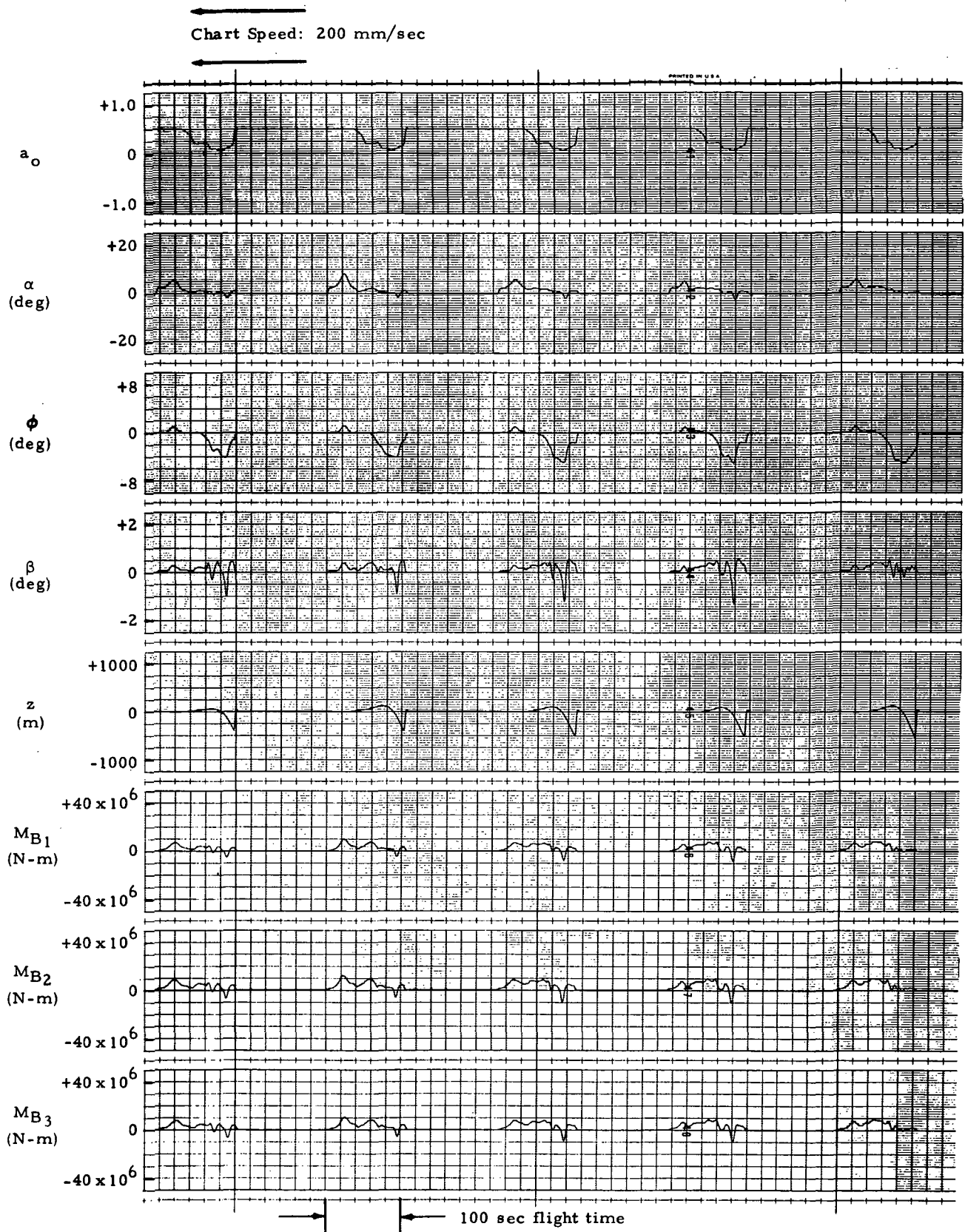


Fig. 6-4 - High Speed Recordings of INT-21 Response to Measured Winds  
(Controller Gain Schedules of Fig. 6-1 Used. System Fast-Timed  
by 750.)

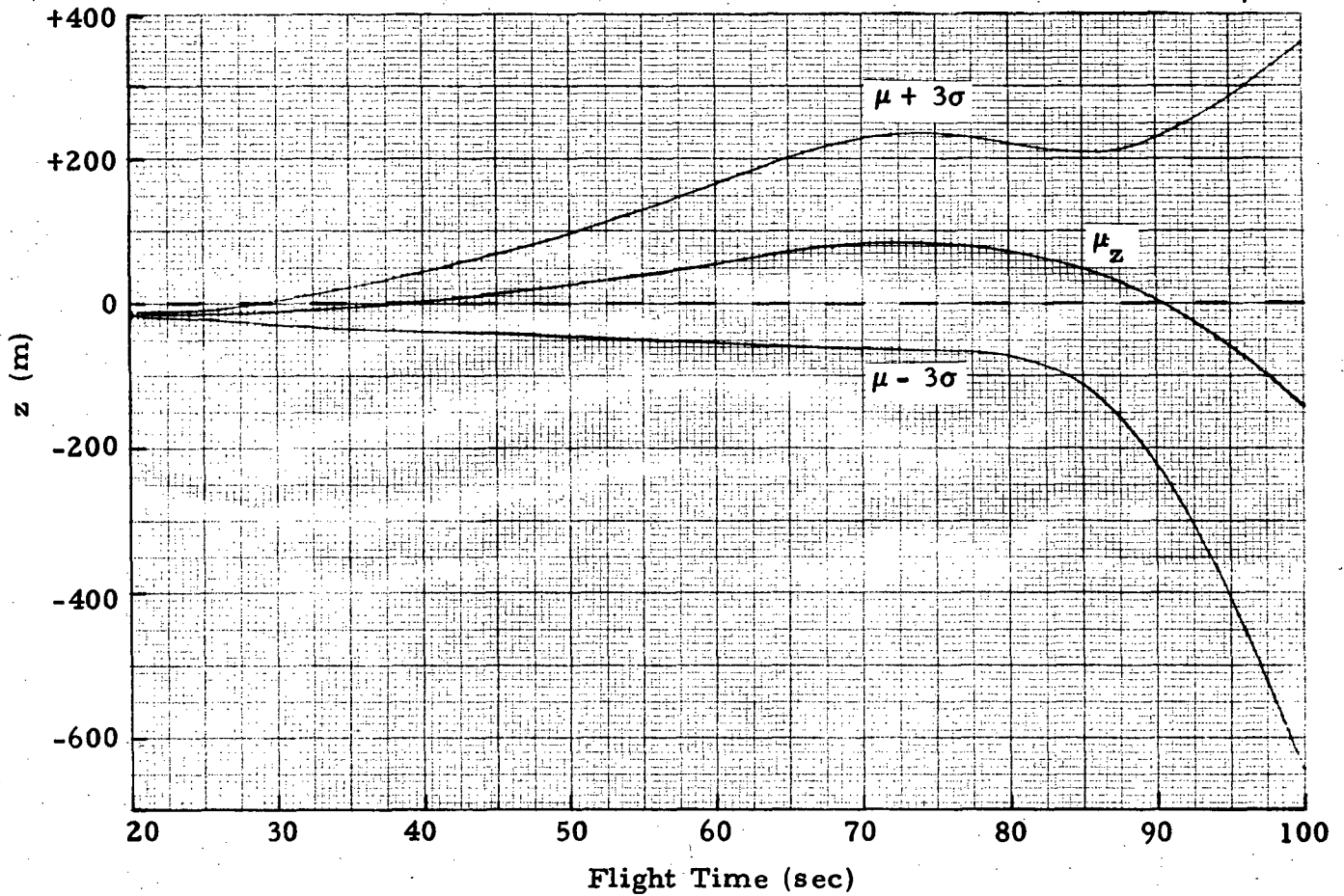


Fig. 6-5 - Mean ( $\mu_z$ ) and  $3\sigma$  Features of  $z$  Response to 970 Measured Winds

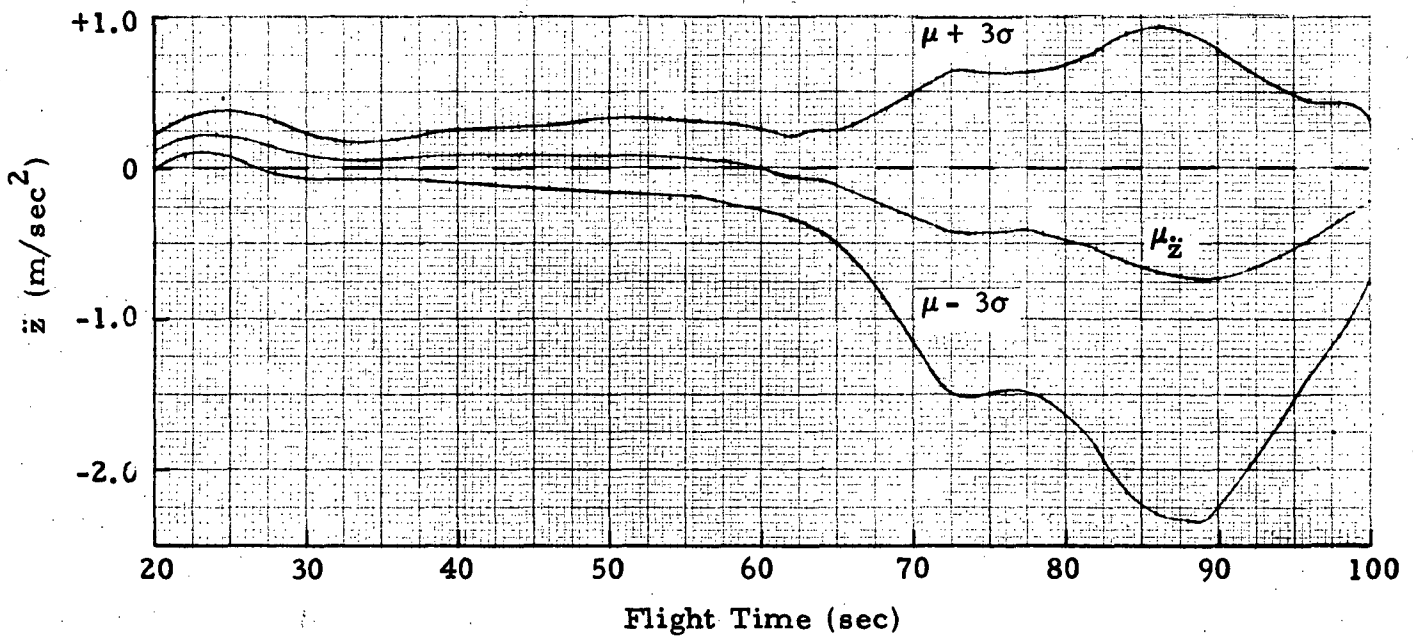


Fig. 6-6 - Mean ( $\mu_{\ddot{z}}$ ) and  $3\sigma$  Features of  $\ddot{z}$  Response to 970 Measured Winds

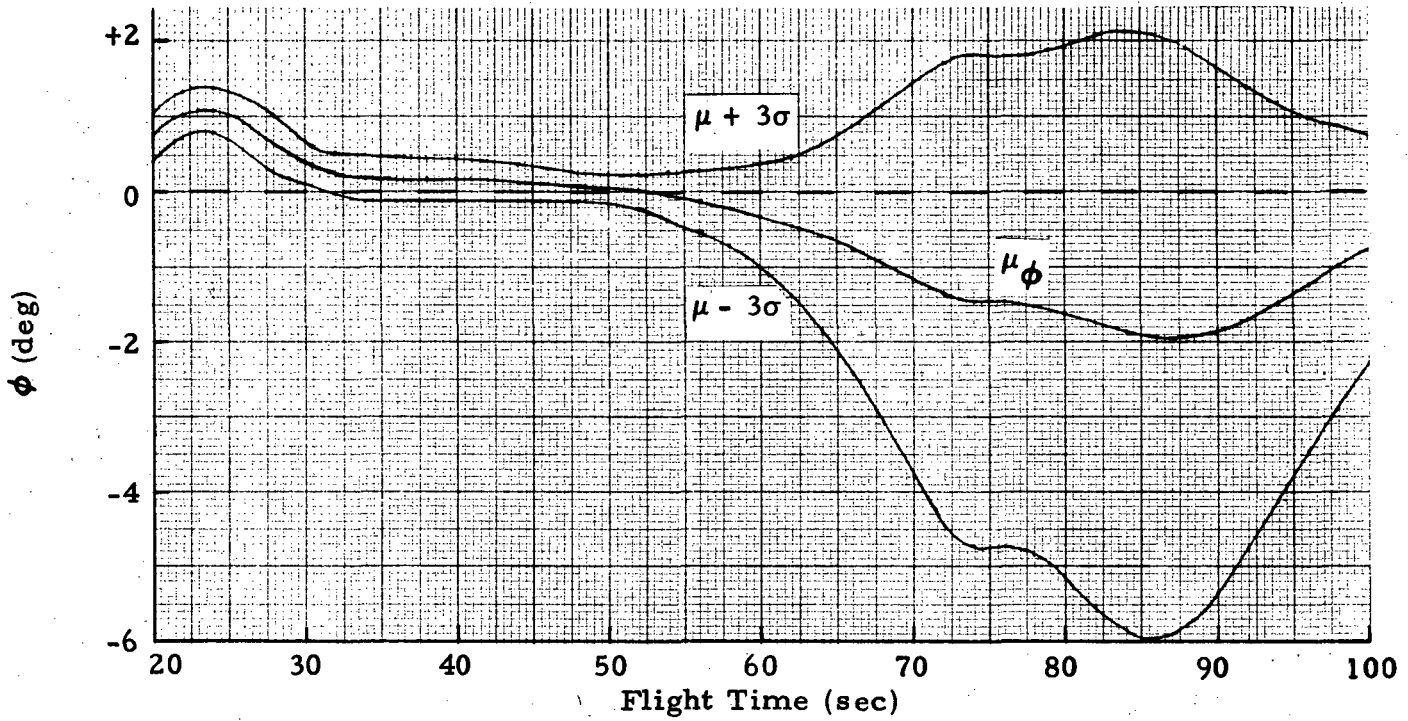


Fig. 6-7 - Mean ( $\mu_\phi$ ) and  $3\sigma$  Features of  $\phi$  Response to 970 Measured Winds

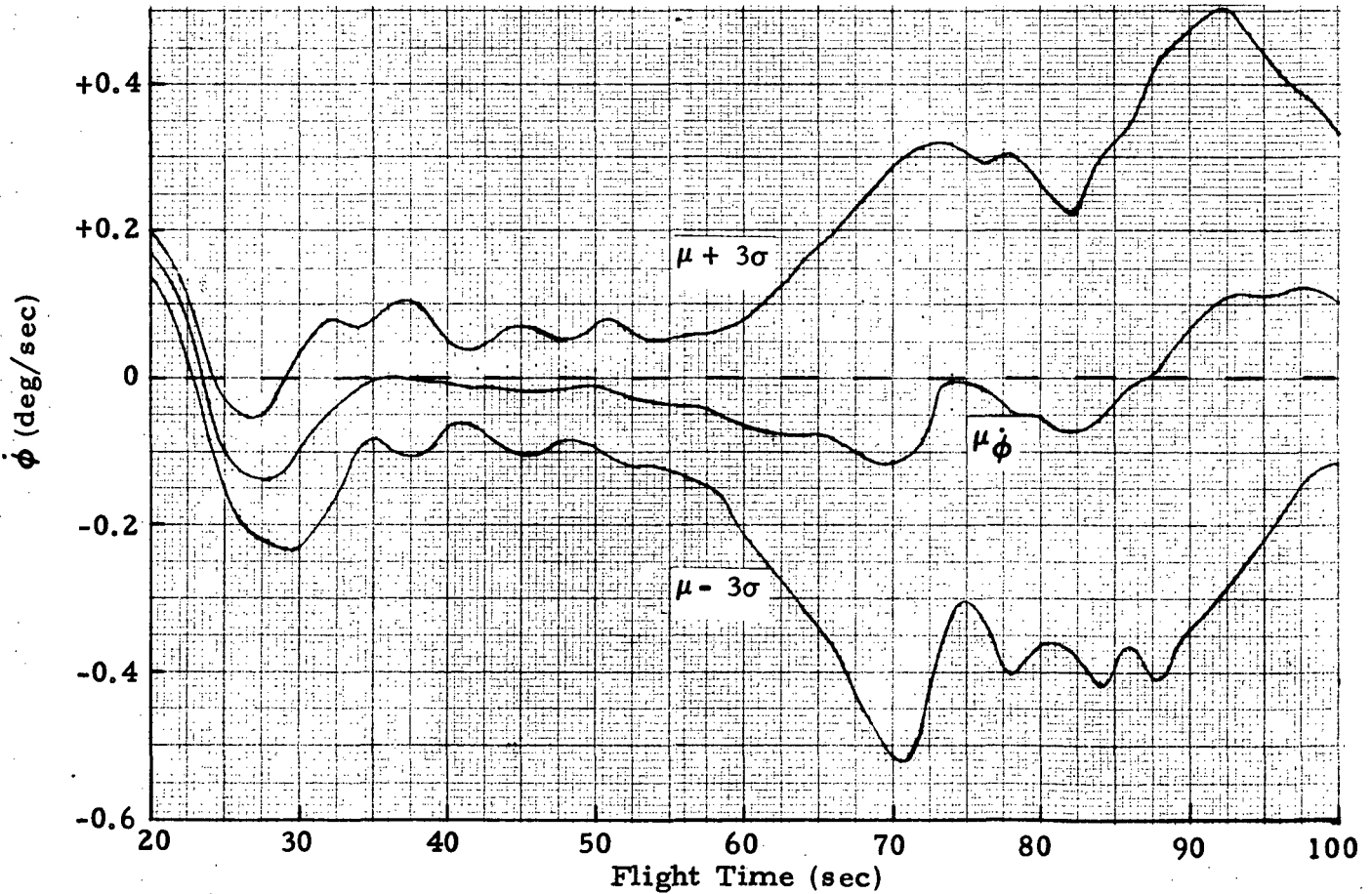


Fig. 6-8 - Mean ( $\mu_{\dot{\phi}}$ ) and  $3\sigma$  Features of  $\dot{\phi}$  Response to 970 Measured Winds

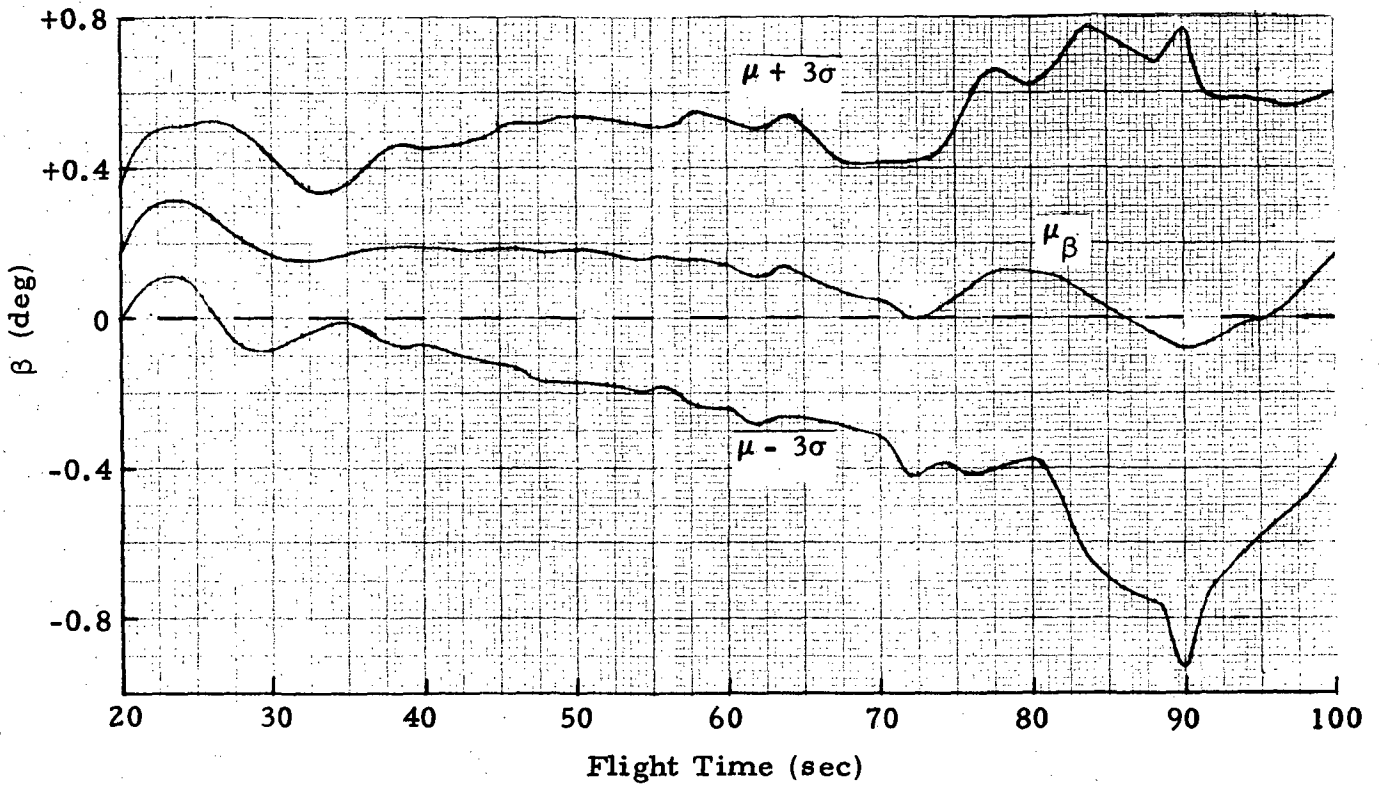


Fig. 6-9 - Mean ( $\mu_\beta$ ) and  $3\sigma$  Features of  $\beta$  Response to 970 Measured Winds

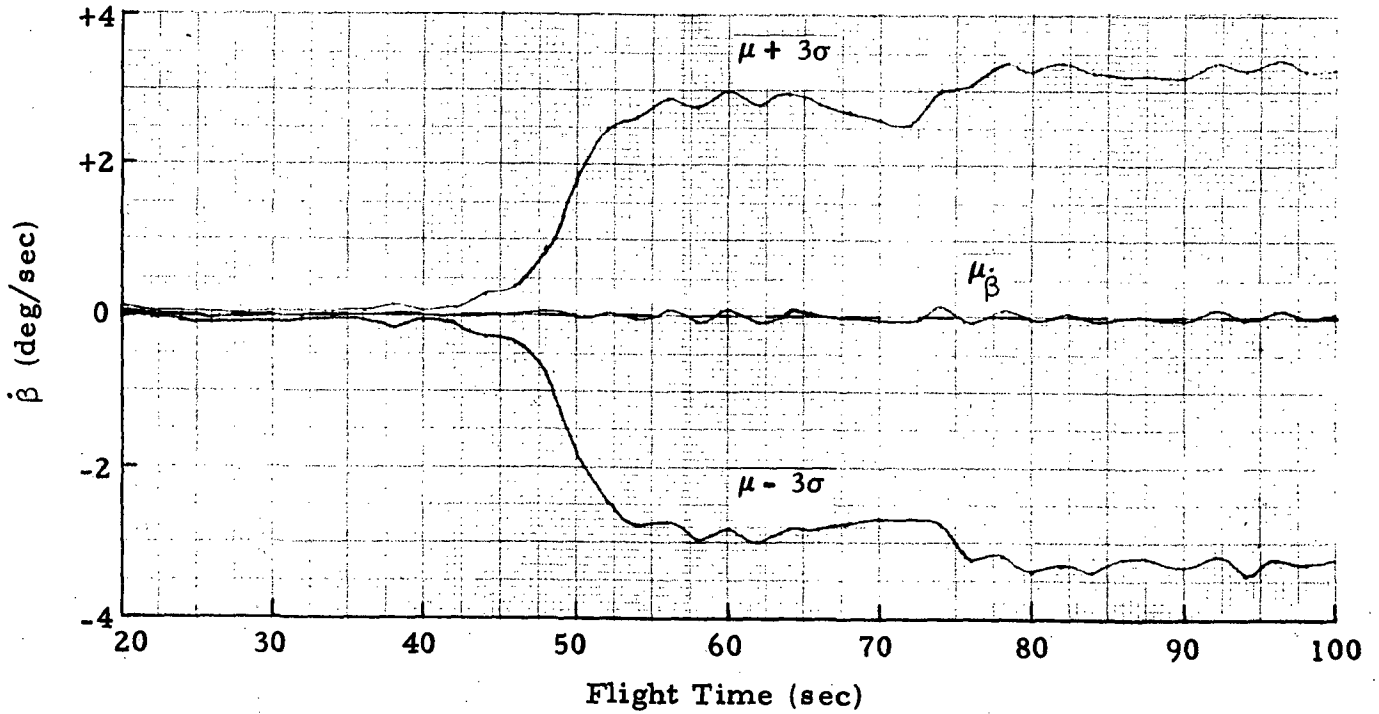


Fig. 6-10 - Mean ( $\mu_{\dot{\beta}}$ ) and  $3\sigma$  Features of  $\dot{\beta}$  Response to 970 Measured Winds

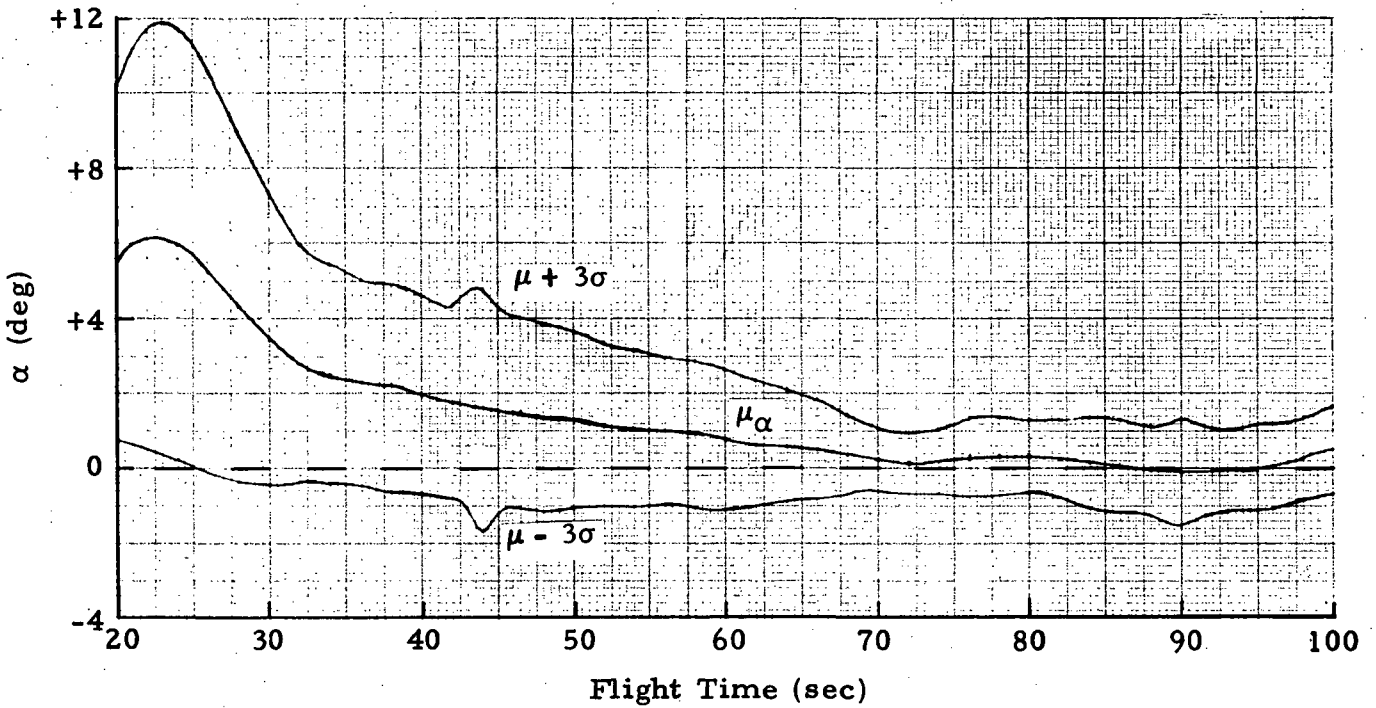


Fig. 6-11 - Mean ( $\mu_\alpha$ ) and  $3\sigma$  Features of  $\alpha$  Response to 970 Measured Winds

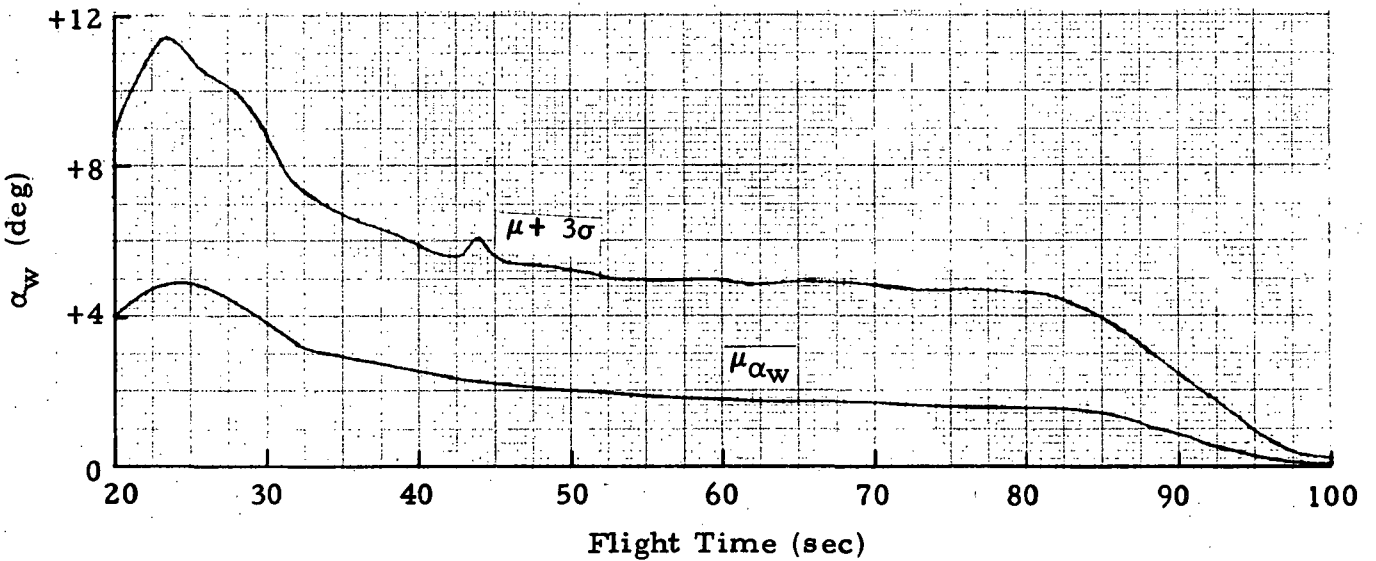


Fig. 6-12 - Mean ( $\mu_{\alpha_w}$ ) and  $3\sigma$  Features of  $\alpha_w$  Resulting from 970 Measured Winds



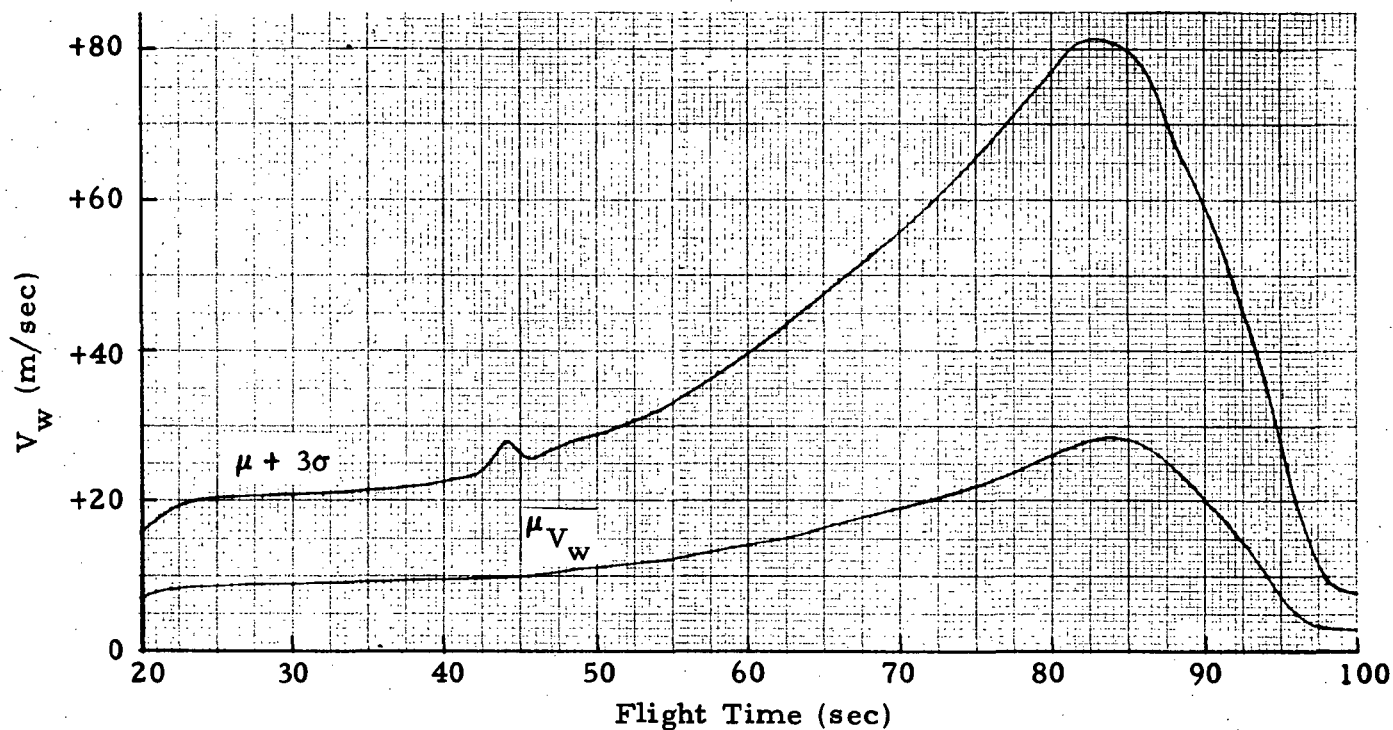


Fig. 6-13 - Mean ( $\mu_{V_w}$ ) and  $3\sigma$  Features of  $V_w$  Resulting from 970 Measured Winds

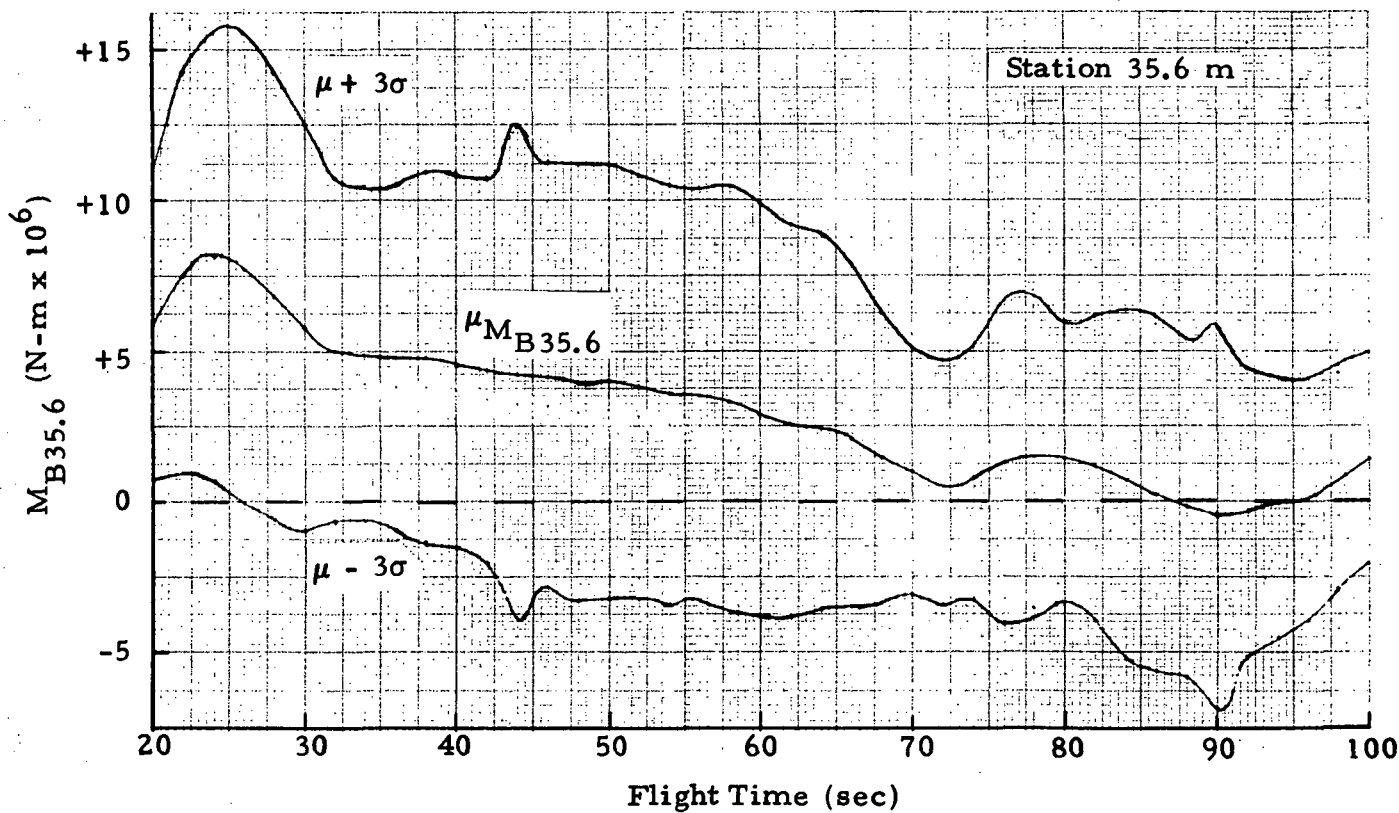


Fig. 6-14 - Mean ( $\mu_{M_{B35.6}}$ ) and  $3\sigma$  Features of  $M_{B35.6}$  Response to 970 Measured Winds

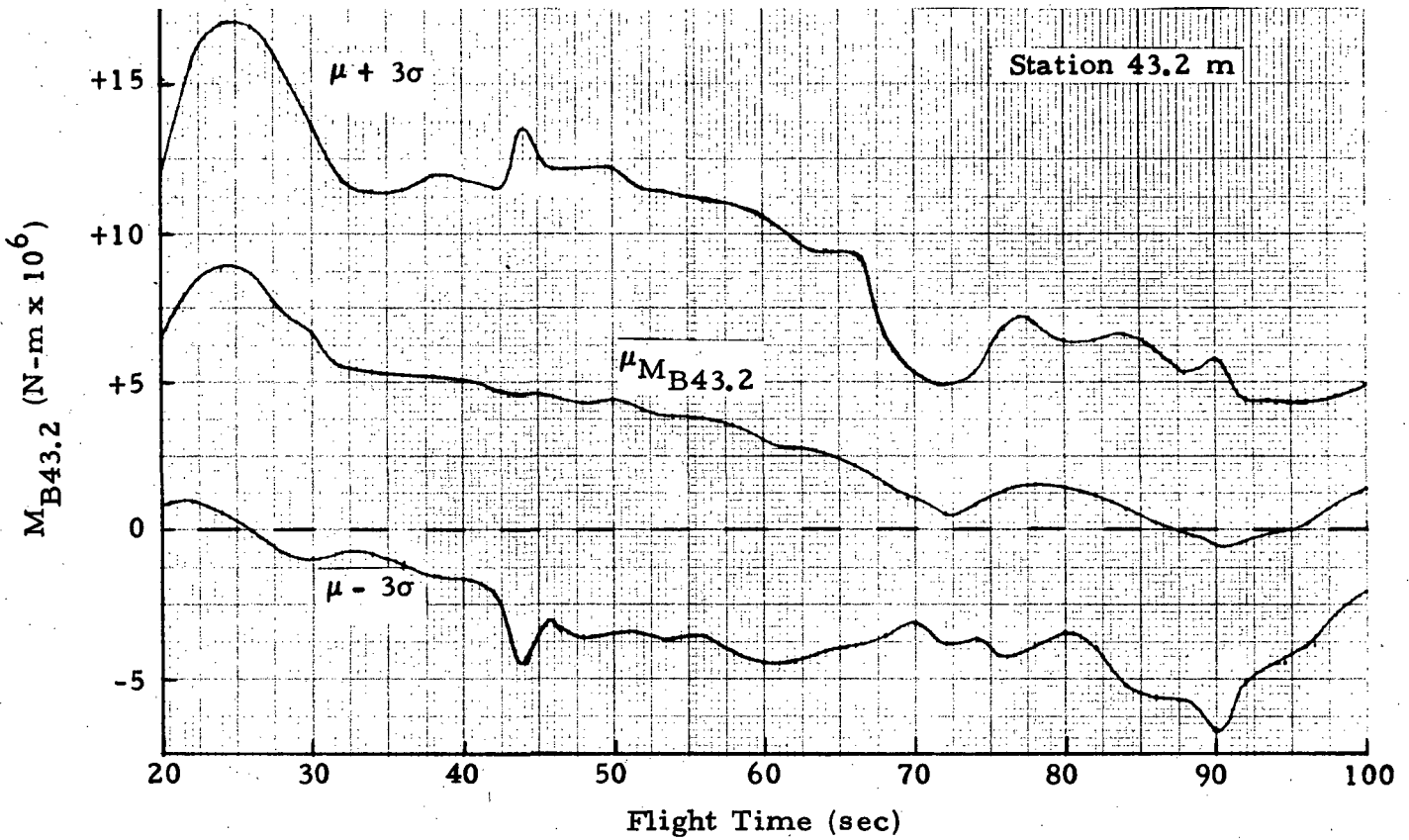


Fig. 6-15 - Mean ( $\mu_{M_{B43.2}}$ ) and  $3\sigma$  Features of  $M_{B43.2}$  Response to 970 Measured Winds

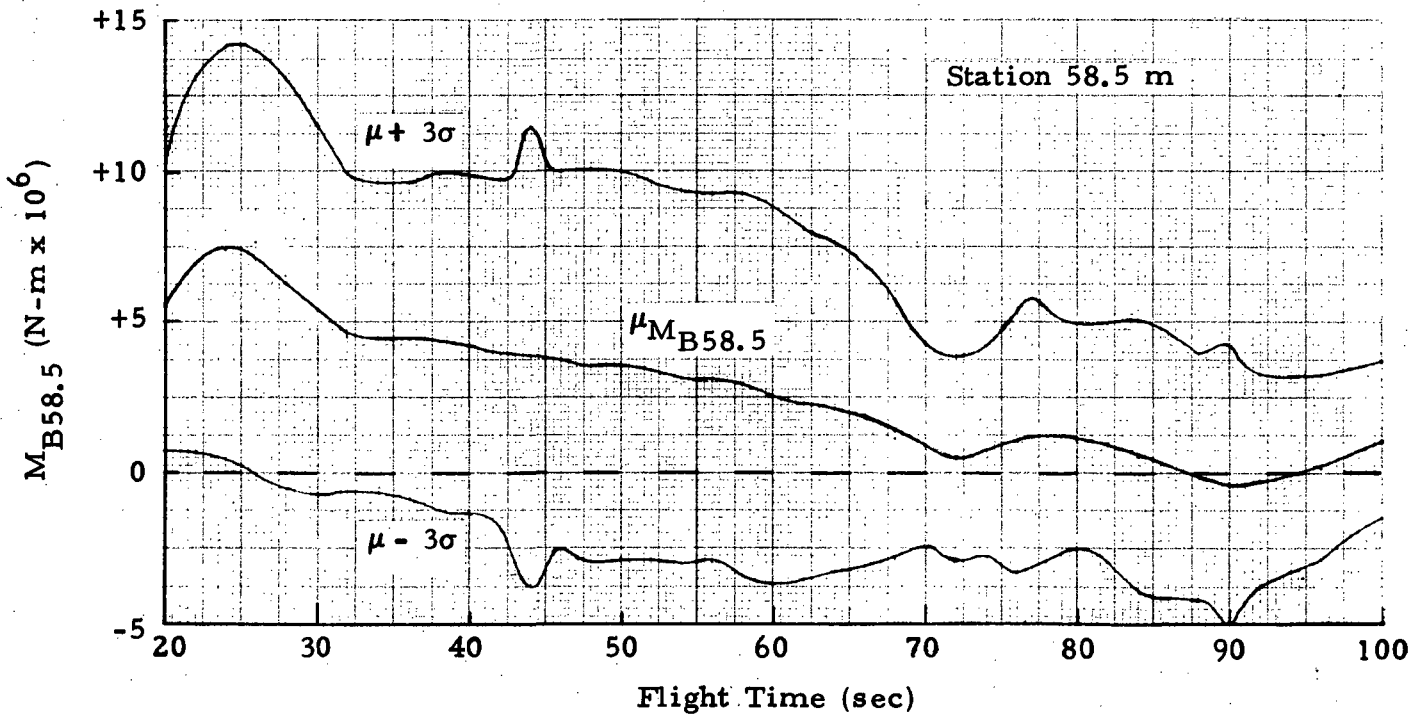


Fig. 6-16 - Mean ( $\mu_{M_{B58.5}}$ ) and  $3\sigma$  Features of  $M_{B58.5}$  Response to 970 Measured Winds

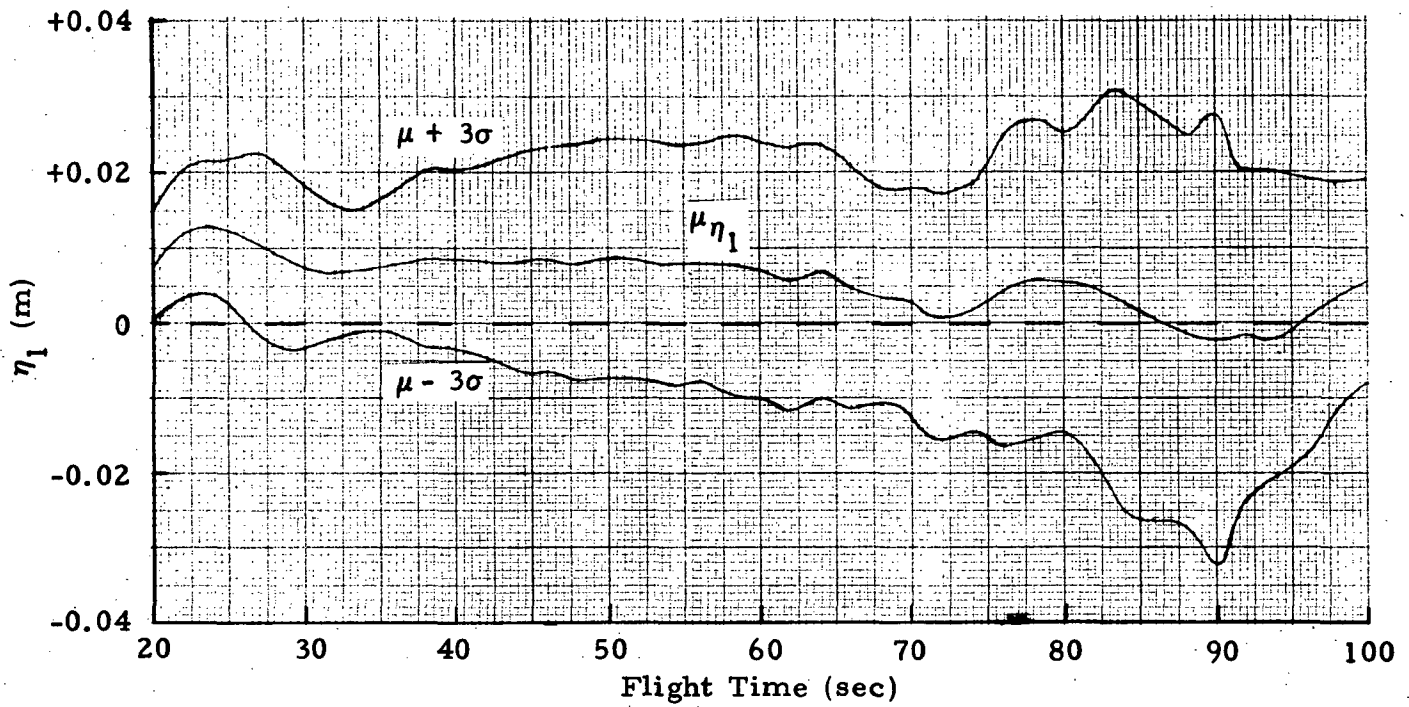


Fig. 6-17 - Mean ( $\mu \eta_1$ ) and  $3\sigma$  Features of  $\eta_1$  Response to 970 Measured Winds

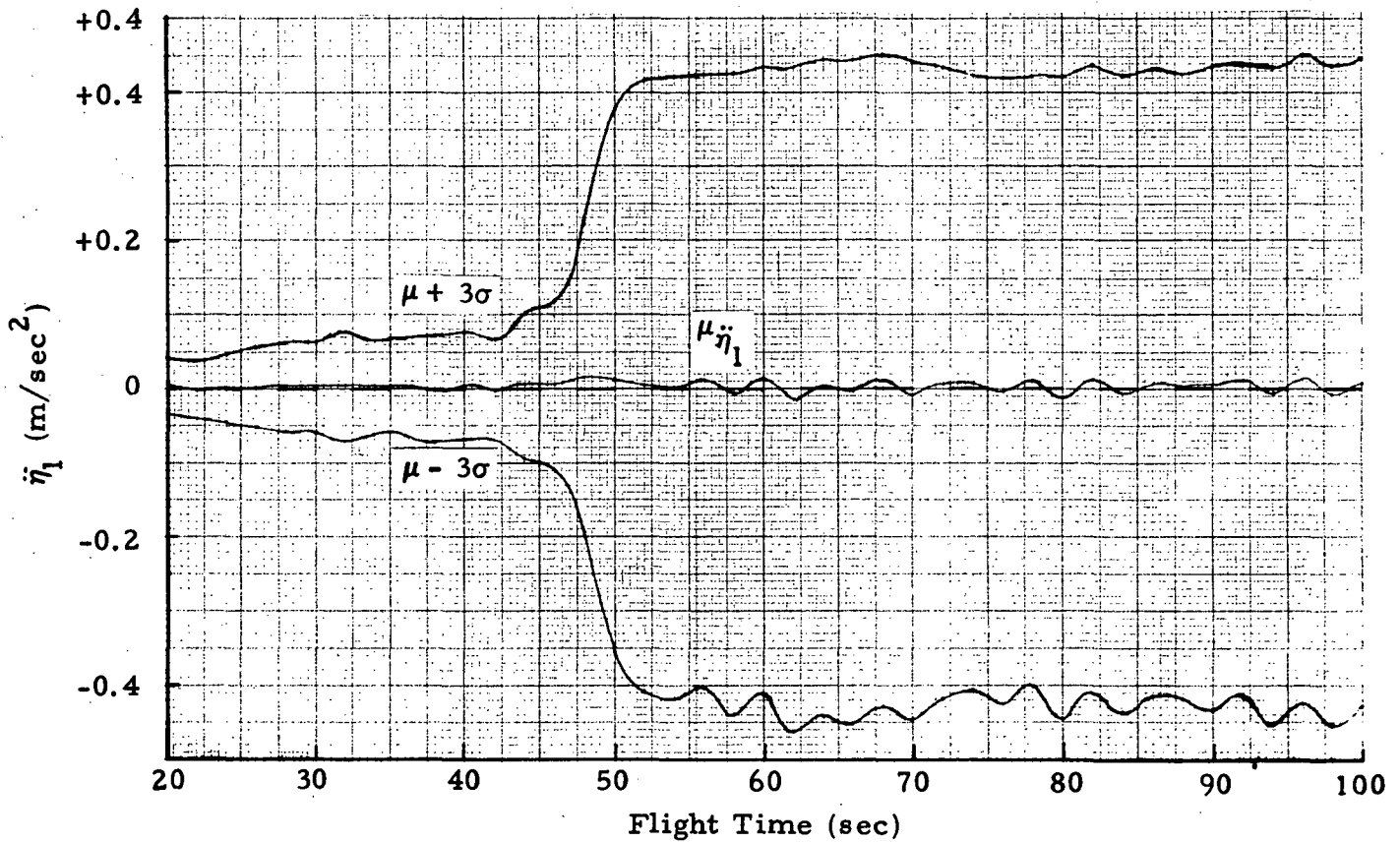


Fig. 6-18 - Mean ( $\mu \ddot{\eta}_1$ ) and  $3\sigma$  Features of  $\ddot{\eta}_1$  Response to 970 Measured Winds

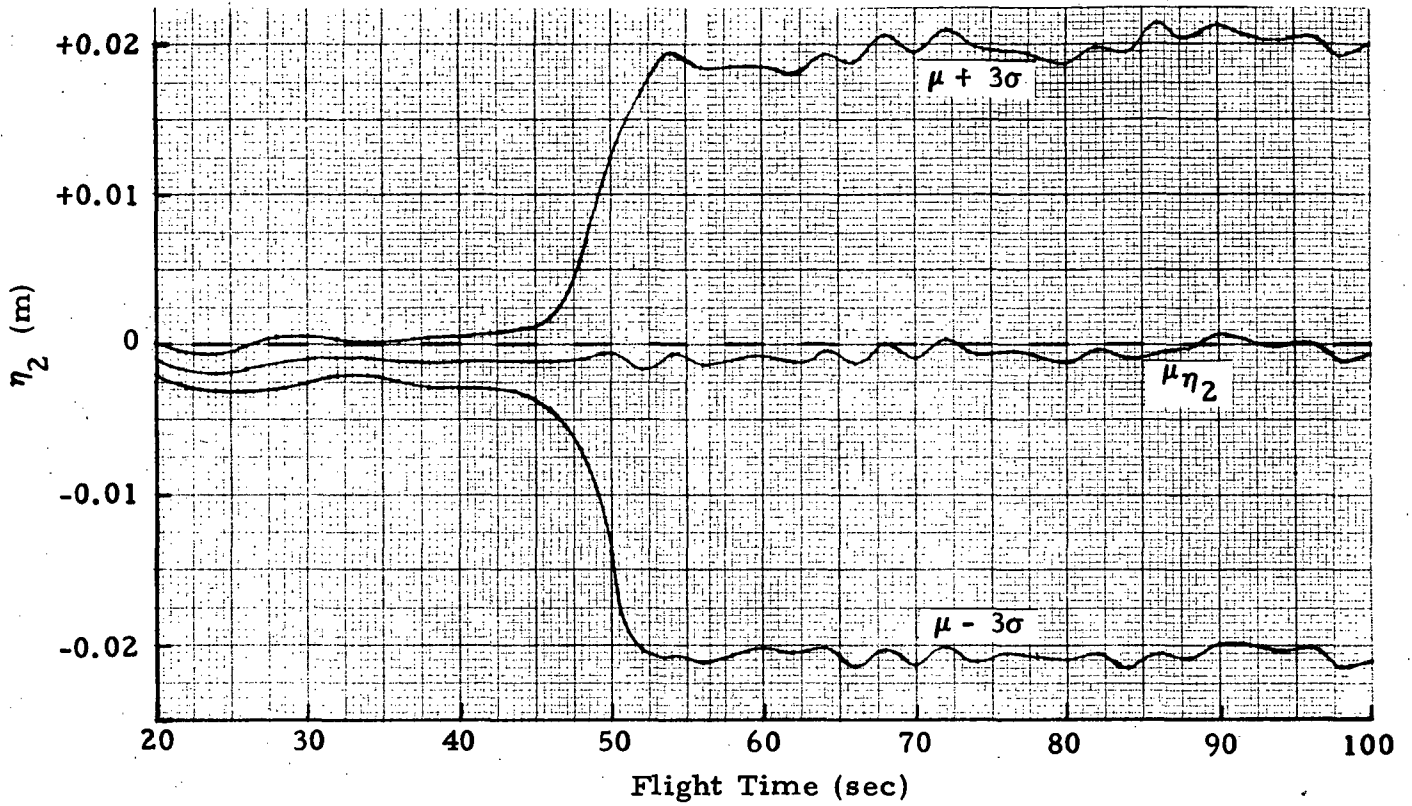


Fig. 6-19 - Mean ( $\mu\eta_2$ ) and  $3\sigma$  Features of  $\eta_2$  Response to 970 Measured Winds

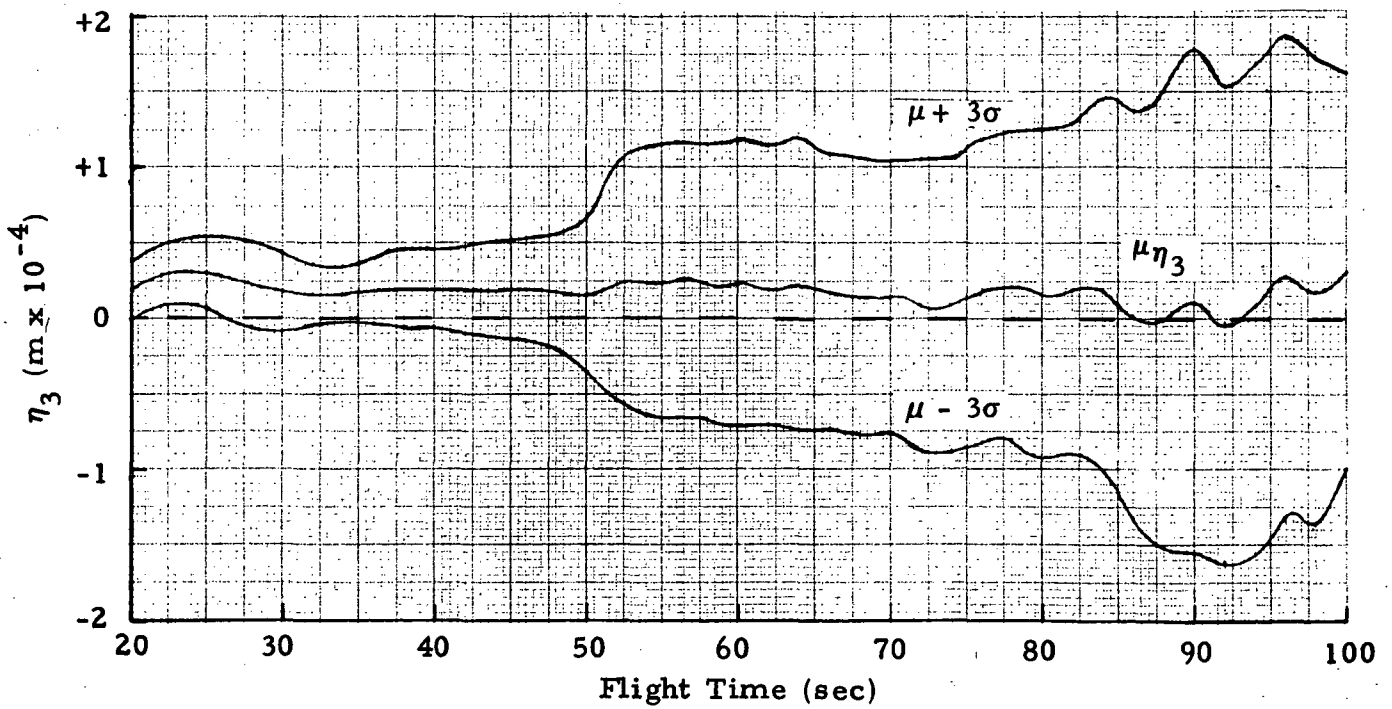


Fig. 6-20 - Mean ( $\mu\eta_3$ ) and  $3\sigma$  Features of  $\eta_3$  Response to 970 Measured Winds

1. The converging  $3\sigma$  limits closely match the shape of the bending moment capability versus flight time presented in Fig. 3-5. This desirable result verifies the effectiveness of the design approach employed in this study.
2. These bending moment results point out that use of only a few design winds is justified. Use of these synthetic design winds yields a conservative controller, as is evidenced by the low bending moment levels apparent in Figs. 6-14 through 6-16.

Results of the exceedance count portion of the statistical evaluation are presented in Figs. 6-21 and 6-22. Exceedance probability information for  $\beta$ ,  $\beta$ ,  $M_{B35.6}$ ,  $M_{B43.2}$ , and  $M_{B58.5}$  is presented in these figures.

Finally, oscilloscope traces of  $V_w$ ,  $\alpha_w$ ,  $\alpha$ ,  $\beta$ ,  $M_{B58.5}$  are presented in Figs. 6-23 through 6-26 for all 970 measured winds. These pictures may be used to determine envelopes, or boundaries, within which these variables remained.

The foregoing statistical results were not very difficult to generate by making use of an operational analog simulation of INT-21 flight dynamics. Considering this fact, as well as the valuable information produced by such an effort, it is recommended that a similar performance verification step be performed in all future ascent control studies.

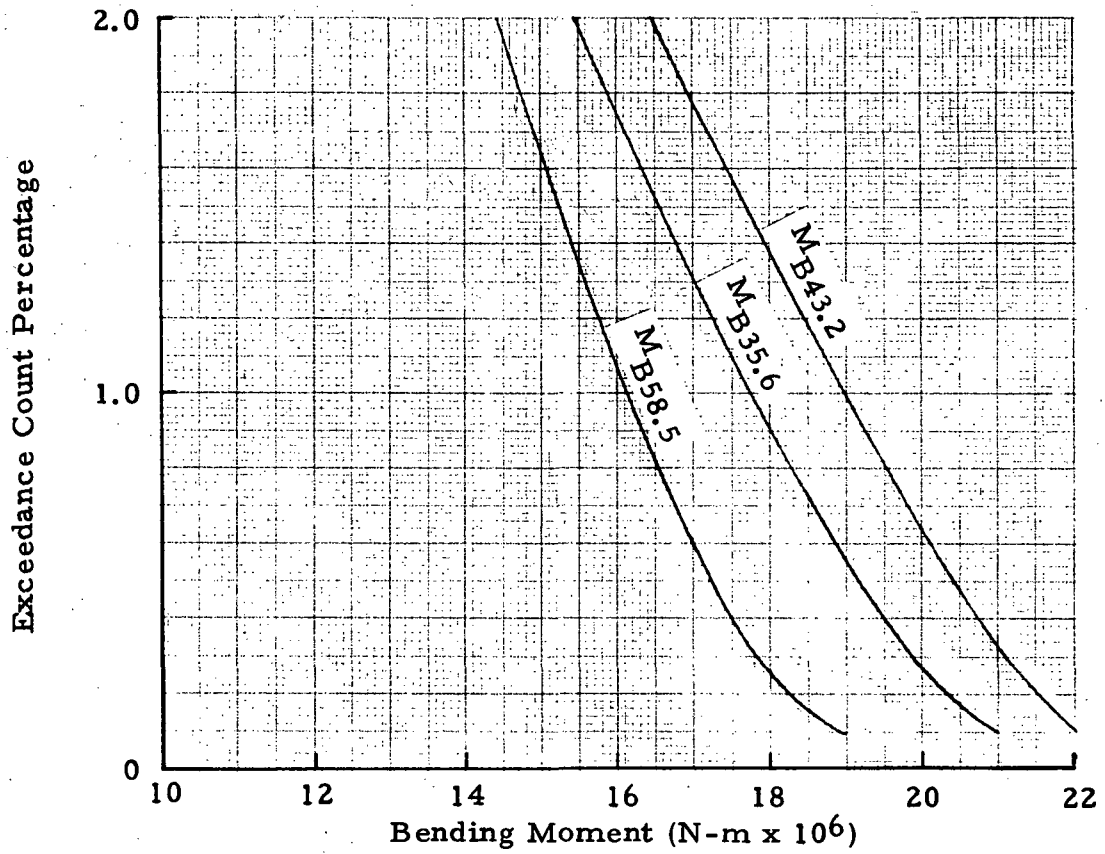


Fig. 6-21 - Exceedance Probability vs Bending Moment Level

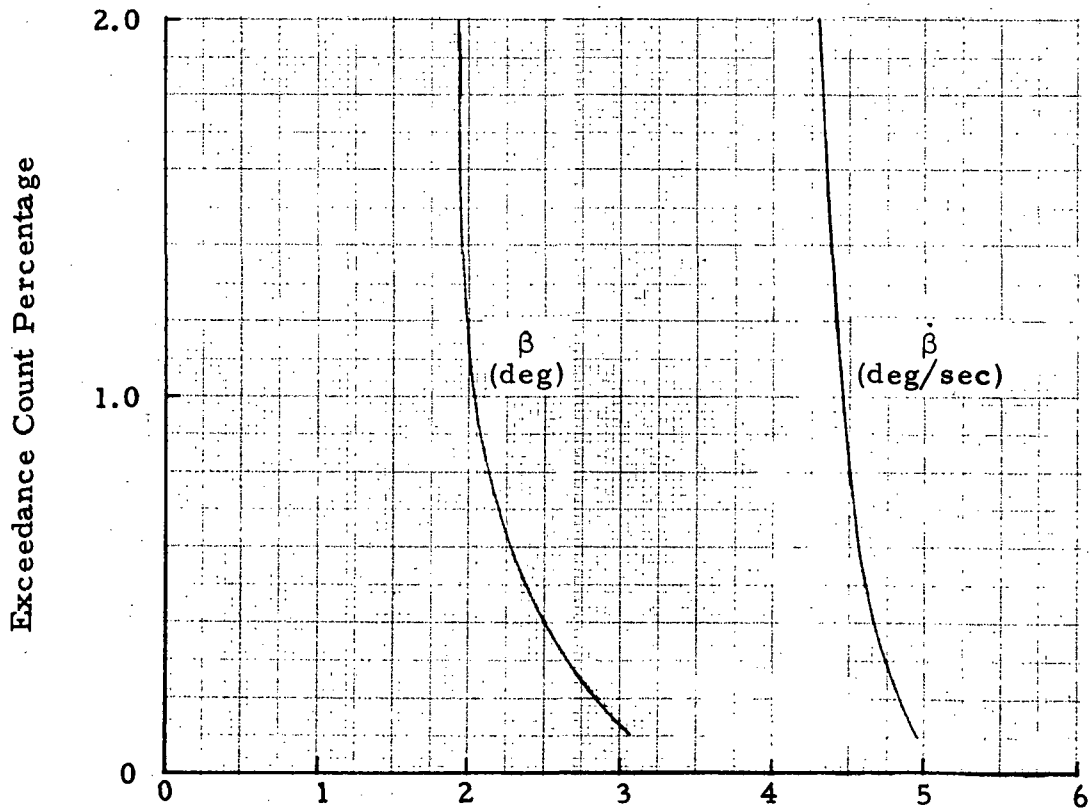


Fig. 6-22 - Exceedance Probability vs Engine Deflection and Deflection Rate

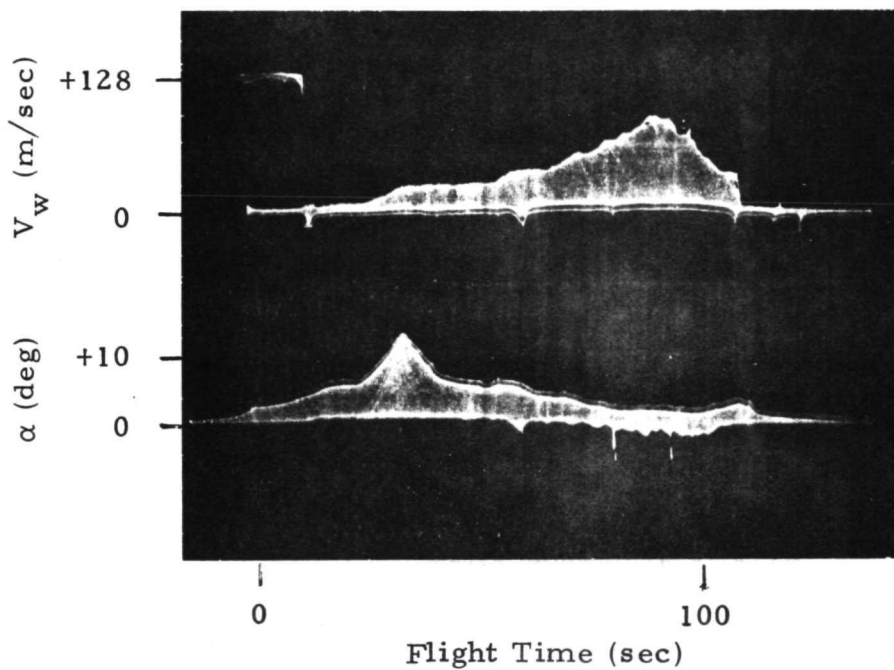


Fig. 6-23 -  $V_w$  and  $\alpha$  vs Flight Time: 970 Measured Winds

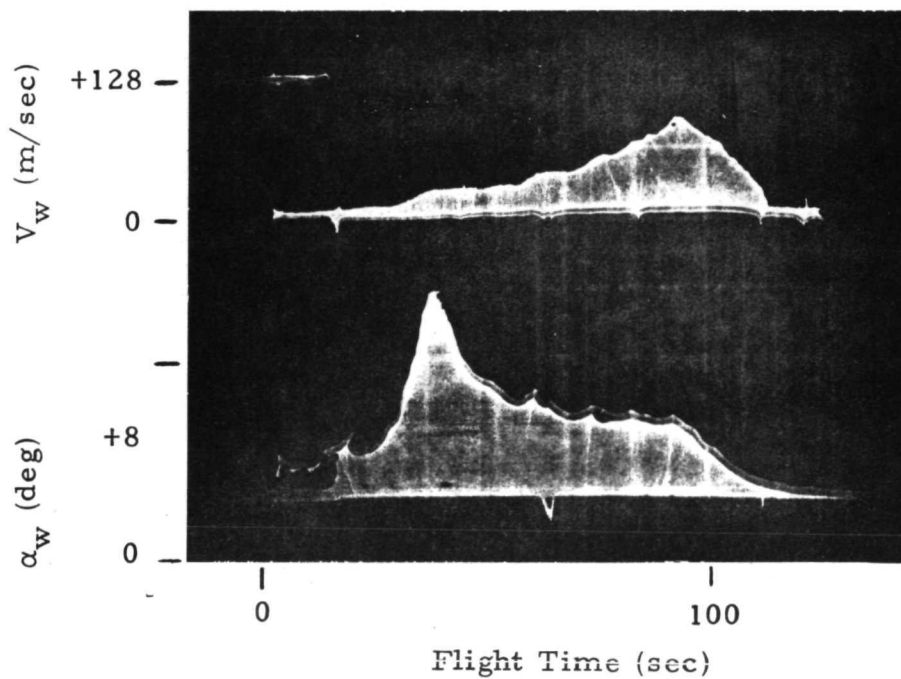


Fig. 6-24 -  $V_w$  and  $\alpha_w$  vs Flight Time: 970 Measured Winds

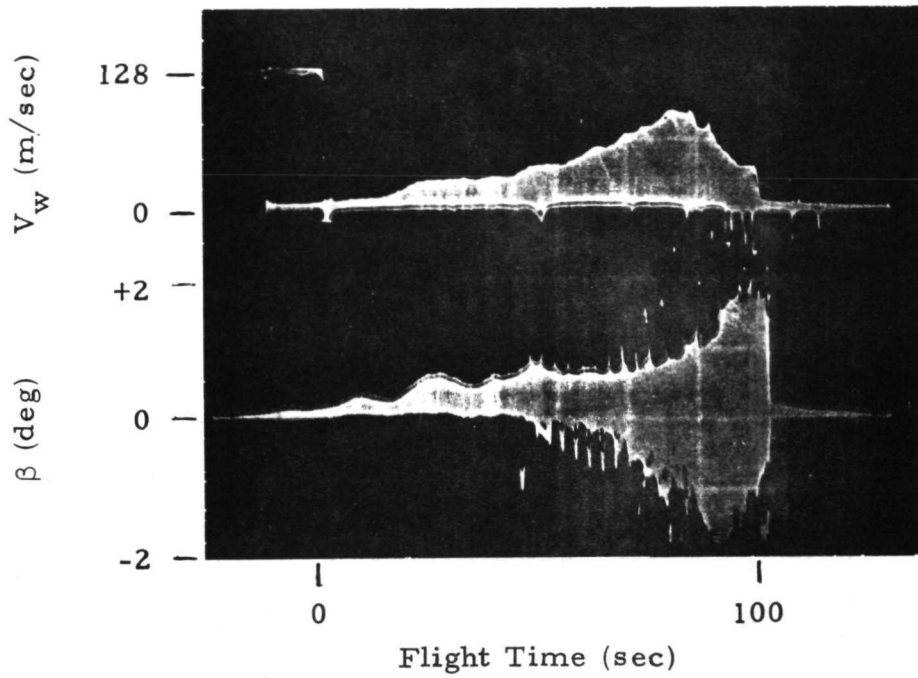


Fig. 6-25 -  $V_w$  and  $\beta$  vs Flight Time: 970 Measured Winds

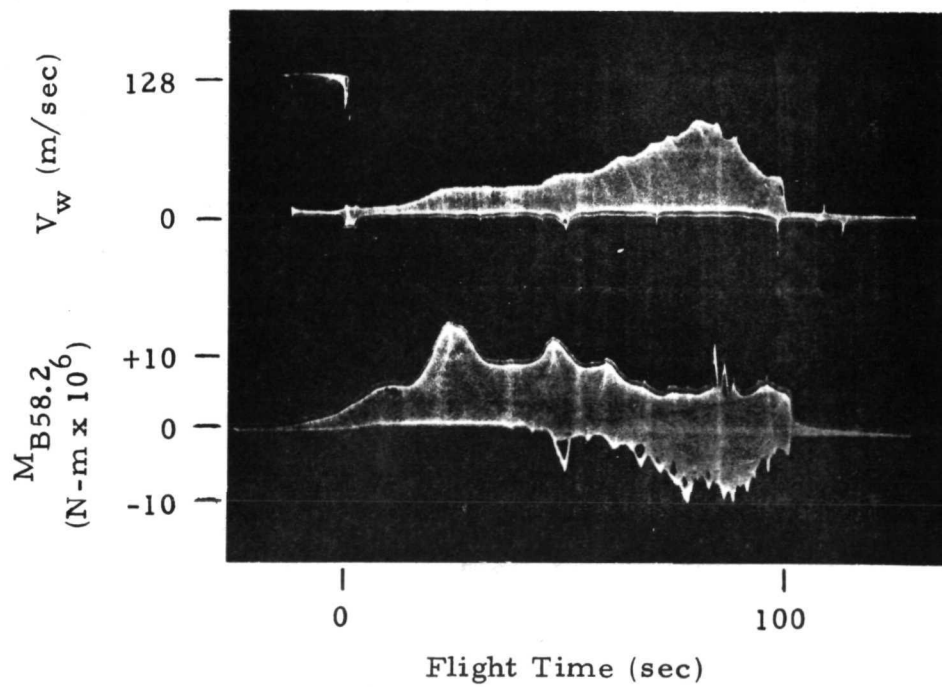


Fig. 6-26 -  $V_w$  and  $M_{B58.2}$  vs Flight Time: 970 Measured Winds



## Section 7

## CONCLUSIONS AND RECOMMENDATIONS

## 7.1 CONTROLLER DESIGN AND OPTIMIZATION

## 7.1.1 Conclusions

By using Lockheed's hybrid optimizer technique, working with a realistic fast-time INT-21 flexible body analog simulation, optimal load relief controller gain schedules have been determined. These optimized controller gain schedules yield significantly better max  $q\alpha$  load relief and drift characteristics than is the case for any previous known INT-21 controller designs. Further, Lockheed's control system produces the additional desired features:

1. Bending moments during reduced structural capability portion of ascent flight (after  $t = 73$  sec) are about one-half or less of peak bending moments.
2. Engine swivel angle and rate are kept low (less than 2.0 deg and 2.0 deg/sec, respectively) throughout ascent flight.
3. Terminal drift is low (less than 1,700 meters).
4. First bending mode amplitude is well behaved (less than 0.08 m peak) and flexible body effects on vehicle control present no great difficulties.

By allowing the use of a free-form performance measure, Lockheed's hybrid optimizer was able to utilize a direct performance criterion based essentially on minimizing peak structural loads at critical vehicle stations. This particular application of Lockheed's hybrid optimizer further demonstrates that the optimizer is a practical and economical design tool which allows the control system designer to formulate design objectives in

meaningful engineering terms. The results presented above are a direct measure of the value of this approach.

System sensitivity to wind conditions was somewhat reduced by using more than one synthetic design wind. Either a more judicious selection of two synthetic design winds, or use of more than two design winds, should further reduce system sensitivity to wind conditions.

Bending moment results would probably have been better if an exact  $M'_\alpha(t)$  had been available for use instead of the conservative estimate applied in this study.

#### 7.1.2 Recommendations

If INT-21 becomes a serious candidate for future missions, further hybrid optimizer studies should be performed, including the following:

- Control system filter time constants systematically adjusted for best performance.
- Sensor locations optimized.
- Incorporate correct  $M'_\alpha(t)$
- Include slosh or total system modes.
- Use sequential pairing of buildup and reverse shear winds.
- Further investigate the merits/demerits of control laws 3, 4 and 5.
- Optimize (and desensitize) for parameter uncertainties, generally.

Once a control system design is "finalized" it should be tested in the following ways:

- Check system performance against each of many diverse synthetic winds in the
  - a. analog simulation, and in the
  - b. digital simulation

- Use the measured winds and hybrid setup to perform a statistical evaluation of critical parameters and thereby provide a realistic check of system performance.

The payload characteristics need to be better defined so that a more meaningful study might be accomplished.

A hybrid computer program for ascent studies was developed during this study. The major features built into this program are: flexible on-line engineering interface, high speed operation, capability for future expansion and modification, and applicability to a wide range of vehicle configurations and trajectories.

A digital computer program has been developed which receives and prints raw mass, aerodynamic, propulsion, structural dynamics, and trajectory data. It also receives and prints wind speed versus altitude data for up to ten different synthetic wind speed curves. Using these inputs, plus the desired control law, it generates, prints, and plots:

1. Time-varying coefficients (TVC's) of EOM for internal use in the digital simulation and/or outside use in the analog simulation.
2. Up to ten different synthetic wind speed curves (converts wind speed vs altitude to wind angle vs time, for a given nominal flight profile) for use both in the digital and analog simulations.
3. Solution of the launch vehicle ascent equations of motion, which can be used for verifying analog simulation results.

This digital program has been kept as general as possible and is available for use in studies of a wide class of launch vehicles.

These two general programs are available and highly recommended for future launch vehicle studies.

## 7.2 PERFORMANCE VERIFICATION

### 7.2.1 Conclusions

Confidence in control system capabilities and effectiveness is considerably enhanced when vehicle response to many measured winds shows desirable statistical features. Conversely, should vehicle response exhibit undesirable statistical characteristics, further control system analyses and design would probably be in order.

The statistical response results presented in Section 6 confirm the effectiveness of Control Law 3 used in conjunction with the optimized controller gain schedules. These results signify that a commendable control system design has been achieved.

It would be difficult to devise a more practical test procedure than the statistical evaluation of response to measured winds which are representative of the actual flight conditions INT-21 could be expected to encounter. Therefore, it is concluded that performance verification via statistical evaluation techniques is a valuable step in the overall design-verification procedure.

Furthermore, for linear systems with time-varying coefficients (as in the present study) or for nonlinear systems, the hybrid computer statistical evaluation technique is the preferred method of computing statistical response characteristics.

### 7.2.2 Recommendations

For final verification of control system performance, statistical evaluation of critical response variables is highly recommended. It provides one of the most realistic measures of system performance that can be generated short of assembly and testing of actual flight hardware.

This technique might also be applied to the evaluation of system response characteristics when parameter uncertainties other than atmospheric wind conditions are of interest, and is hereby recommended for these additional applications.

The particular wind tapes which Lockheed-Huntsville used in this hybrid study are preprocessed functions of flight time, of use only for one predetermined flight profile. Generally, it would be better if the original form of the data (wind speed versus altitude) could be used. This would greatly increase the flexibility of this technique, and flight simulations could be perturbed from any arbitrary nominal trajectory.

Additionally, in the case of nonlinear or of more sophisticated mathematical models of system dynamics, the flight trajectory could be defined as a parameter dependent on vehicle response and/or time.

Section 8  
REFERENCES

1. Trautwein, W., and C.L. Connor, "Hybrid Computer Solutions for Optimal Control of Time-Varying Systems with Parameter Uncertainties," Proceedings, Fall Joint Computer Conf., Houston, Texas, 1970, pp. 135-142.
2. Fletcher, R., and M.J.D. Powell, "A Rapidly Convergent Descent Method for Minimization," Computer J., Vol. 6, 1963.
3. Trautwein, W., and J.G. Tuck, "Control System Optimization for Saturn V Launch Vehicles Using Gradient Techniques," Final Report, LMSC-HREC A791836, Lockheed Missiles & Space Co., Huntsville, Ala., October 1968.
4. Daniels, Glenn E. (Editor), "Terrestrial Environment (Climatic) Criteria Guidelines for Use in Space Vehicle Development, 1971 Revision," NASA TM X-64589, Marshall Space Flight Center, 10 May 1971.
5. Sharp, J.B., L.W. Foster and D.R. Kennemur, "Intermediate-21 Load Relief Attitude Control," M-795-895, Northrop Corp., Huntsville, Ala., March 1971.
6. Trautwein, W., C.L. Connor, and J.M. Livingston, "Computerized Optimal Control System Design for Reusable and Expendable Boost Vehicles," AIAA 10th Aerospace Sciences Meeting, AIAA Paper No. 72-98, San Diego, Calif., 17 January 1972.
7. Garner, D., "Control Theory Handbook," NASA TM X-53036, Marshall Space Flight Center, Huntsville, Ala., 22 April 1964.
8. Coyne, G.W., "Nonlinear Accelerometer Load Relief," LMSC-HREC A783386, Lockheed Missiles & Space Co., Huntsville, Ala., October 1966.
9. Chichester, D.E., and W.E. Row, "Application of Saturn V Intermediate Launch Vehicles to Space Station/Space Base Missions, Contract NAS8-5608, Schedule II, Part VII, Task 9.0, DRL No. 188, Line Item 4, The Boeing Company, Southeast Division, Huntsville, Ala., 30 June 1971.

10. Ericsson, L. E., J. P. Reding, and R. A. Guenther, "Launch Vehicle Gust Penetration Loads," AIAA Paper No. 71-178, AIAA 9th Aerospace Sciences Meeting, New York, N. Y., 25-27 January 1971.
11. Livingston, J. M., Jr., and J. R. Redus, "Load-Reducing Flight Control Systems for the Saturn V with Various Payloads," AIAA Guidance, Control, and Flight Dynamics Conf., AIAA Paper No. 72-98, Pasadena, Calif., 12-14 August 1968.
12. Ryan, R. S., and H. Harcrow, "A Technique for Analyzing Control Gains Using Frequency Response Methods," J. Spacecraft Rockets, Vol. 4, No. 3, March, 1967.
13. Daughtrey, T. W., "High-Speed Simulation of Saturn V Launch," Simulation Department Publication 67-21-20, Computer Sciences Corporation, Huntsville, Ala., September 1967.
14. Feng, G. C., and M. L. Pearson, "Propellant Slosh Coupling with Bending," Interim Report, LMSC-HREC D148988, Lockheed Missiles & Space Co., Huntsville, Ala., June 1969.
15. Feng, G. C., and D. L. Grady, "Propellant Slosh Coupling with Bending," LMSC-HREC D149410, Lockheed Missiles & Space Co., Huntsville, Ala., December 1969.
16. Lockheed Missiles & Space Co., "Atmospheric Flight Simulation Techniques for Large Complex Space Vehicles," Technical Brief, LMSC-HREC D149463, Huntsville, Ala., December 1969.
17. Bekey, G. A., and W. J. Karplus, Hybrid Computation, Wiley, New York, 1968.
18. Korn, G. A., and T. M. Korn, Electronic Analog and Hybrid Computers, McGraw-Hill, New York, 1964.
19. Greenwood, D. T., Principles of Dynamics, Prentice-Hall, Inc., Englewood Cliffs, N. J., 1965.

Appendix A

INT-21 RAW DATA PACKAGE AND EOM  
TIME-VARYING COEFFICIENTS (TVC's)



Appendix A

This appendix presents all raw mass, structural, propulsion, aerodynamic, and trajectory data for the INT-21 vehicle with 141-foot payload. Also included, in plot form, are the time-varying coefficients (TVC's) generated from this data.


A-2

t (sec)	V (m/sec)	$\chi_c$ (rad)	F (N)	D (N)	m (kg)	Q (N/m <sup>2</sup> )	$C_{N\alpha}$ (dim'less)	$F_c$ (N)	$I_{yy_2}$ (kg-m <sup>2</sup> )
0	0.0	0.0	$33.8 \times 10^6$	0.0	$2.86 \times 10^6$	0.0	4.56	$27.05 \times 10^6$	$854 \times 10^6$
10	20.0	0.007	$33.9 \times 10^6$	$0.03 \times 10^6$	$2.73 \times 10^6$	$0.4 \times 10^3$	4.58	$27.12 \times 10^6$	$846 \times 10^6$
20	50.0	0.009	$34.1 \times 10^6$	$0.11 \times 10^6$	$2.60 \times 10^6$	$1.7 \times 10^3$	4.60	$27.38 \times 10^6$	$839 \times 10^6$
30	90.0	0.057	$34.5 \times 10^6$	$0.12 \times 10^6$	$2.47 \times 10^6$	$4.5 \times 10^3$	4.62	$27.60 \times 10^6$	$831 \times 10^6$
40	135.0	0.125	$35.1 \times 10^6$	$0.23 \times 10^6$	$2.34 \times 10^6$	$9.0 \times 10^3$	4.70	$28.08 \times 10^6$	$822 \times 10^6$
50	190.0	0.237	$35.8 \times 10^6$	$0.38 \times 10^6$	$2.22 \times 10^6$	$15.4 \times 10^3$	4.90	$28.64 \times 10^6$	$812 \times 10^6$
60	266.0	0.370	$36.4 \times 10^6$	$0.63 \times 10^6$	$2.08 \times 10^6$	$23.3 \times 10^3$	5.60	$29.12 \times 10^6$	$800 \times 10^6$
70	358.0	0.500	$37.2 \times 10^6$	$1.38 \times 10^6$	$1.96 \times 10^6$	$31.0 \times 10^3$	5.80	$29.76 \times 10^6$	$788 \times 10^6$
80	470.0	0.625	$38.0 \times 10^6$	$1.28 \times 10^6$	$1.83 \times 10^6$	$35.5 \times 10^3$	4.65	$30.40 \times 10^6$	$774 \times 10^6$
90	605.0	0.740	$38.4 \times 10^6$	$0.90 \times 10^6$	$1.70 \times 10^6$	$32.5 \times 10^3$	4.43	$30.72 \times 10^6$	$756 \times 10^6$
100	755.0	0.840	$38.7 \times 10^6$	$0.53 \times 10^6$	$1.57 \times 10^6$	$22.2 \times 10^3$	4.40	$30.96 \times 10^6$	$737 \times 10^6$
110	965.0	0.920	$38.8 \times 10^6$	$0.30 \times 10^6$	$1.44 \times 10^6$	$13.5 \times 10^3$	4.50	$31.04 \times 10^6$	$713 \times 10^6$
120	1180.0	1.000	$38.9 \times 10^6$	$0.18 \times 10^6$	$1.30 \times 10^6$	$9.0 \times 10^3$	4.65	$31.12 \times 10^6$	$683 \times 10^6$

t (sec)	$Y_1'(x_E)$ (1/m)	$Y_2'(x_E)$	$Y_3'(x_E)$	$Y_1(x_E)$ (dim'less)	$Y_2(x_E)$	$Y_3(x_E)$	$x_{cg}$ (m)
0	-0.0110	0.0134	-0.0276	0.22	-0.225	0.0360	27.12
10	-0.0111	0.0144	-0.0245	0.22	-0.240	0.0300	27.12
20	-0.0112	0.0154	-0.0213	0.22	-0.250	0.0250	27.12
30	-0.0113	0.0164	-0.0182	0.22	-0.265	0.0210	27.20
40	-0.0114	0.0175	-0.0151	0.22	-0.275	0.0174	27.25
50	-0.0115	0.0186	-0.0120	0.22	-0.280	0.0125	27.40
60	-0.0116	0.0147	-0.0089	0.22	-0.300	0.0090	27.64
70	-0.0117	0.0207	-0.0057	0.22	-0.320	0.0050	28.15
80	-0.0118	0.0218	-0.0026	0.22	-0.335	0.0025	28.43
90	-0.0119	0.0260	-0.0020	0.22	-0.375	0.0020	28.95
100	-0.0120	0.0304	-0.0020	0.22	-0.435	0.0020	29.68
110	-0.0120	0.0363	-0.0020	0.22	-0.495	0.0020	30.76
120	-0.0120	0.0422	-0.0020	0.22	-0.550	0.0020	32.00

t (sec)	$\omega_{b1}$ (rad/sec)	$\omega_{b2}$	$\omega_{b3}$	$T_1$ (kg)	$T_2$	$T_3$	$x_{cg}$ (m)
0	7.04	13.95	27.55	$55.2 \times 10^3$	$86.0 \times 10^3$	$168.0 \times 10^3$	47.30
10	7.36	14.08	27.66	$54.4 \times 10^3$	$89.0 \times 10^3$	$120.0 \times 10^3$	47.24
20	7.48	14.27	28.32	$53.8 \times 10^3$	$92.0 \times 10^3$	$94.0 \times 10^3$	47.20
30	7.55	14.40	29.54	$52.6 \times 10^3$	$95.0 \times 10^3$	$72.0 \times 10^3$	47.00
40	7.61	14.52	30.88	$51.6 \times 10^3$	$99.0 \times 10^3$	$54.0 \times 10^3$	46.50
50	7.67	14.58	32.00	$50.8 \times 10^3$	$103.0 \times 10^3$	$40.0 \times 10^3$	45.25
60	7.73	14.65	32.60	$50.0 \times 10^3$	$107.0 \times 10^3$	$32.0 \times 10^3$	41.62
70	7.86	15.02	33.06	$49.0 \times 10^3$	$111.0 \times 10^3$	$24.0 \times 10^3$	43.42
80	8.05	15.40	33.12	$48.0 \times 10^3$	$115.0 \times 10^3$	$18.4 \times 10^3$	56.50
90	8.24	15.84	33.12	$46.8 \times 10^3$	$128.0 \times 10^3$	$18.0 \times 10^3$	62.40
100	8.24	16.53	33.20	$45.0 \times 10^3$	$146.0 \times 10^3$	$18.0 \times 10^3$	65.23
110	8.30	17.47	33.20	$44.0 \times 10^3$	$158.0 \times 10^3$	$18.0 \times 10^3$	67.10
120	8.30	18.60	33.20	$42.2 \times 10^3$	$170.0 \times 10^3$	$18.0 \times 10^3$	67.30

A-4

t (sec)	$C_{Abl_1}$ (dimi'less)	$C_{Abl_2}$	$C_{Abl_3}$	h (m)
0	0.0040	0.0110	0.0	0.0
10	0.0040	0.0110		$0.11 \times 10^3$
20	0.0039	0.0110		$0.54 \times 10^3$
30	0.0038	0.0110		$1.20 \times 10^3$
40	0.0037	0.0110		$2.30 \times 10^3$
50	0.0032	0.0112		$3.85 \times 10^3$
60	0.0027	0.0114		$6.00 \times 10^3$
70	0.0022	0.0116		$8.85 \times 10^3$
80	0.0017	0.0118		$12.40 \times 10^3$
90	-0.0020	0.0170		$16.50 \times 10^3$
100	-0.0038	0.0245		$21.25 \times 10^3$
110	-0.0042	0.0500		$26.80 \times 10^3$
120	-0.0047	0.0876		$33.00 \times 10^3$

t (sec)	$Y_{1x_a}$ (m/m)	$Y_{2x_a}$ (m/m)	$Y_{3x_a}$ (m/m)	$Y'_{1x_{rg}}$ (rad/m)	$Y'_{2x_{rg}}$ (rad/m)	$Y'_{3x_{rg}}$ (rad/m)
0.0	-0.120	-0.04	+0.38	+0.0185	+0.01968	0.0
71.3	-0.154	+0.02	+0.08	+0.0191	+0.0189	-0.01573
100.0	-0.160	+0.10	+0.08	+0.0193	+0.0177	-0.01612
120.0	-0.160	+0.20	+0.08	+0.0197	+0.01458	-0.01574

NOTE:  $Y'_{ix_{pg}} = Y'_{ix_{rg}}$

DATA

$$S_A = 79.36 \text{ m}^2$$

$$m_E = 10532.0 \text{ kg}$$

$$l_E = 1.27 \text{ m}$$

$$x_E = 0.0$$

$$I_E = 46351.0 \text{ kg-m}^2$$

$$\zeta_{b_1} = 0.005, \quad \zeta_{b_2} = \zeta_{b_3} = 0.0056, \quad \zeta_{b_4} = 0.0$$

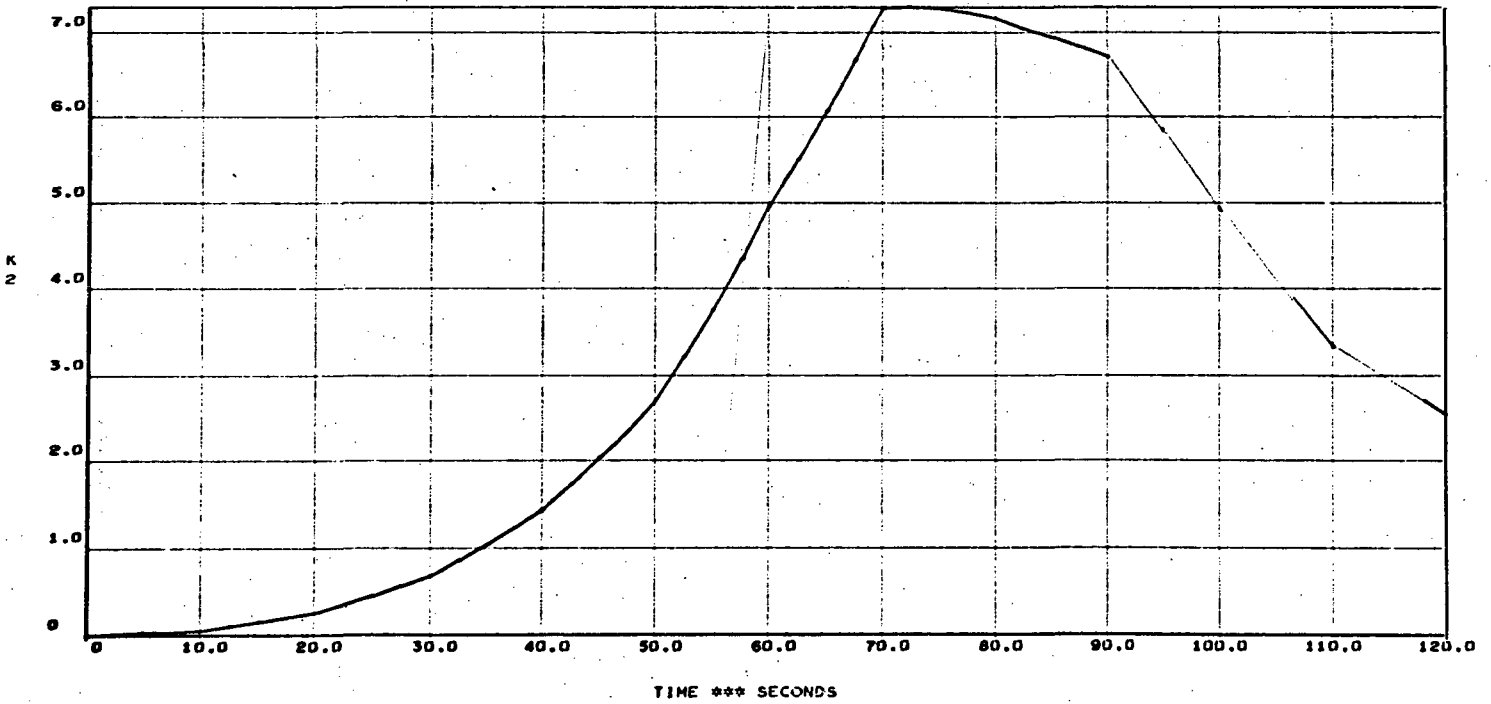
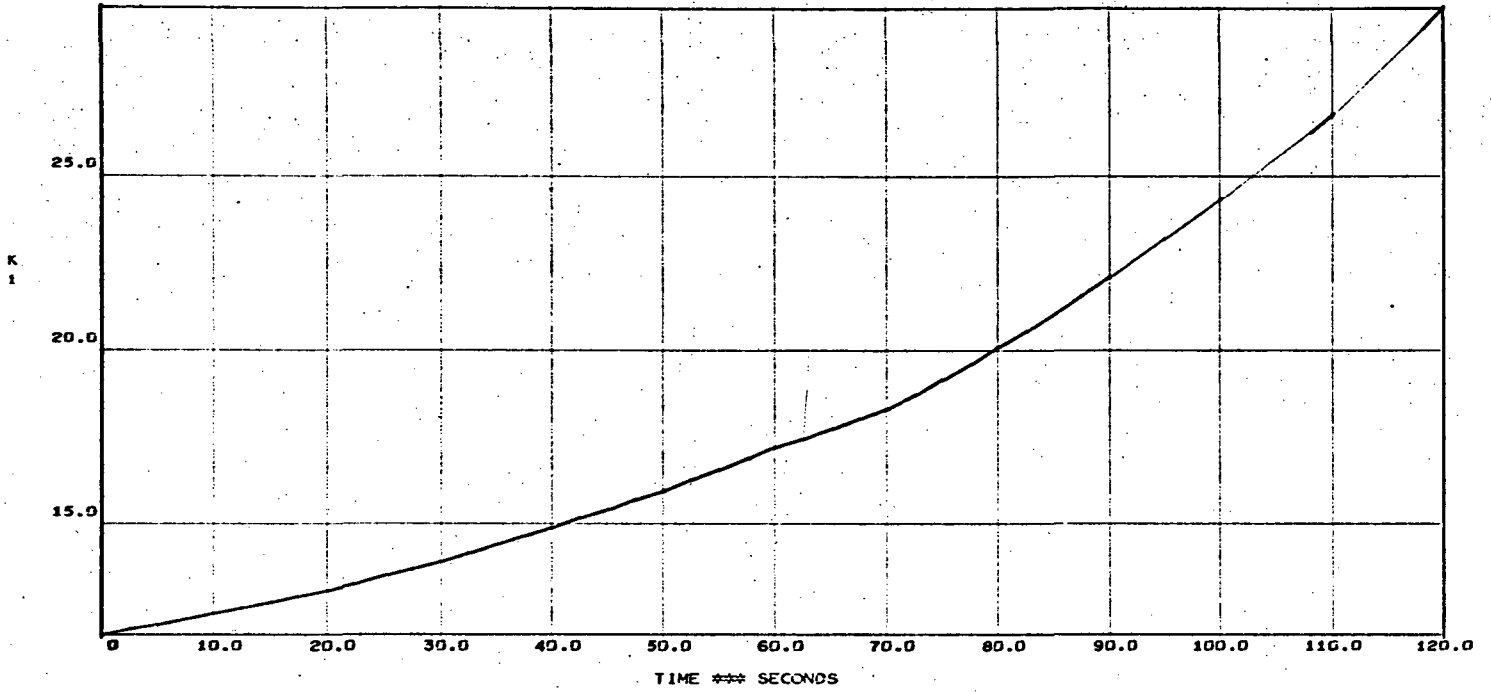
$$\zeta_E = 0.434$$

$$\omega_E = 34.48 \text{ rad/sec}$$

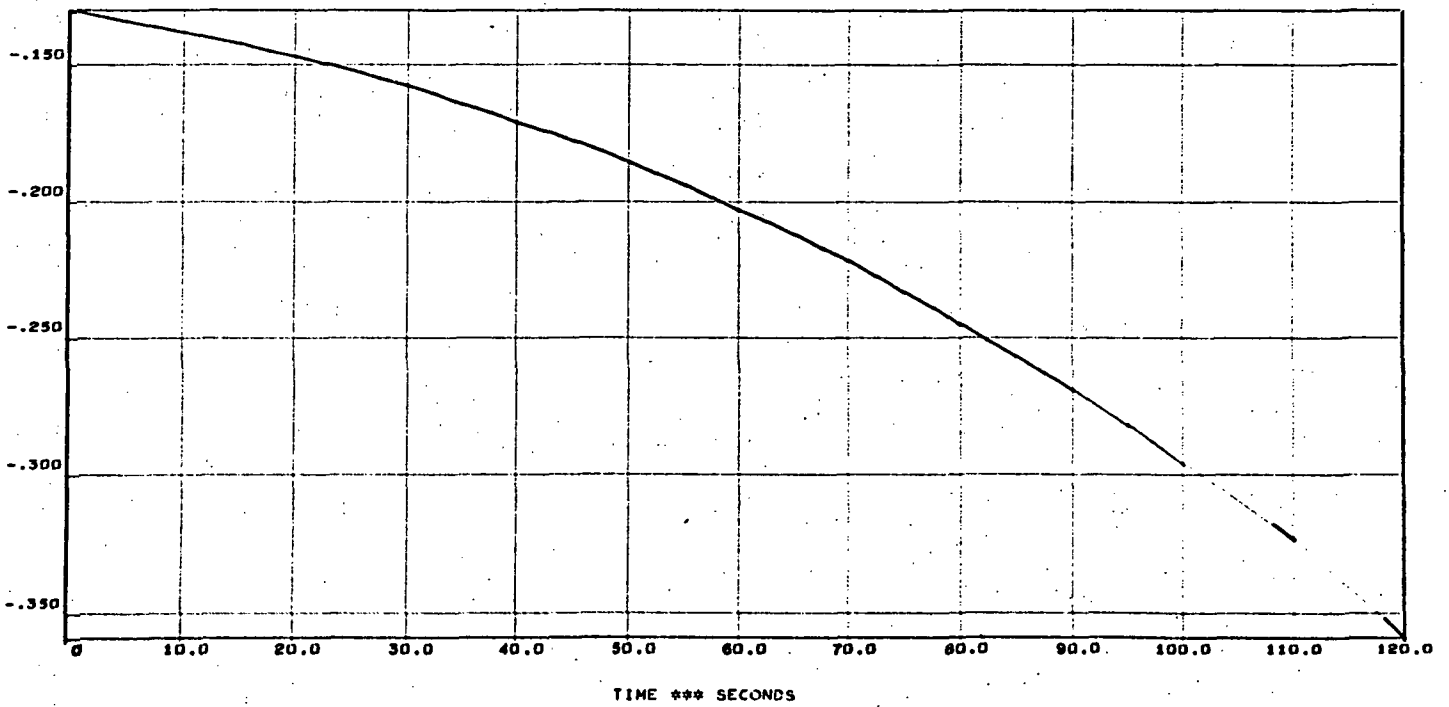
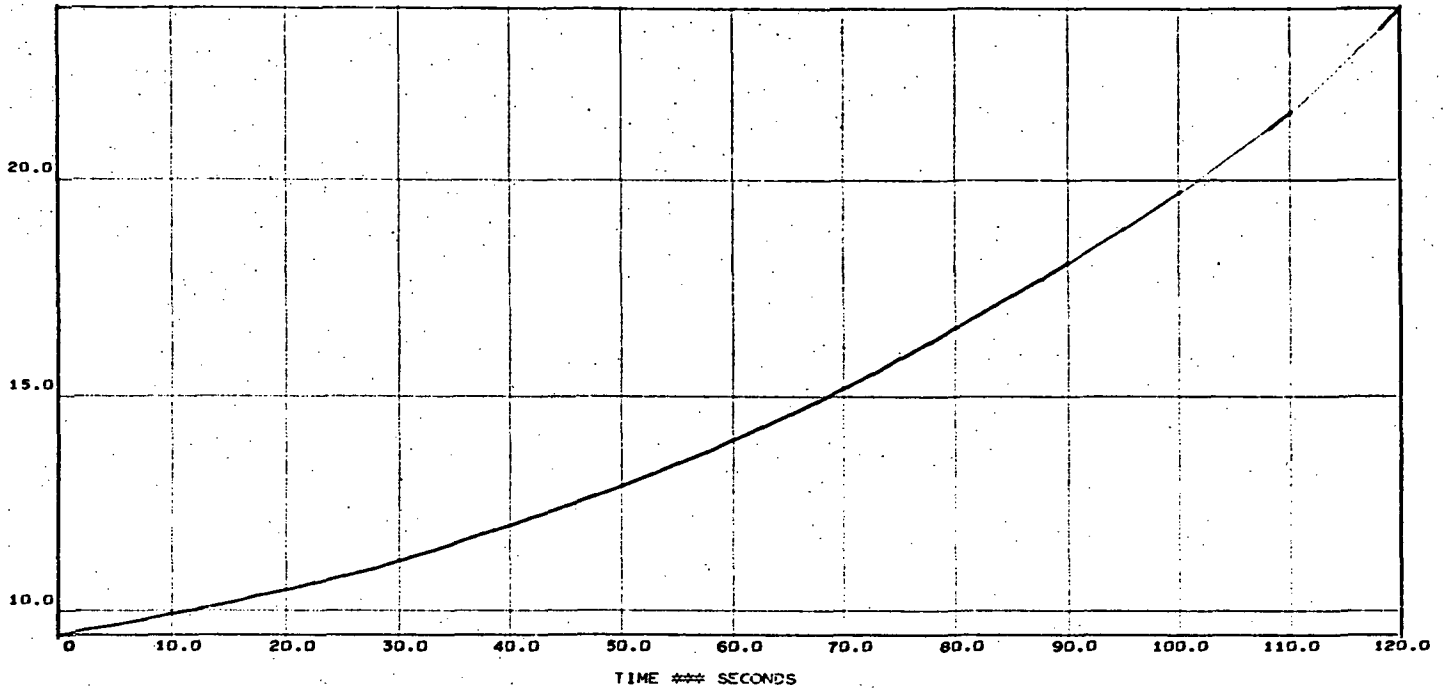
TIME-VARYING COEFFICIENTS



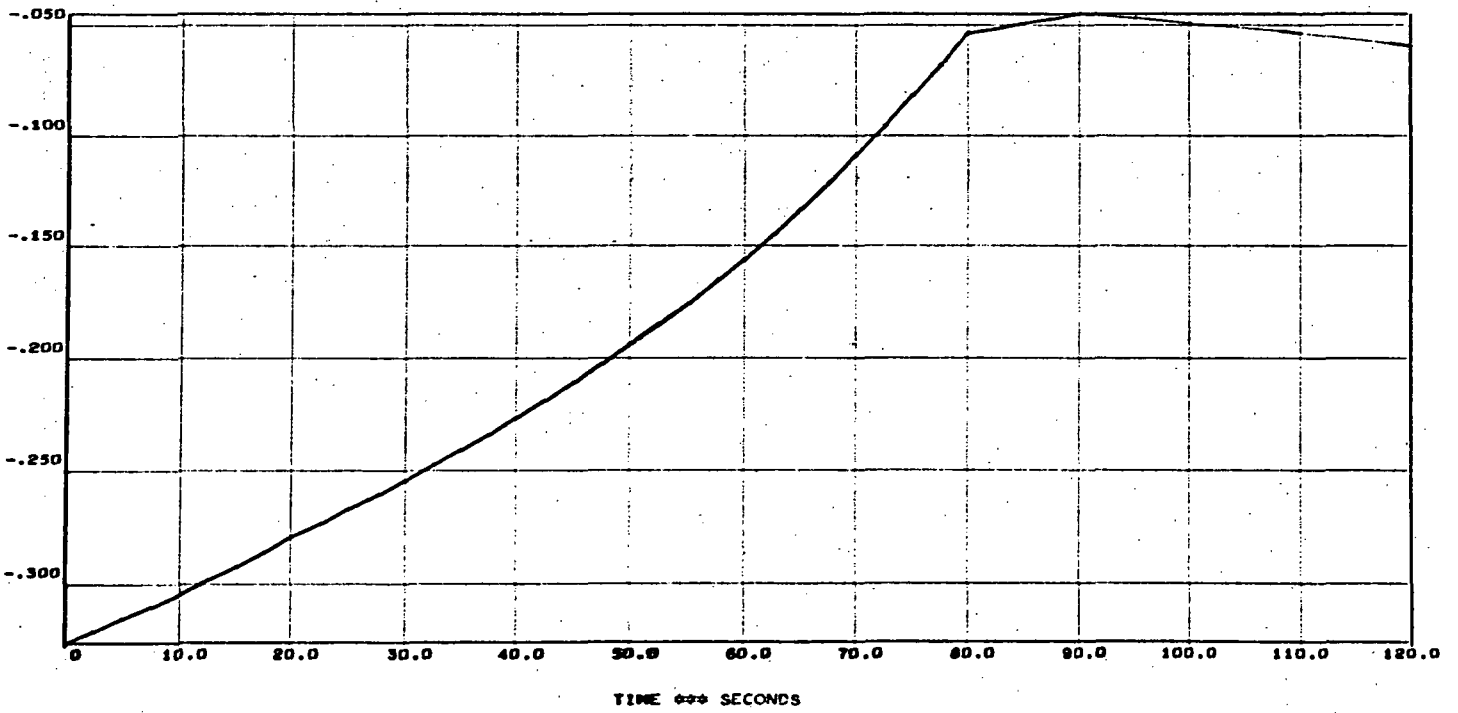
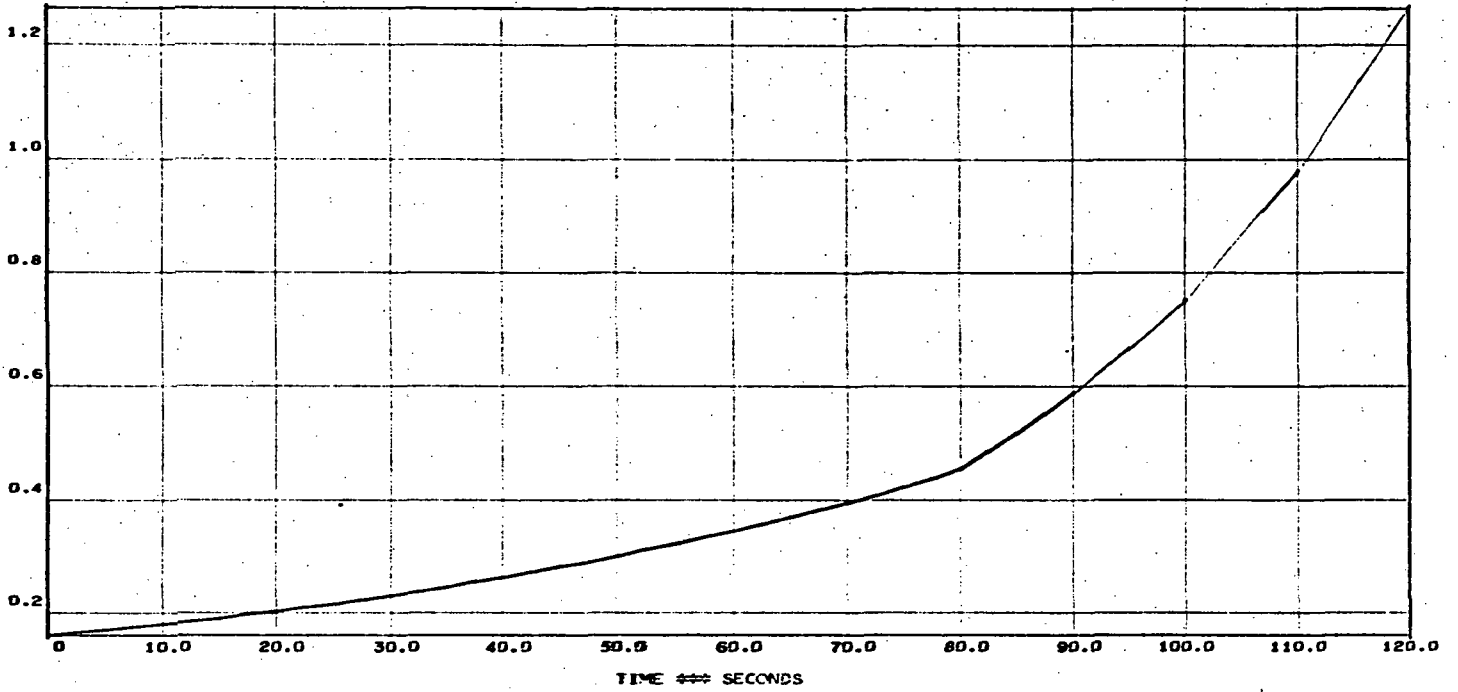
INT-21 ASCENT

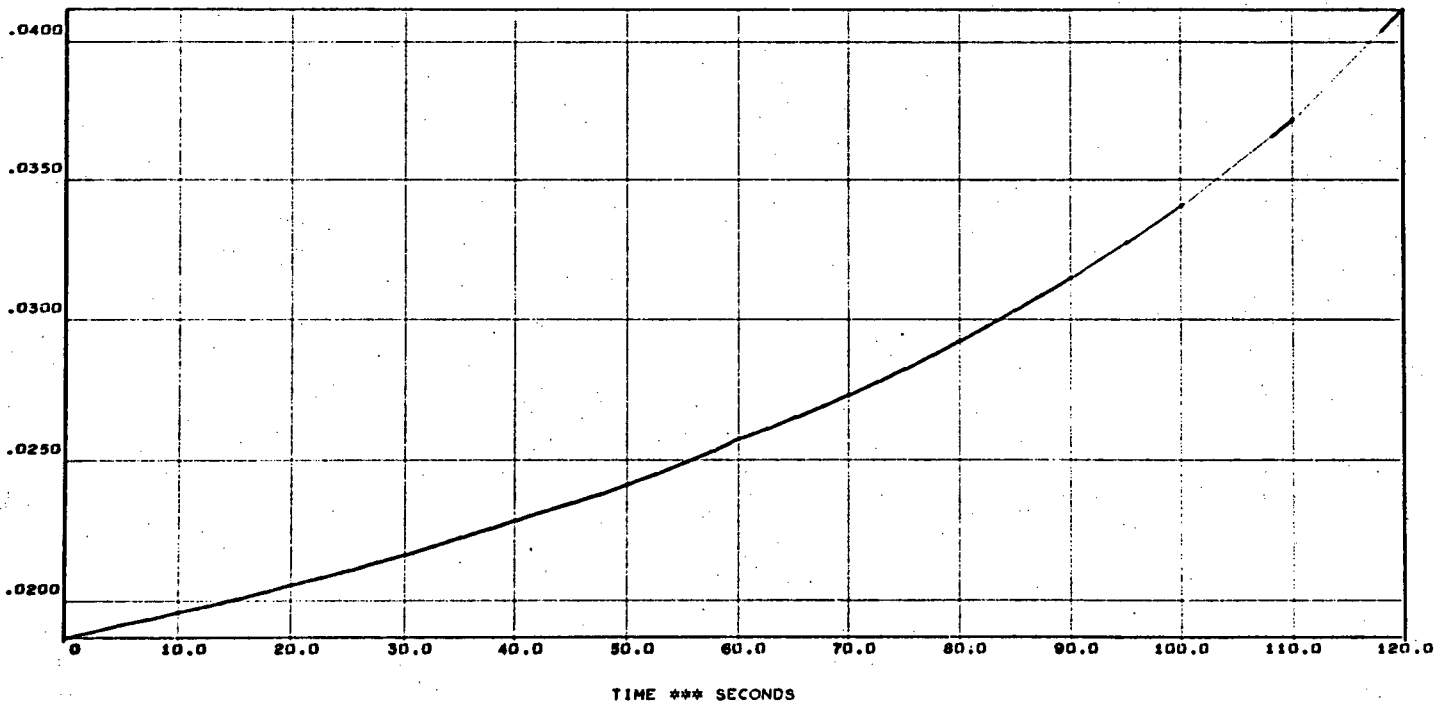


INT-21 ASCENT

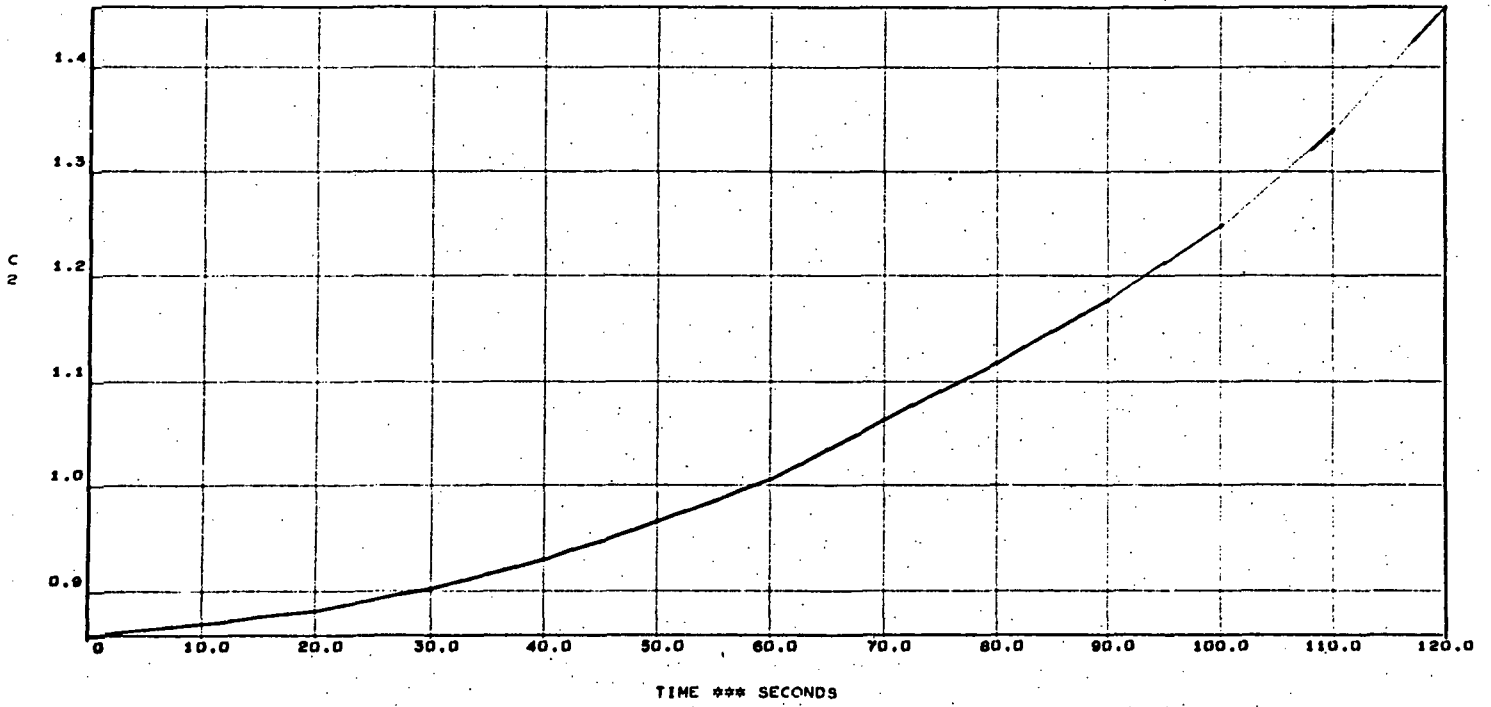
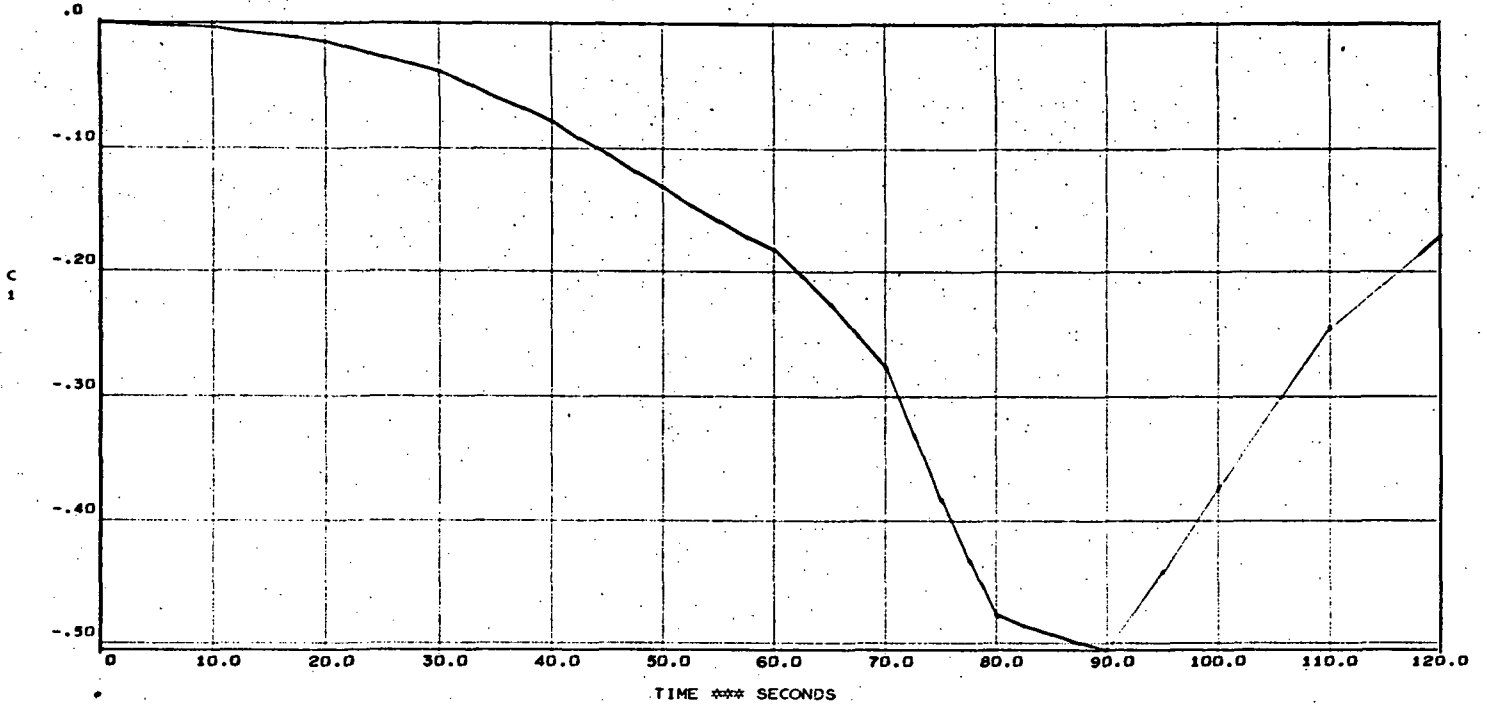


INT-21 ASCENT

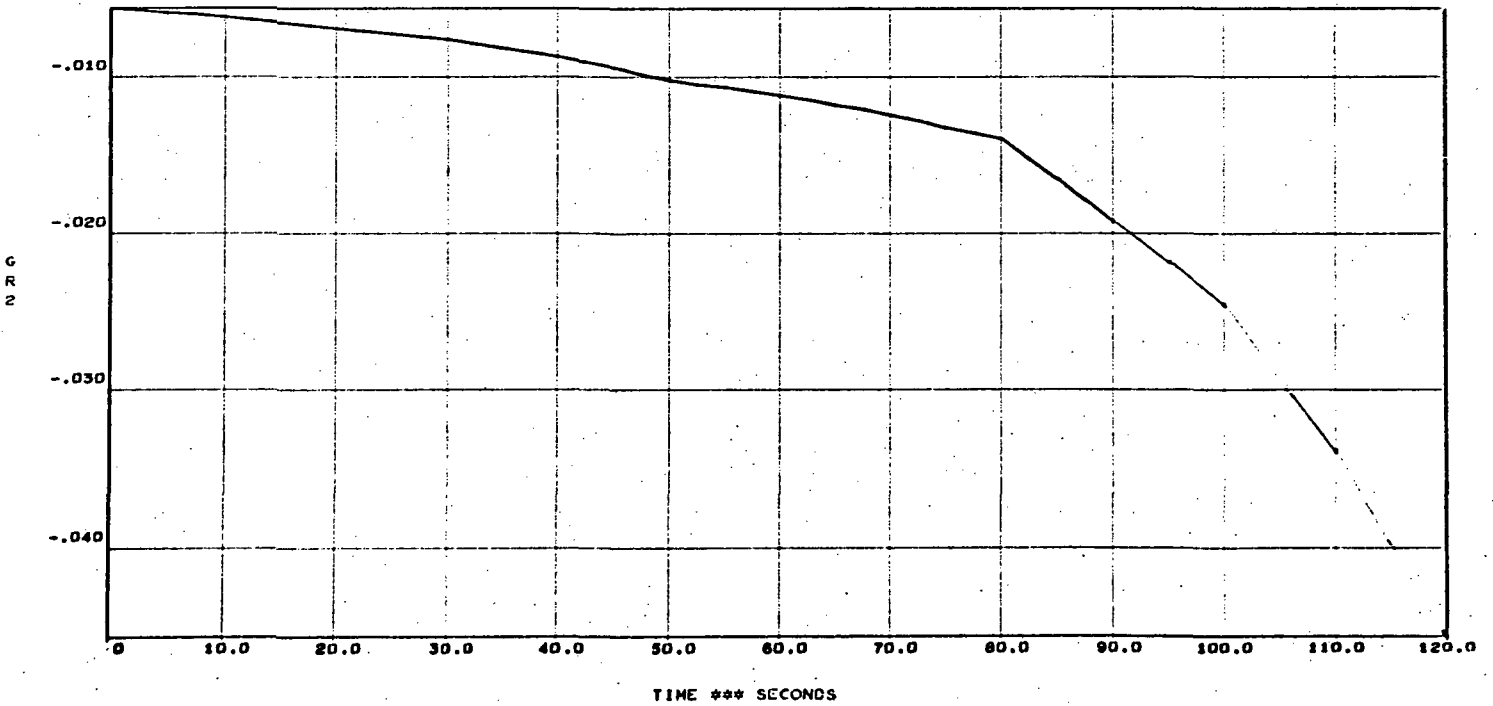
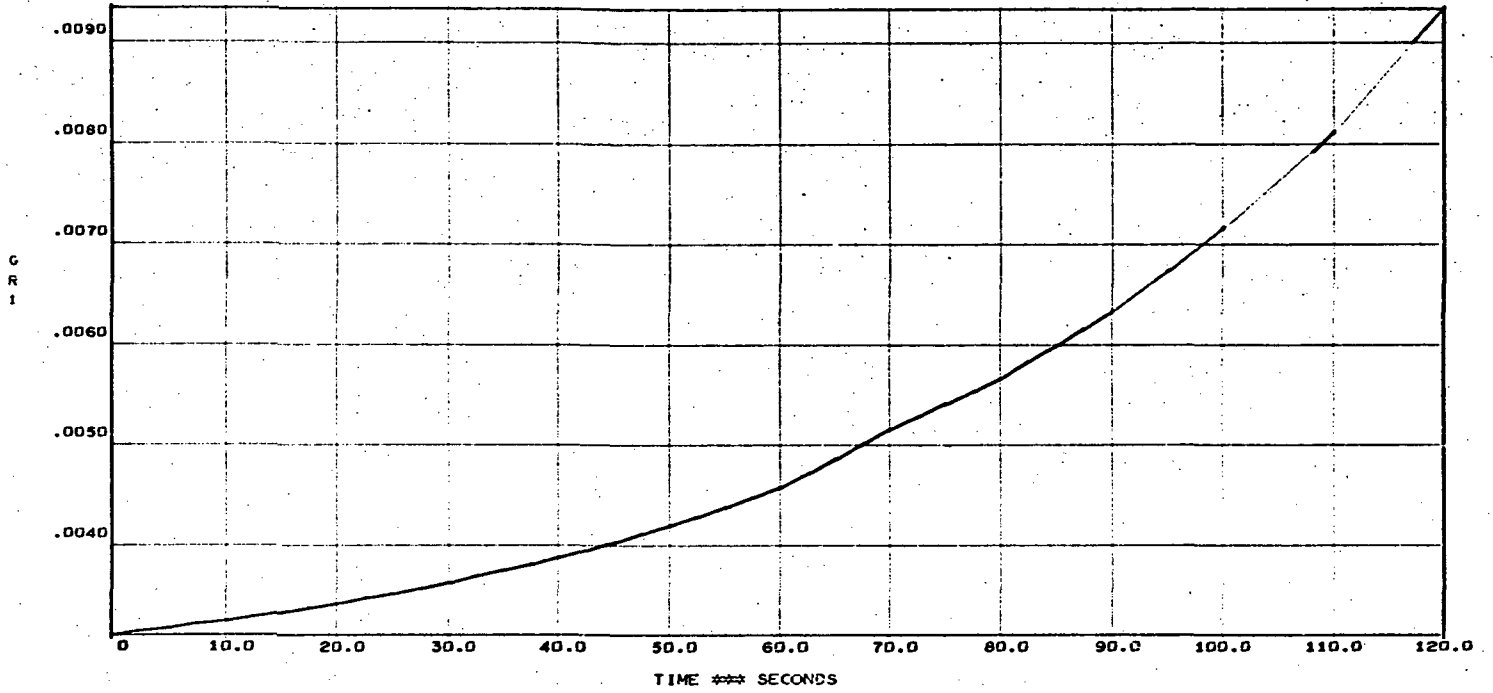




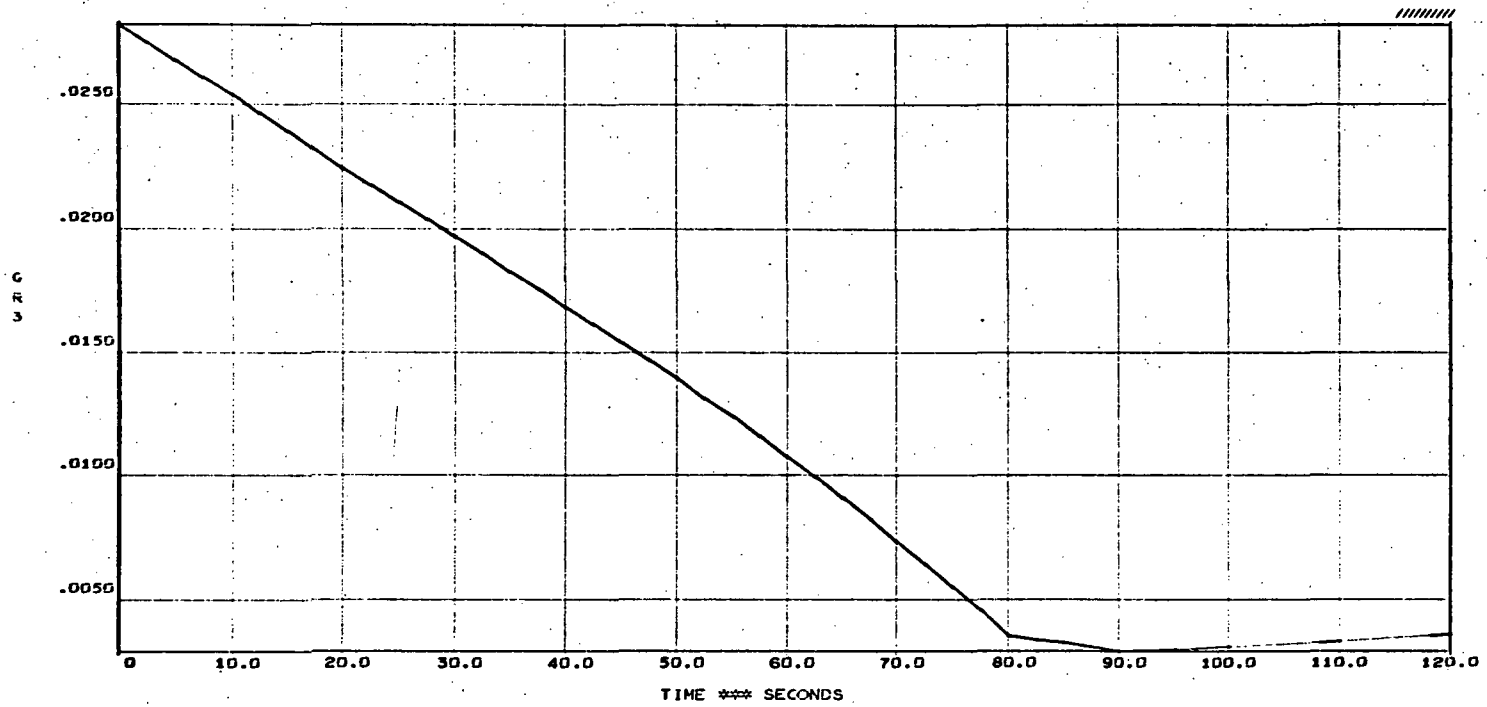
INT-21 ASCENT



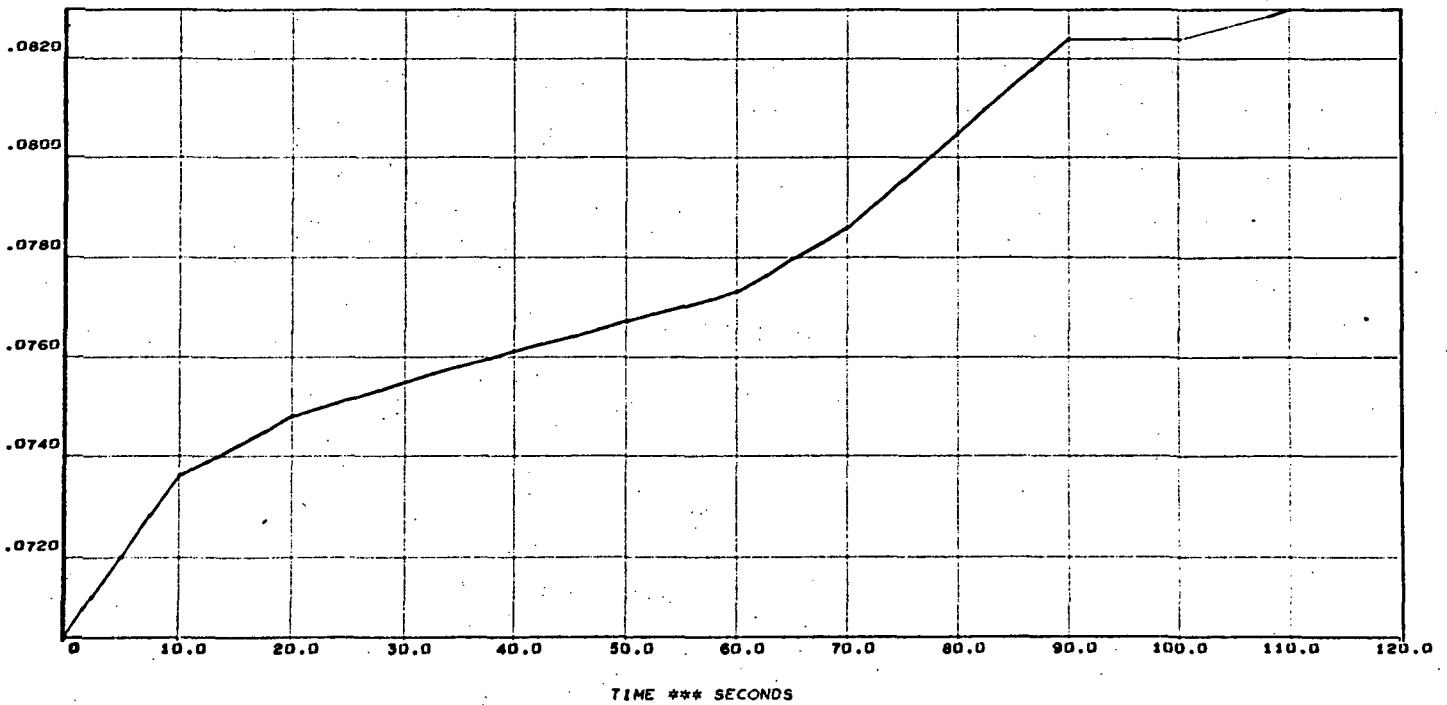
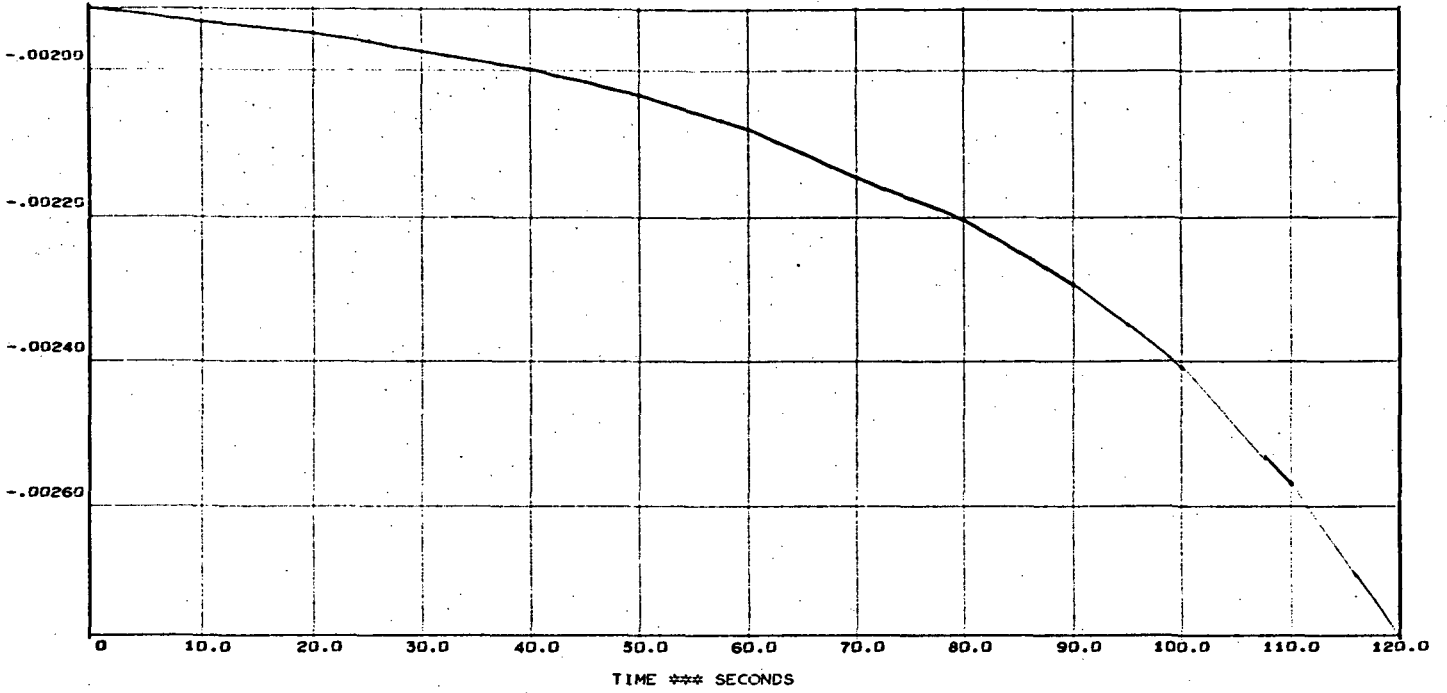
INT-21 ASCENT



INT-21 ASCENT

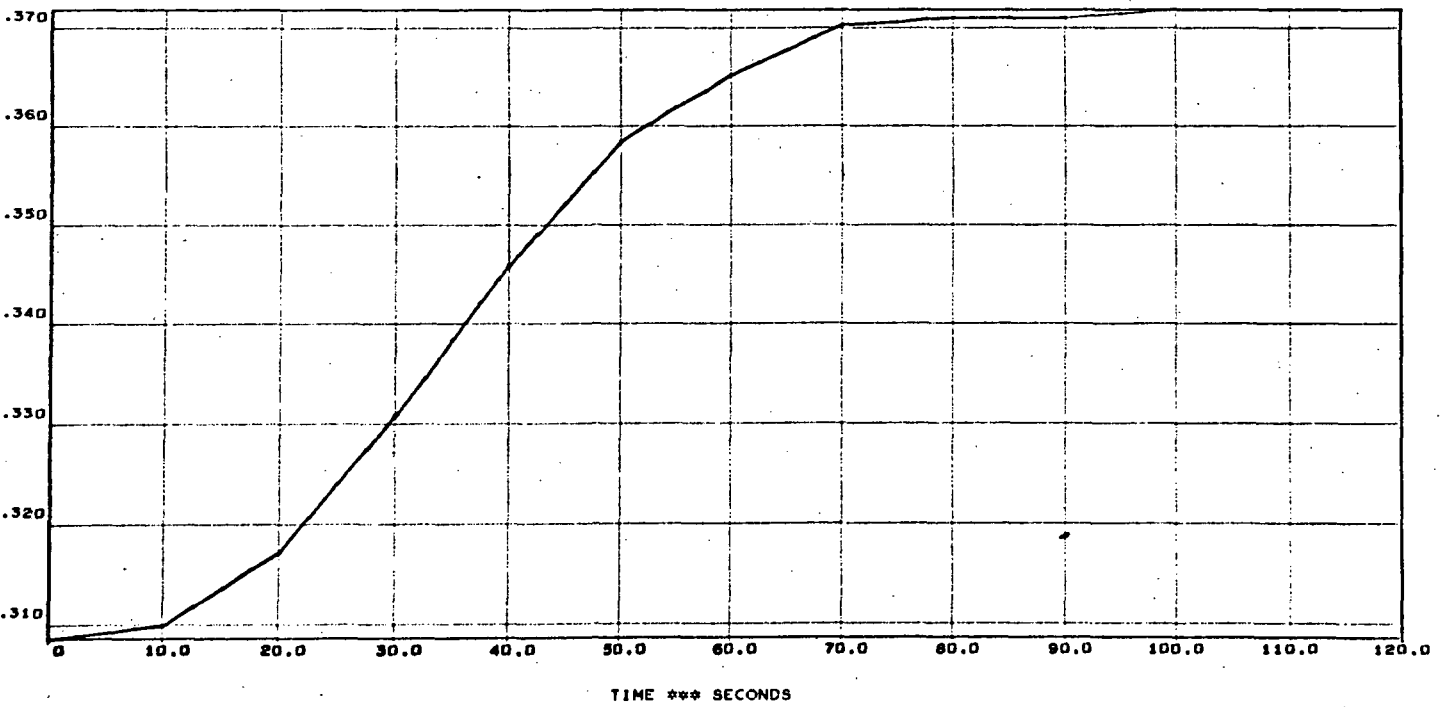
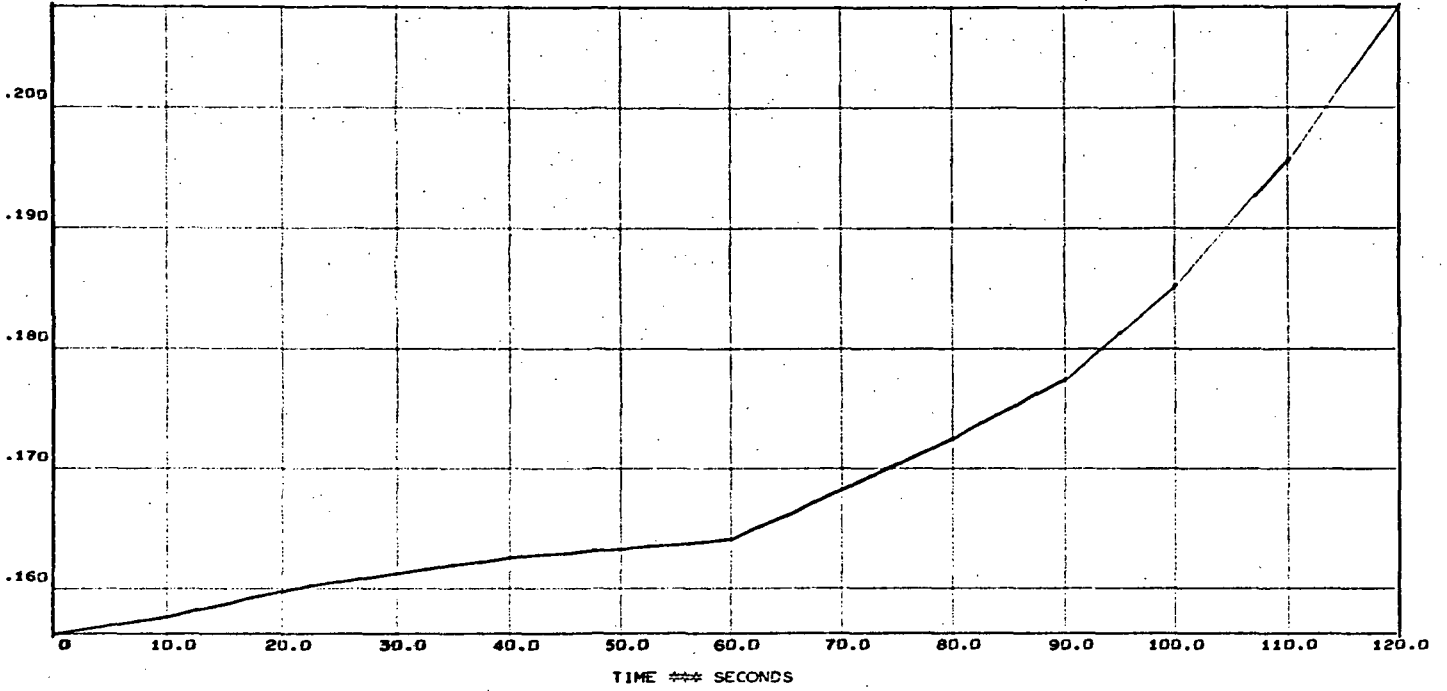


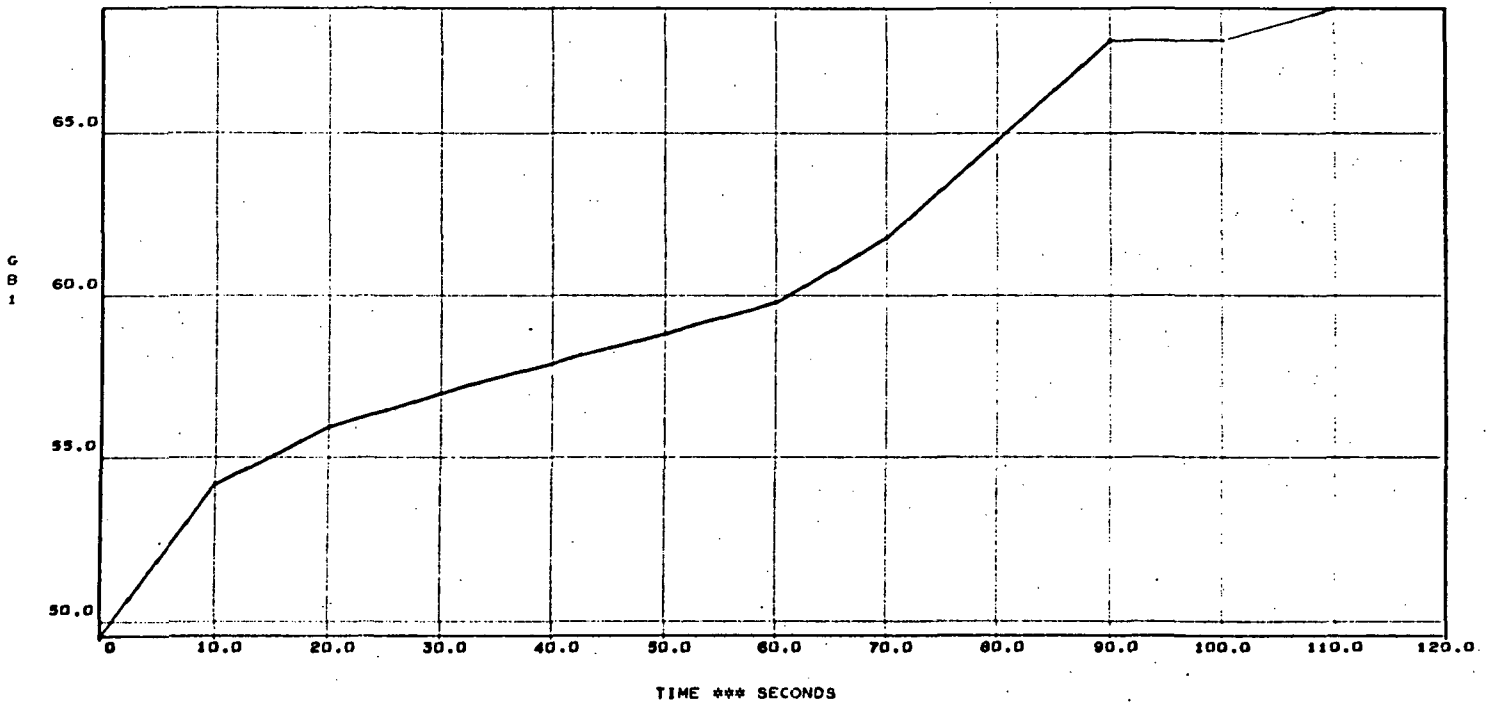
INT-21 ASCENT



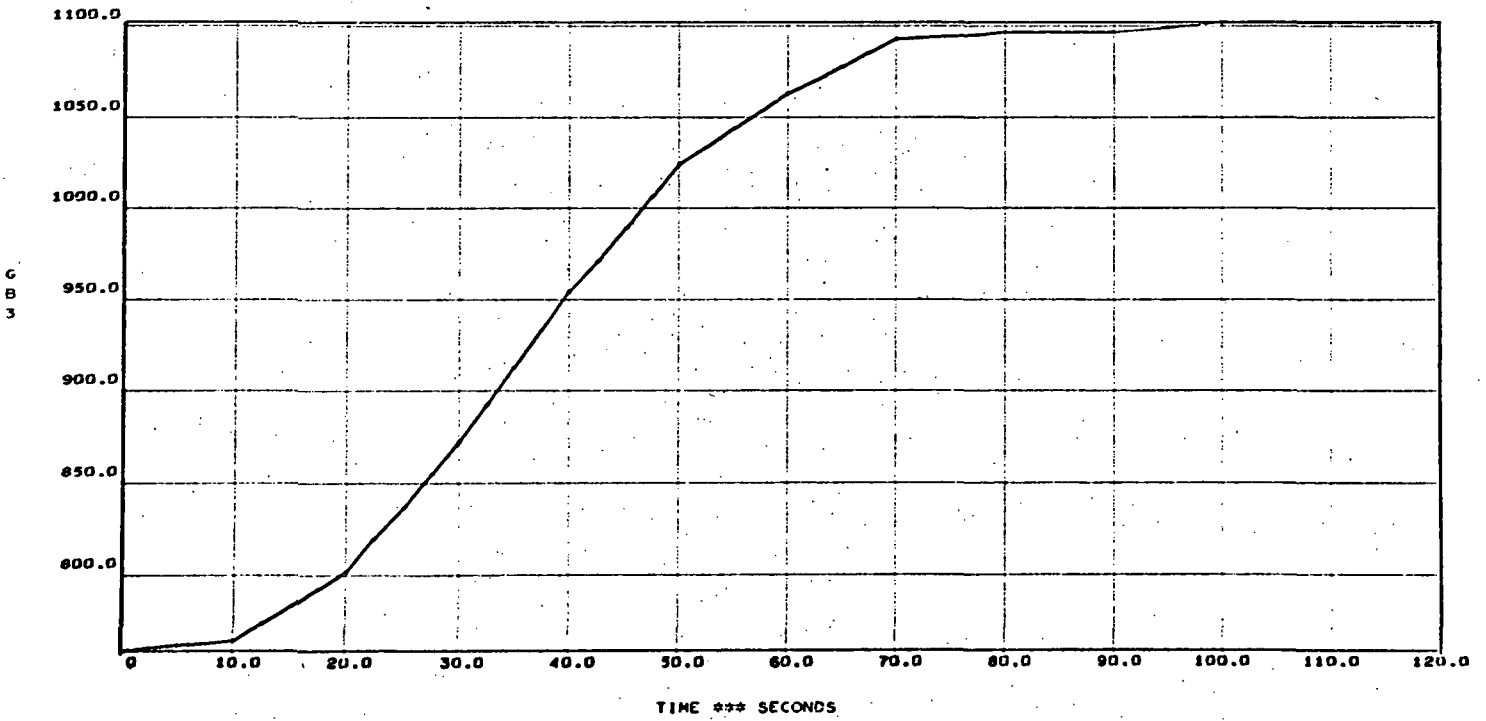
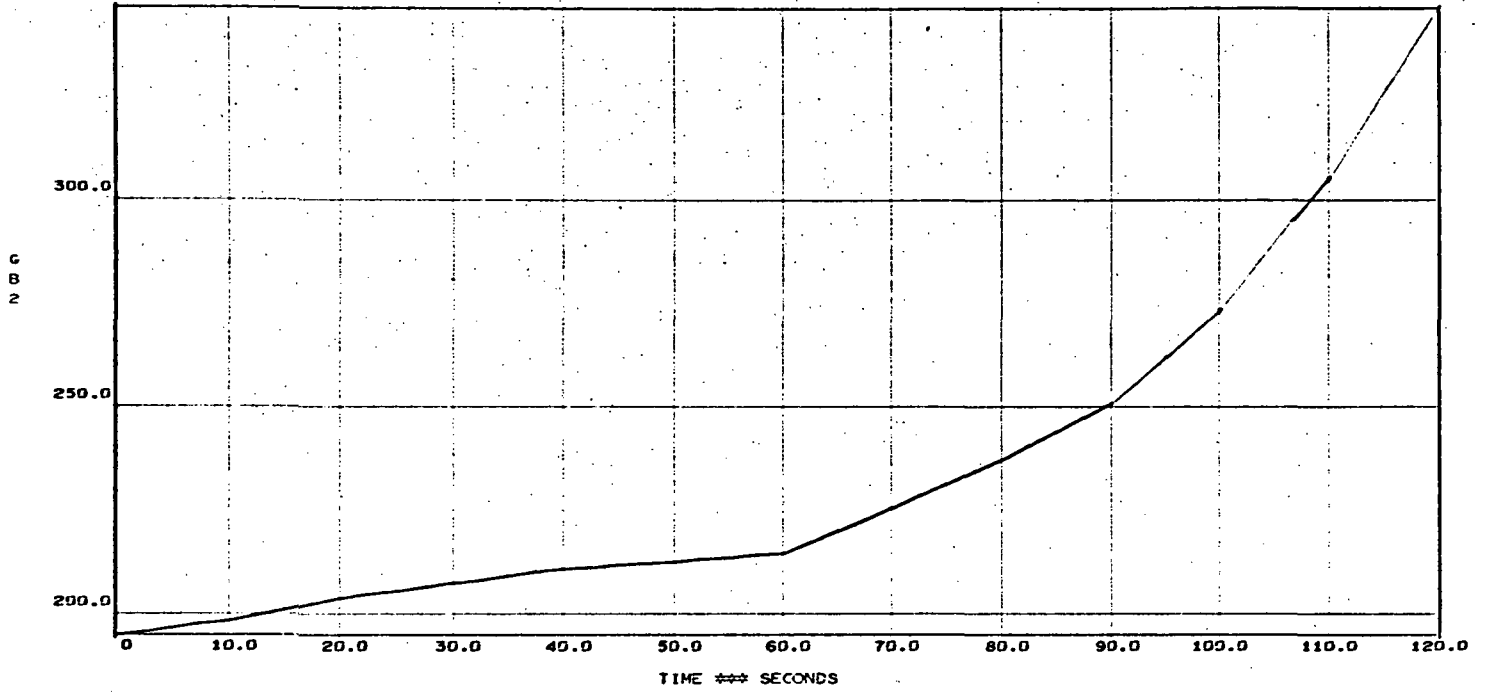


INT-21 ASCENT

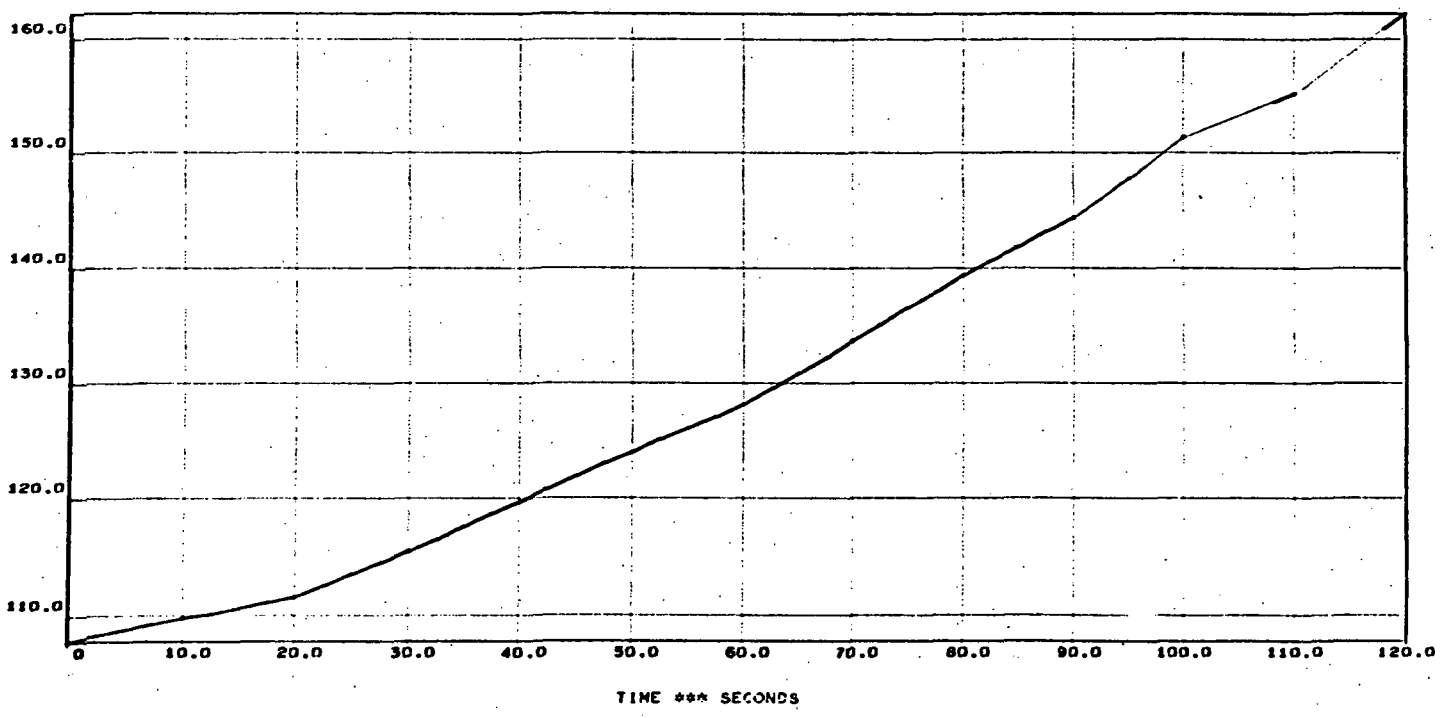




INT-21 ASCENT

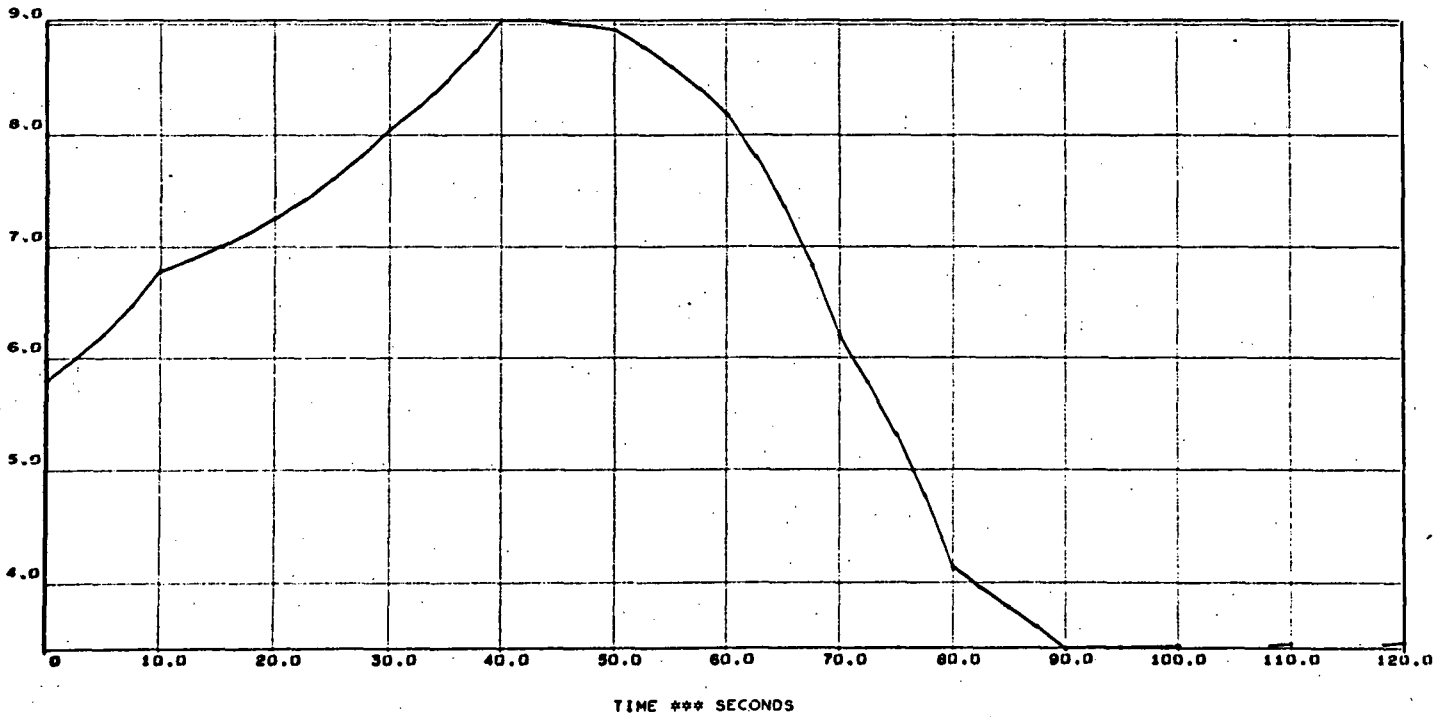
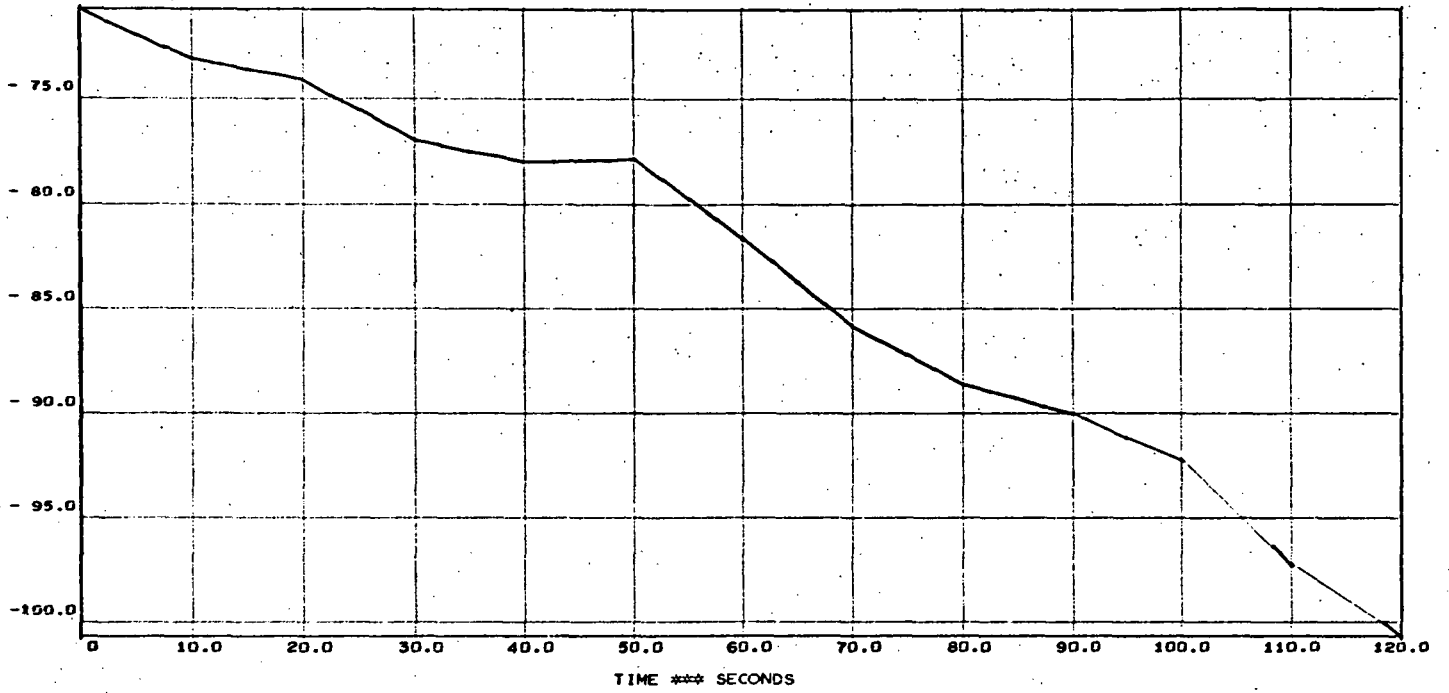


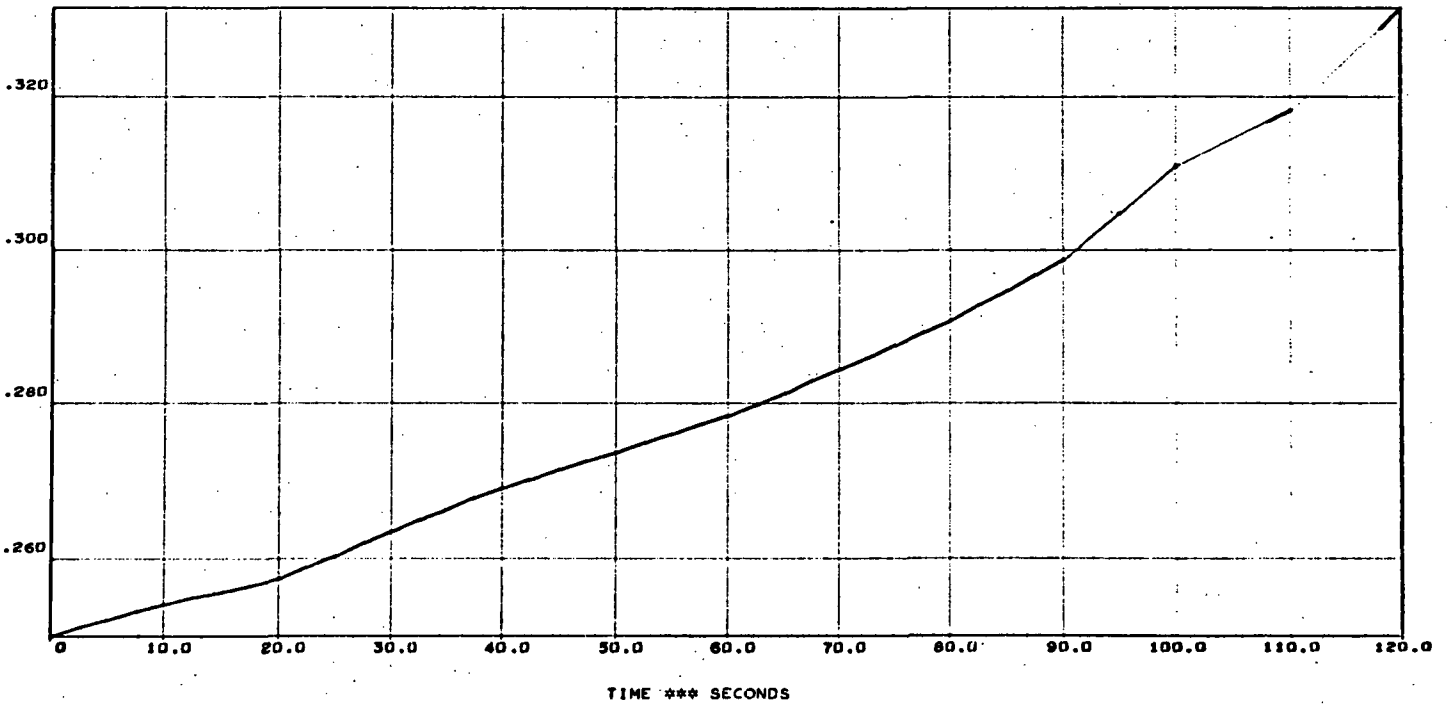
B  
B  
1



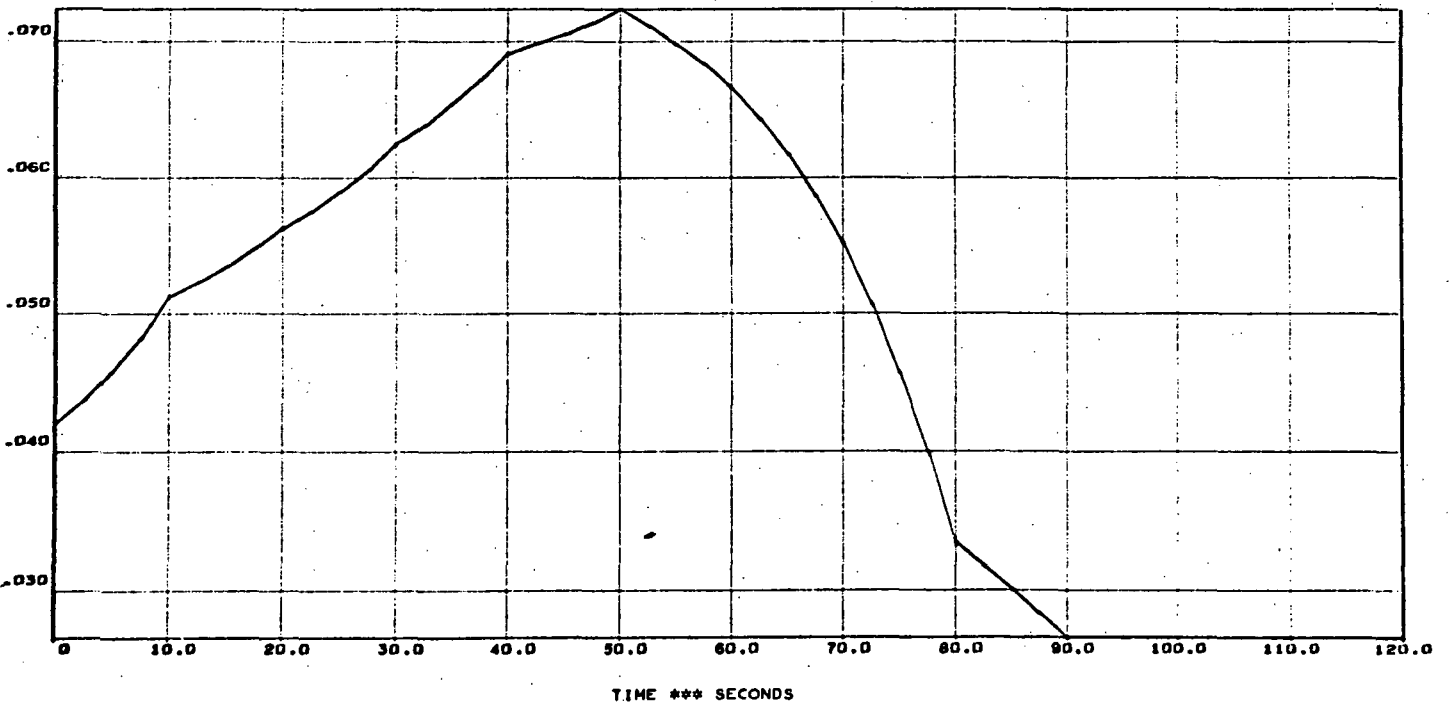
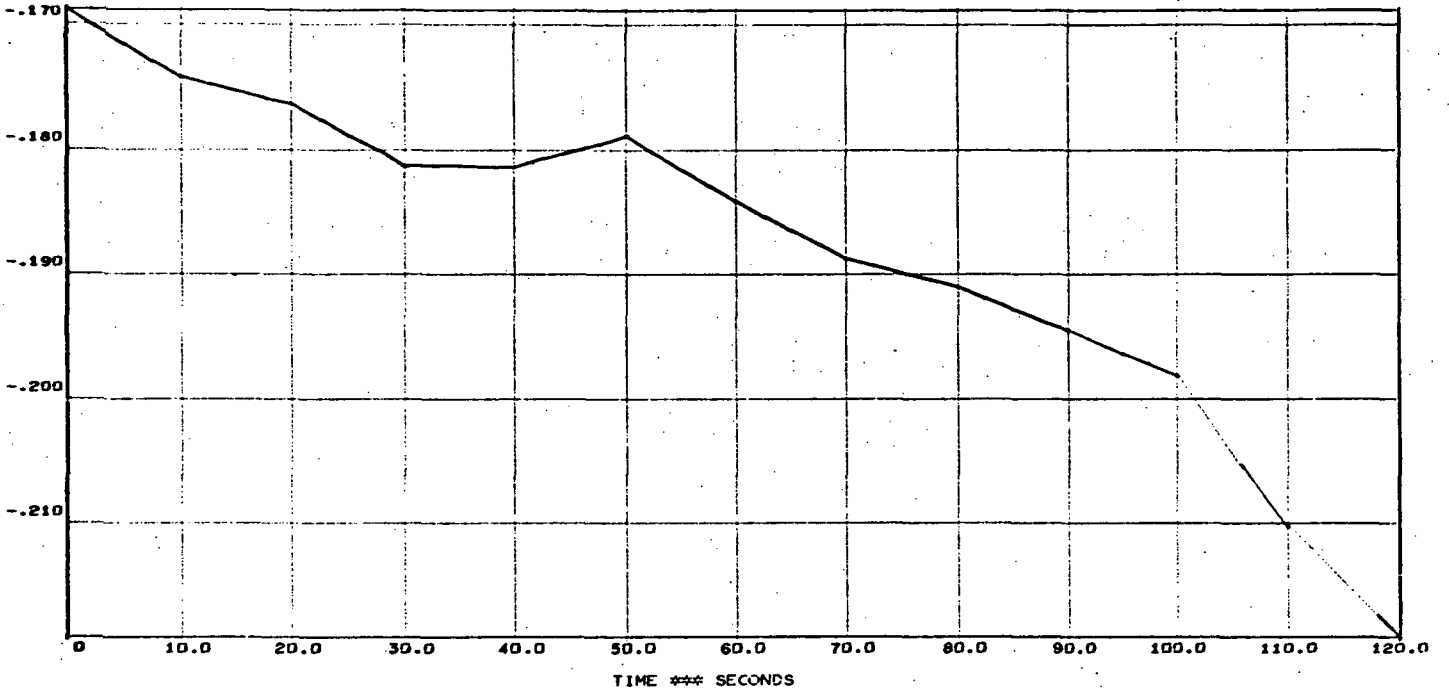
A-20

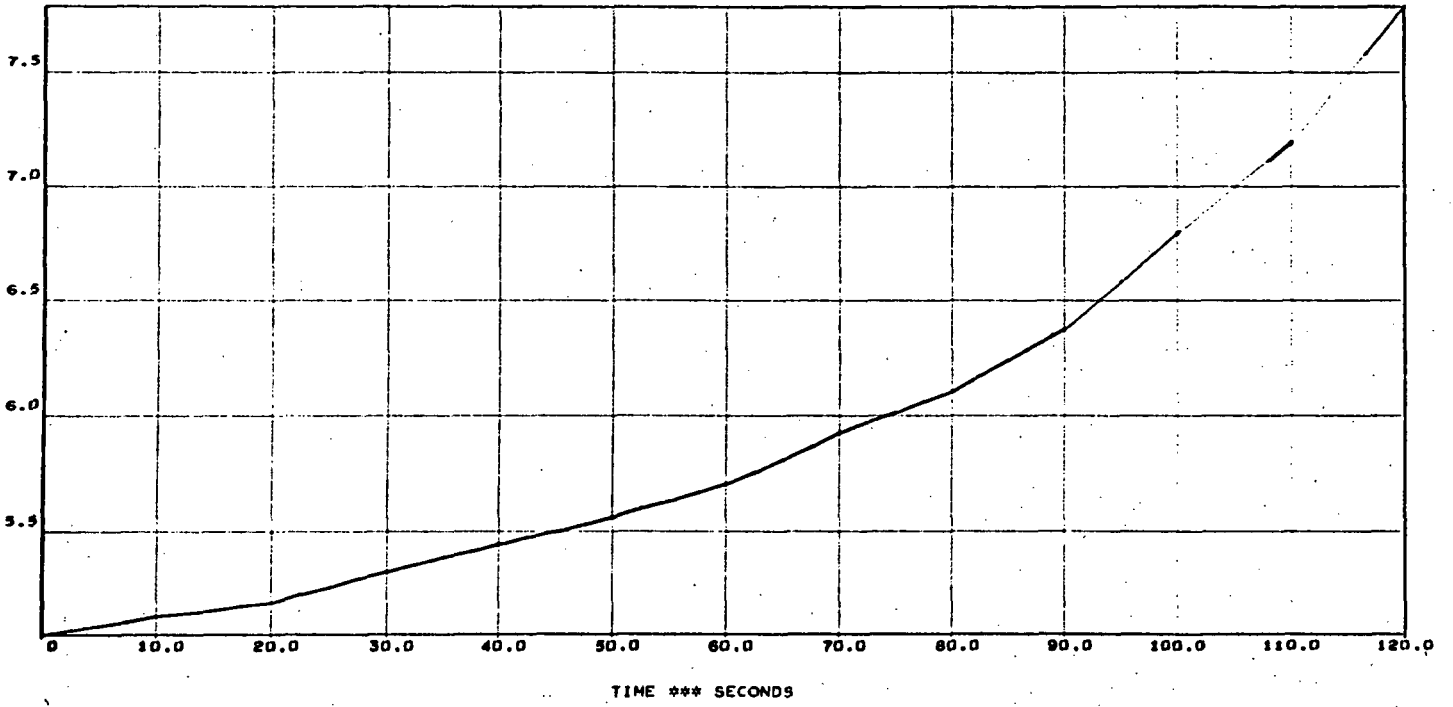
INT-21 ASCENT





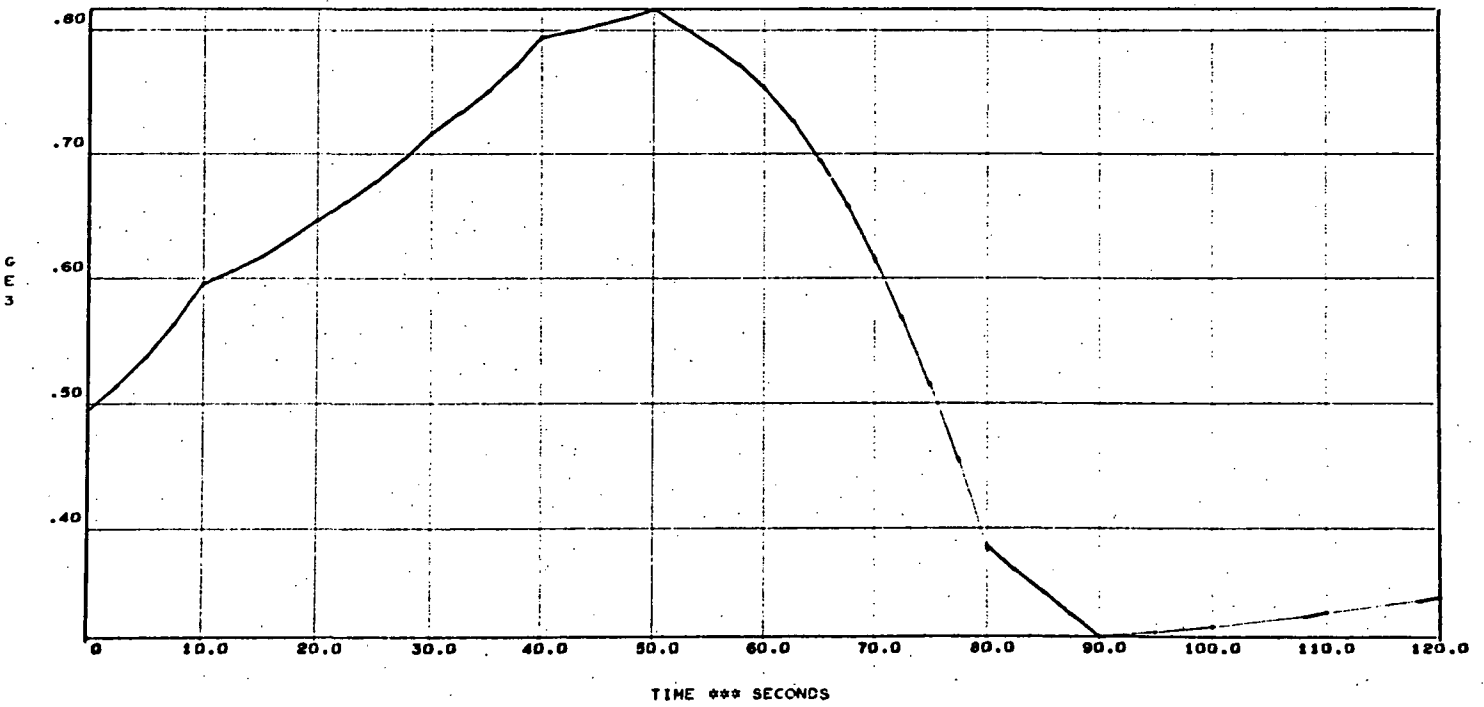
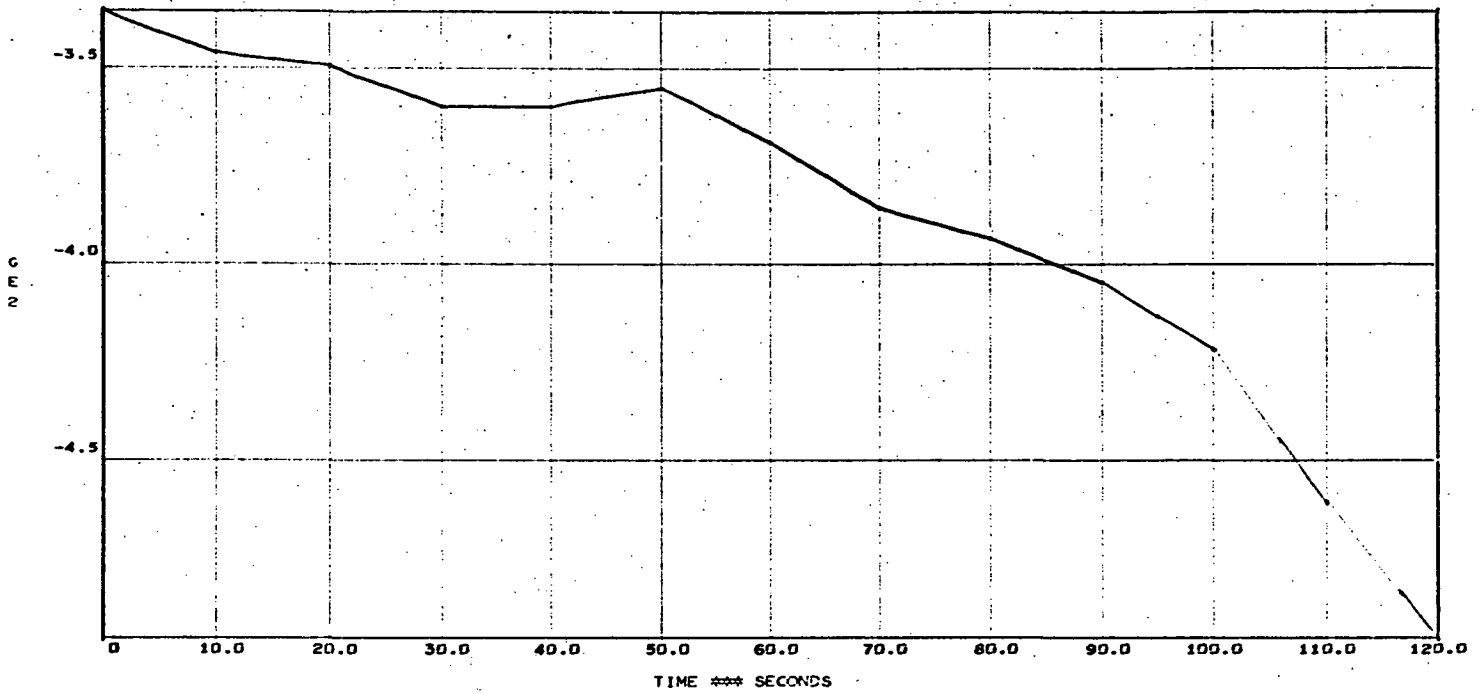
INT-21 ASCENT



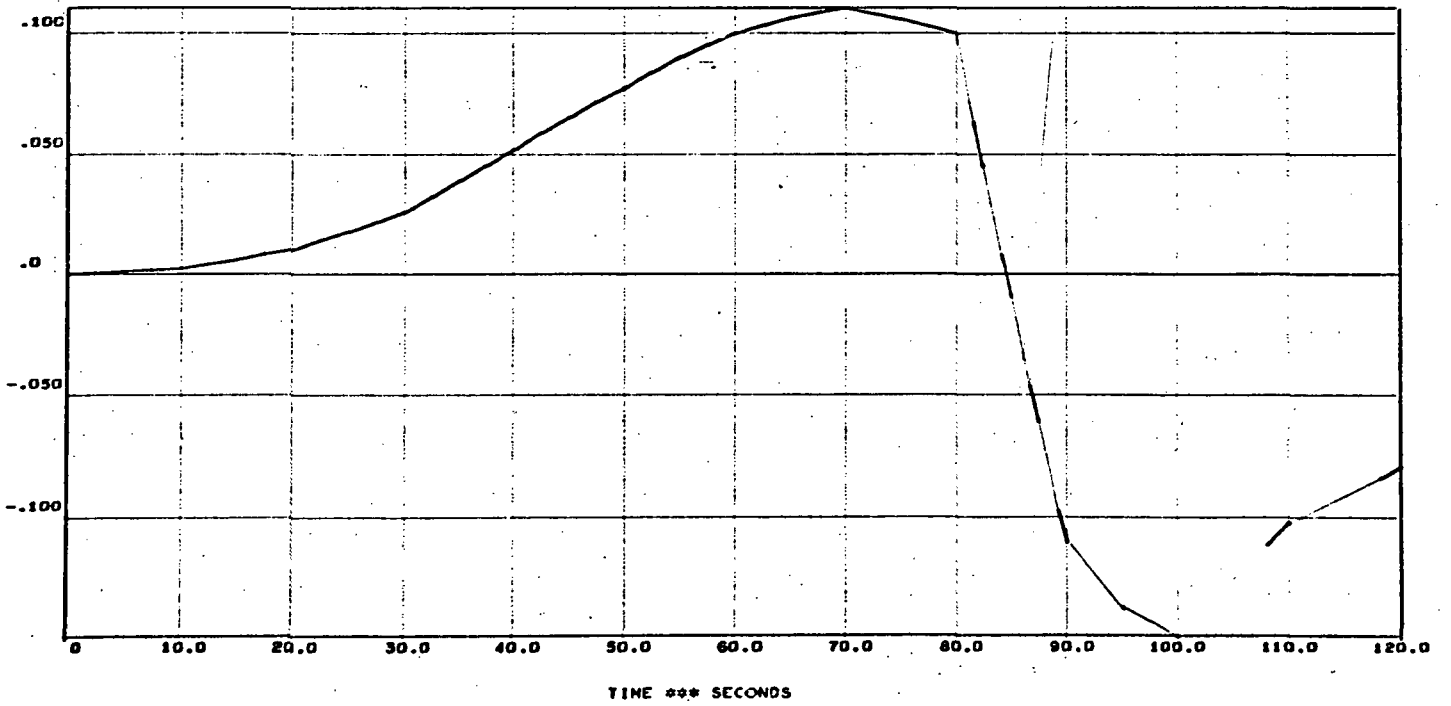
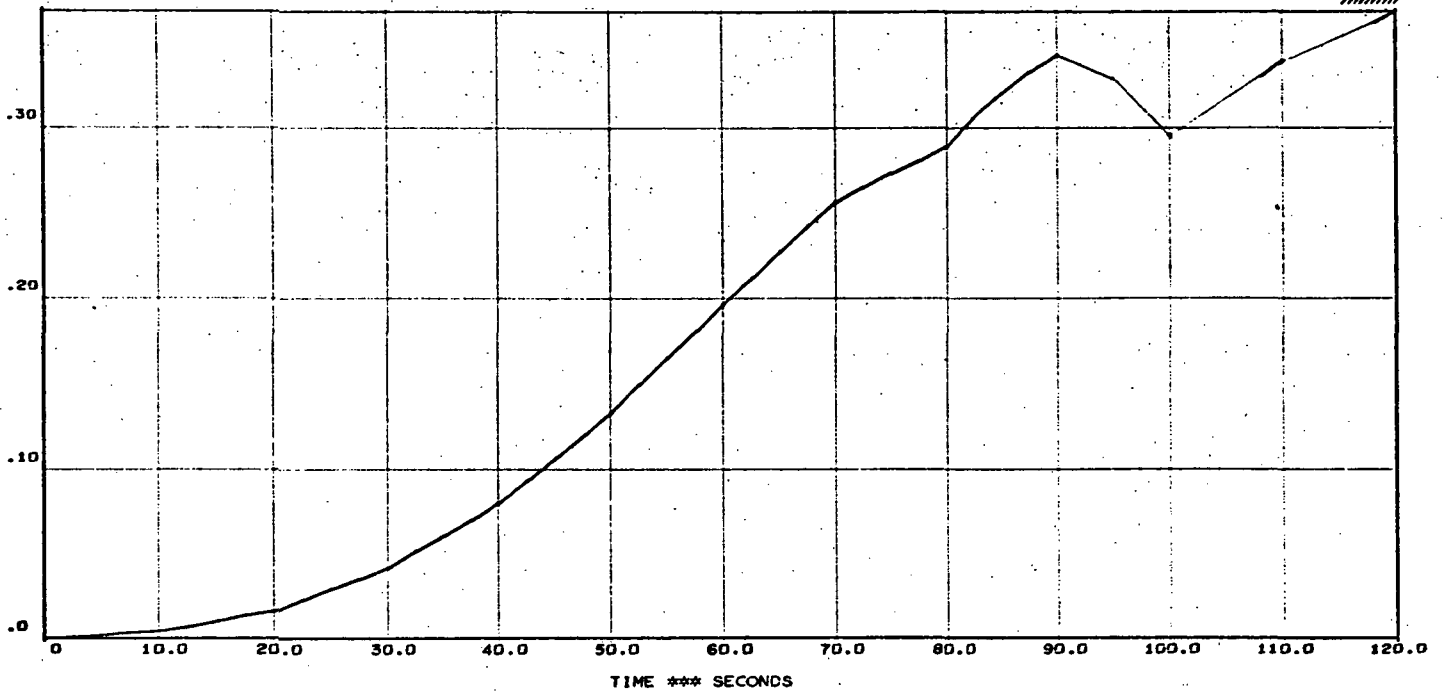


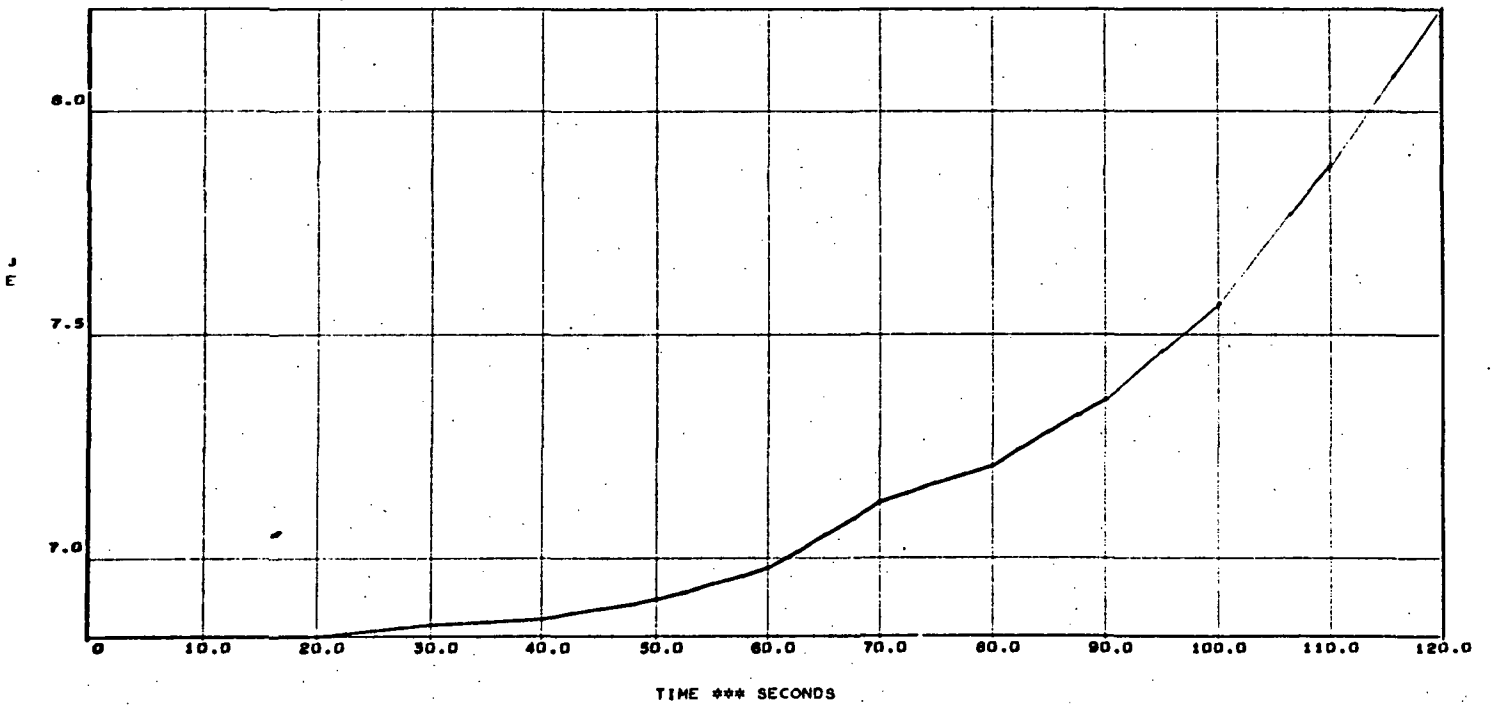


INT-21 ASCENT

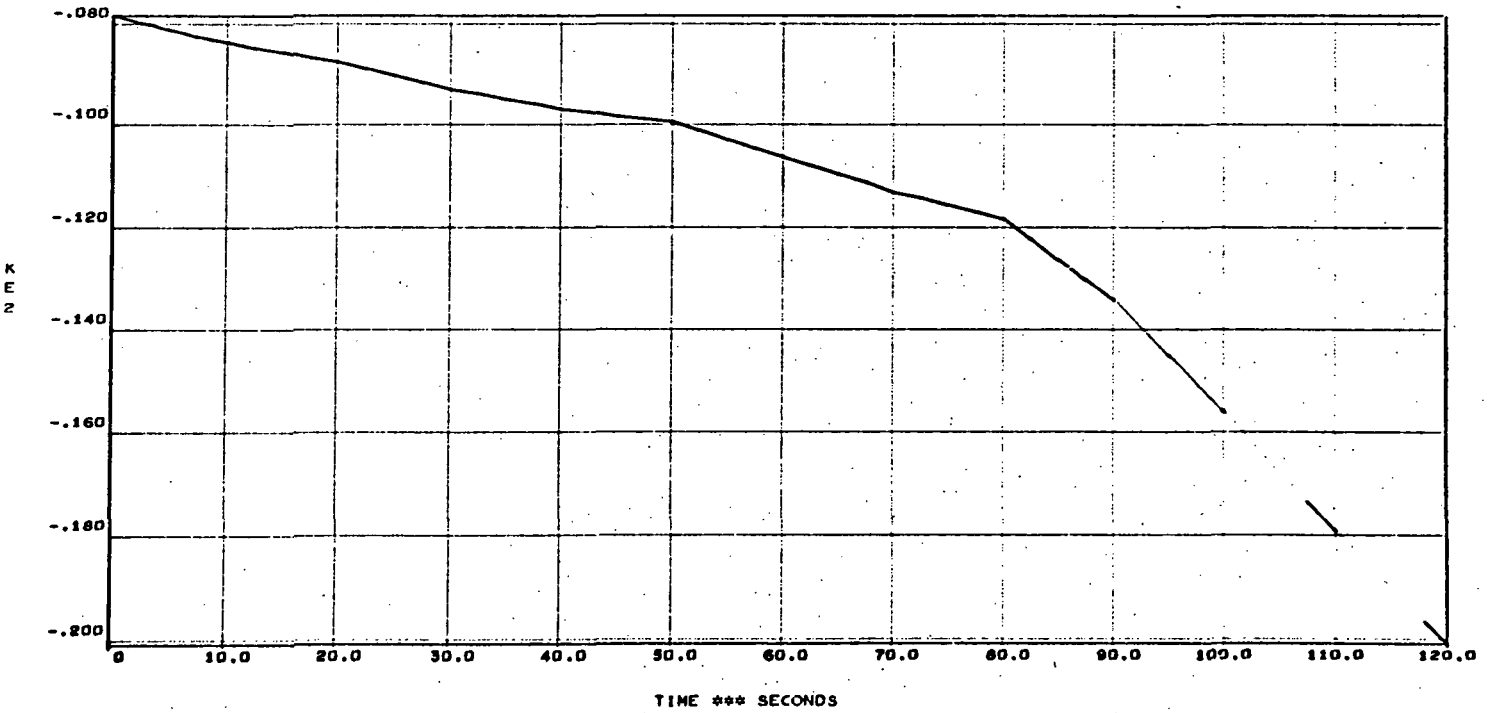
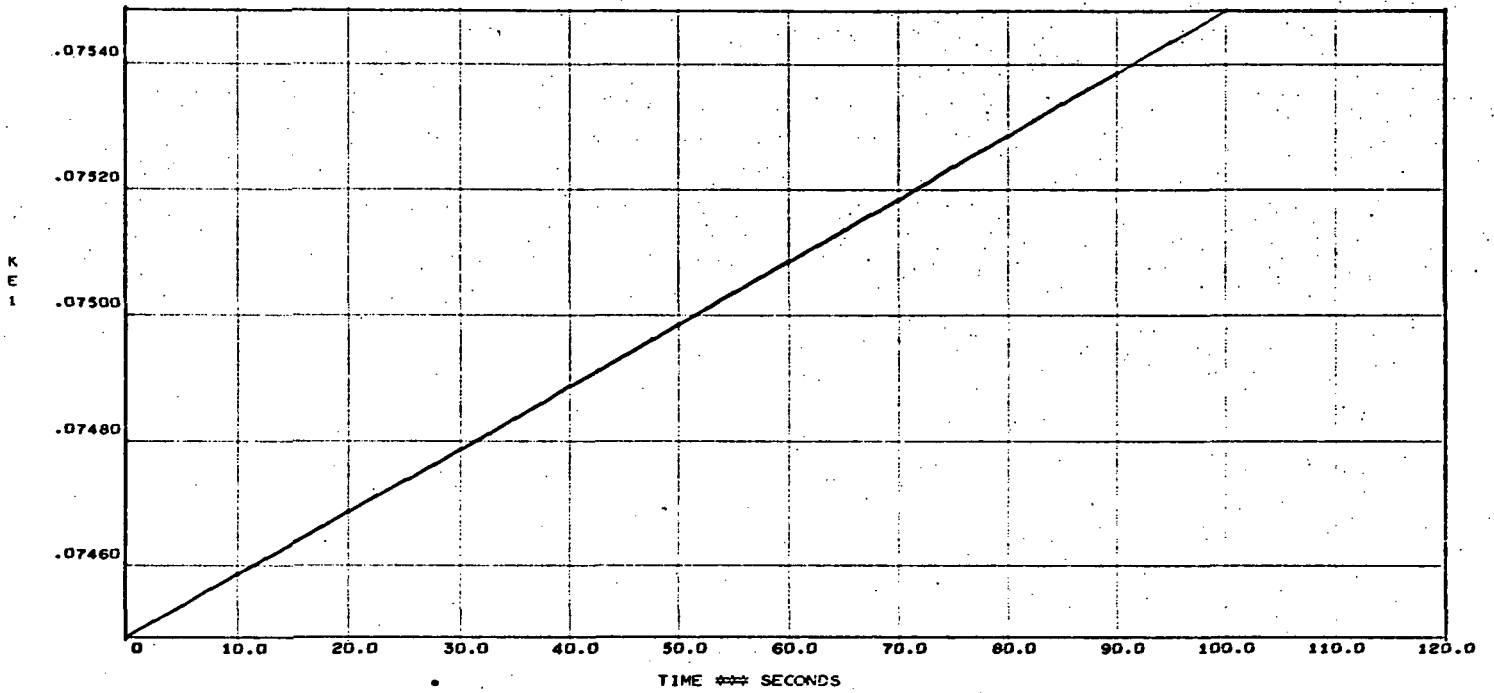


INT-21 ASCENT

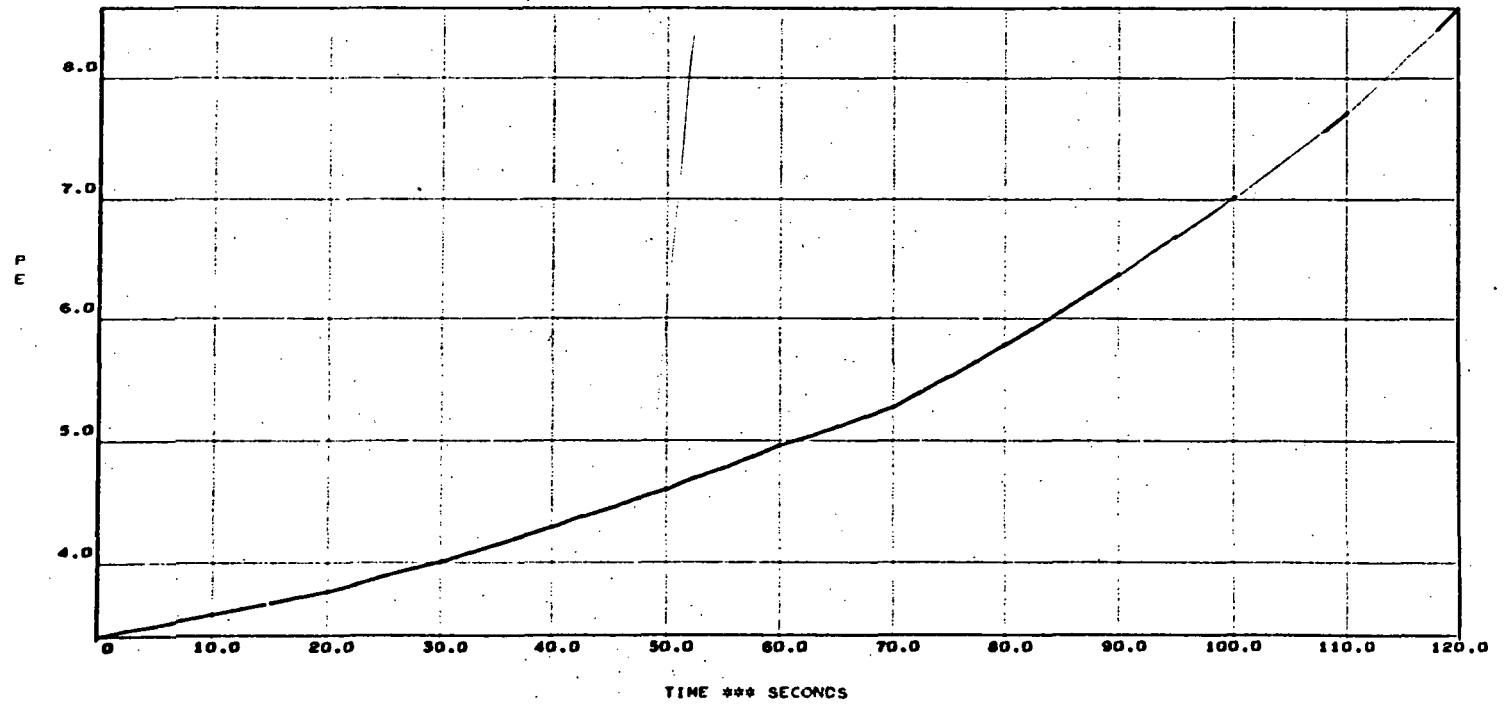
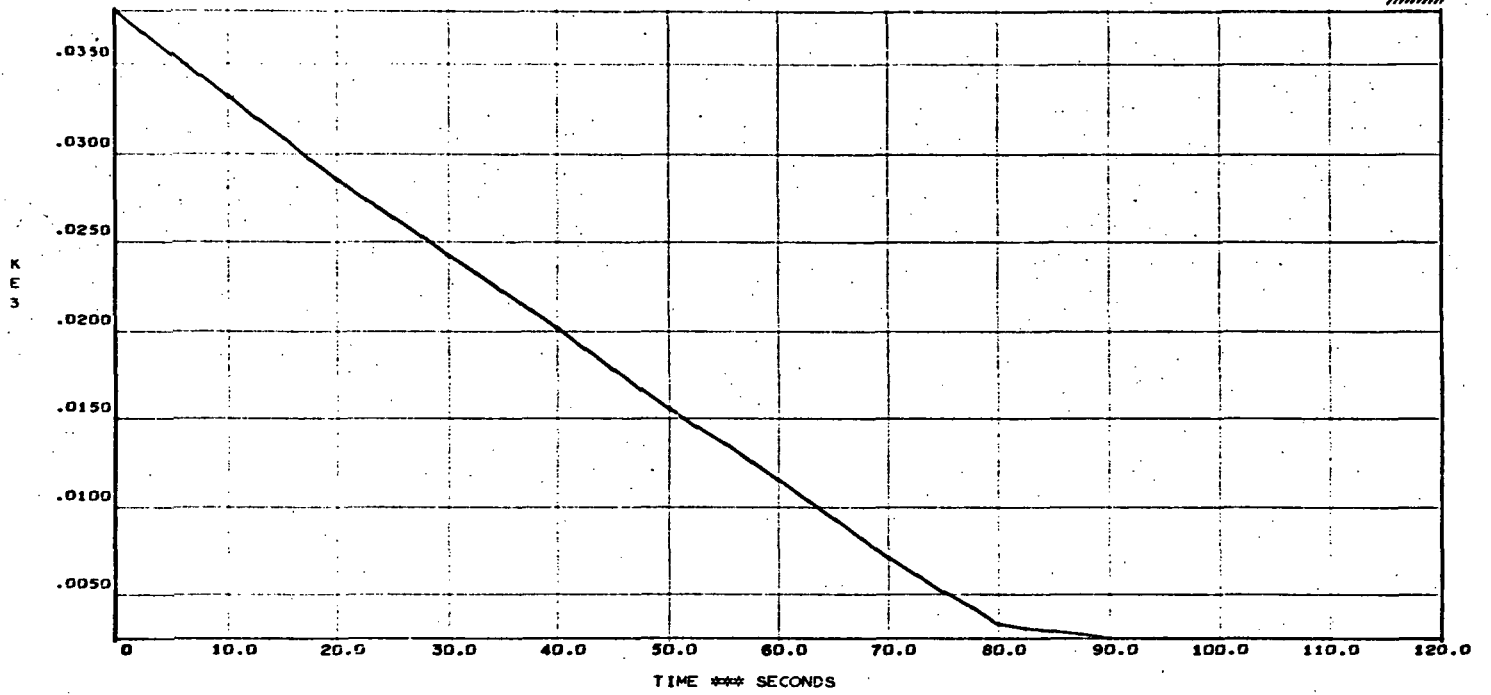


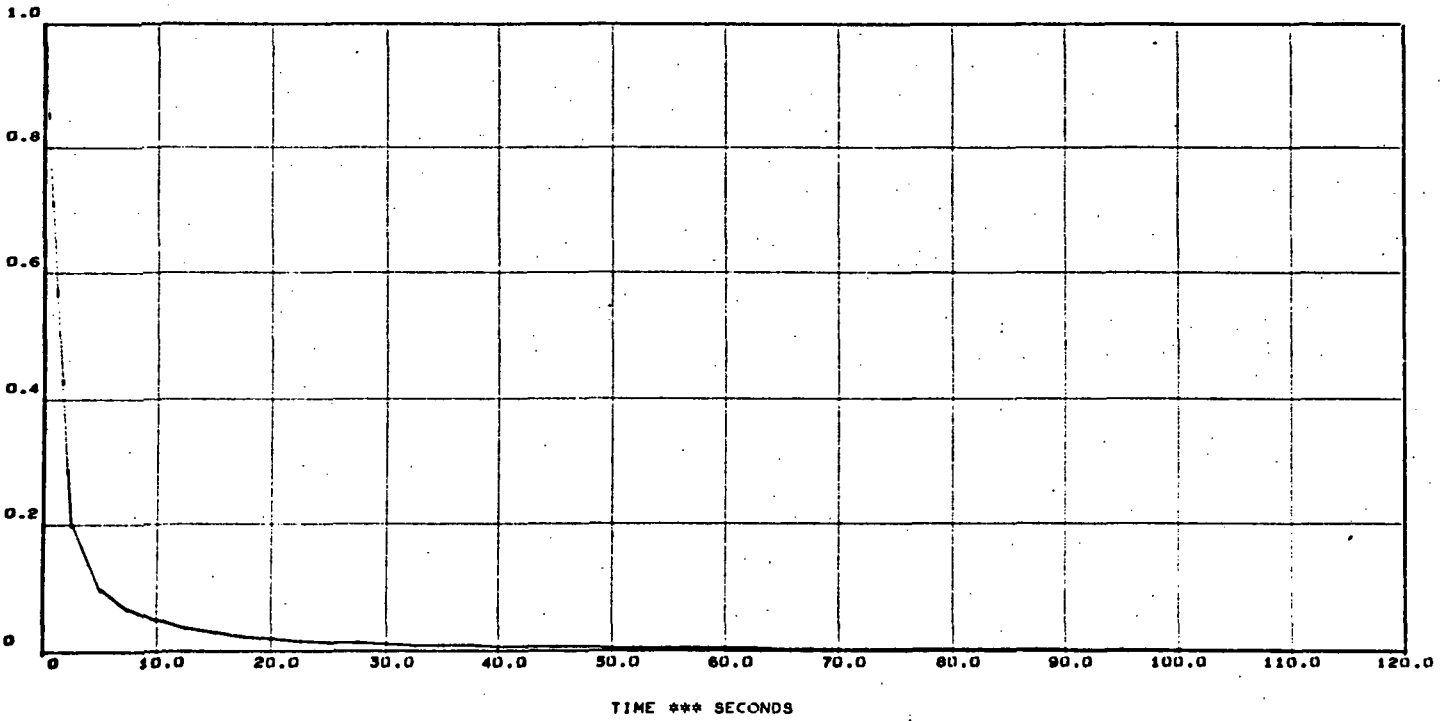


INT-21 ASCENT

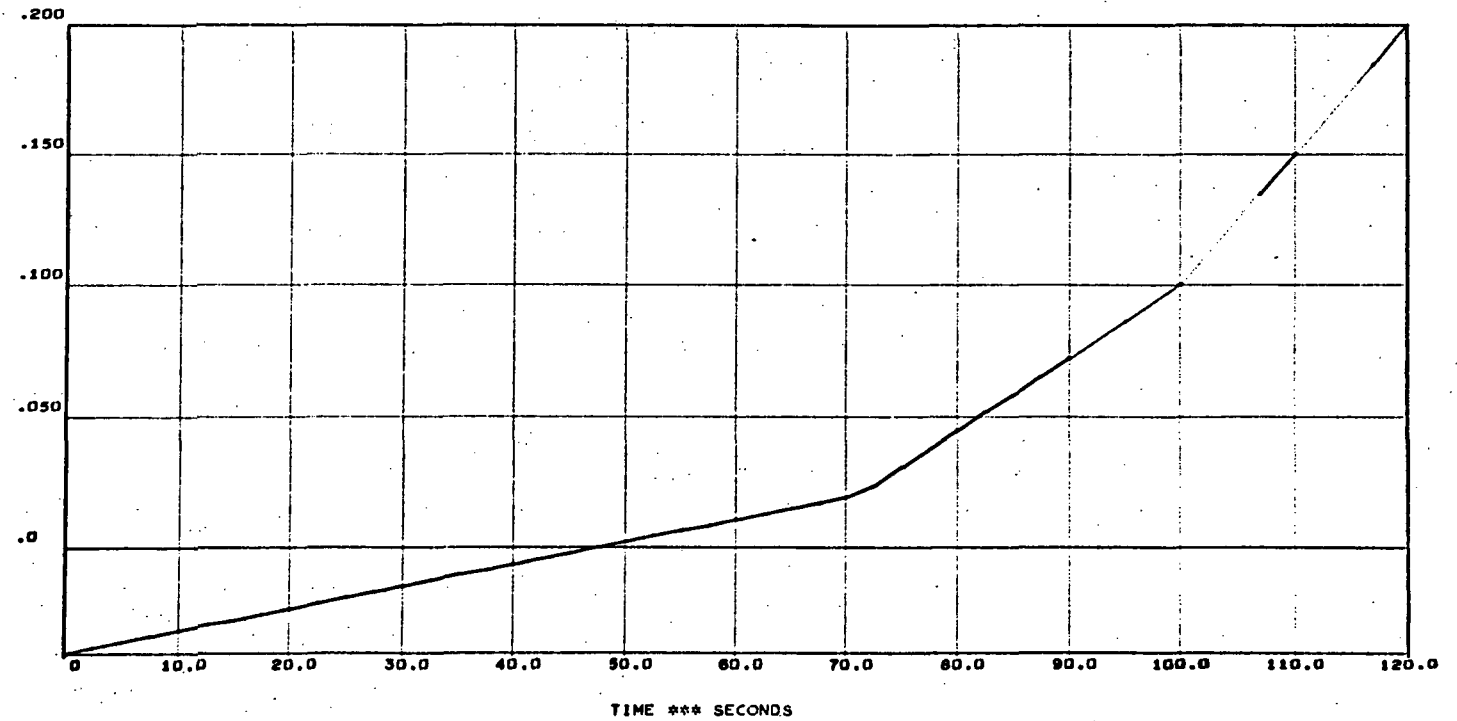
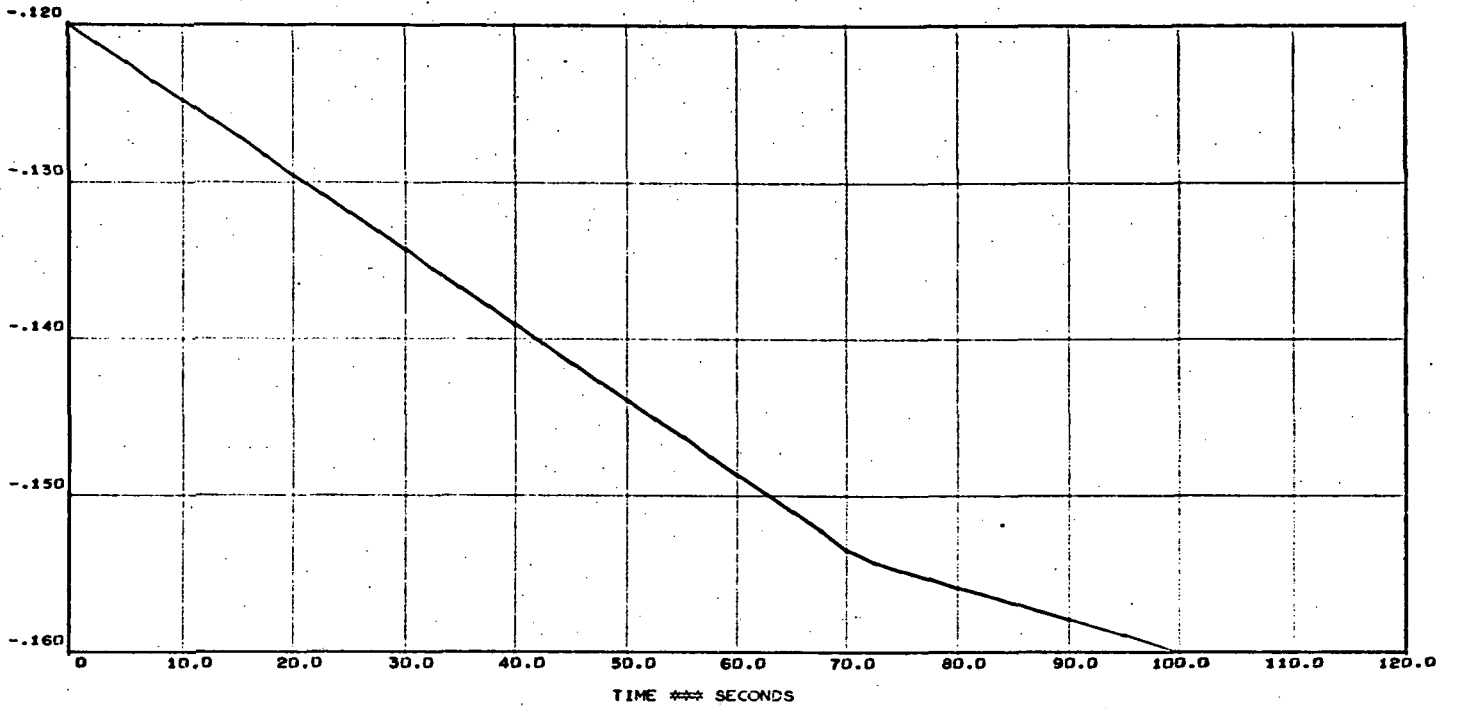


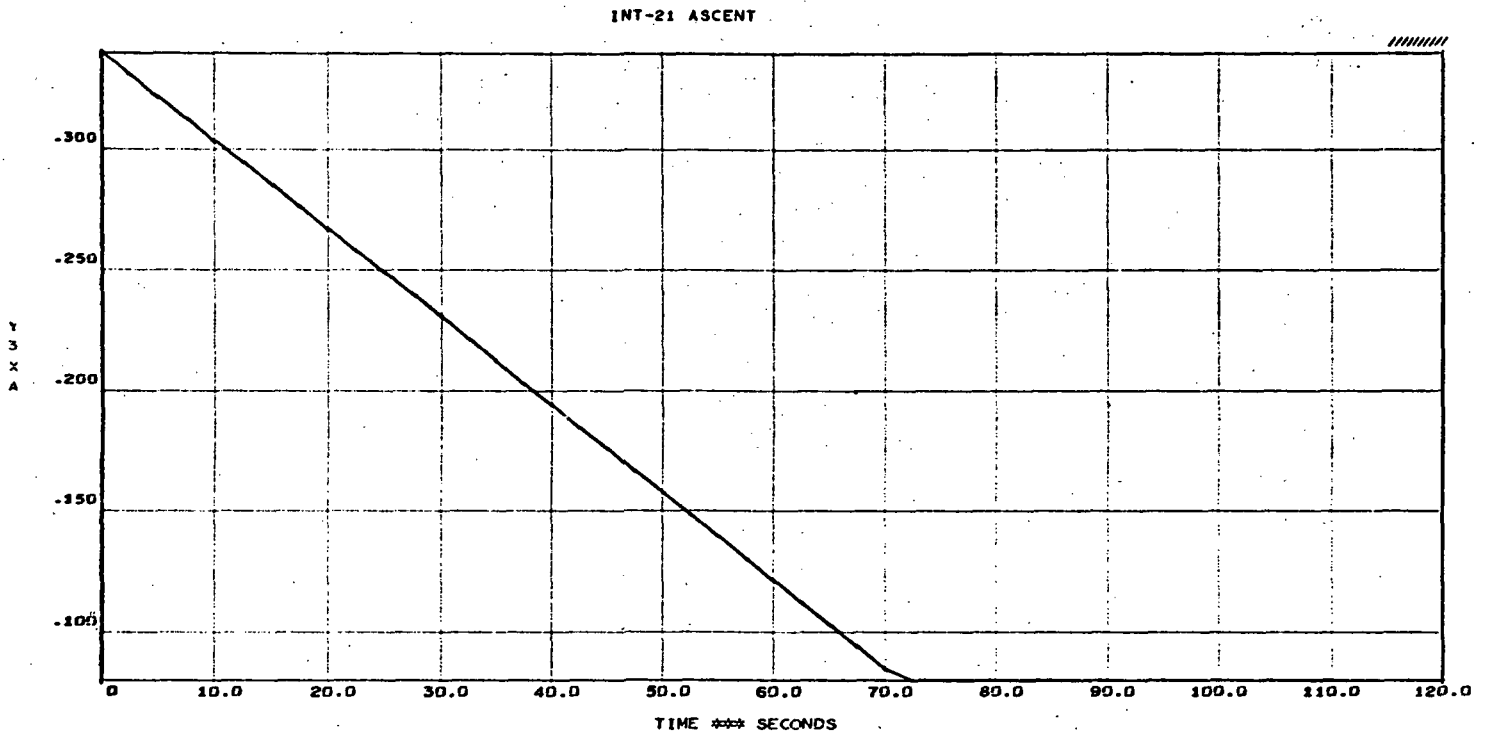
INT-21 ASCENT





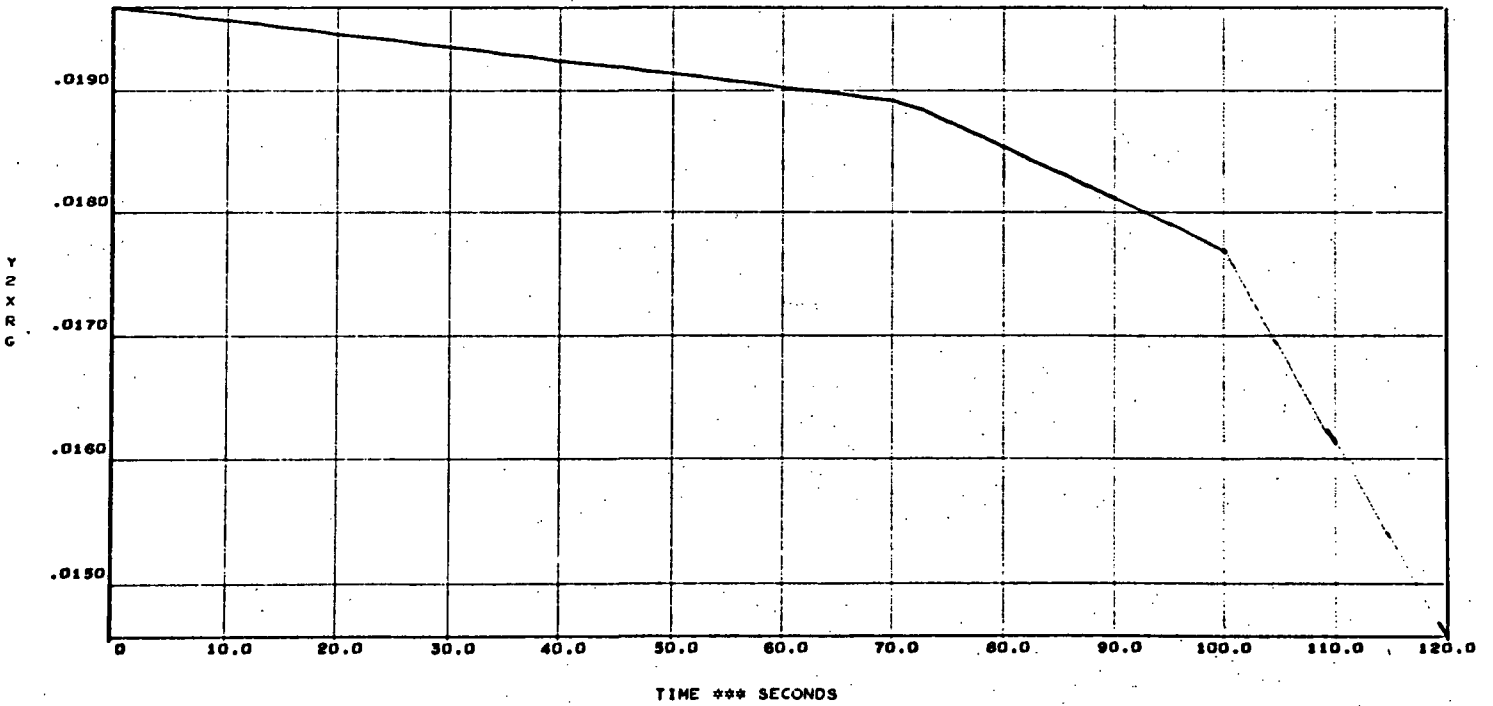
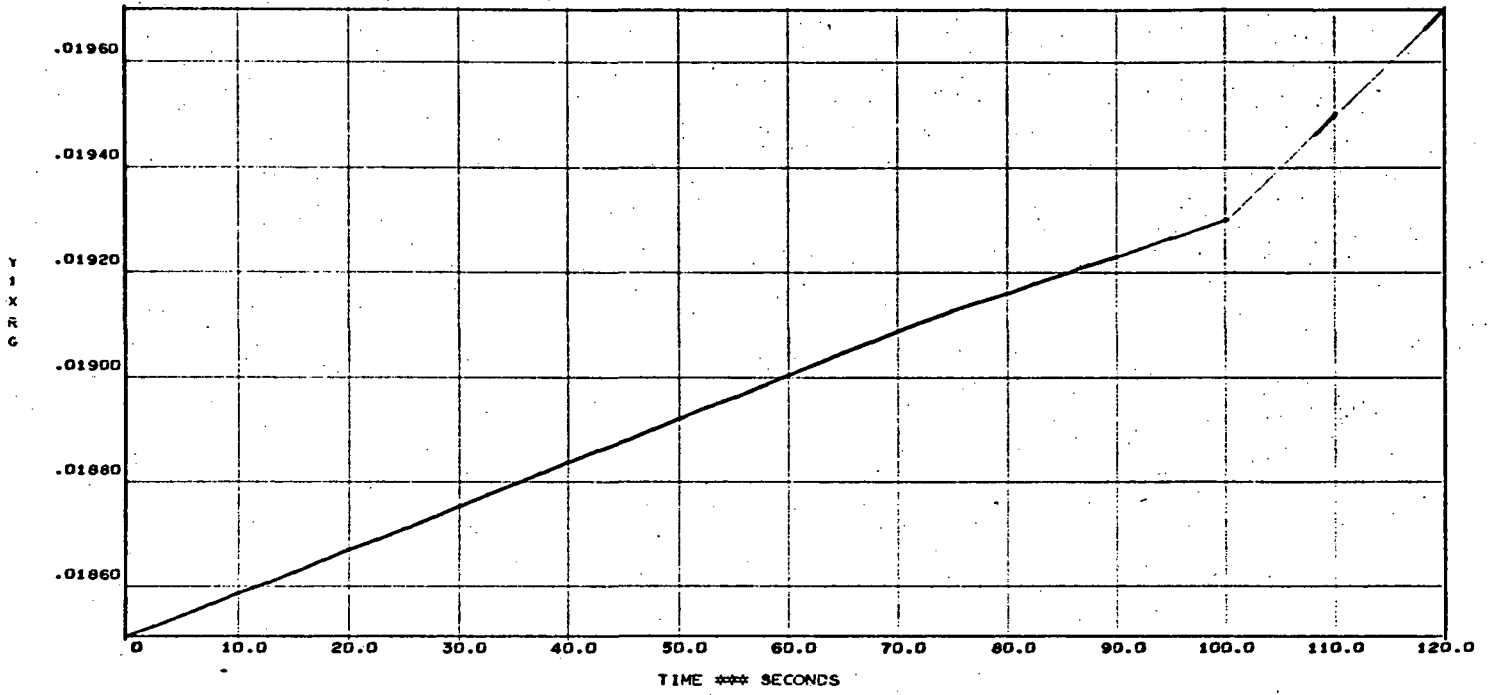
INT-21 ASCENT

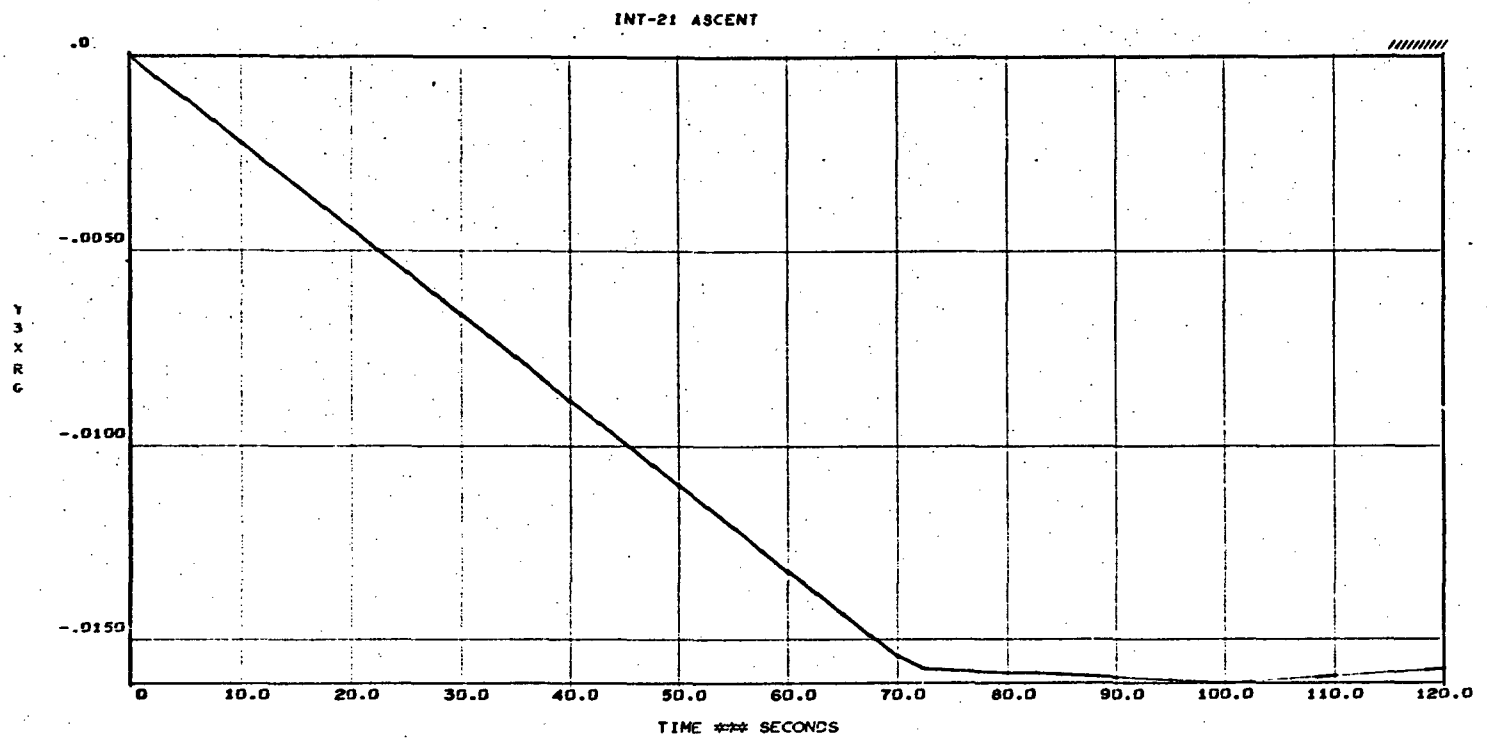




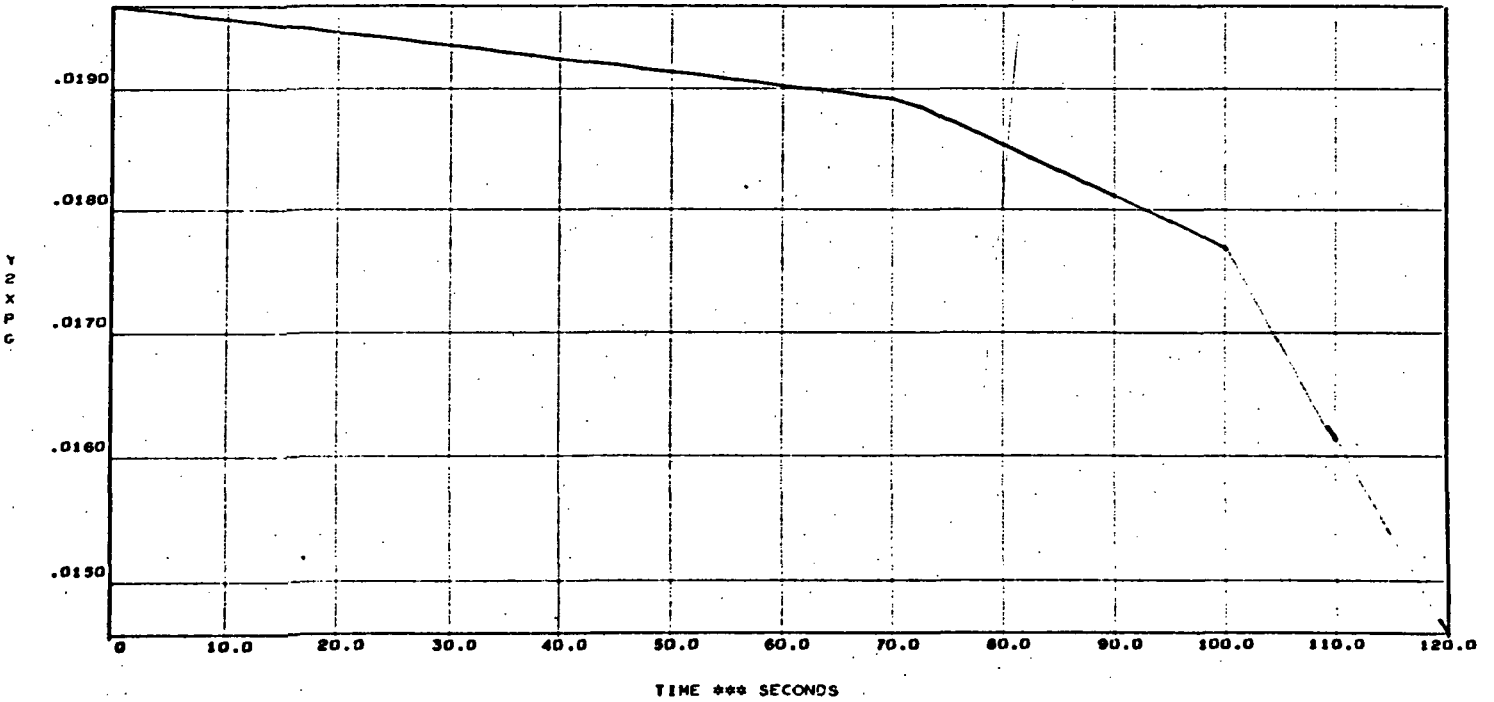
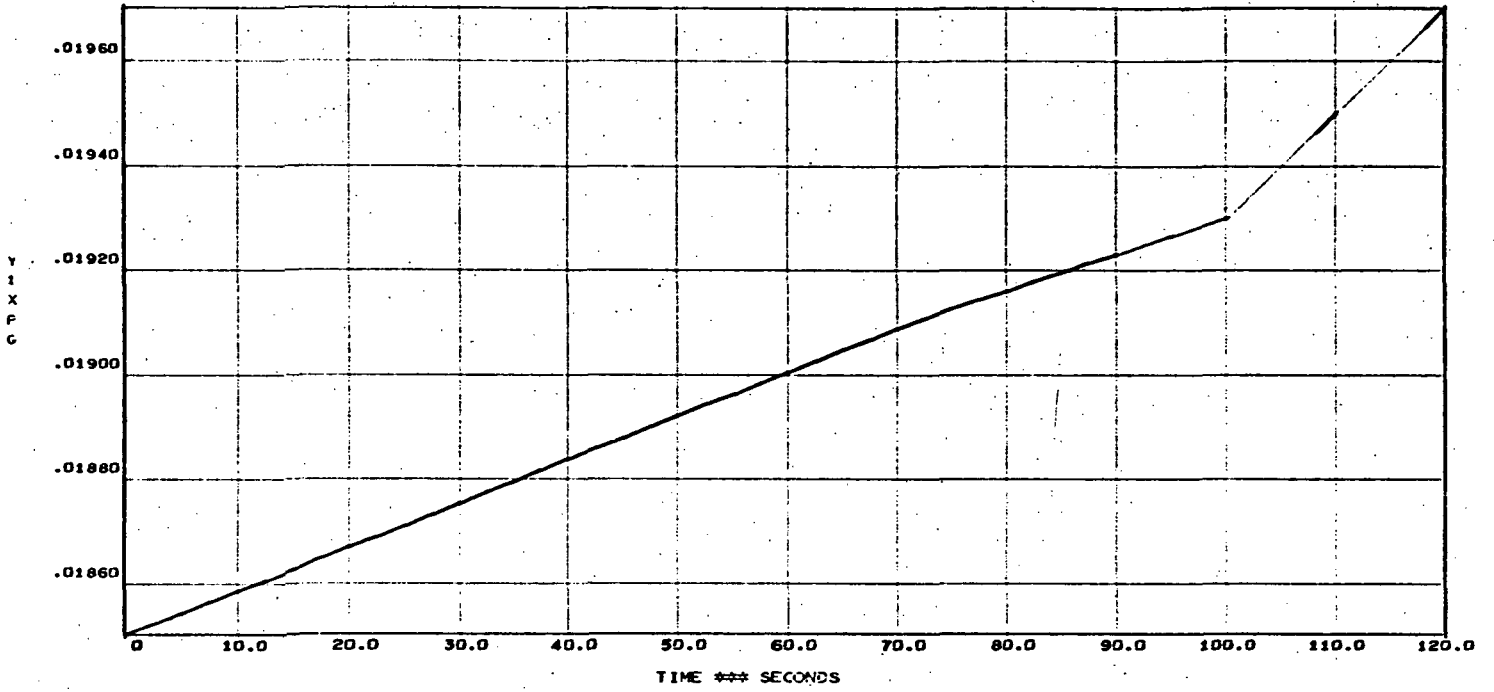


INT-21 ASCENT

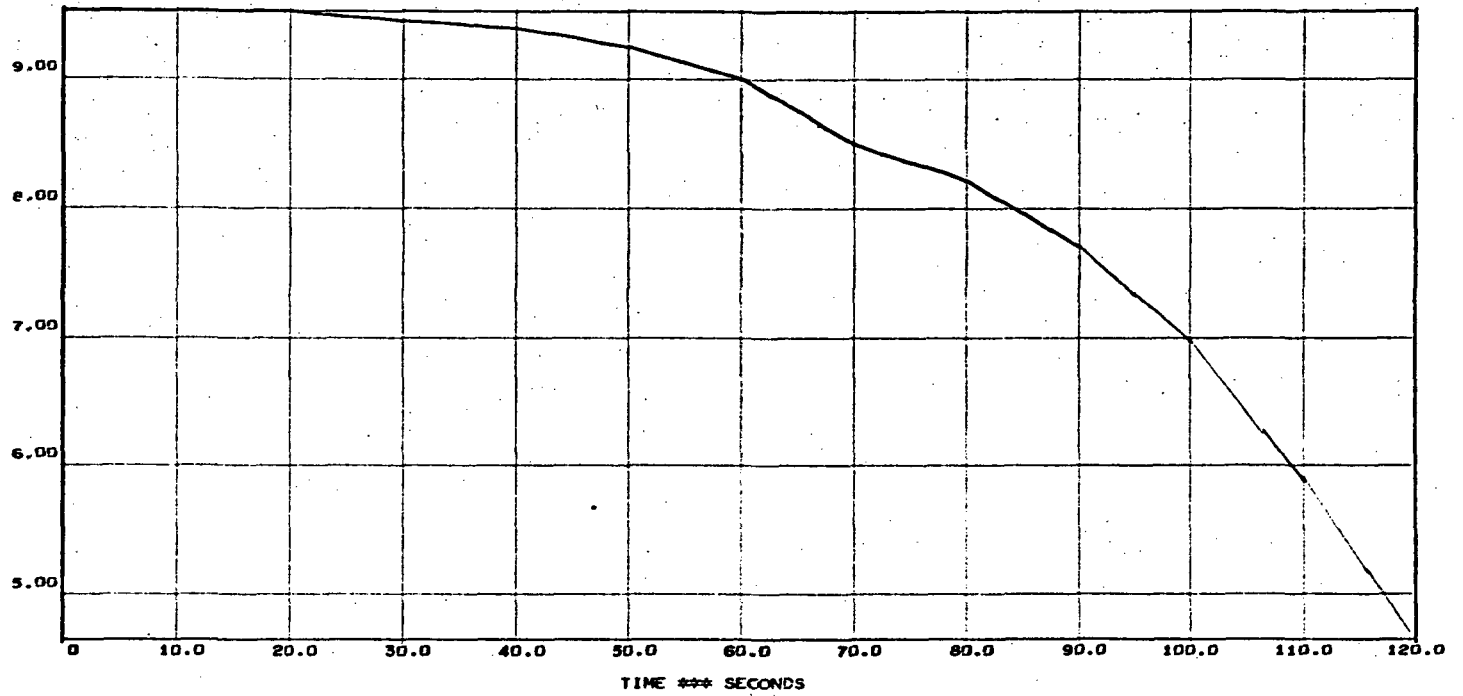
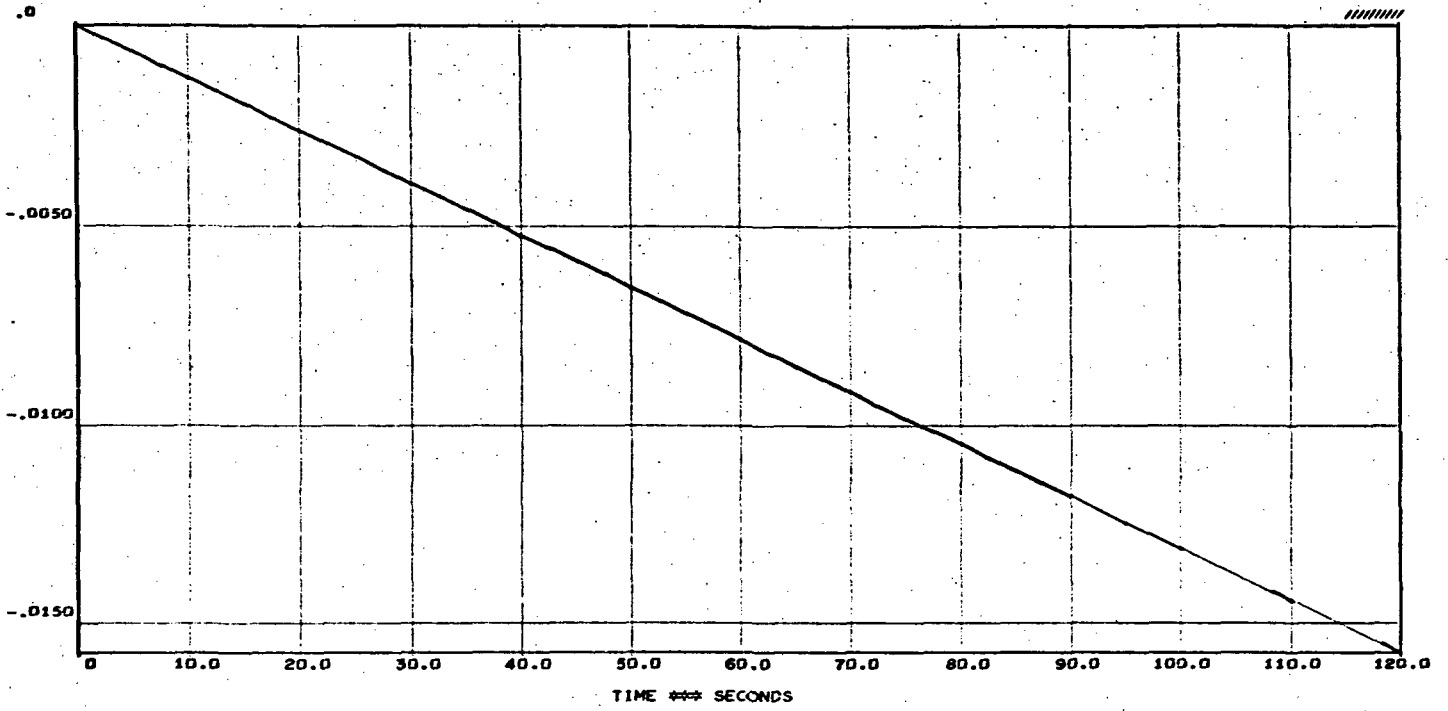




INT-21 ASCENT



INT-21 ASCENT



$$N_{\eta_3} = 0$$

$$\bar{N}_E = 29.92864 \text{ sec}^{-1}$$

$$N_E = 1,188.87 \text{ sec}^{-2}$$

$$L_E = 0.2885728 \text{ m}^{-1}$$

Appendix B  
SYNTHETIC WIND MODELS

Appendix B

This appendix contains plots of the six synthetic winds constructed as design disturbances for use in this study. Each of these winds is clearly identified.

These six winds were constructed using the synthetic wind synthesis procedure outlined in Ref. 4.

INT-21 ASCENT

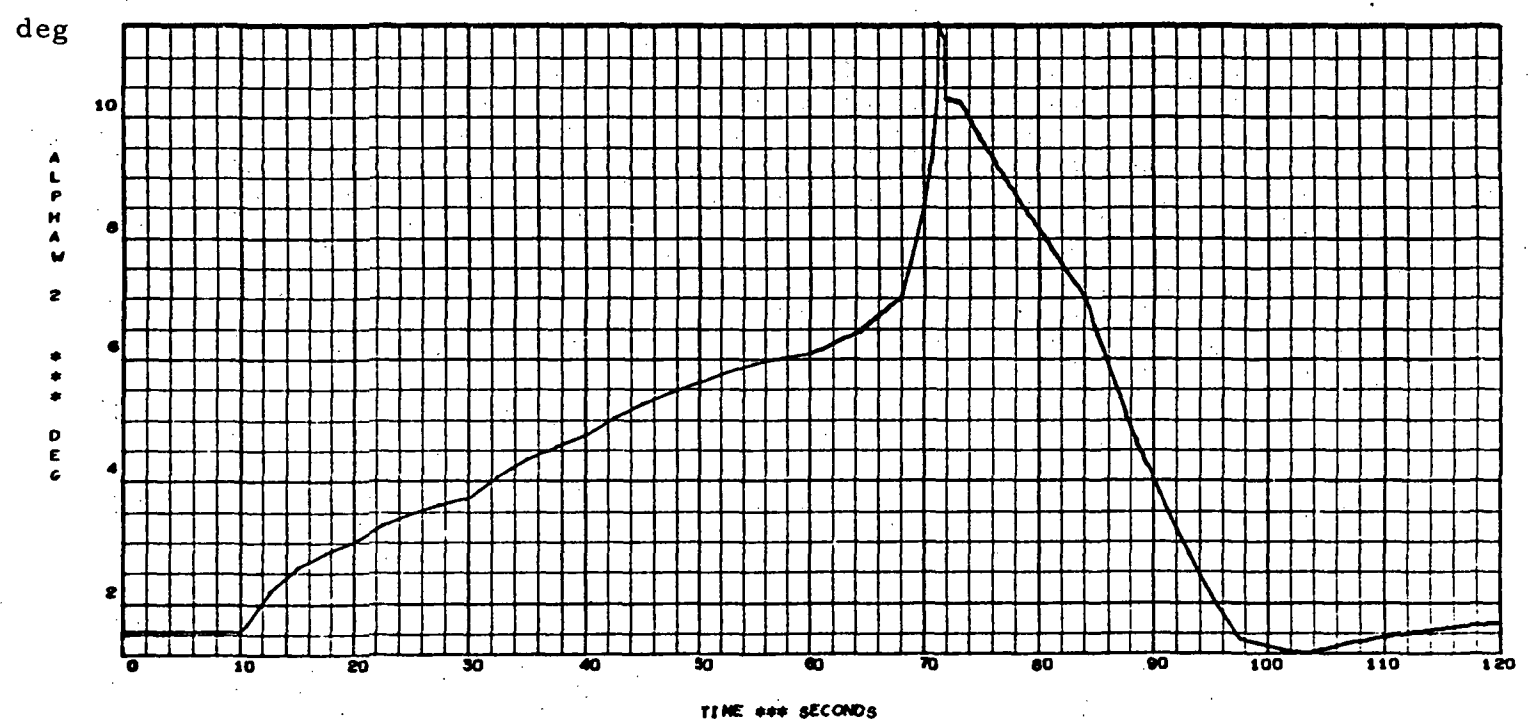
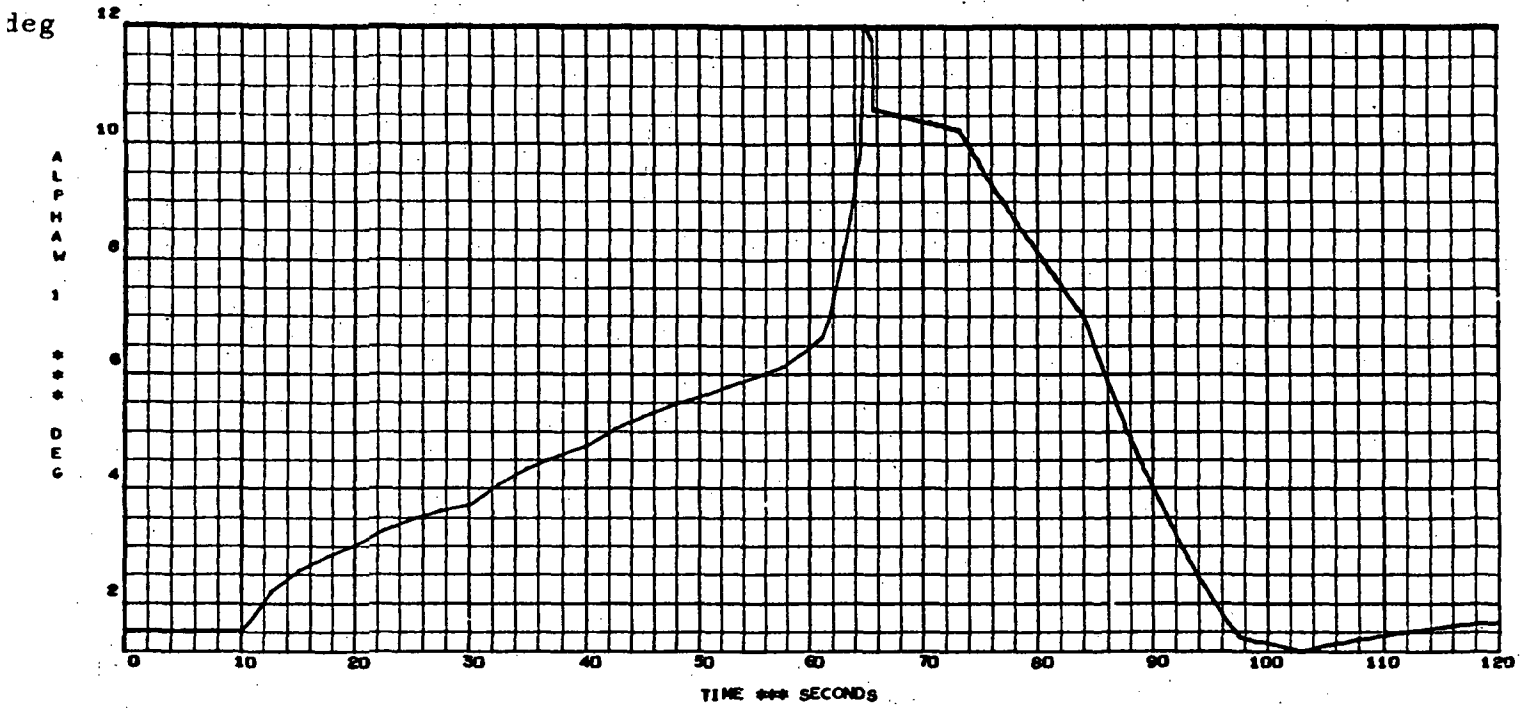


Fig. B-1 - SC 4020 Plots of  $\alpha_{w1}$  and  $\alpha_{w2}$  for INT-21 Ascent

$\alpha_{w1}$  = 95 Percentile Scalar Wind Speed Profile (steady-state) with 85%-Reduced 99 Percentile Shear Buildup and Superimposed 85%-Reduced 99 Percentile Gust at Mach 1.0

$\alpha_{w2}$  = 95 Percentile Scalar Wind Speed Profile (steady-state) with 85%-Reduced 99 Percentile Shear Buildup and Superimposed 85%-Reduced 99 Percentile Gust at Maximum  $q\alpha$



INT-21 ASCENT

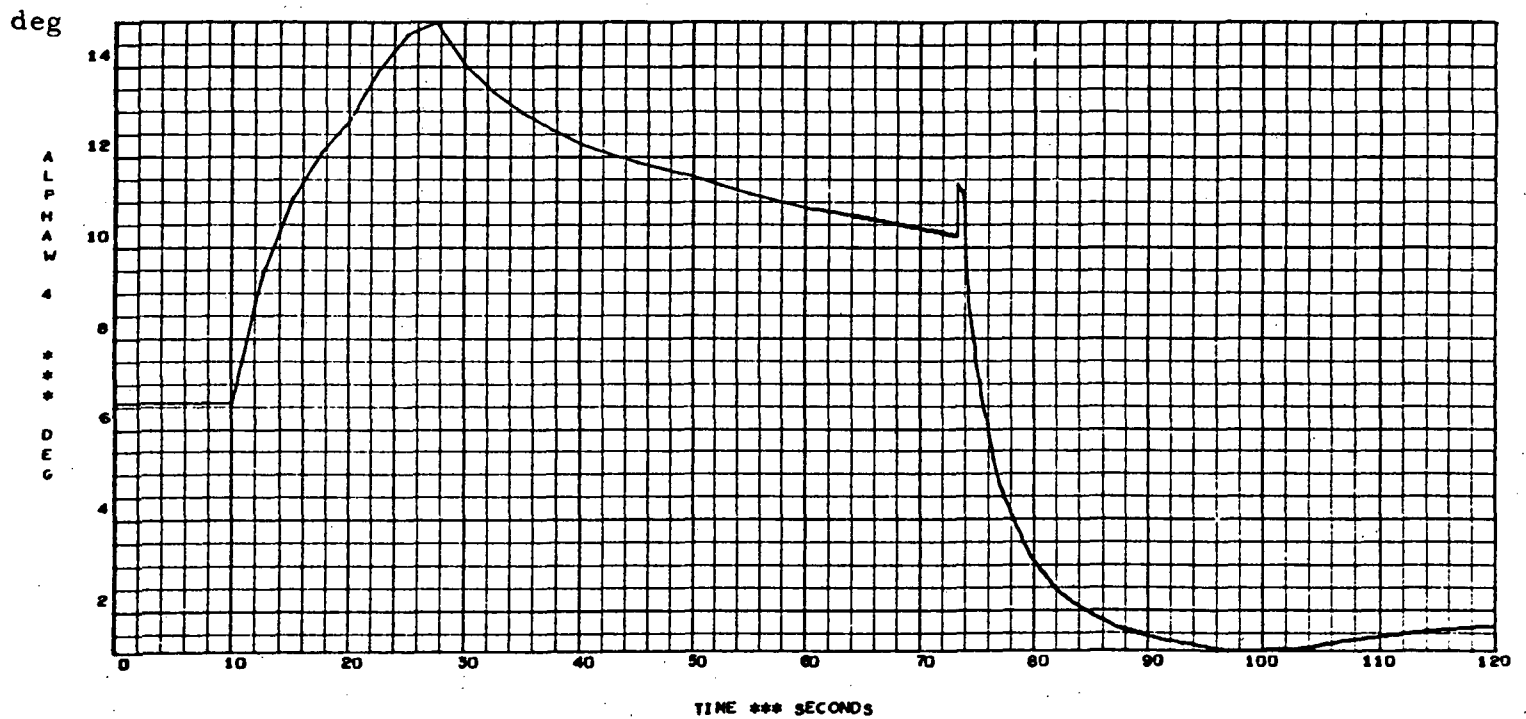
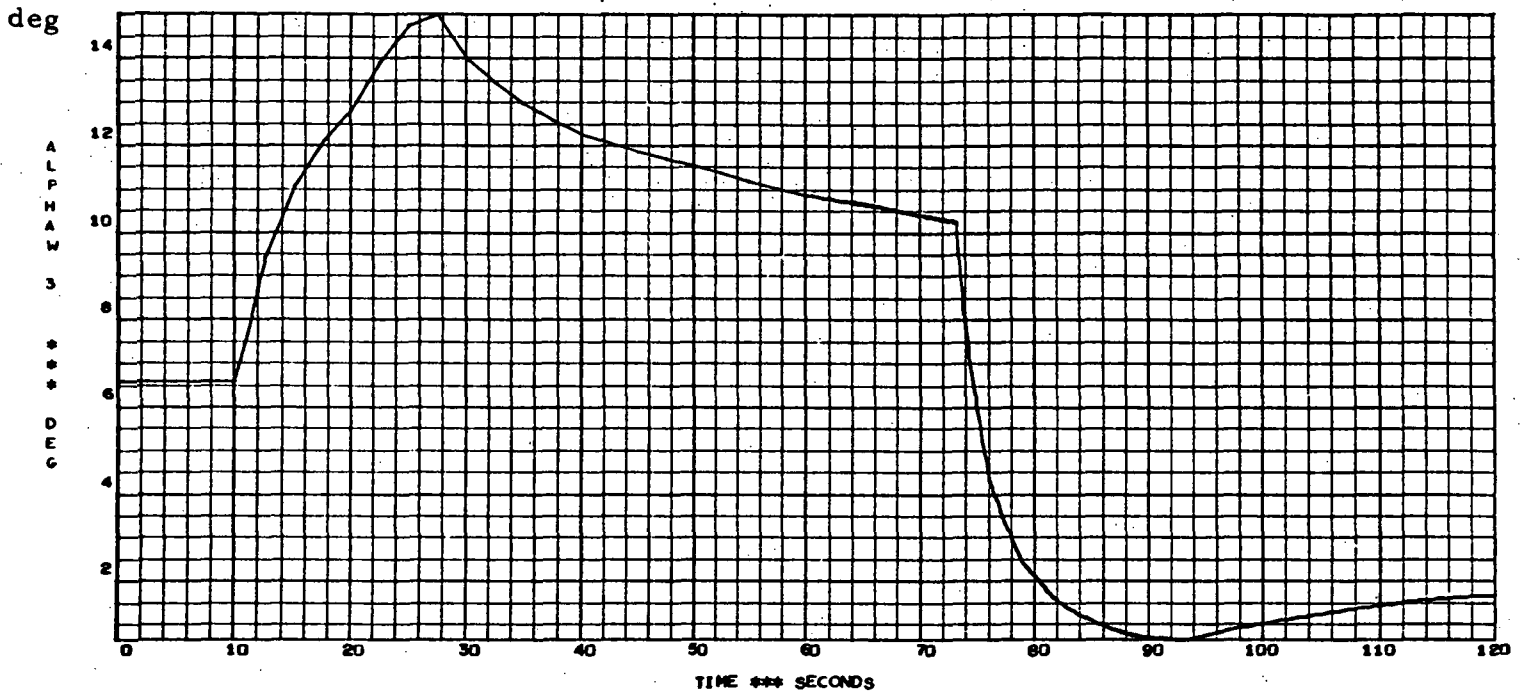


Fig. B-2 - SC 4020 Plots of  $\alpha_w3$  and  $\alpha_w4$  for INT-21 Ascent

$\alpha_w3$  = 95 Percentile Scalar Wind Speed Profile (steady-state) with 99 Percentile Shear Backoff (reversal shear) Starting at 10 km.

$\alpha_w4$  = 95 Percentile Scalar Wind Speed Profile (steady-state) with 85%-Reduced 99 Percentile Gust Superimposed Starting at 10 km and Followed by 85%-Reduced 99 Percentile Shear Backoff (reverse shear)

INT-21 ASCENT

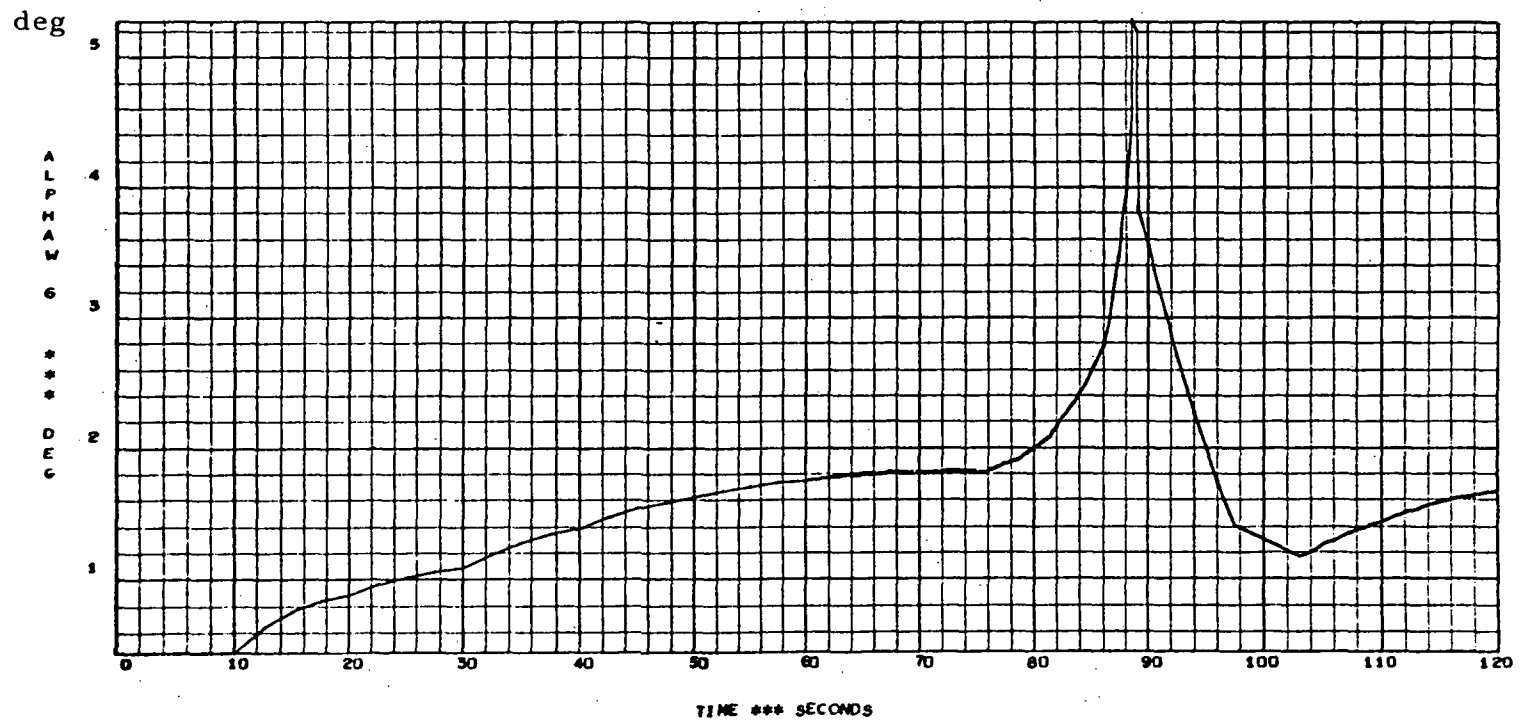
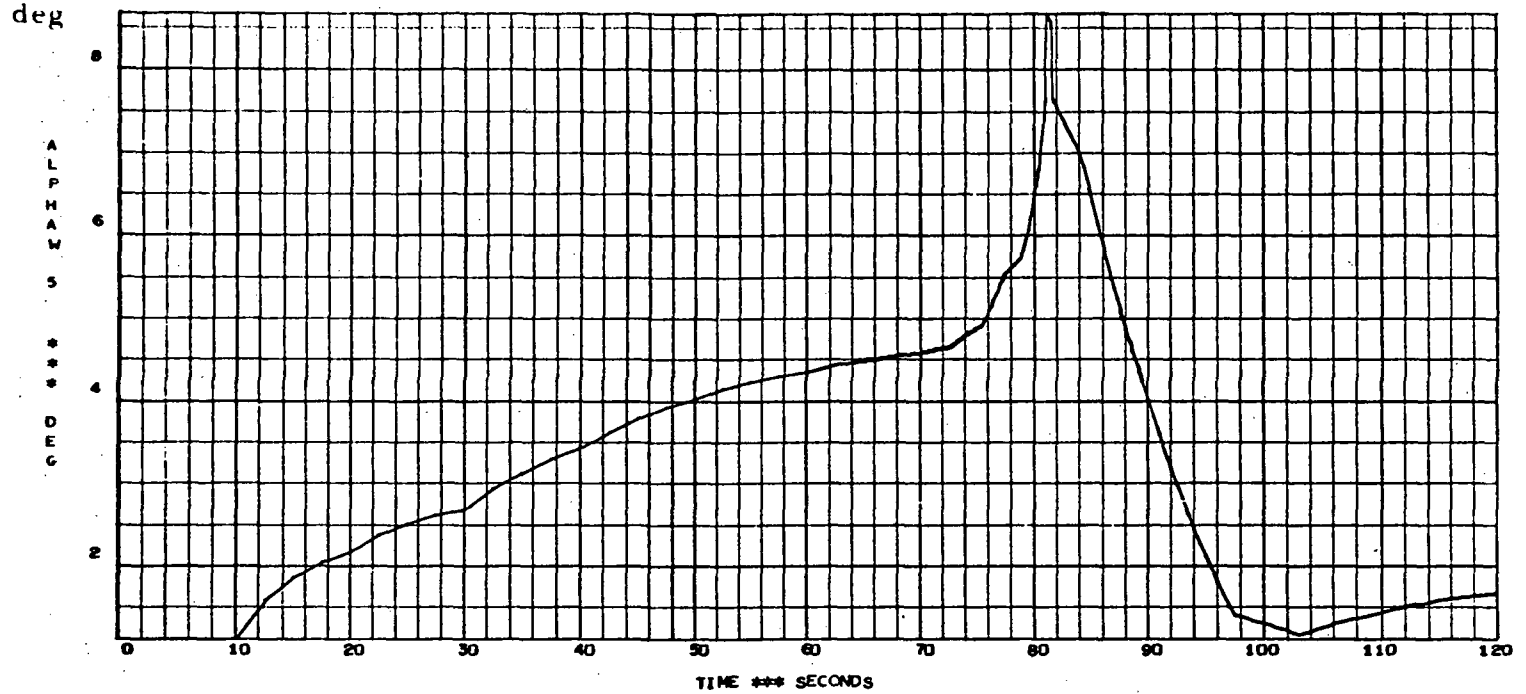


Fig. B-3 - SC 4020 Plots of  $\alpha_w5$  and  $\alpha_w6$  for INT-21 Ascent

$\alpha_w5$  = 95 Percentile Scalar Wind Speed Profile (steady-state) with 85%-Reduced 99 Percentile Shear Buildup and Superimposed 85%-Reduced 99 Percentile Gust at Maximum q

$\alpha_w6$  = 95 Percentile Scalar Wind Speed Profile (steady-state) with 85%-Reduced 99 Percentile Shear Buildup and Superimposed 85%-Reduced 99 Percentile Gust at Mach 2.0

Section C  
ANALOG COMPUTER SIMULATION DIAGRAMS

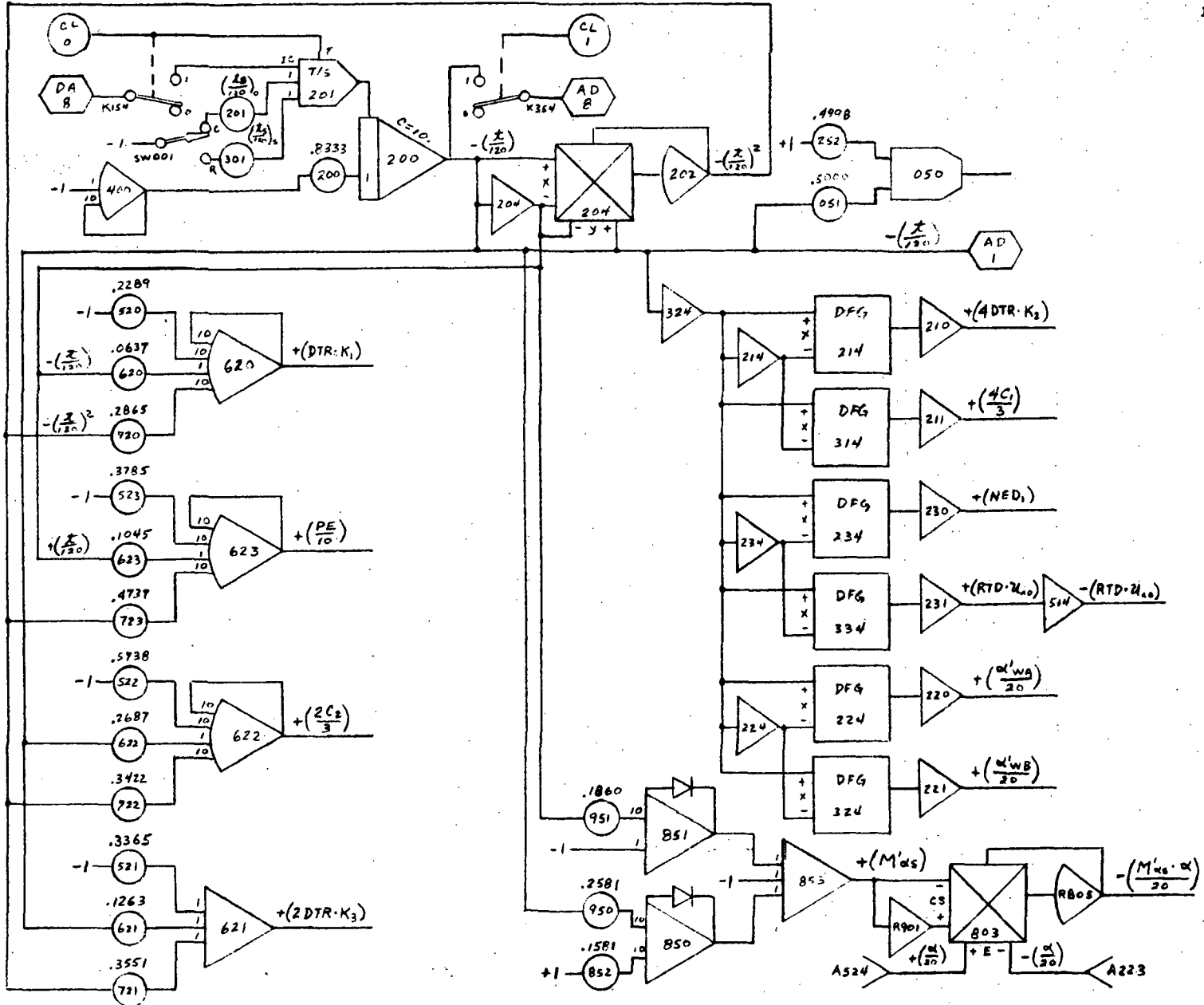
Appendix C

This appendix contains the analog computer simulation diagrams used in this study.

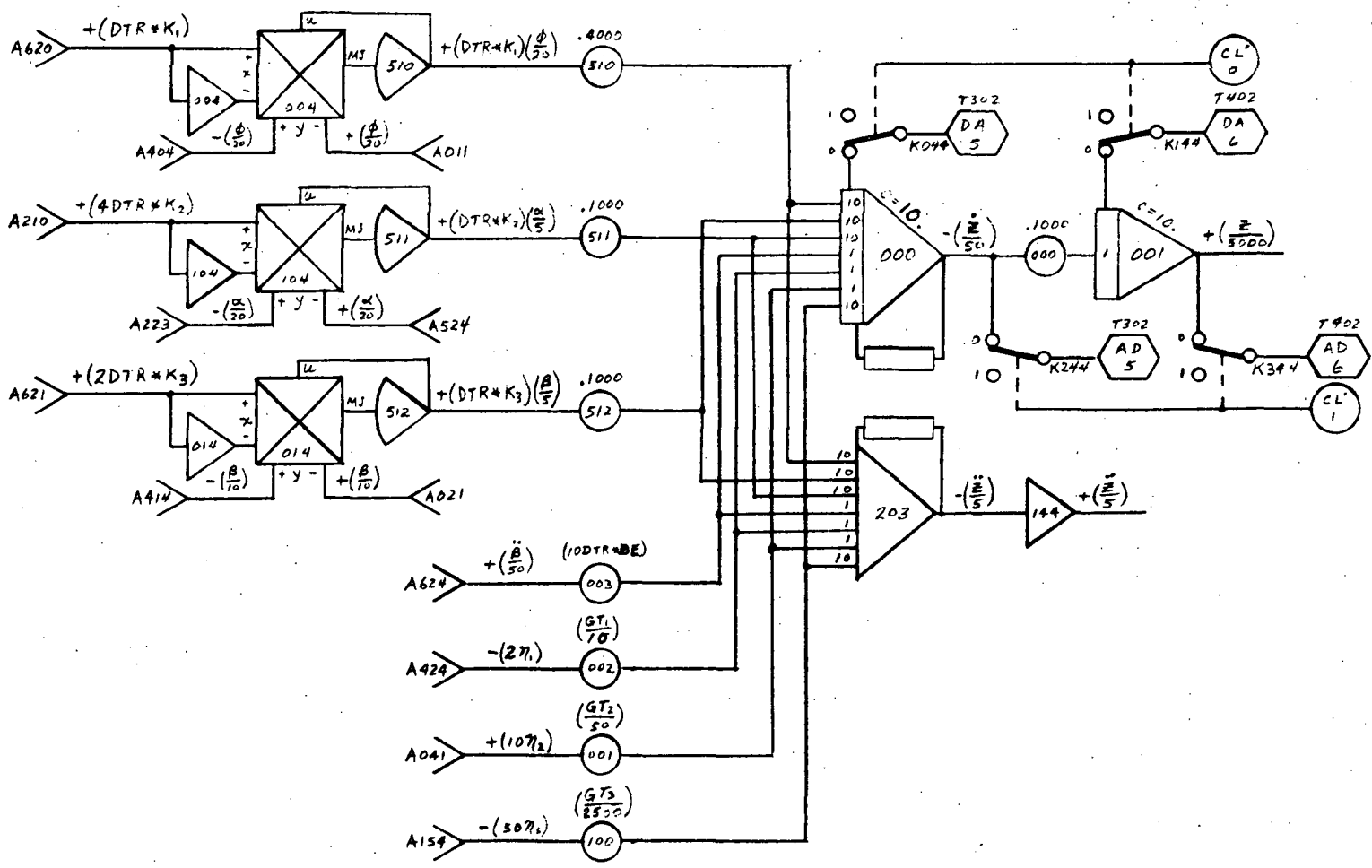
Substantial savings in programming, checkout and simulation effort were realized by using the same analog simulation in all three major study phases, namely:

1. Initial dynamic analysis and exploratory simulations to define candidate control systems;
2. Direct optimization using the hybrid optimizer discussed in Section 2;
3. Performance verification including determination of statistical performance characteristics using up to 970 measured wind profiles stored on tape.

C-2



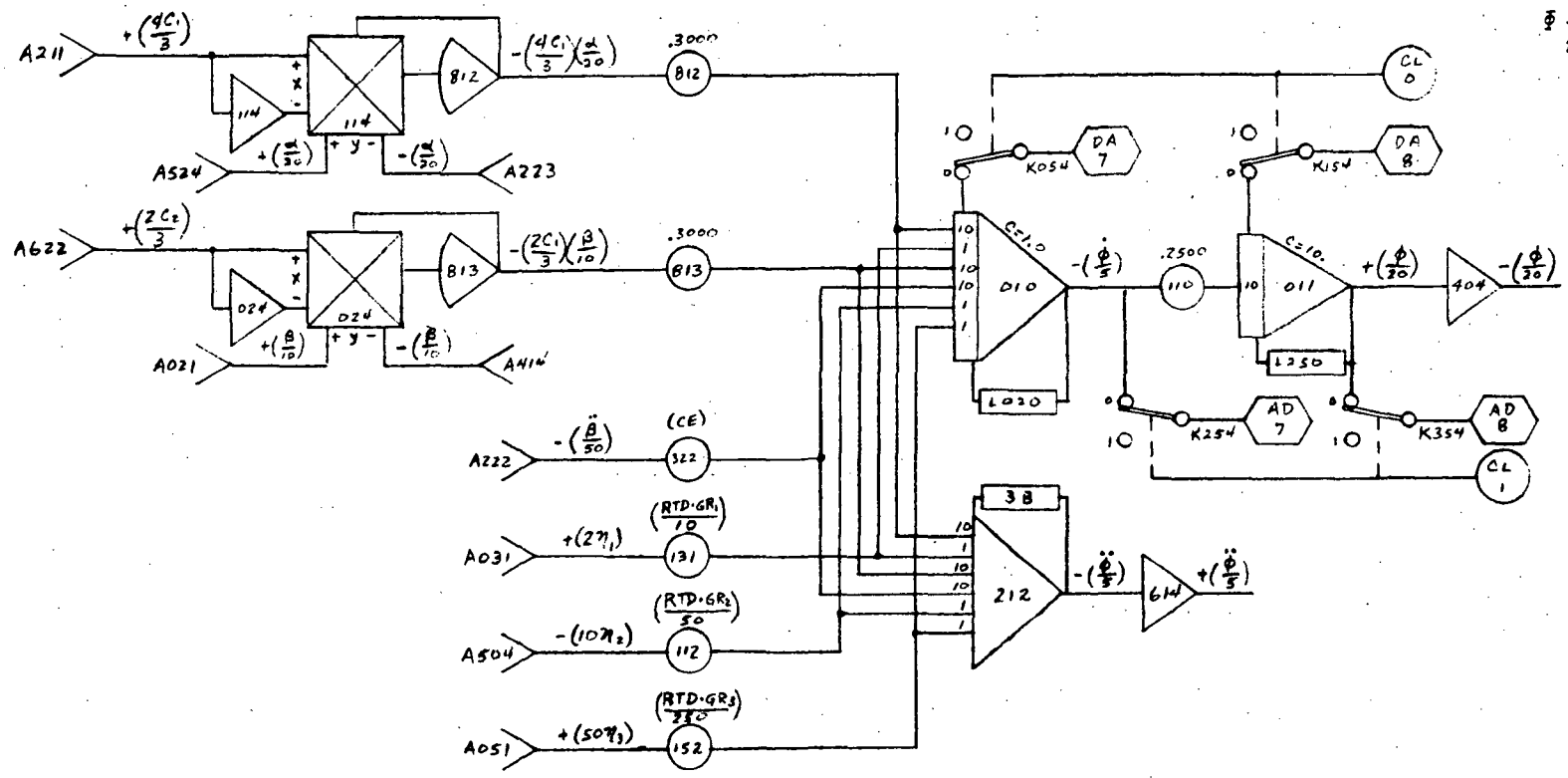
Time-Varying Coefficients for EOM  
INT-21 Ascent Including 141-Foot Payload



Translational Dynamics  
INT-21 Ascent Including 141-Foot Payload

C-3

$\Phi$  - ROTATION  
INT-21 (141)

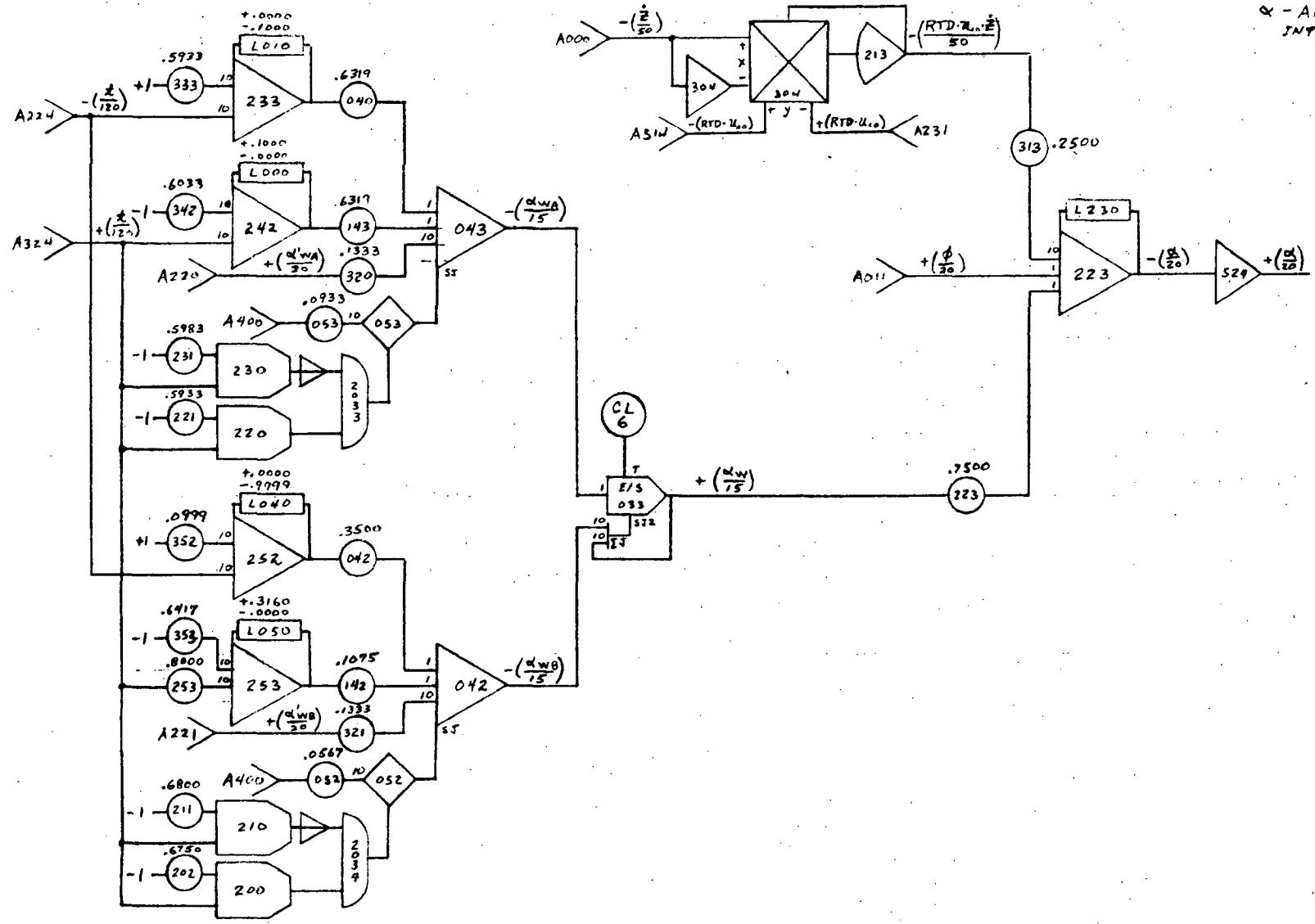


C-4

Rotational Dynamics  
INT-21 Ascent Including 141-Foot Payload

LMSC-HRREC D225737

C-5

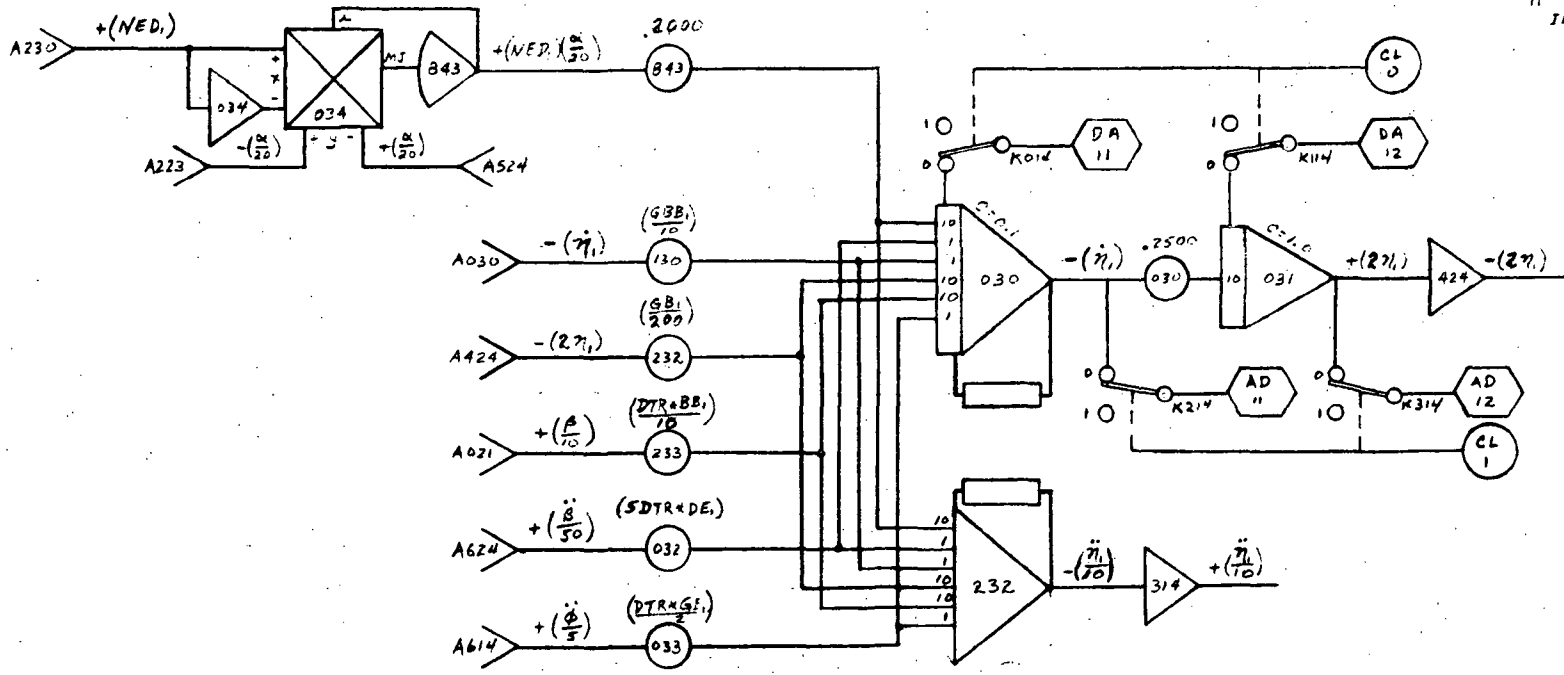


$\alpha$  - ANGLE OF ATTACK  
INT-21 (141)

Synthetic Wind Generation and Angle-of-Attack Development  
INT-21 Ascent Including 141-Foot Payload

LMSC-HREC D225737



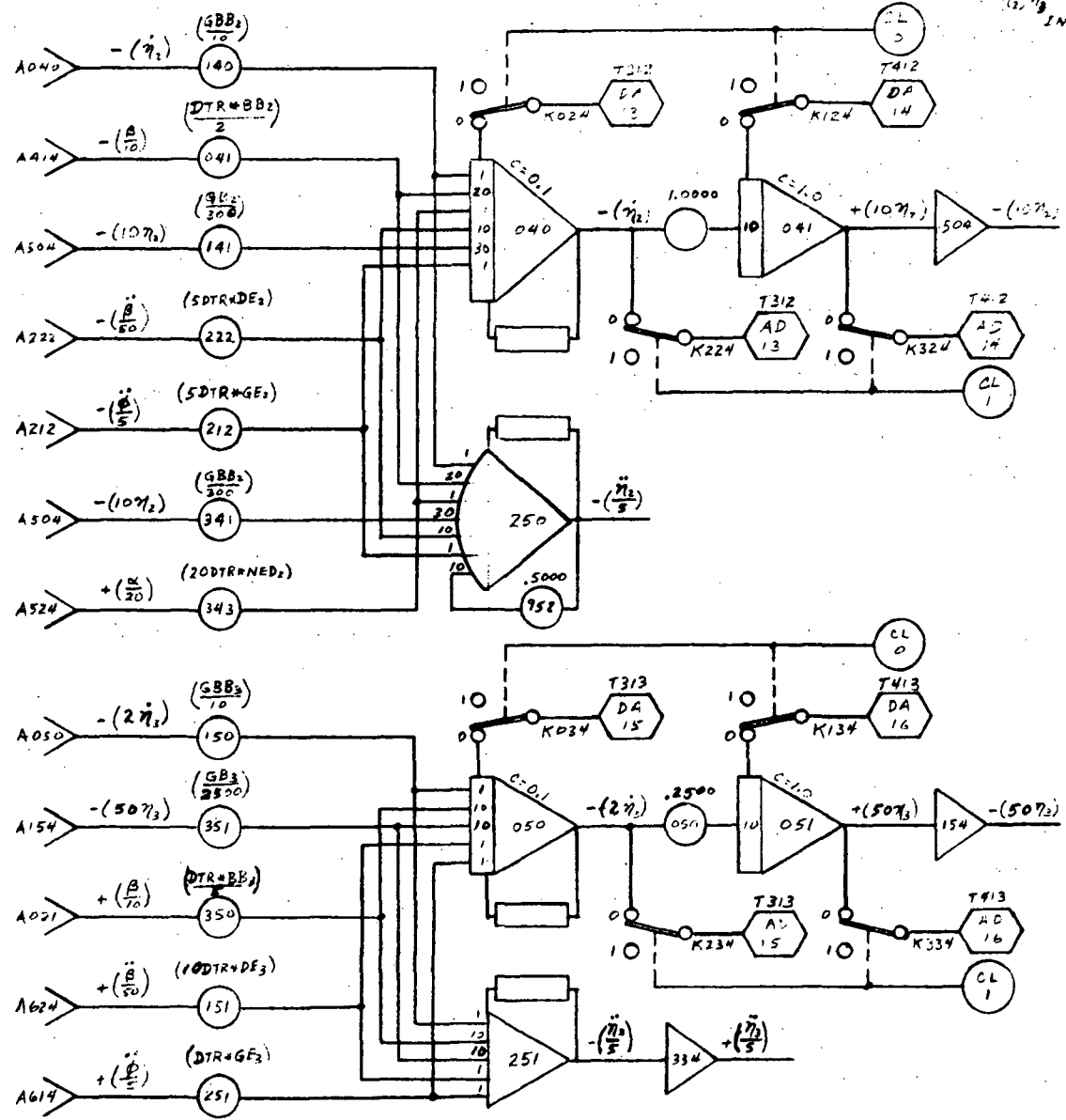


C-6

First Bending Mode Dynamics  
INT-21 Ascent Including 141-Foot Payload

2nd, 3rd BENDING  
INT-21 (141)

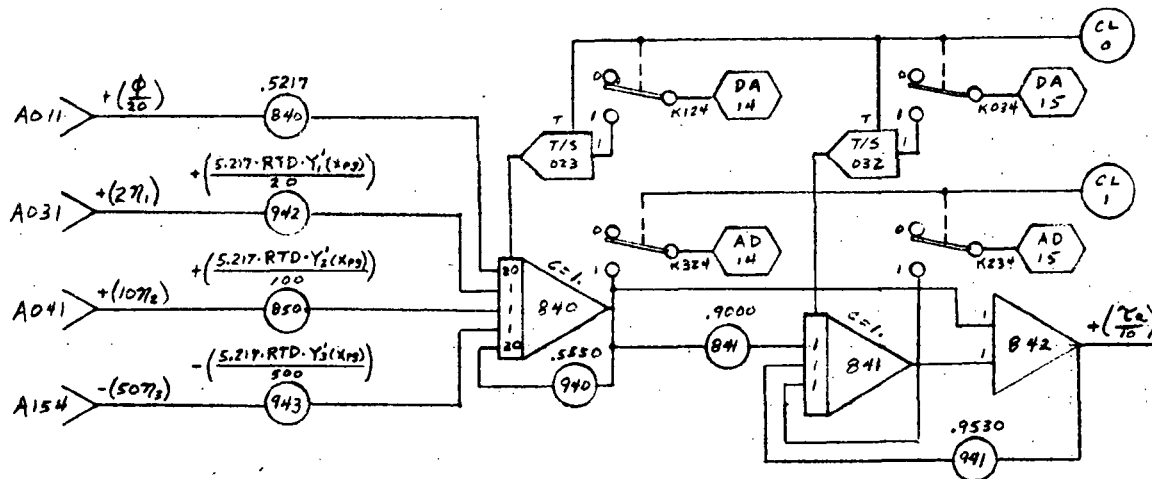
10-1-71



C-7

LMSC-HREC D225737

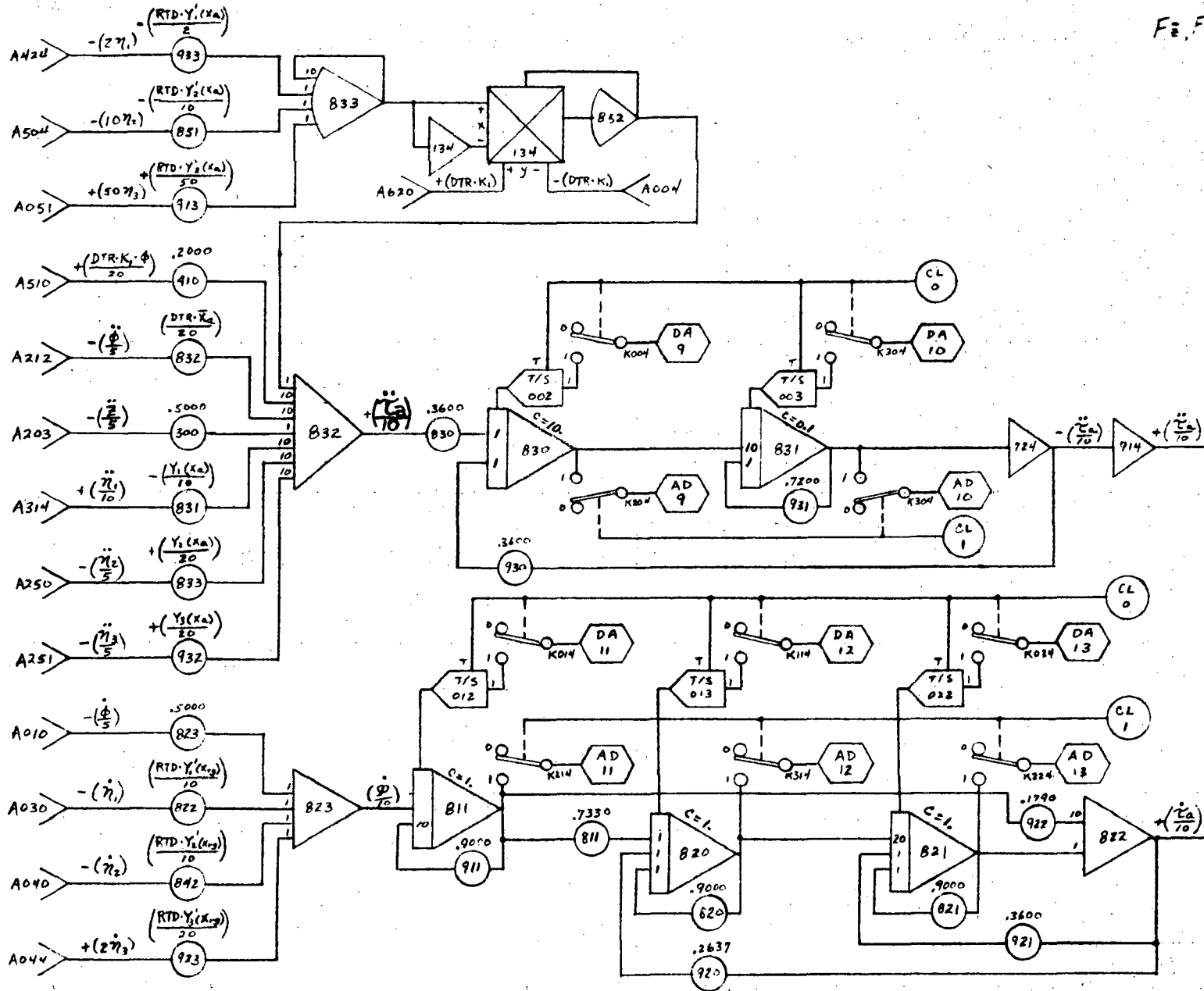
Second and Third Bending Mode Dynamics  
INT-21 Ascent Including 141-Foot Payload



φ Shaping Filter  
INT-21 Ascent Including 141-Foot Payload

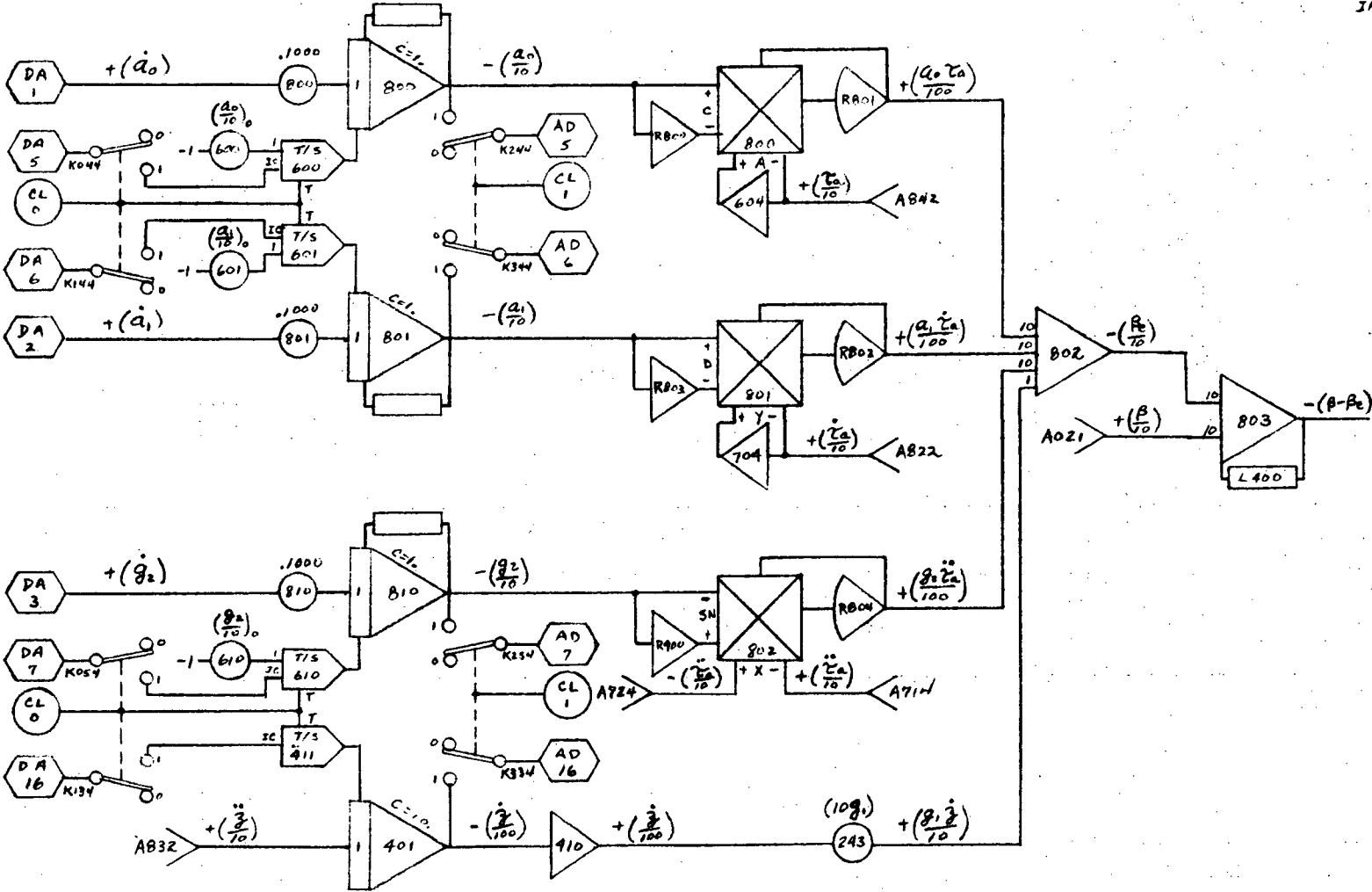
$F_2, F_4$  - FILTERS  
INT-21 (141)

C-9



$\phi$  and  $\ddot{\gamma}_a$  Shaping Filters  
INT-21 Ascent Including 141-Foot Payload

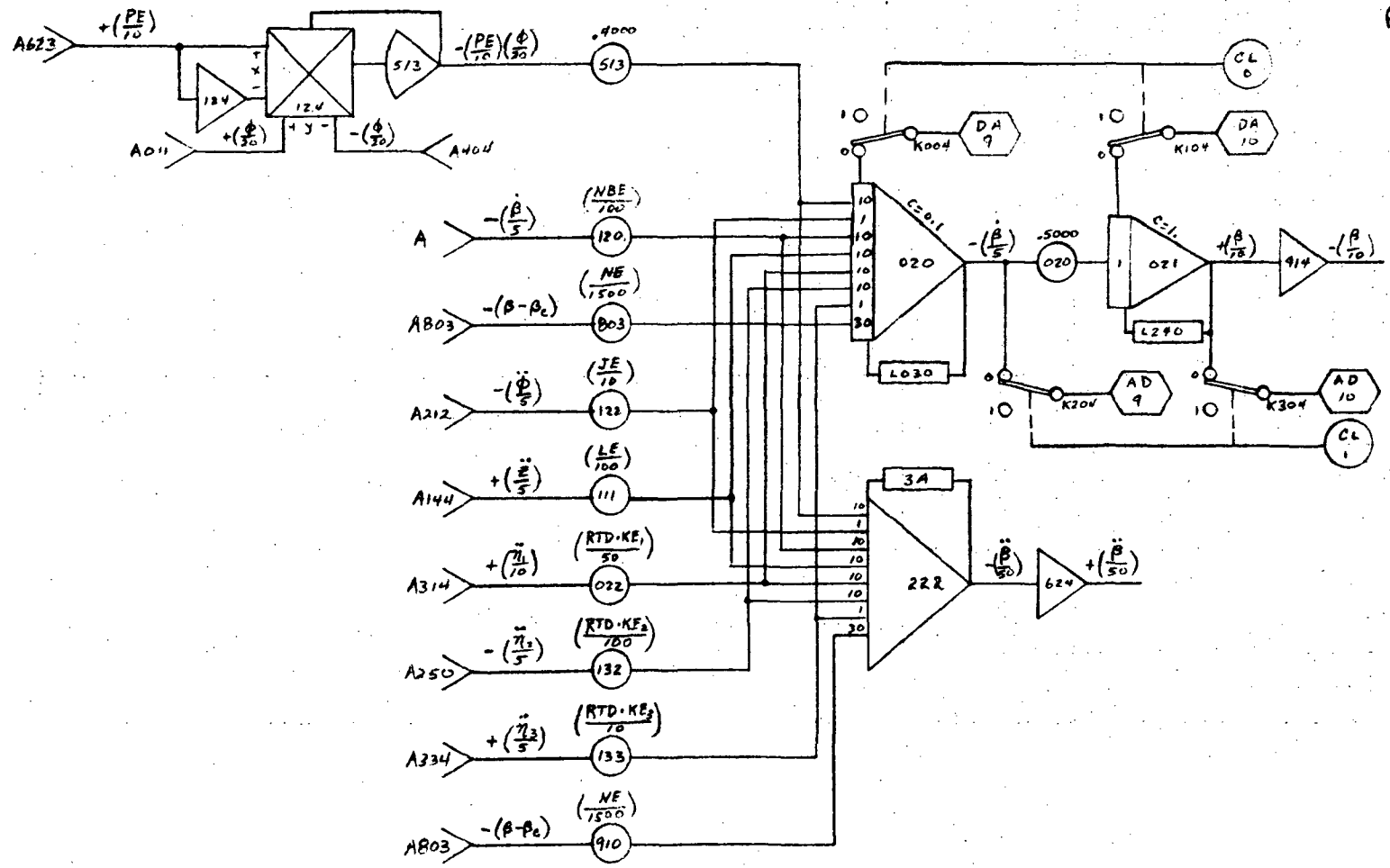
LMSC-HREC D225737



C-10

Load Relief Control Law  
INT-21 Ascent Including 141-Foot Payload

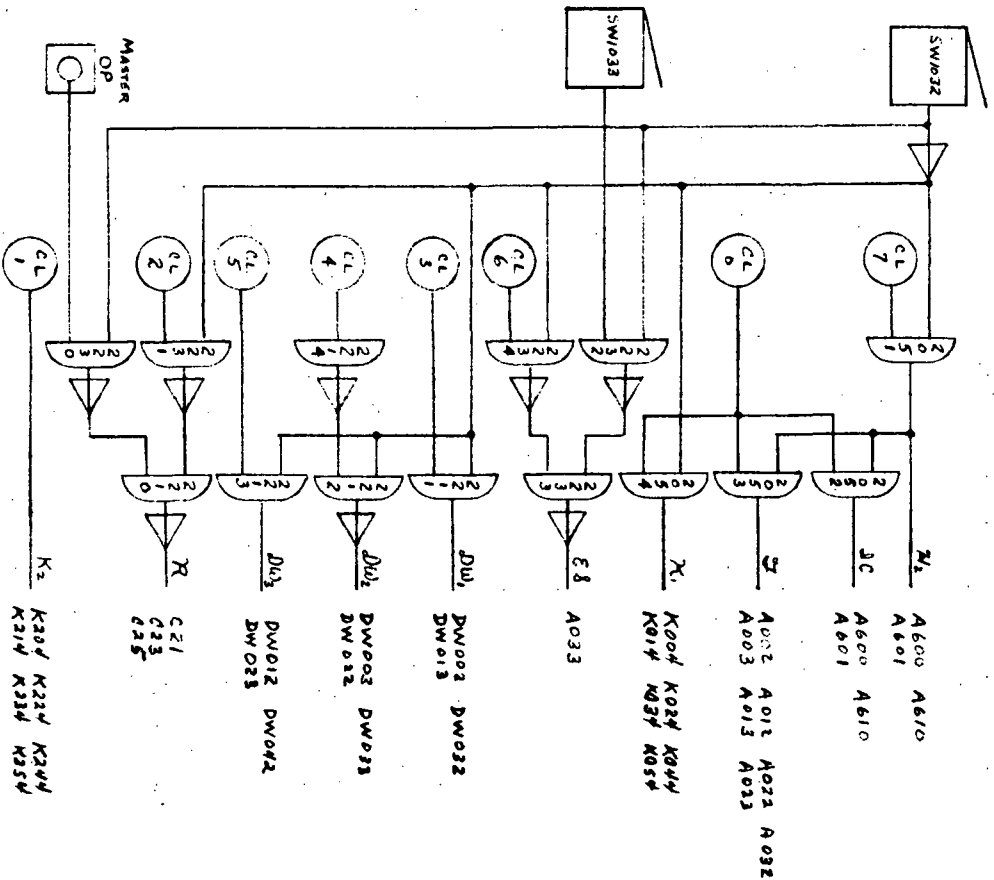
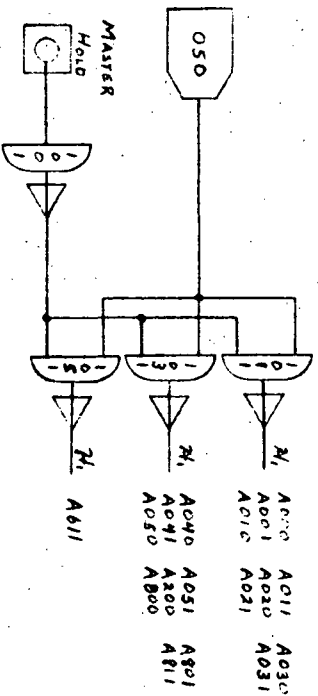
$\beta$  - ENGINE ANGLE  
INT-21 (141)



Engine Swivel Dynamics  
INT-21 Ascent Including 141-Foot Payload

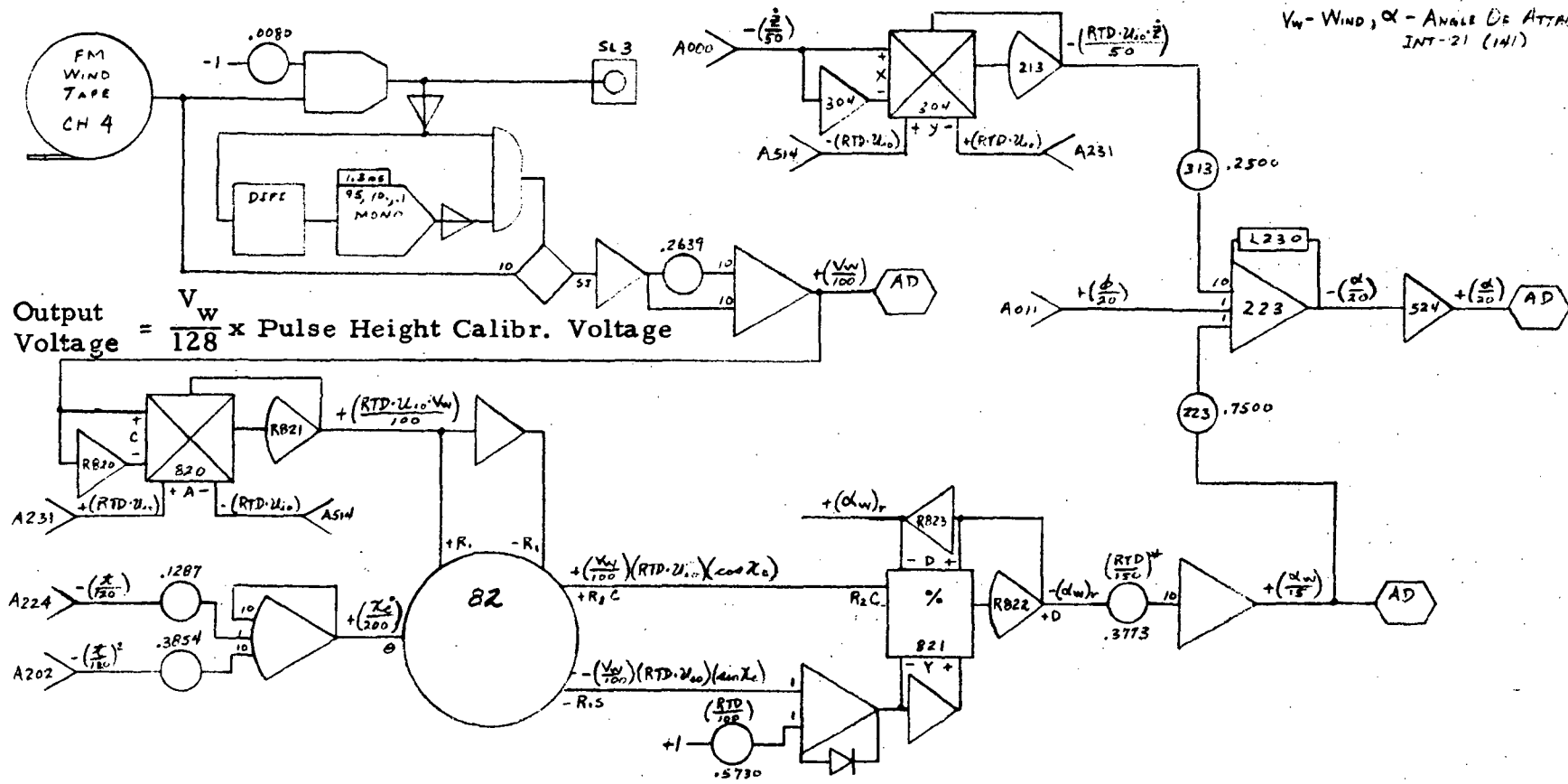
LMSC-HREC D225737

LOGIC  
INT-21 (141)



Hybrid Optimizer Simulation Logic  
INT-21 Ascent Including 141-Foot Payload

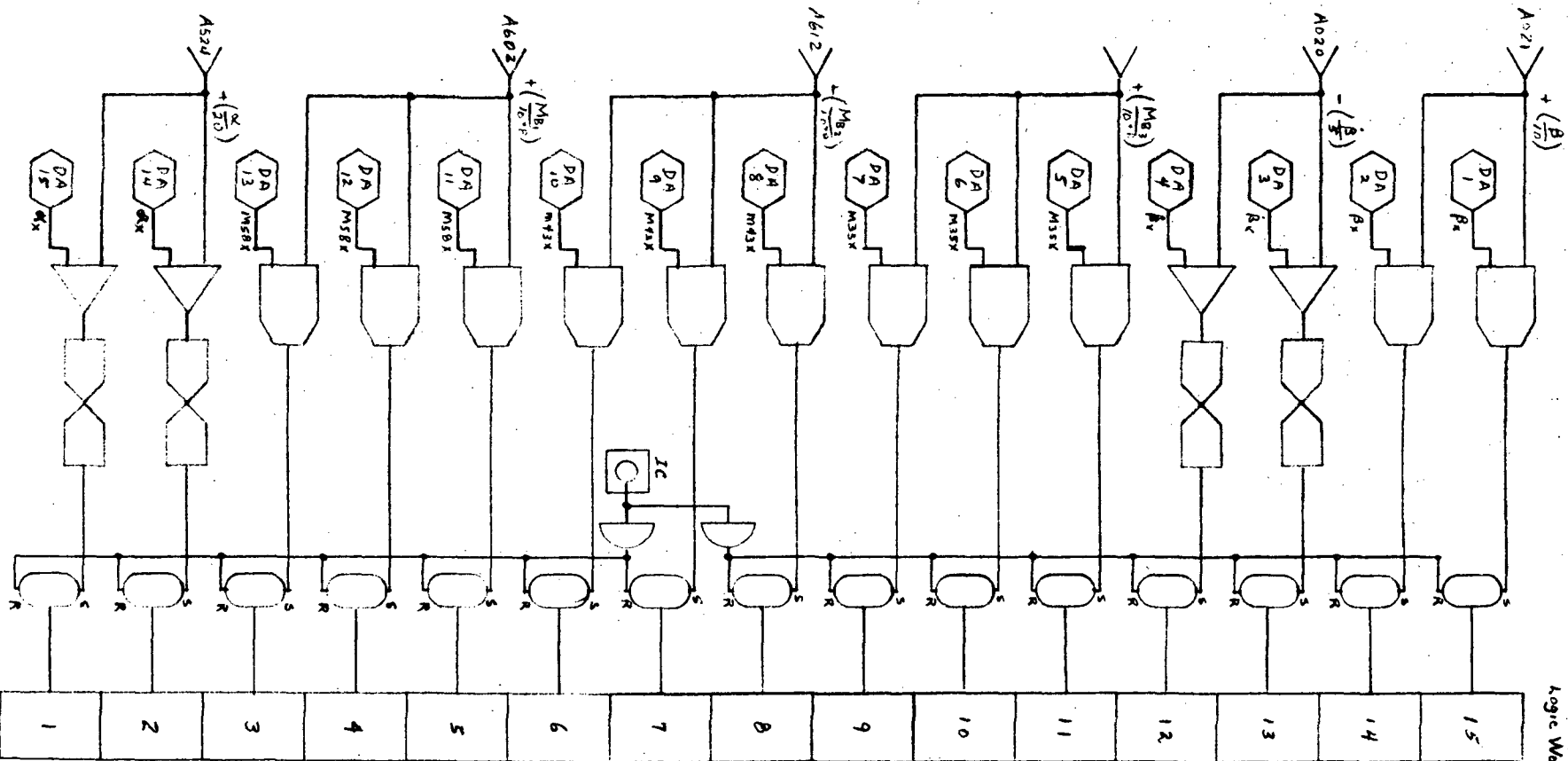
C-13



$V_w$  and  $\alpha_w$  Generation from Tape Output Signal  
INT-21 Ascent Including 141-Foot Payload



Logic Word



Exceedance Count Circuitry for Statistical Evaluation  
INT-21 Ascent Including 141-Foot Payload

**Appendix D**  
**DIGITAL SIMULATION CHECK SOLUTIONS**

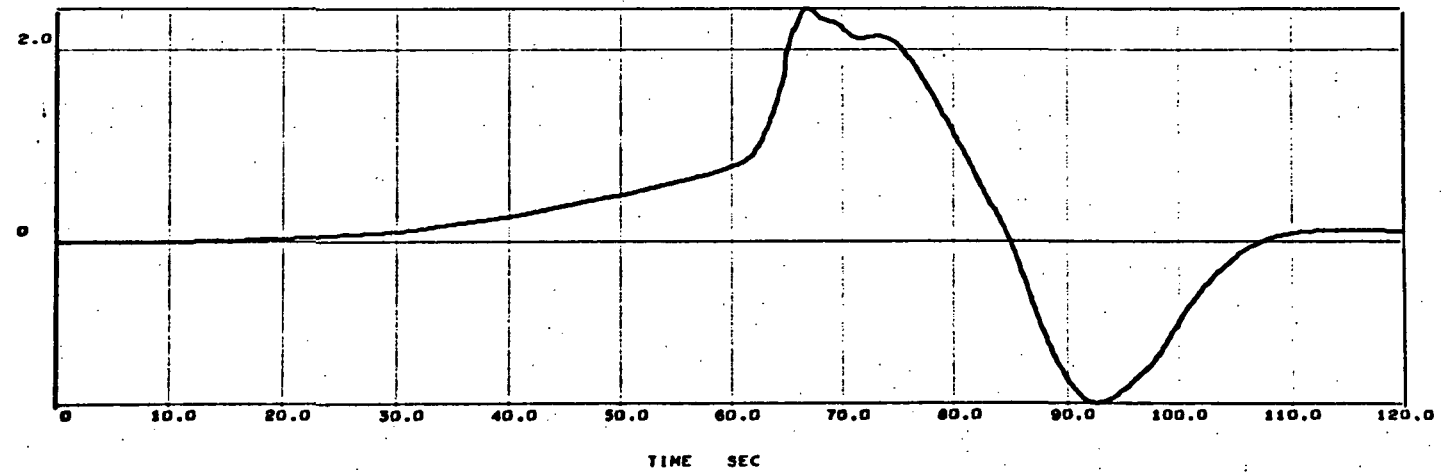
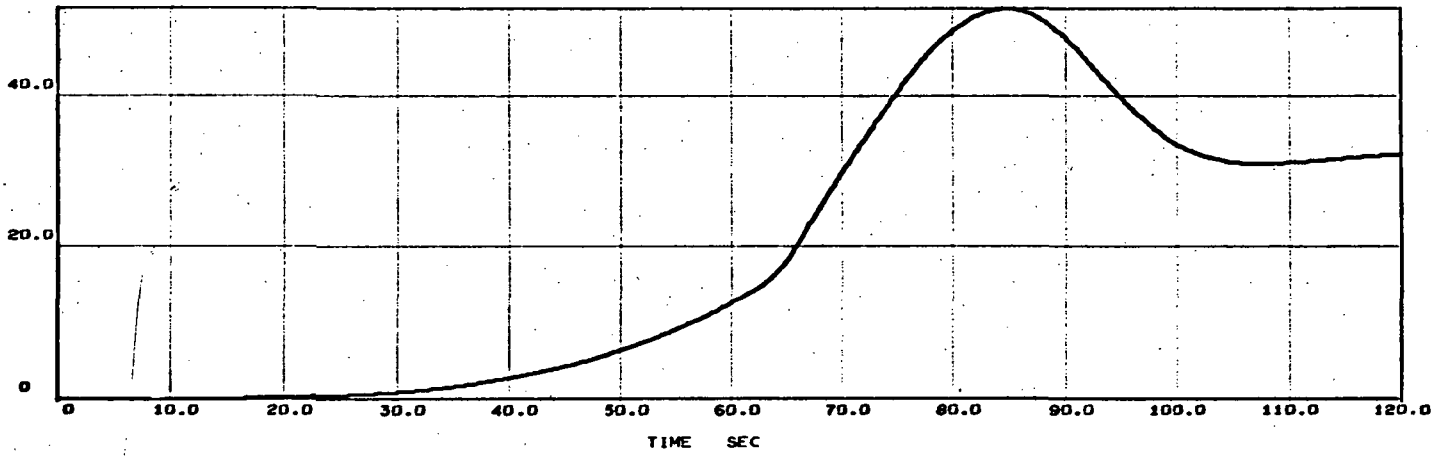
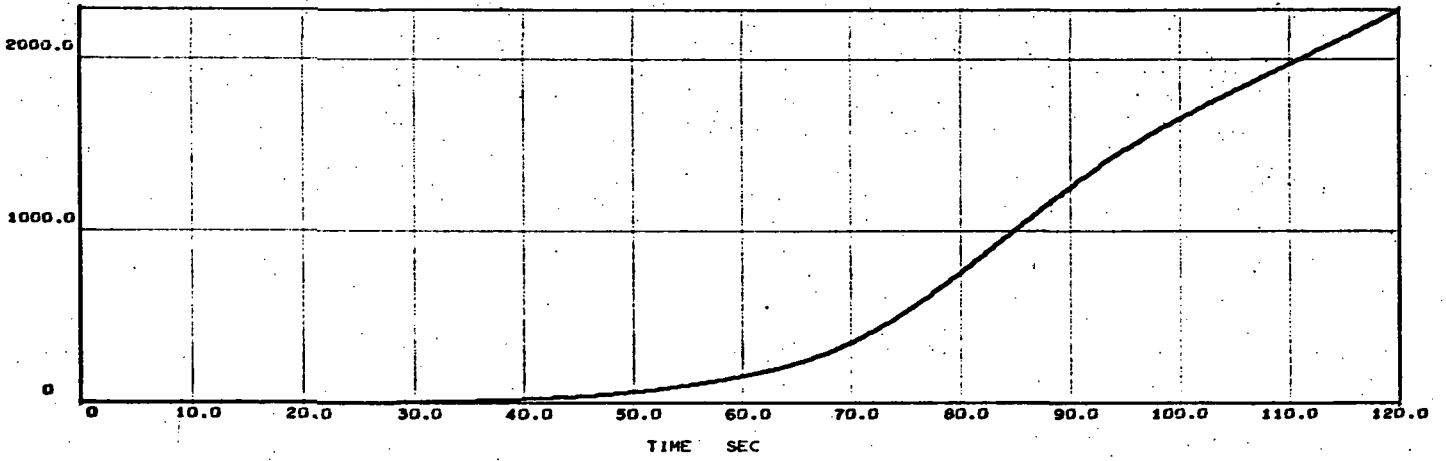
Appendix D

This appendix contains INT-21 (with 141-foot payload) ascent digital simulation solution curves for  $\alpha_w 1$ ,  $\alpha_w 3$ , and  $\alpha_w 6$  forcing functions. (See Appendix B for a complete description of these  $\alpha_{w_i}$ 's). They are one of the outputs of Lockheed's digital computer INT-21 ascent flight simulation. Useful features of this digital simulation include printout and plots of TVC's,  $\alpha_{w_i}$ 's, and flight dynamics solution curves.

The following solution curves present the displacements (and their time derivatives) and rotations (and their time derivatives) resulting when an attitude control (Control Law 1) system is used.  $a_0 = 1.4$  and  $a_1 = 1.0$  sec.

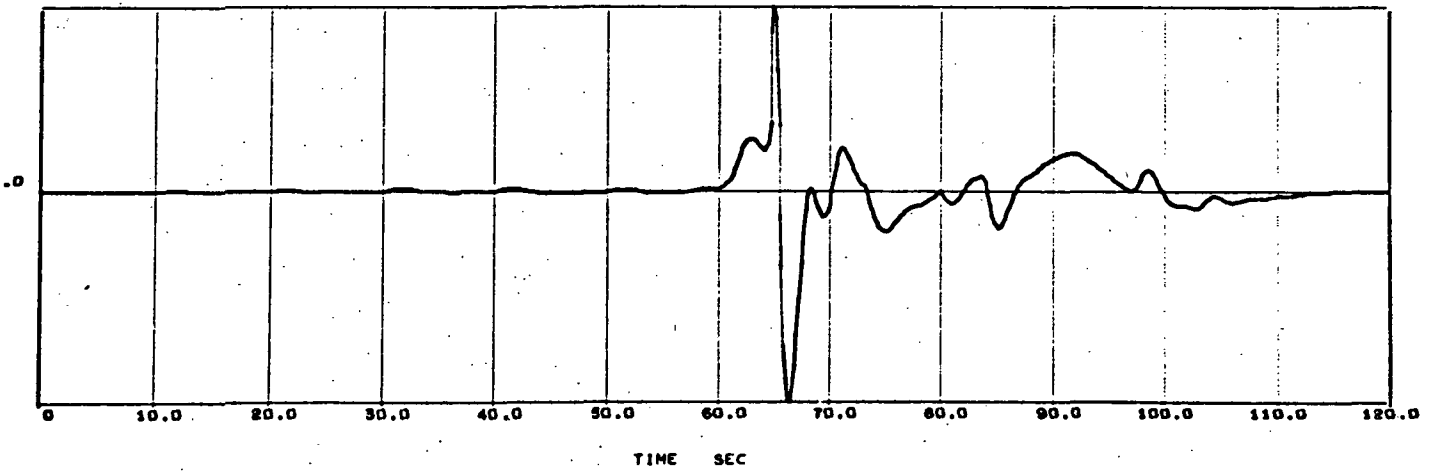
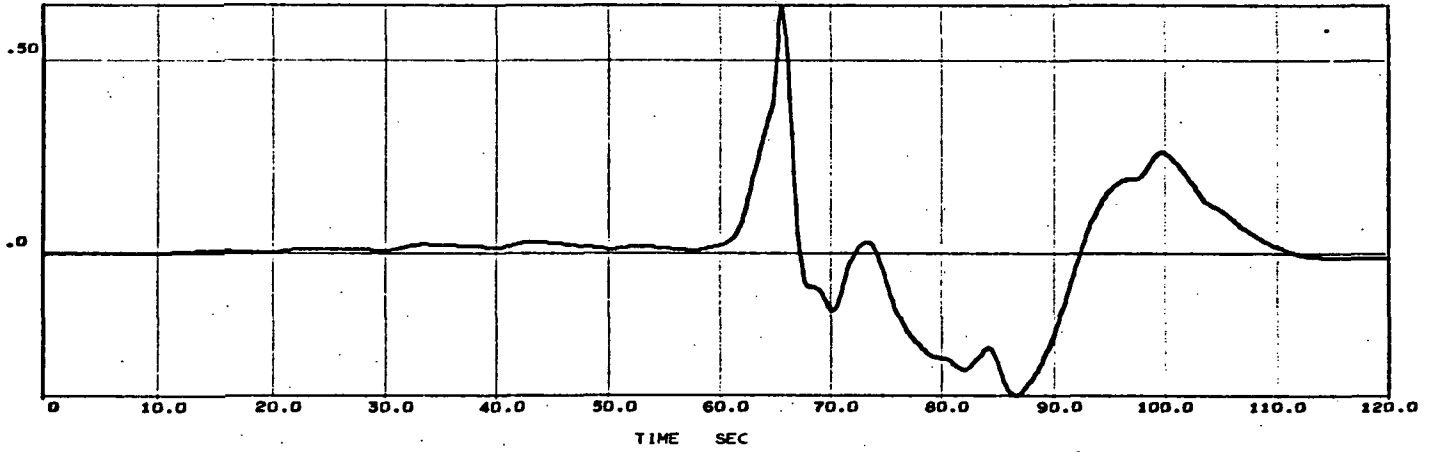
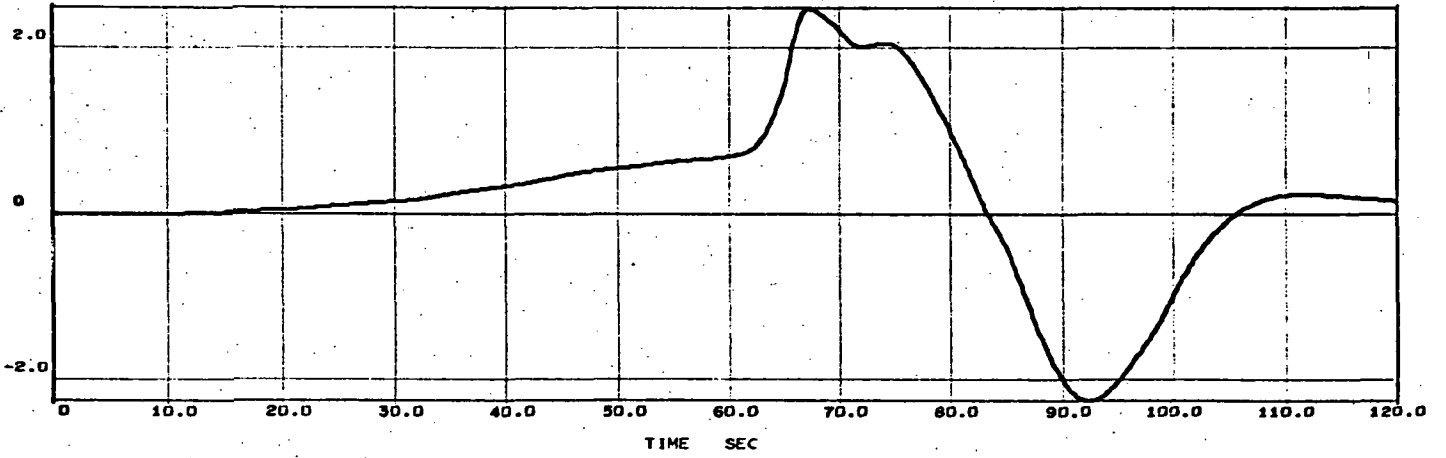
All displacements are in meters and all rotations are in degrees.

INT-21 ASCENT SIMULATION



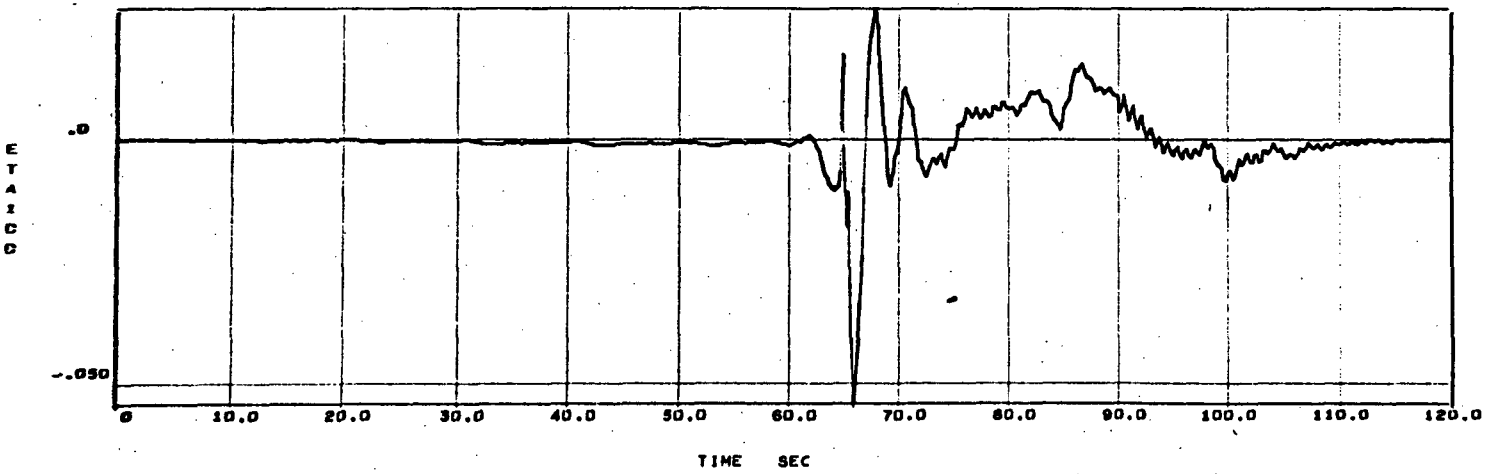
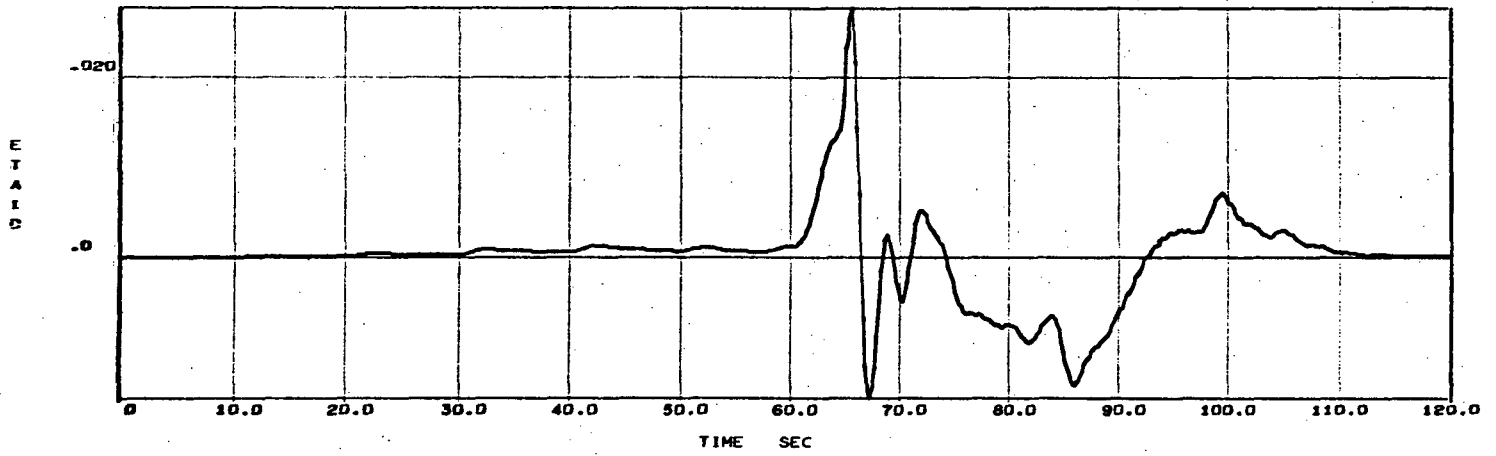
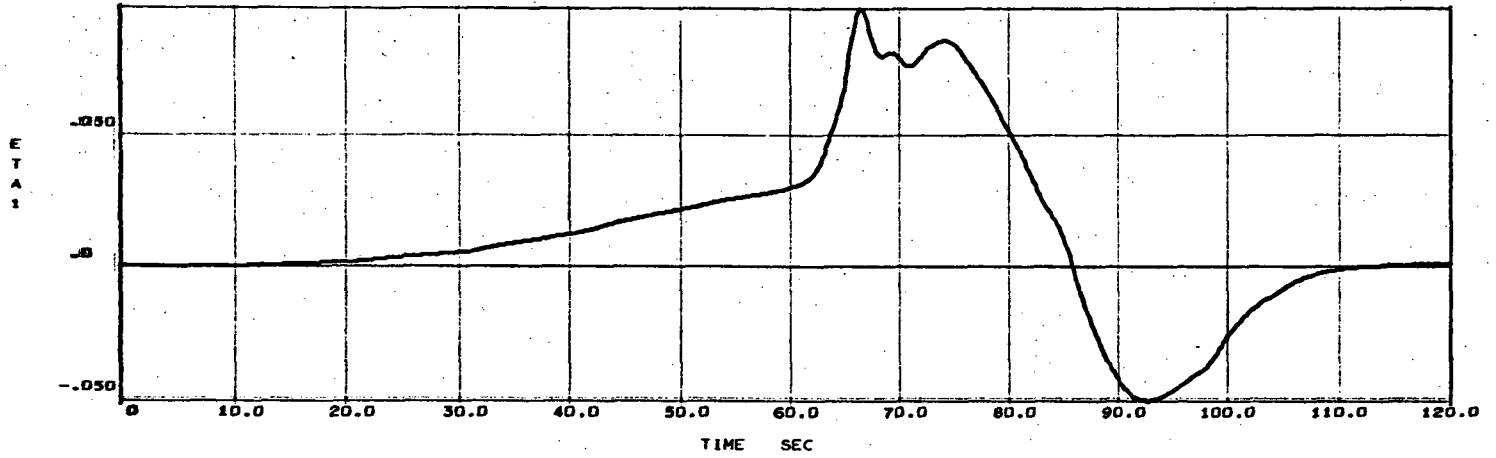
$\alpha_w$  l Response

INT-21 ASCENT SIMULATION



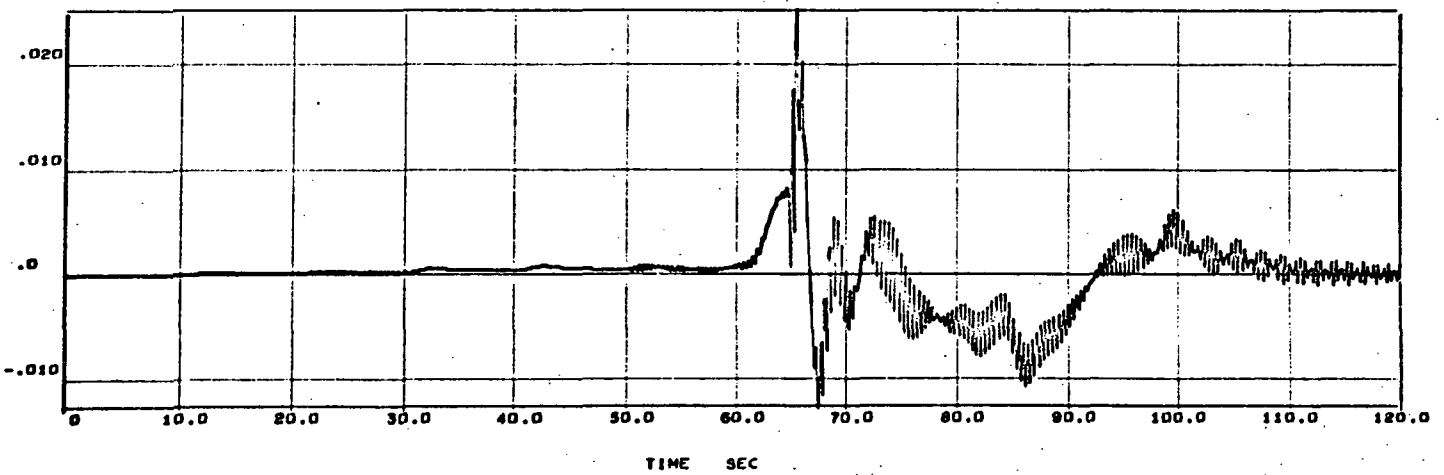
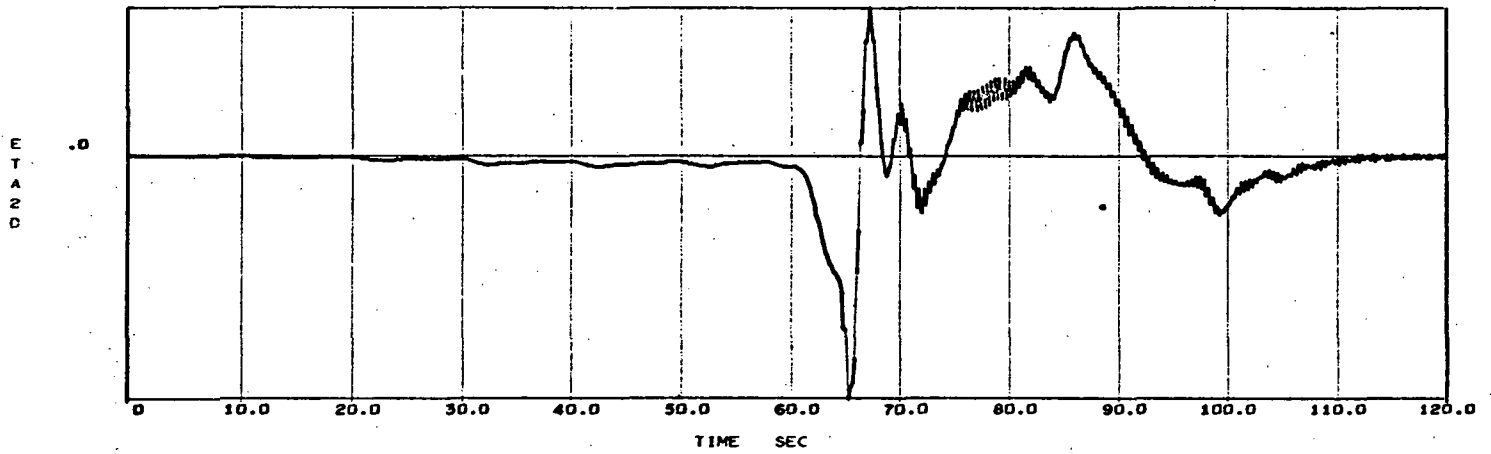
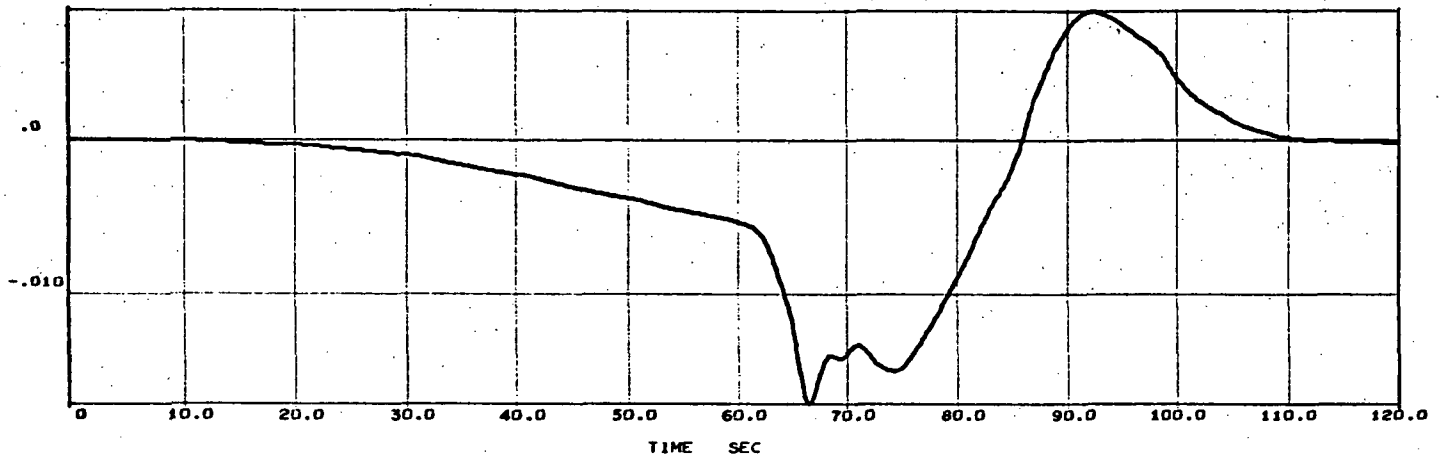
$\alpha_w$  Response

INT-21 ASCENT SIMULATION



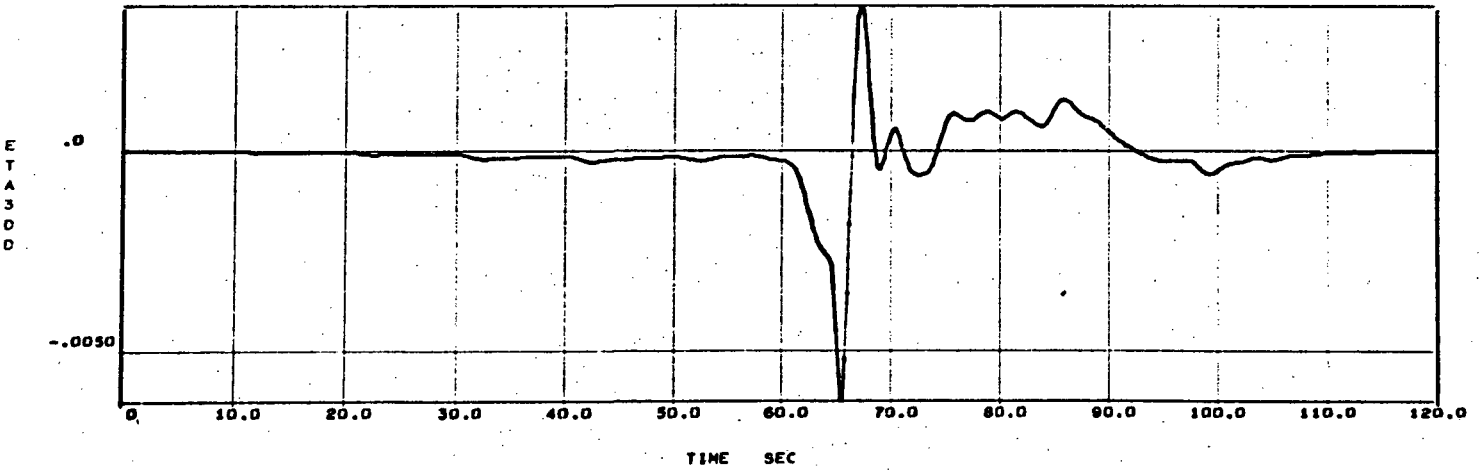
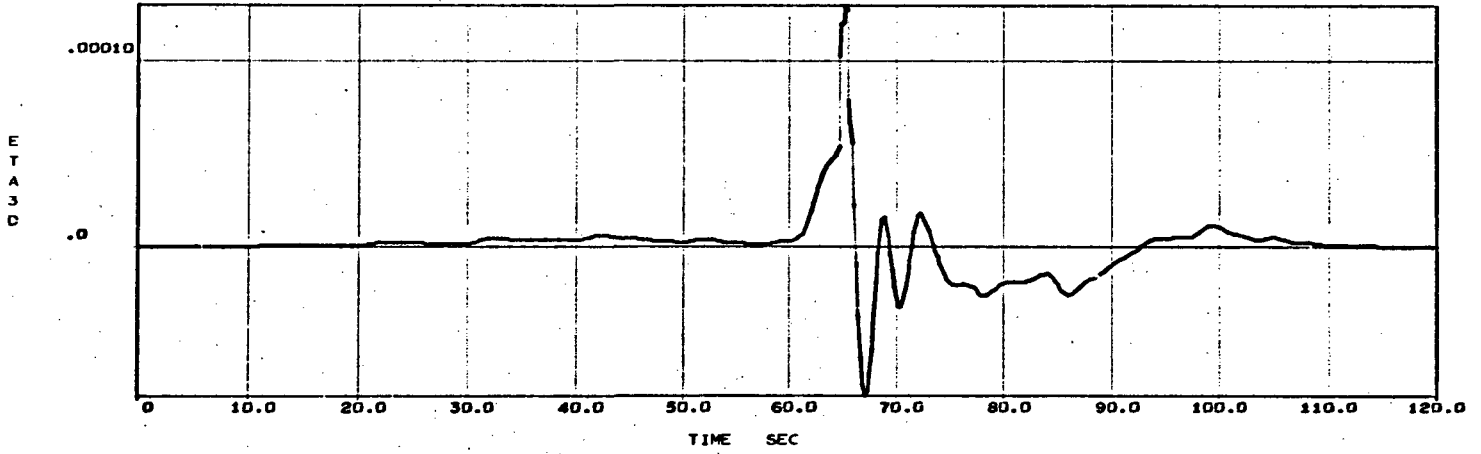
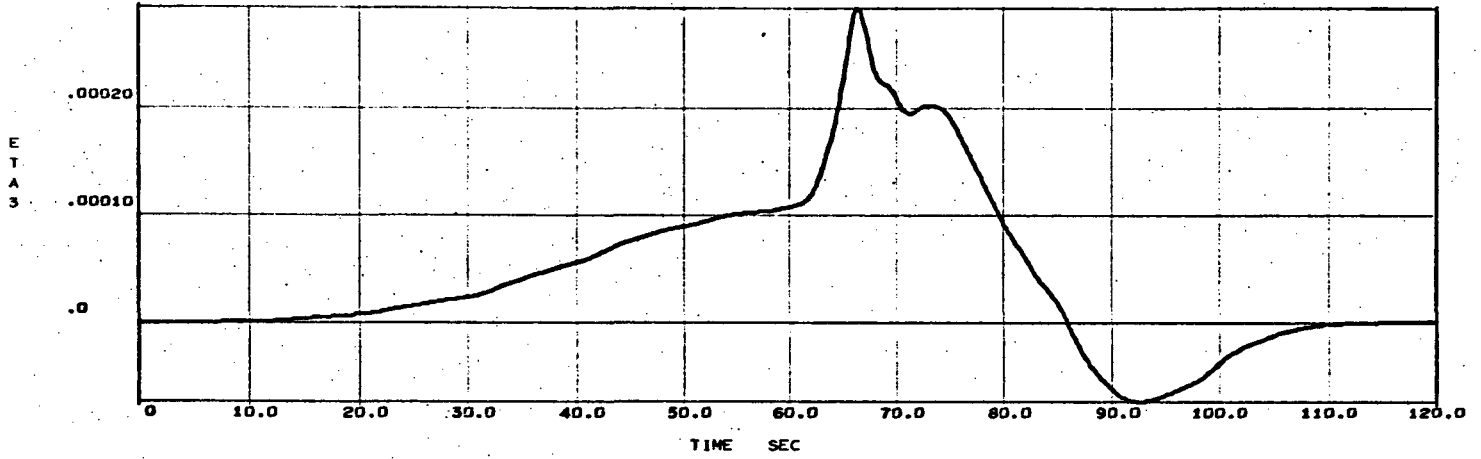
$\alpha_1$  Response

INT-21 ASCENT SIMULATION



$\alpha_w$  Response

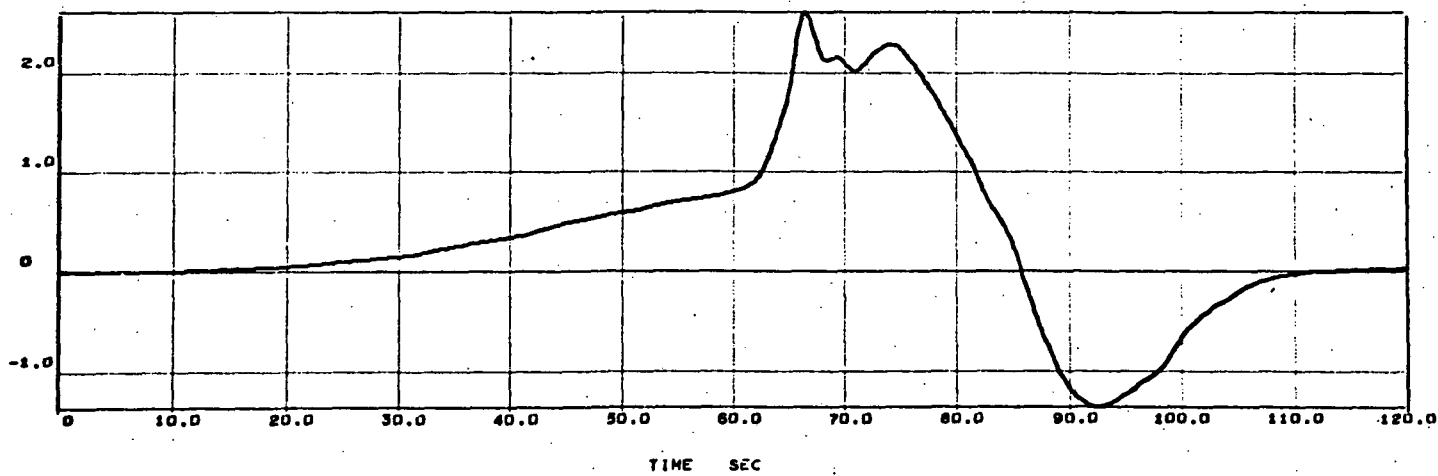
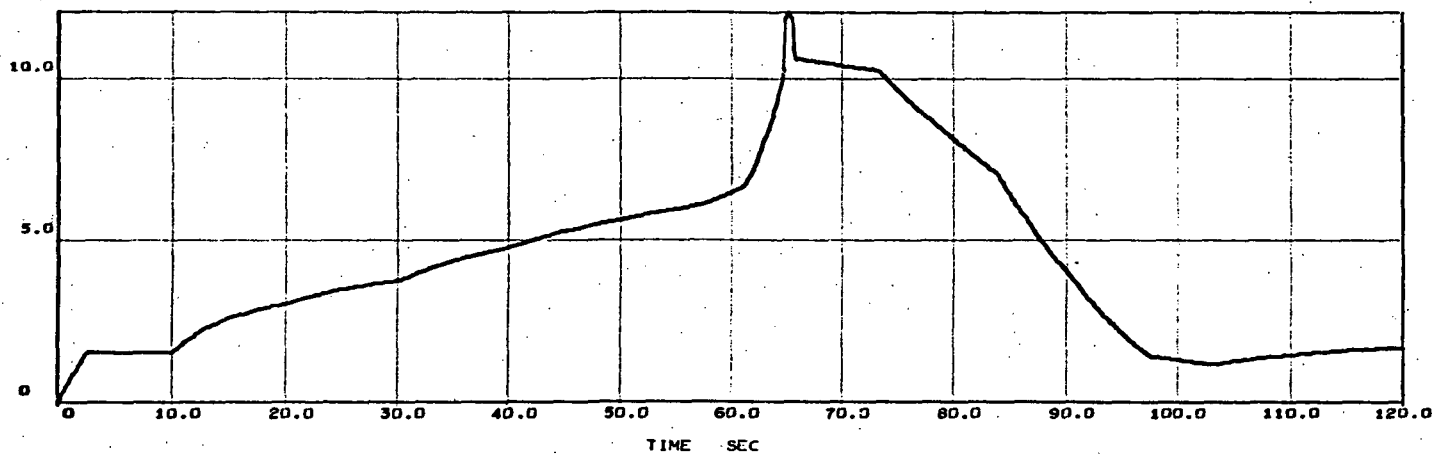
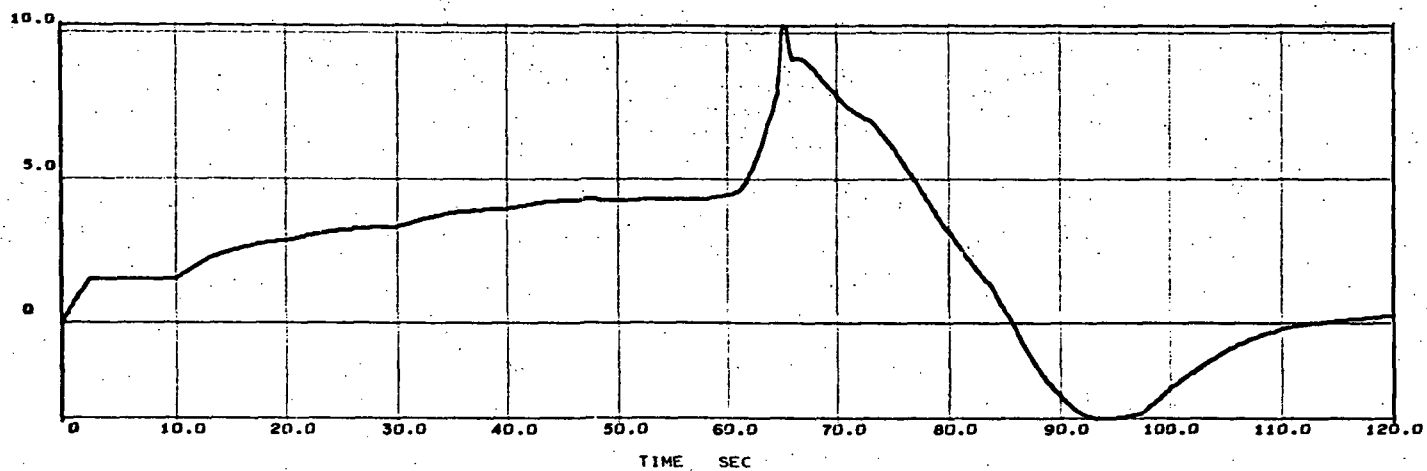
INT-21 ASCENT SIMULATION



$\alpha_w$  Response

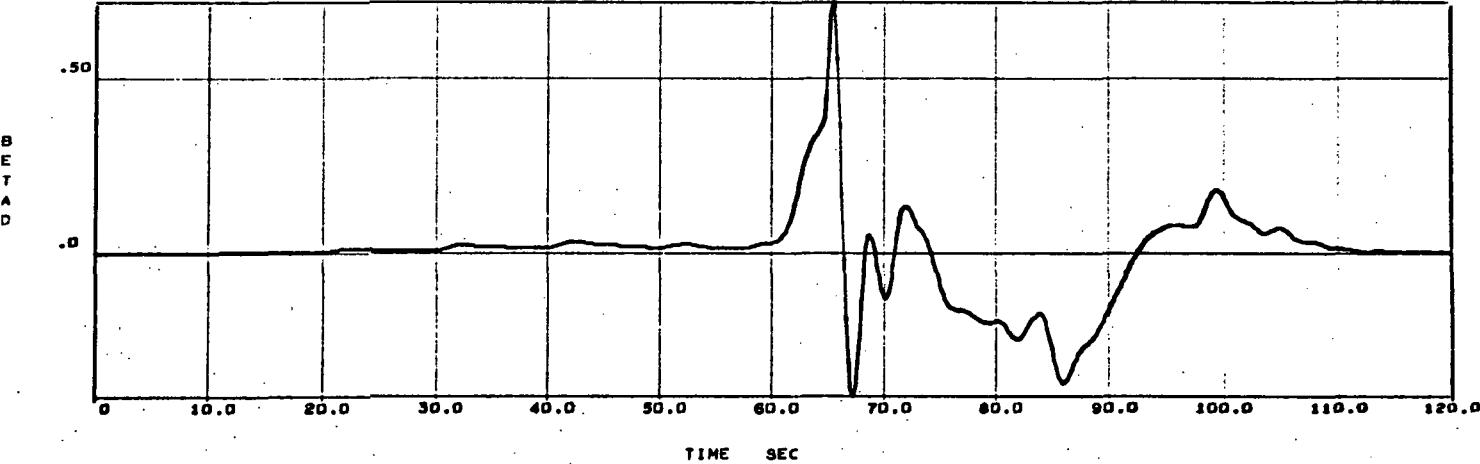
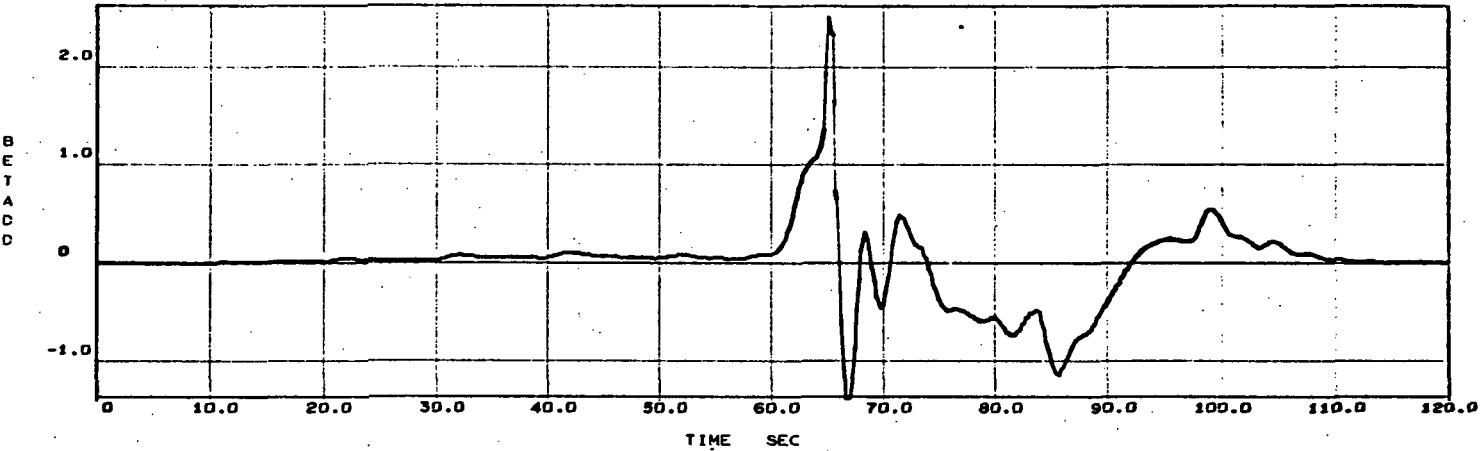


INT-21 ASCENT SIMULATION



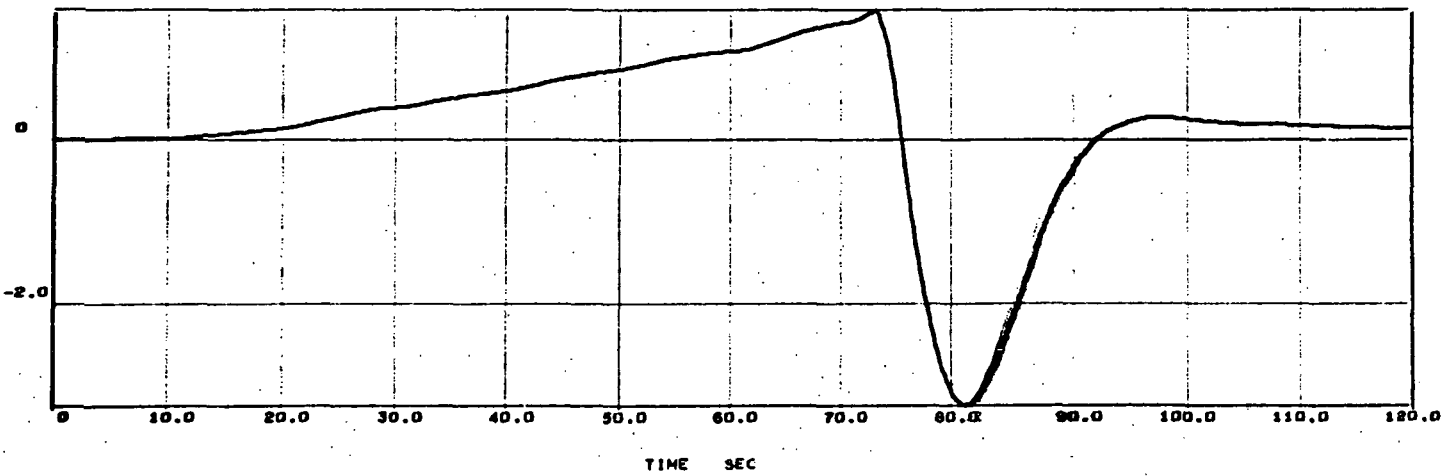
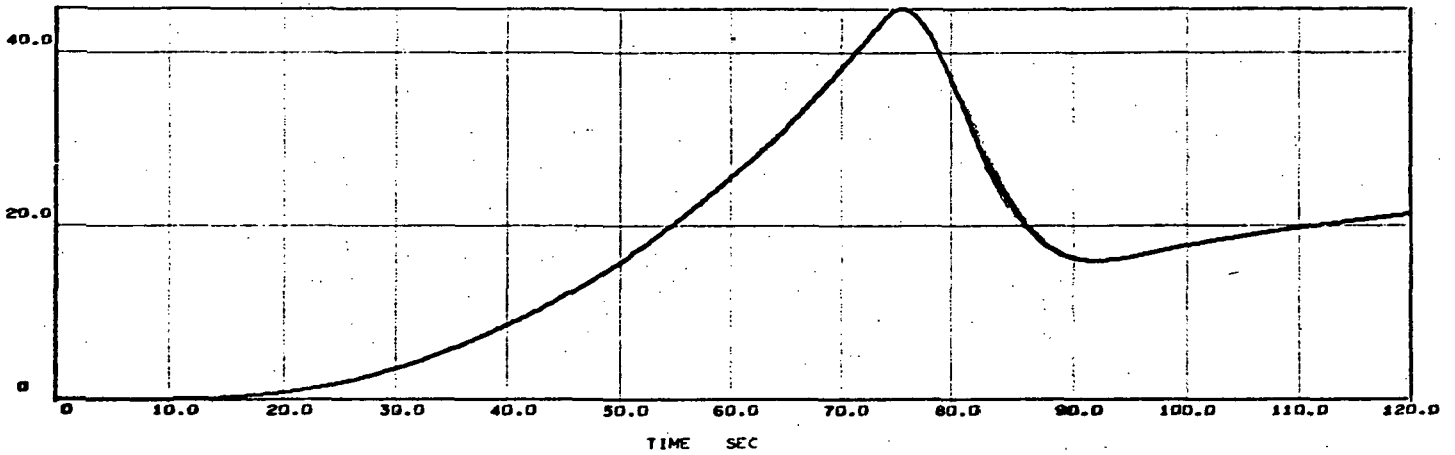
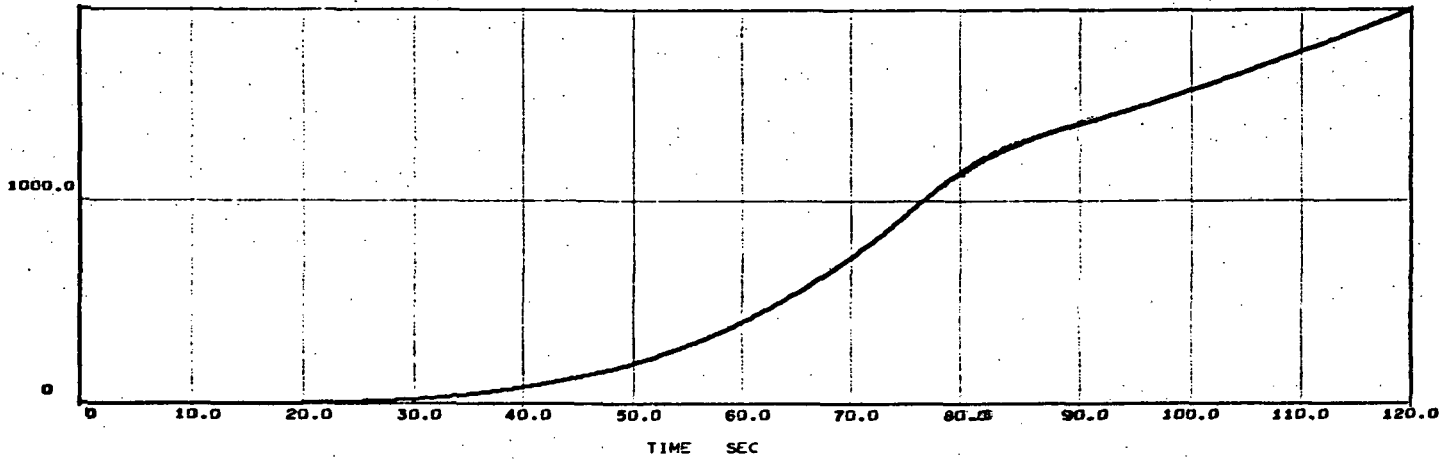
$\alpha_1$  Response

INT-21 ASCENT SIMULATION



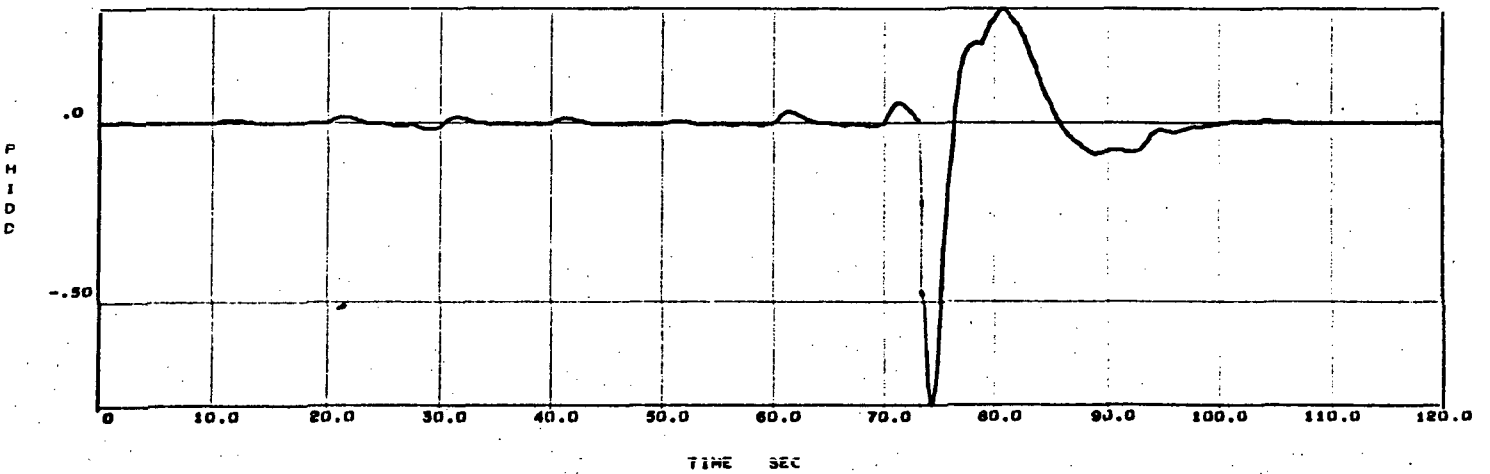
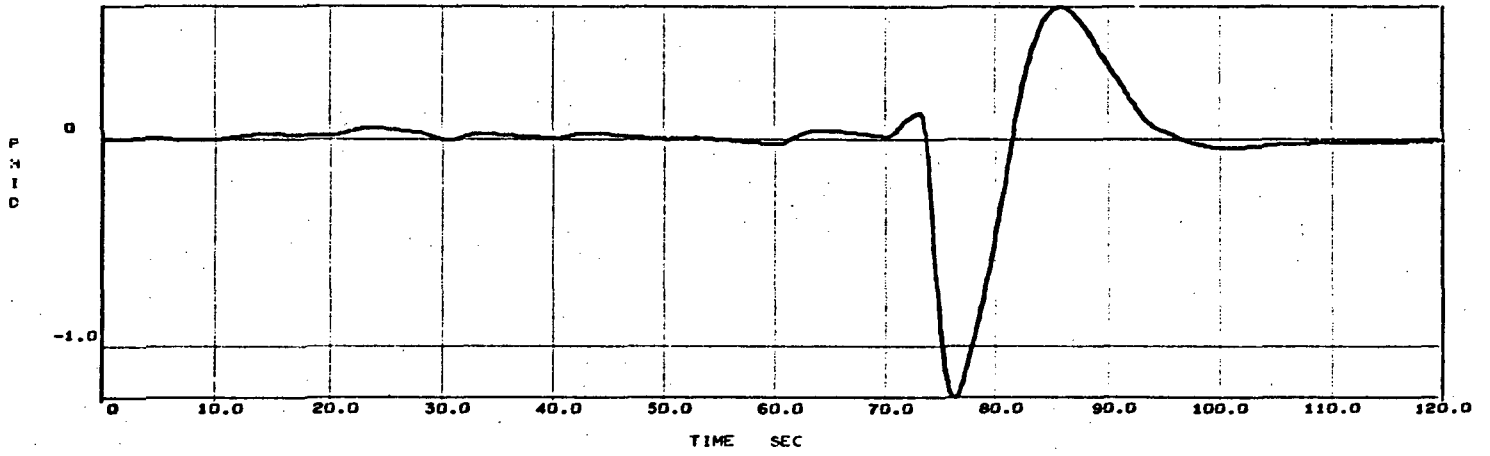
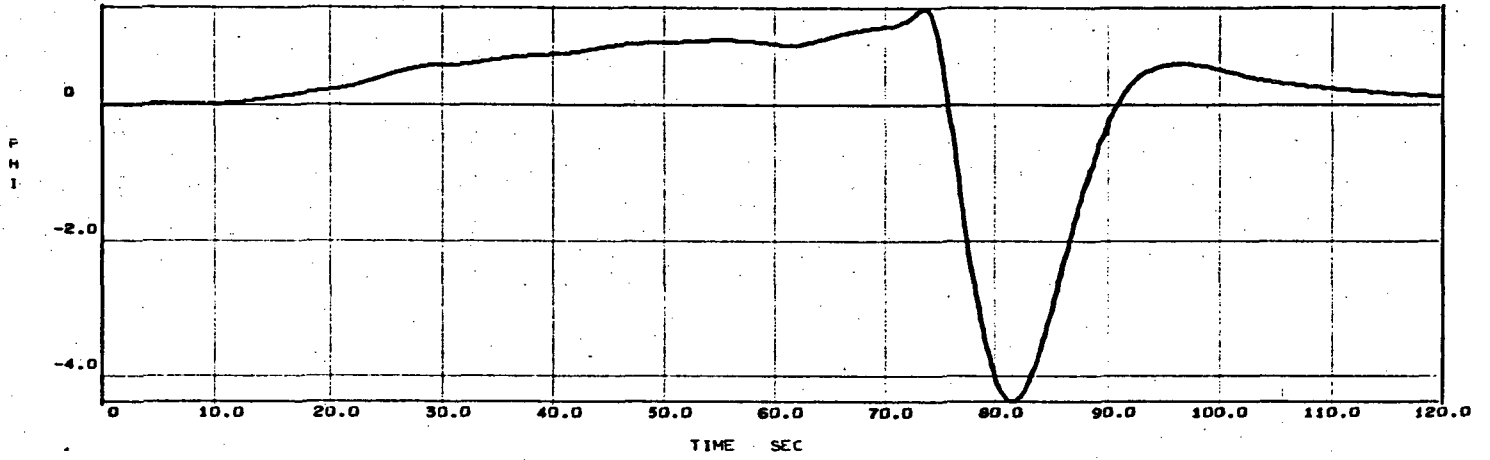
$\alpha_w$  Response

INT-21 ASCENT SIMULATION



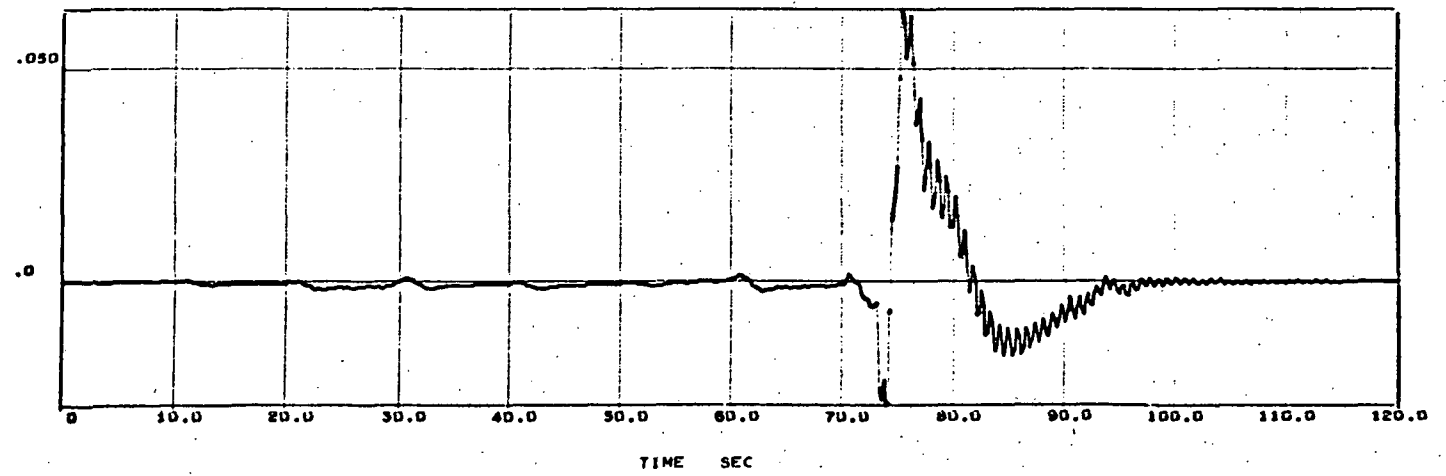
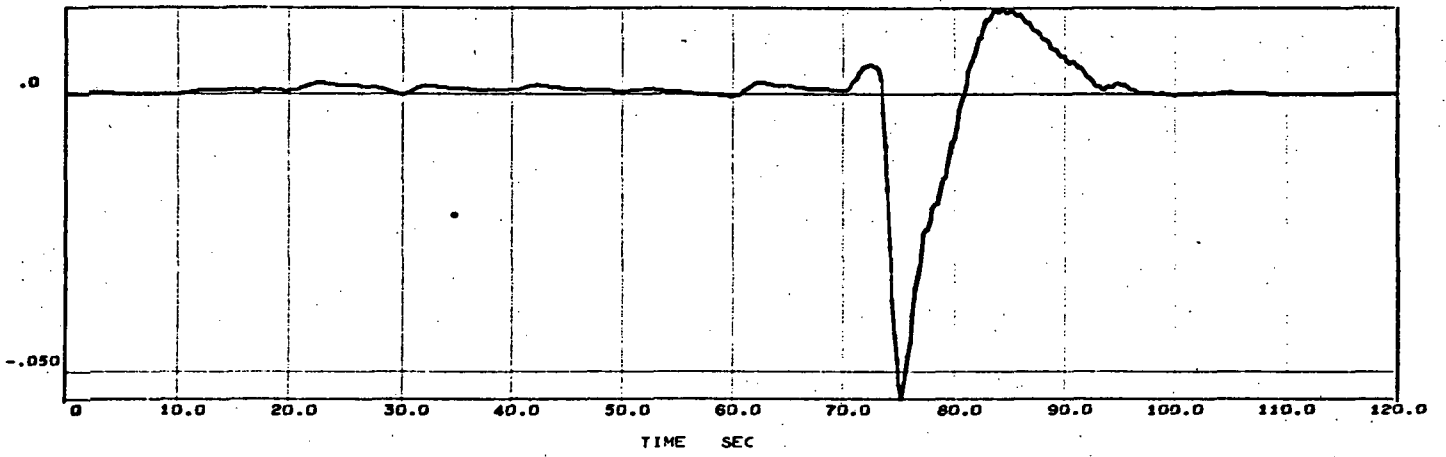
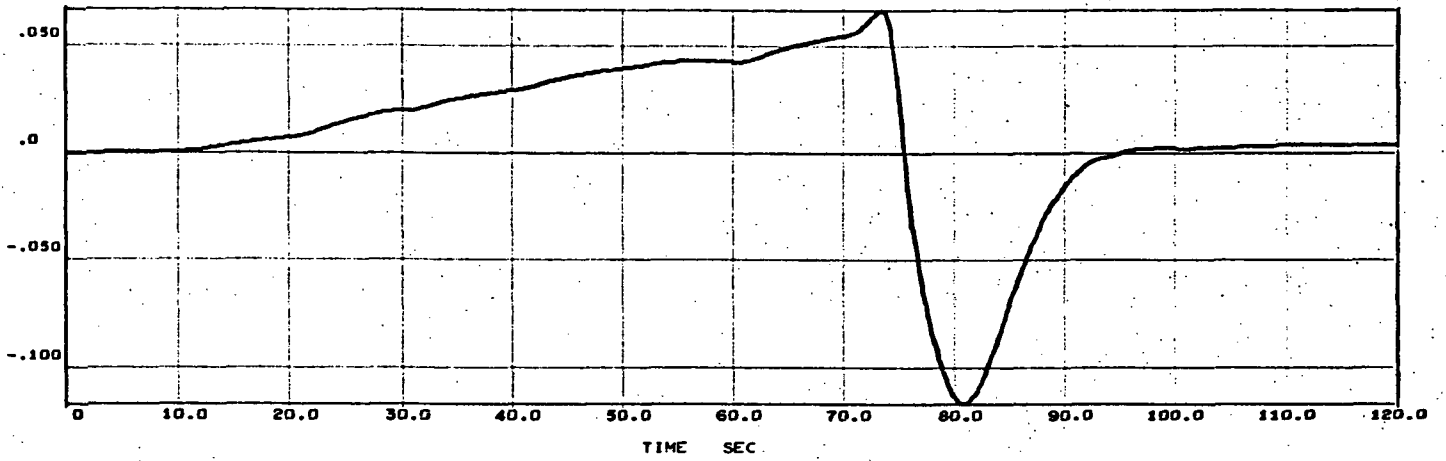
$\alpha_w$  3 Response

INT-21 ASCENT SIMULATION



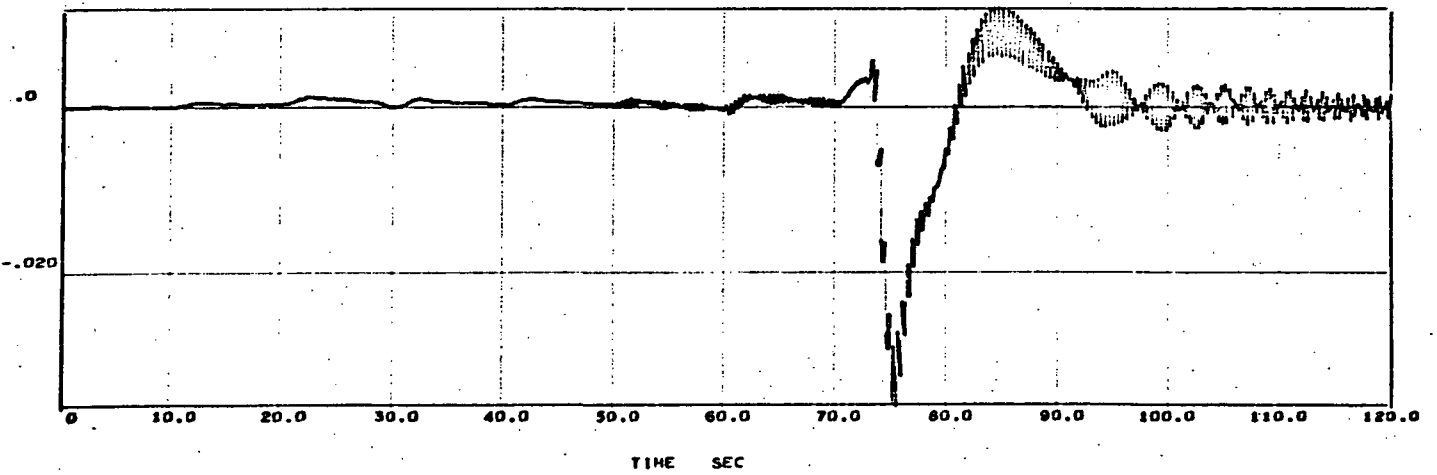
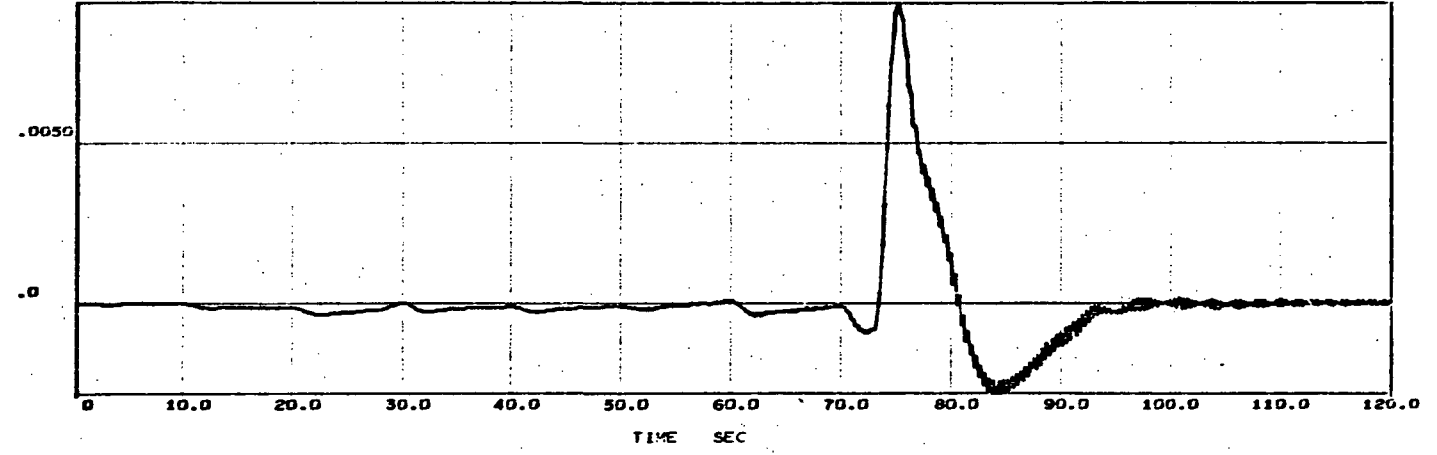
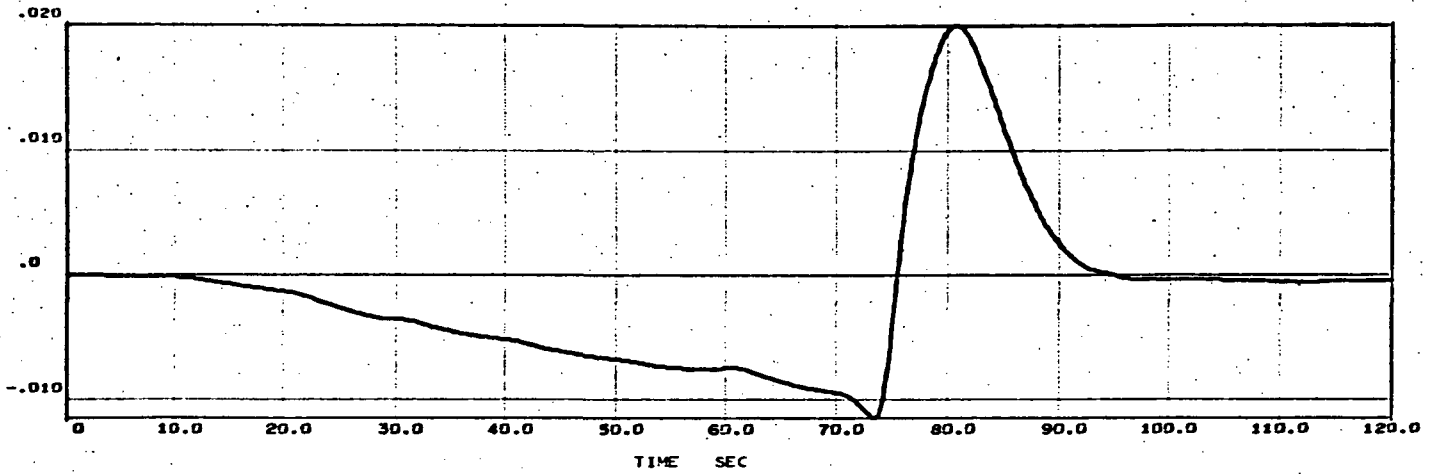
$\alpha_w$  3 Response

INT-21 ASCENT SIMULATION



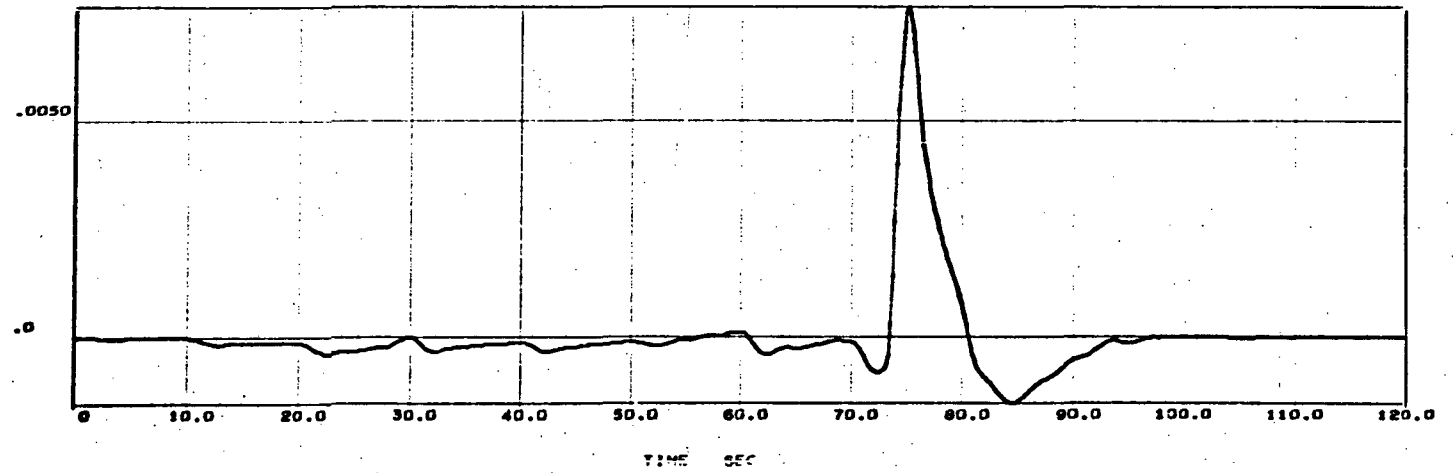
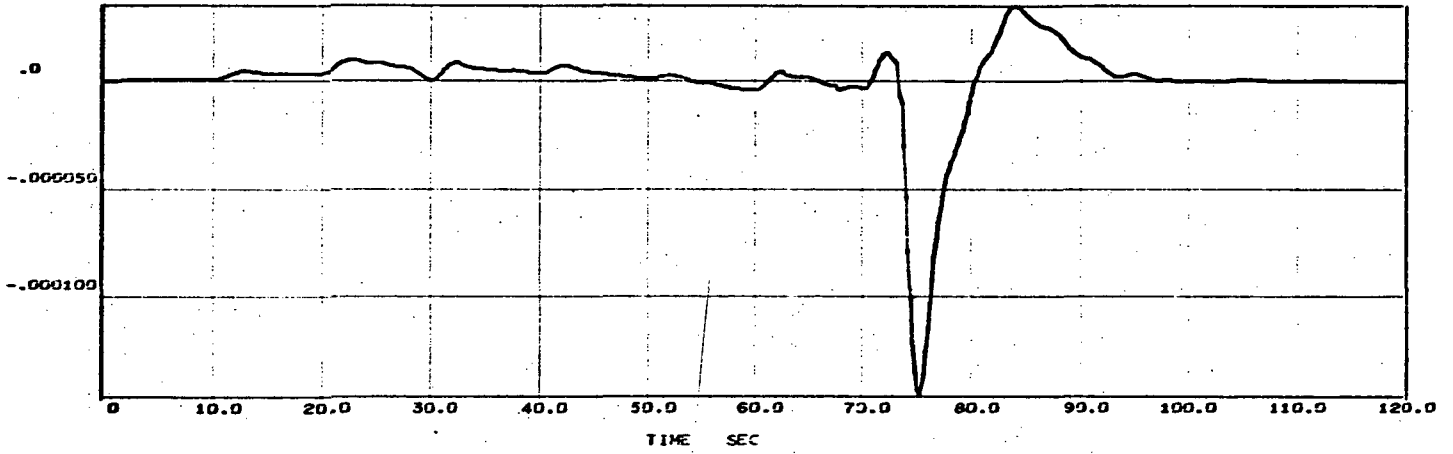
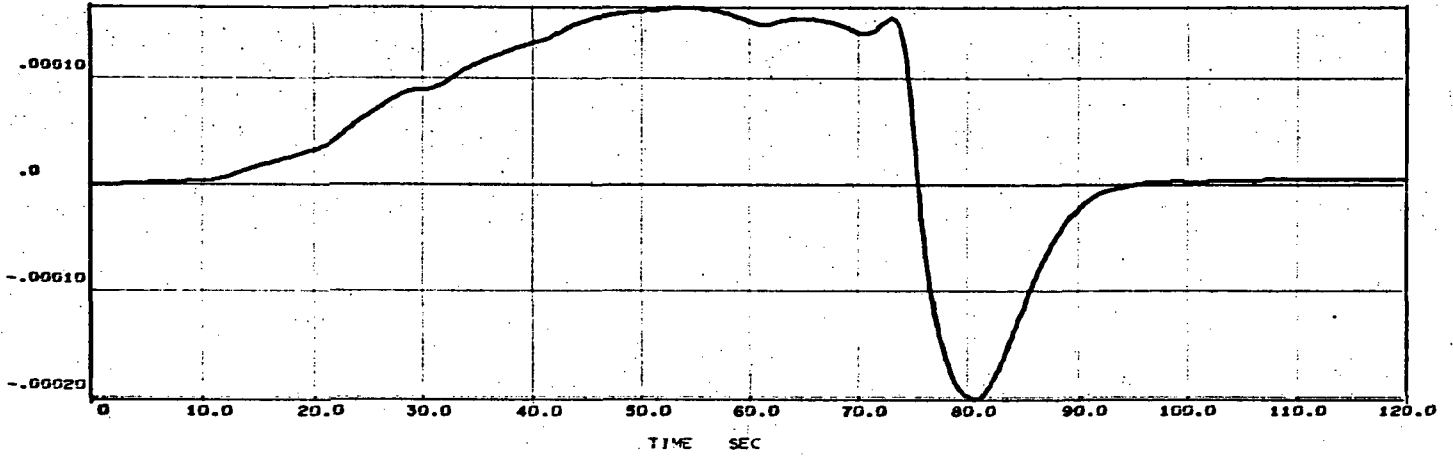
$\alpha_w$  3 Response

INT-21 ASCENT SIMULATION



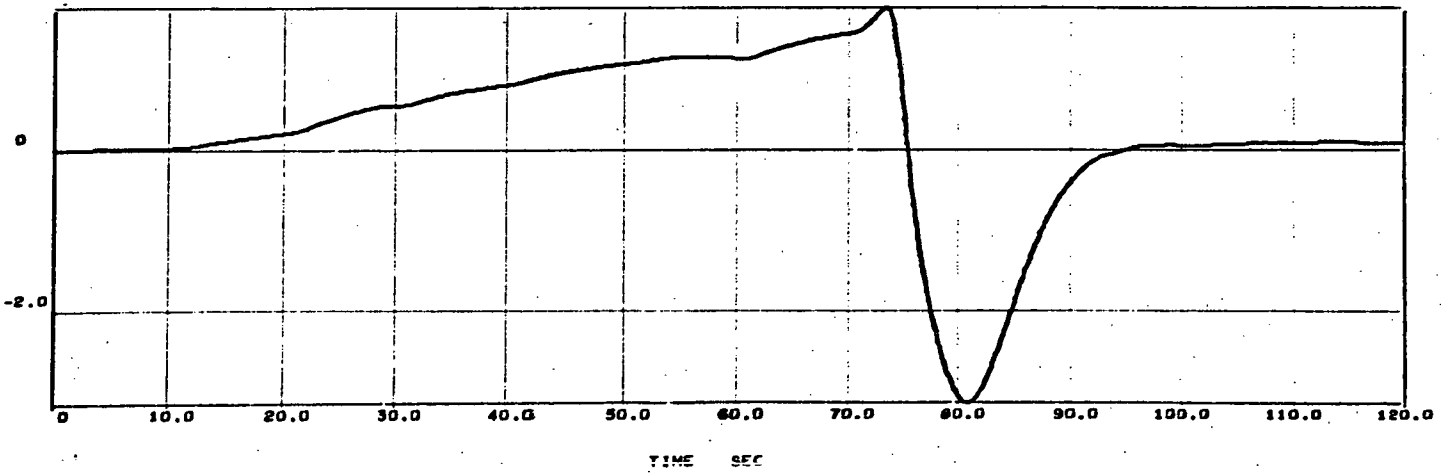
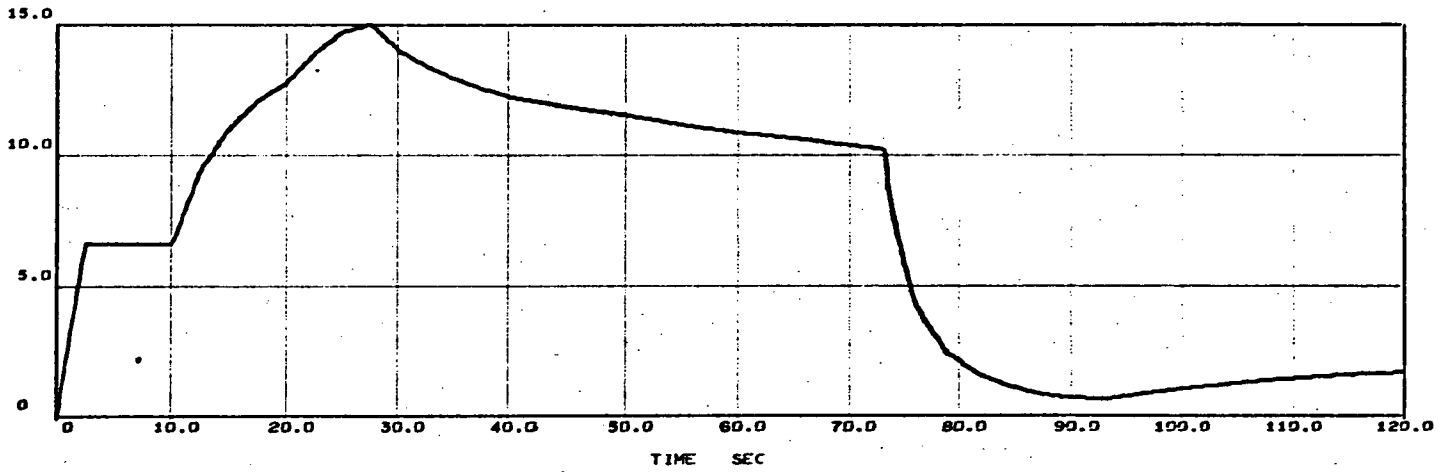
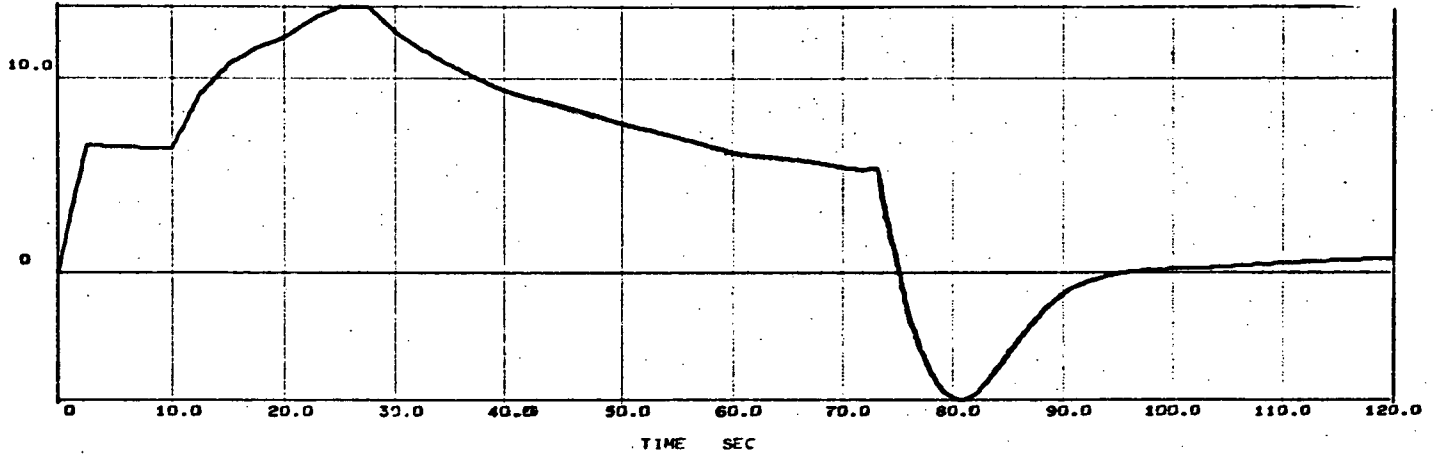
$\alpha_w$  3 Response

INT-21 ASCENT SIMULATION



$\alpha_w$  3 Response

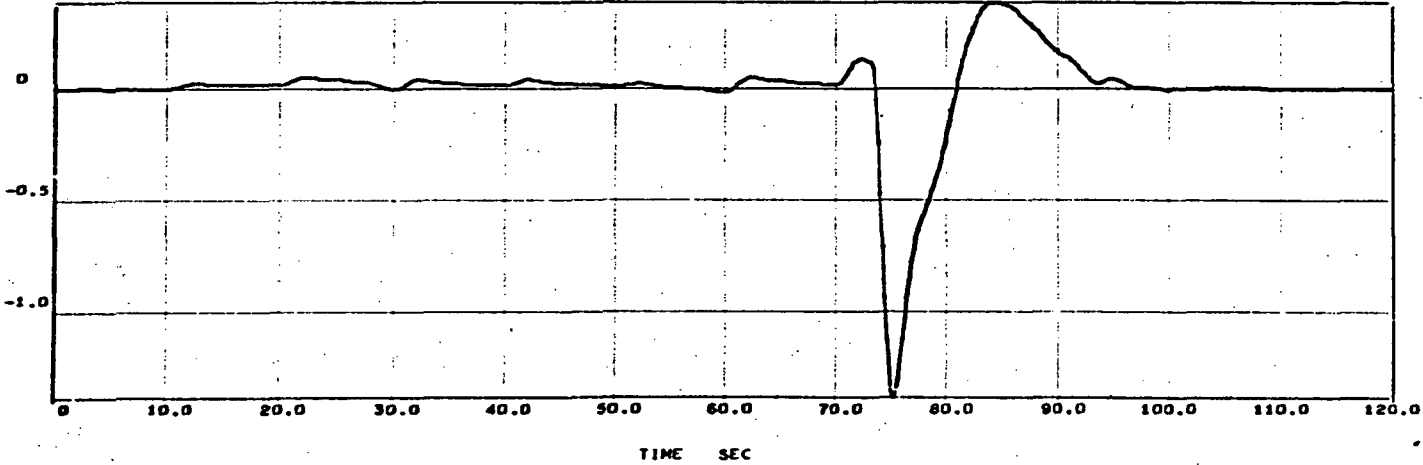
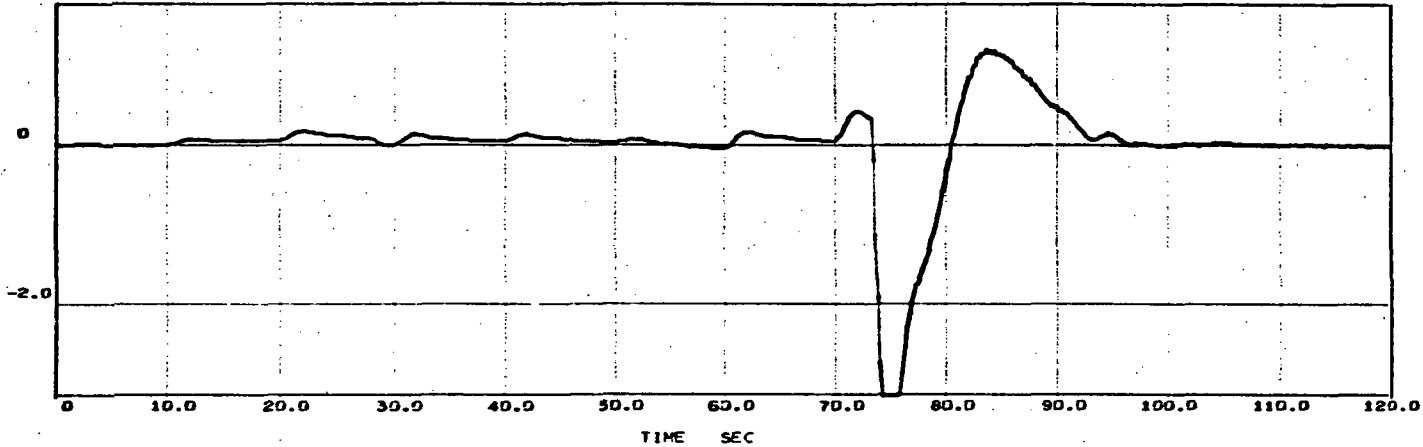
INT-21 ASCENT SIMULATION



$\alpha_w$  3 Response

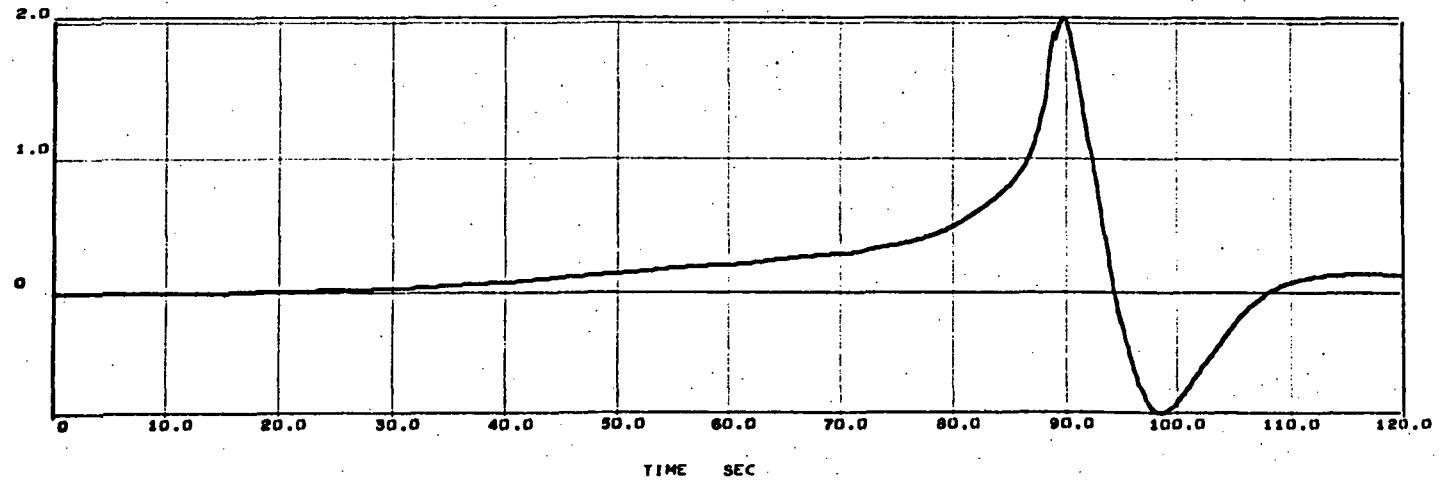
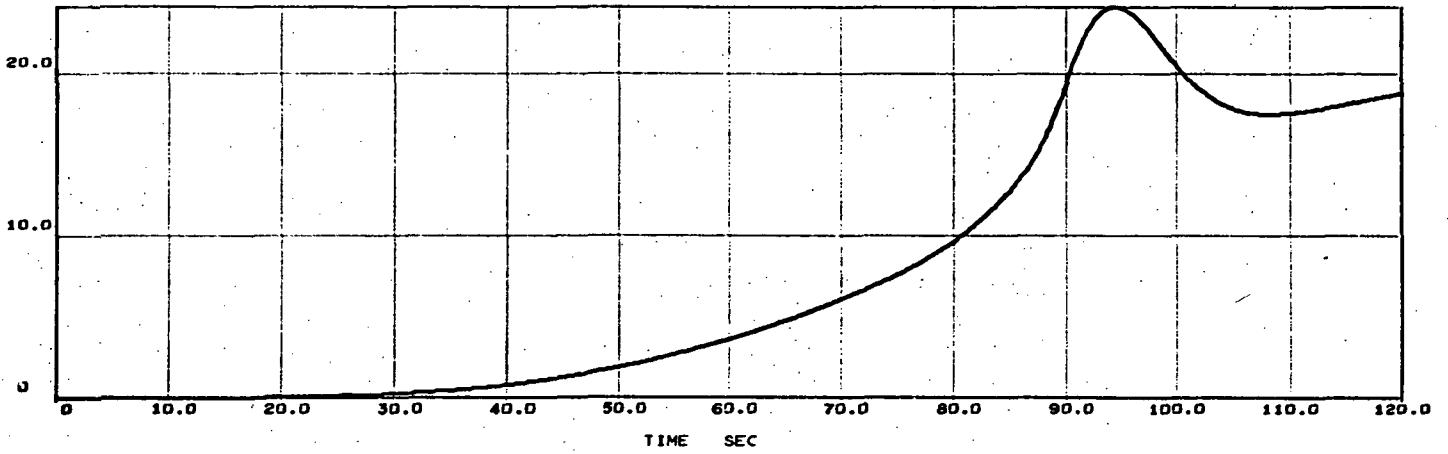
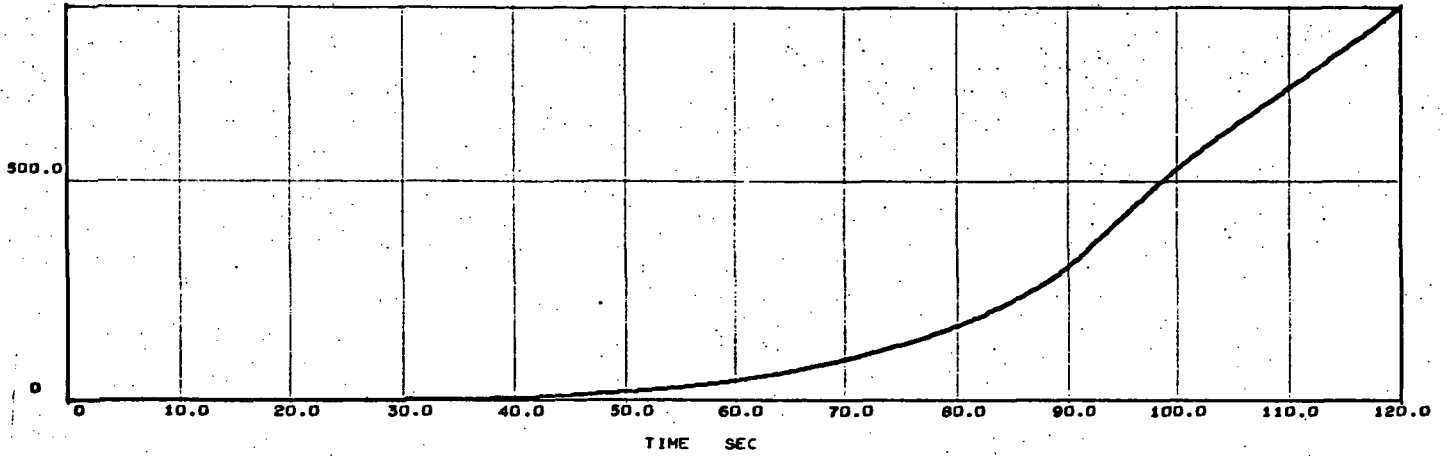


INT-21 ASCENT SIMULATION



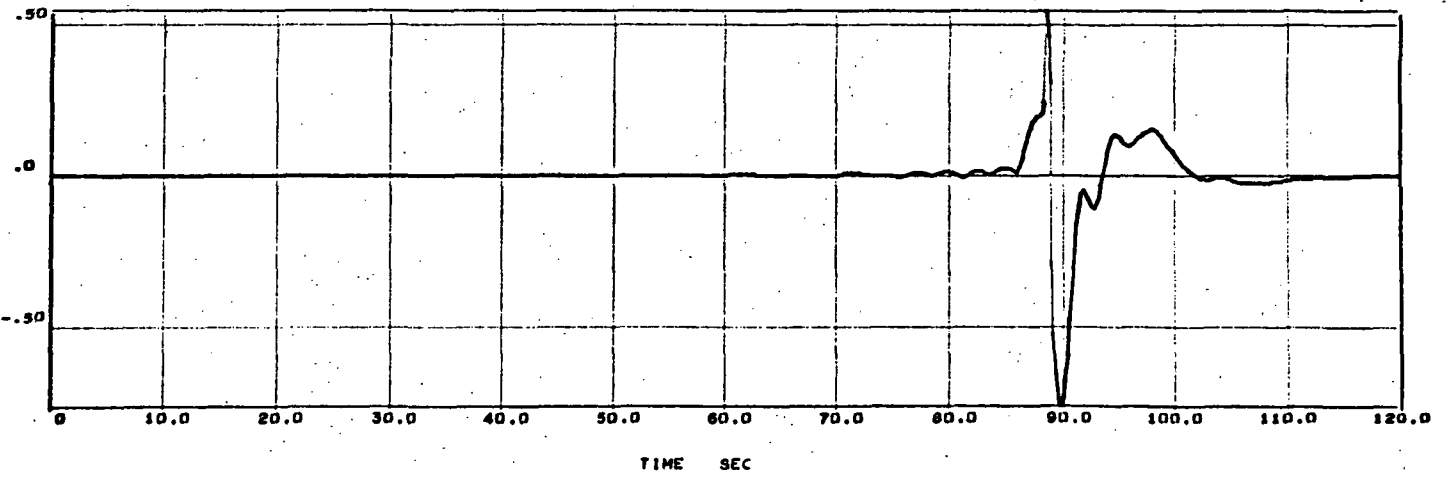
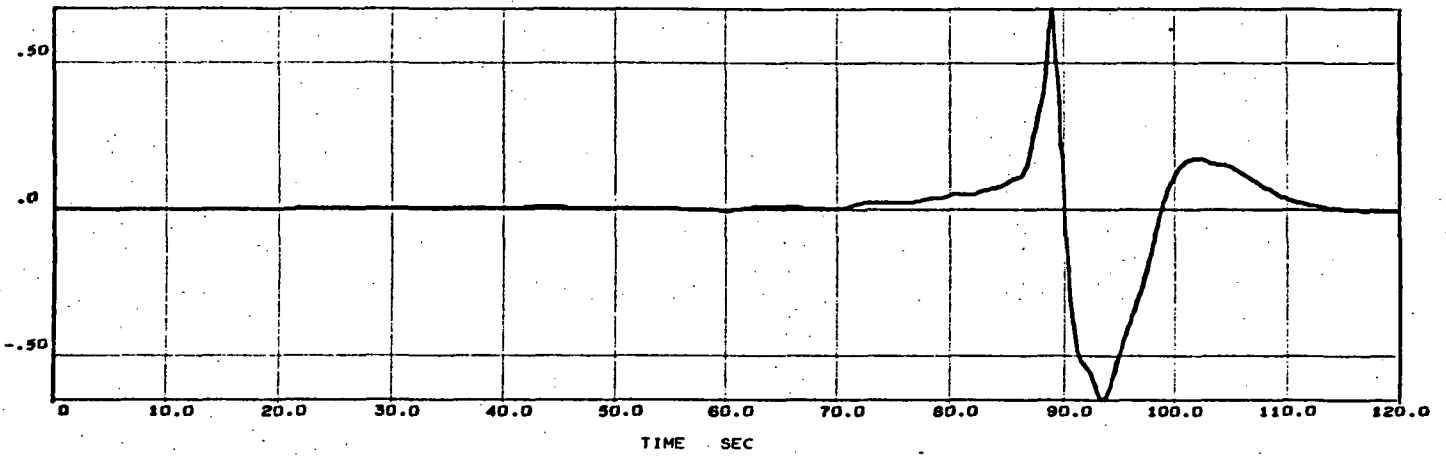
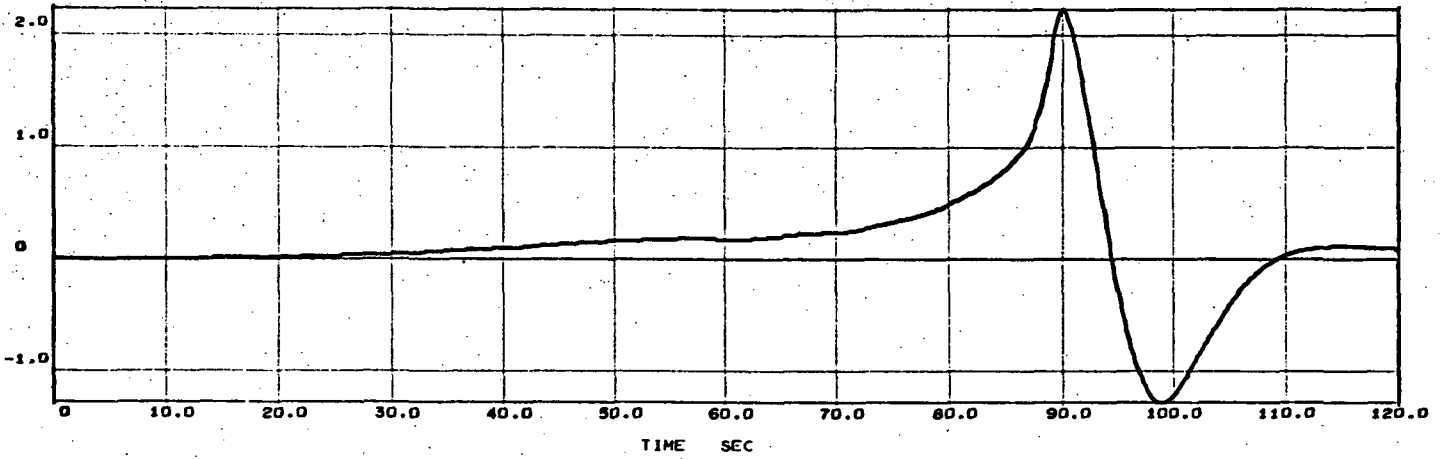
$\alpha_w$  3 Response

INT-21 ASCENT SIMULATION



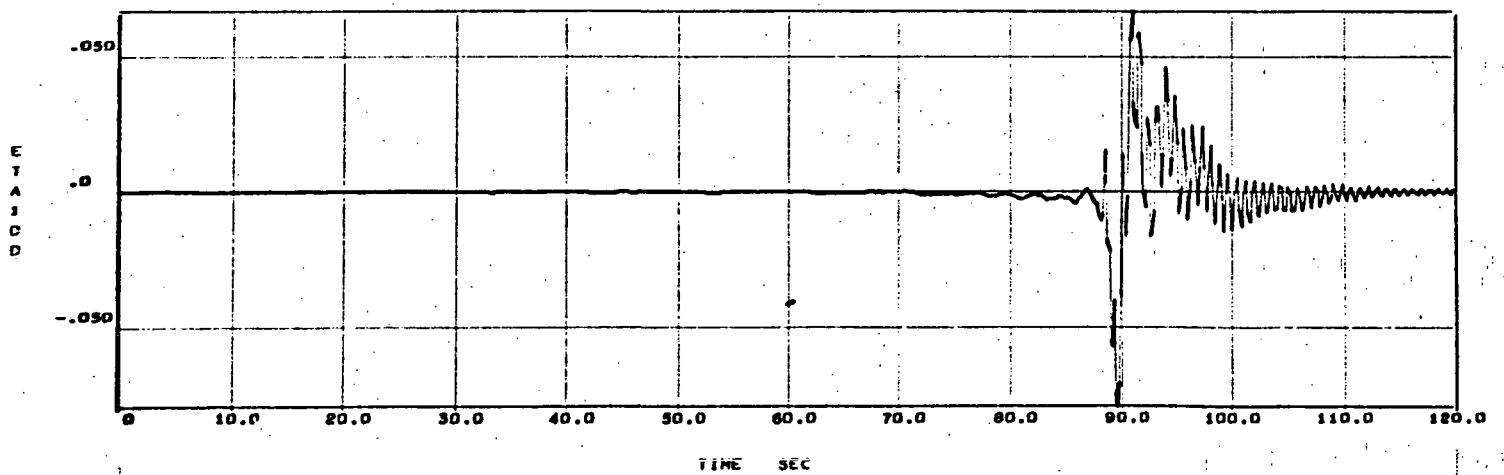
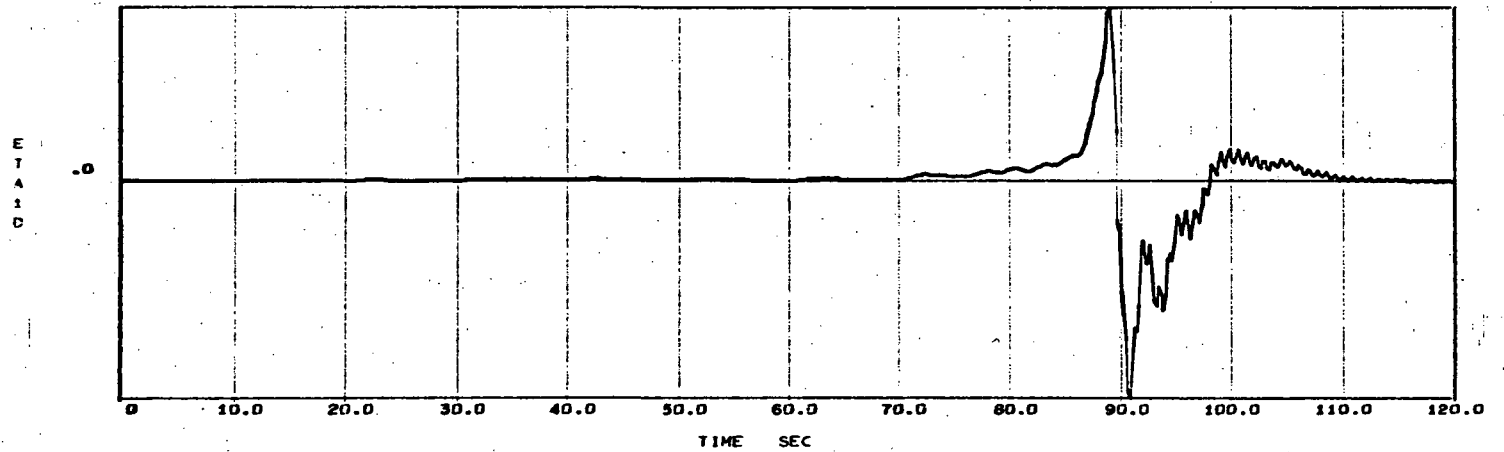
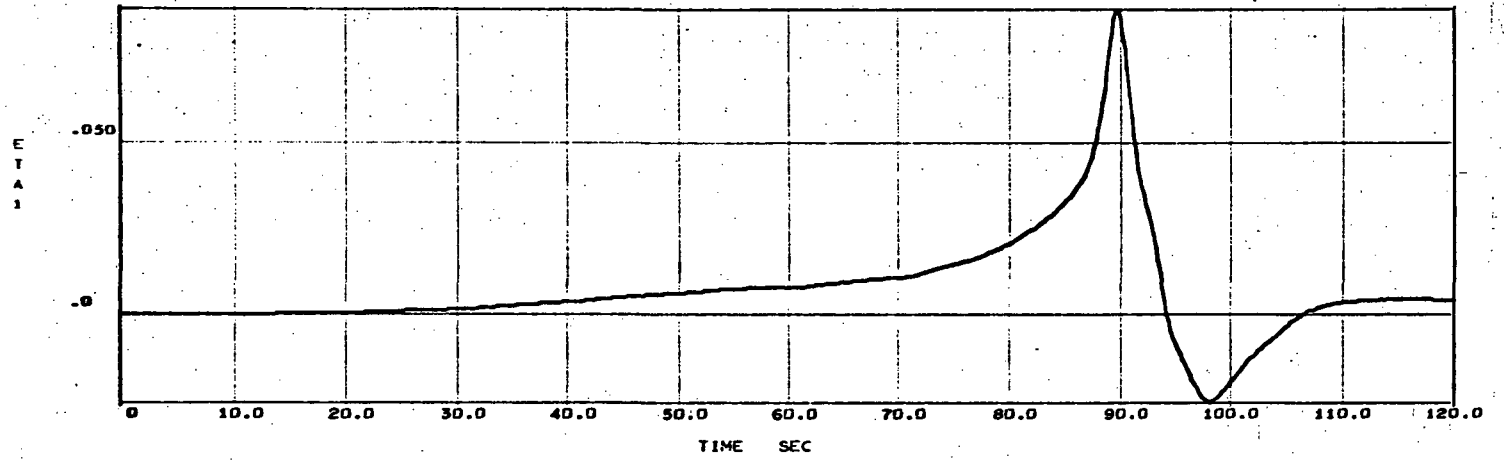
$\alpha_w$  6 Response

INT-21 ASCENT SIMULATION



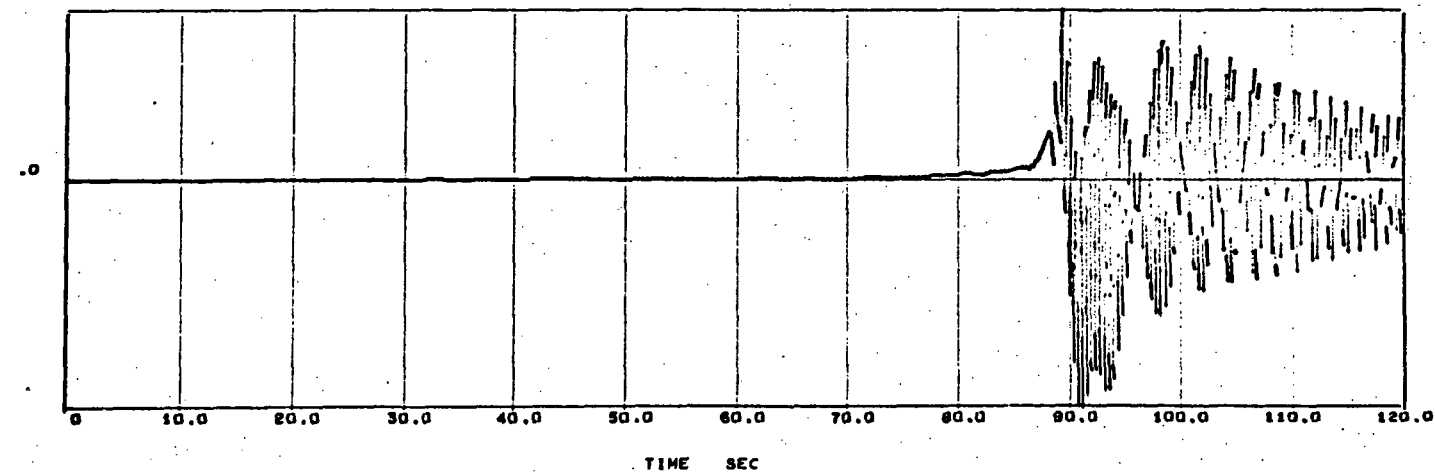
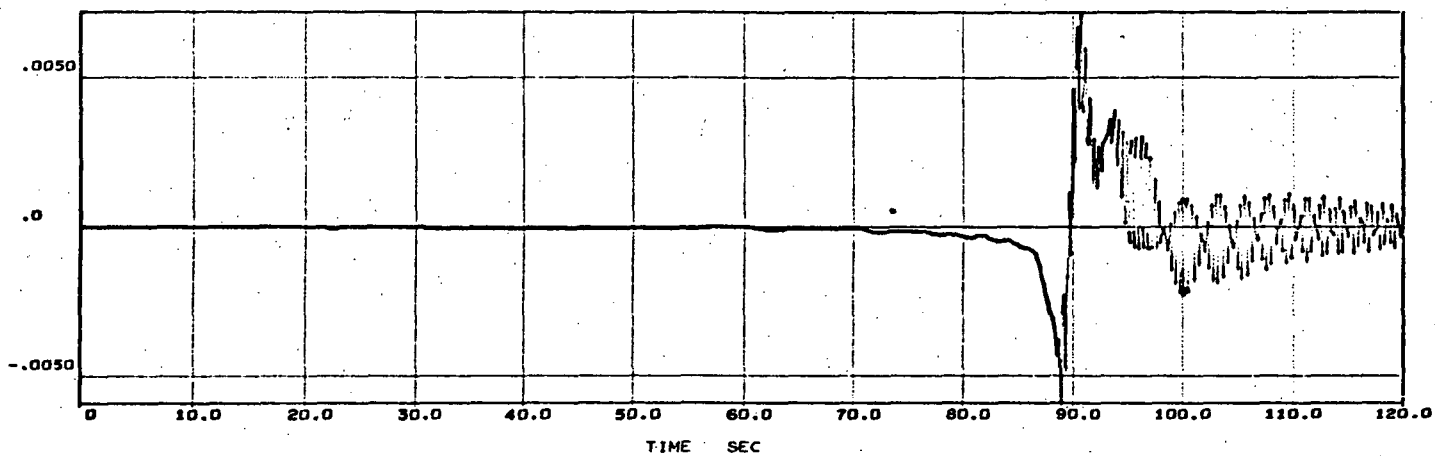
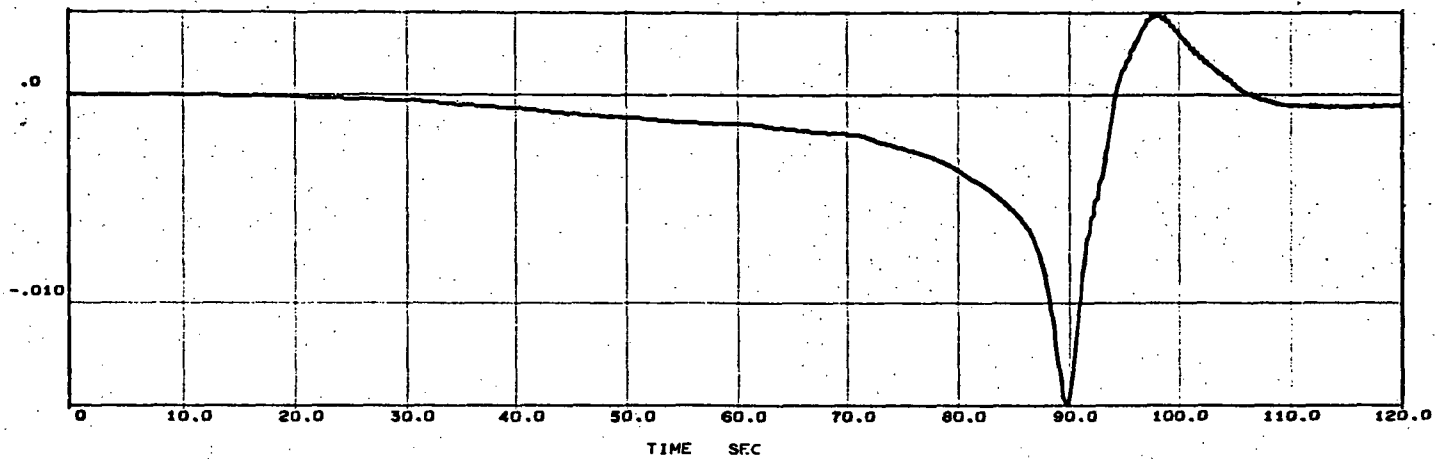
$\alpha_w$  6 Response

INT-21 ASCENT SIMULATION



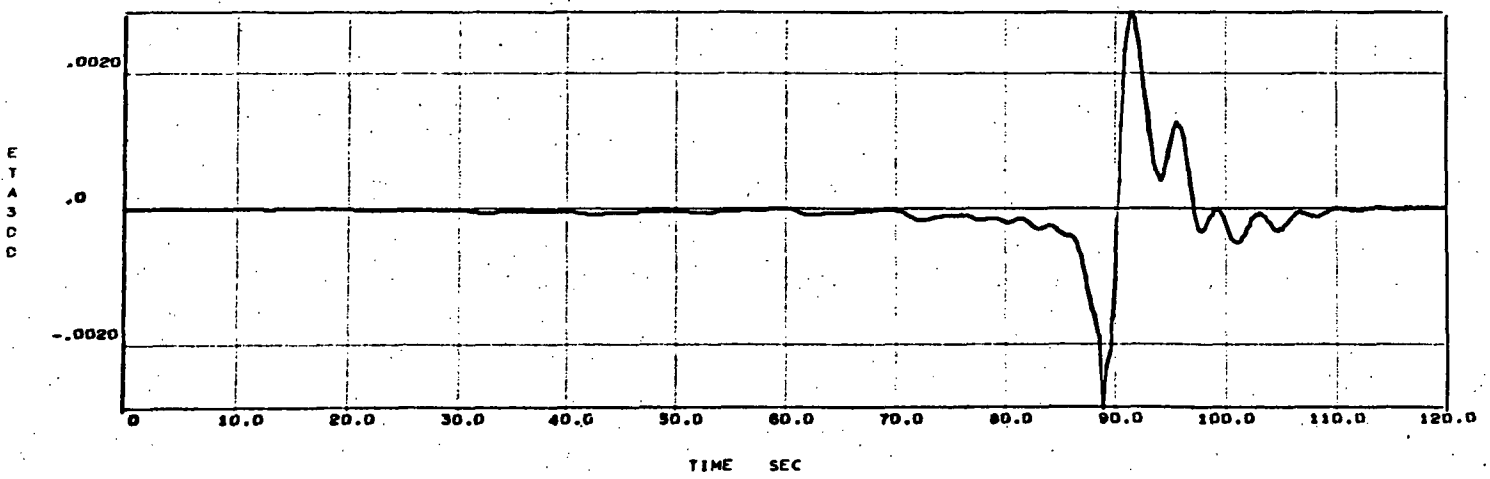
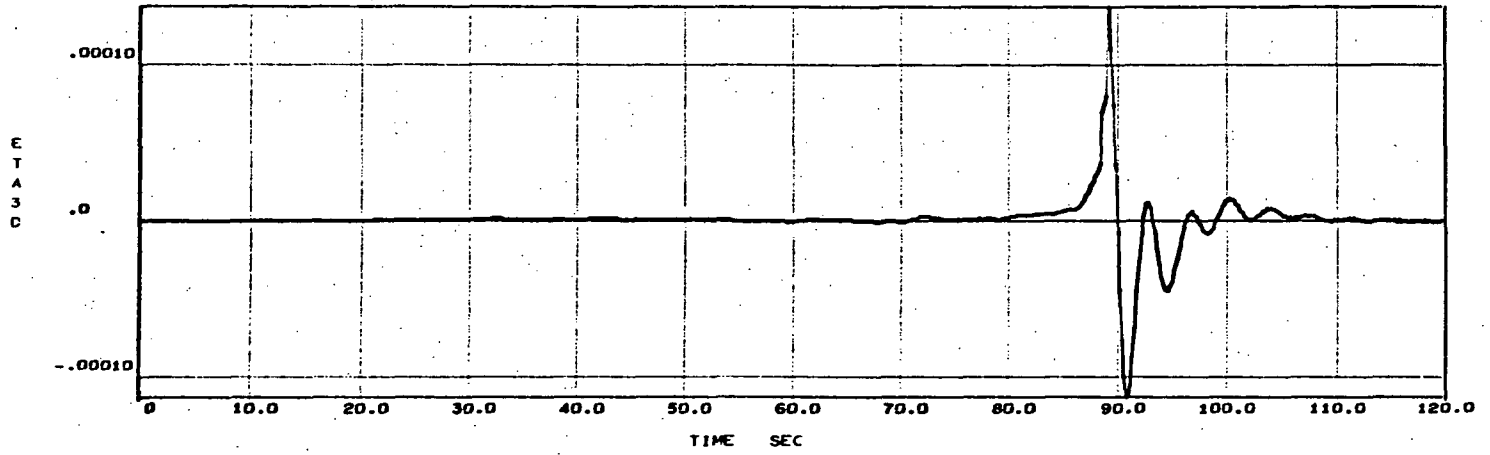
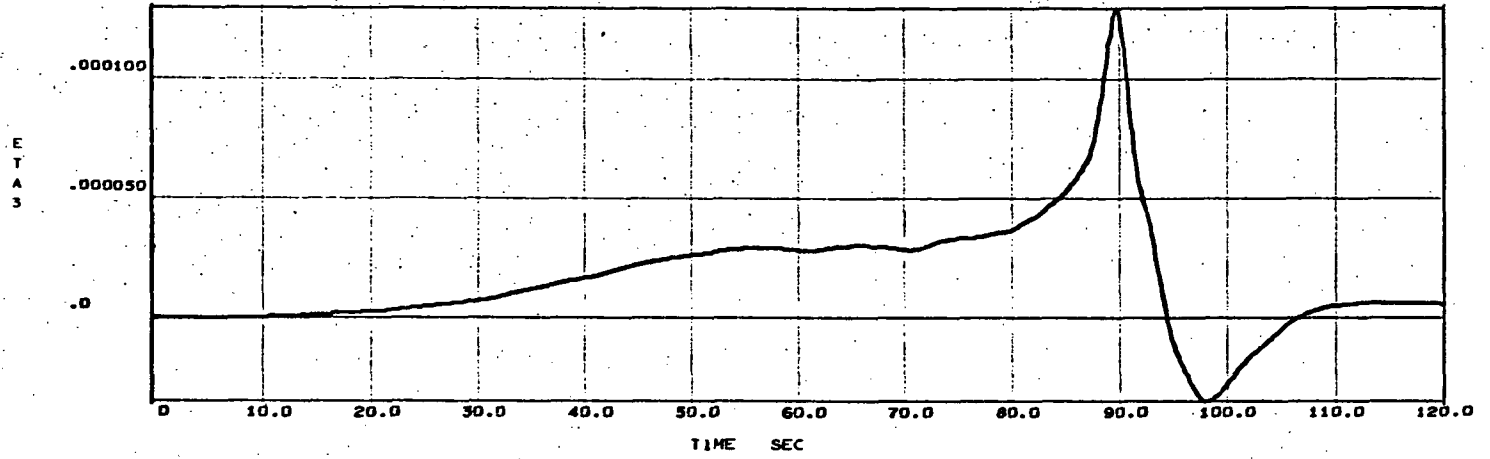
$\alpha_w$  6 Response

INT-21 ASCENT SIMULATION



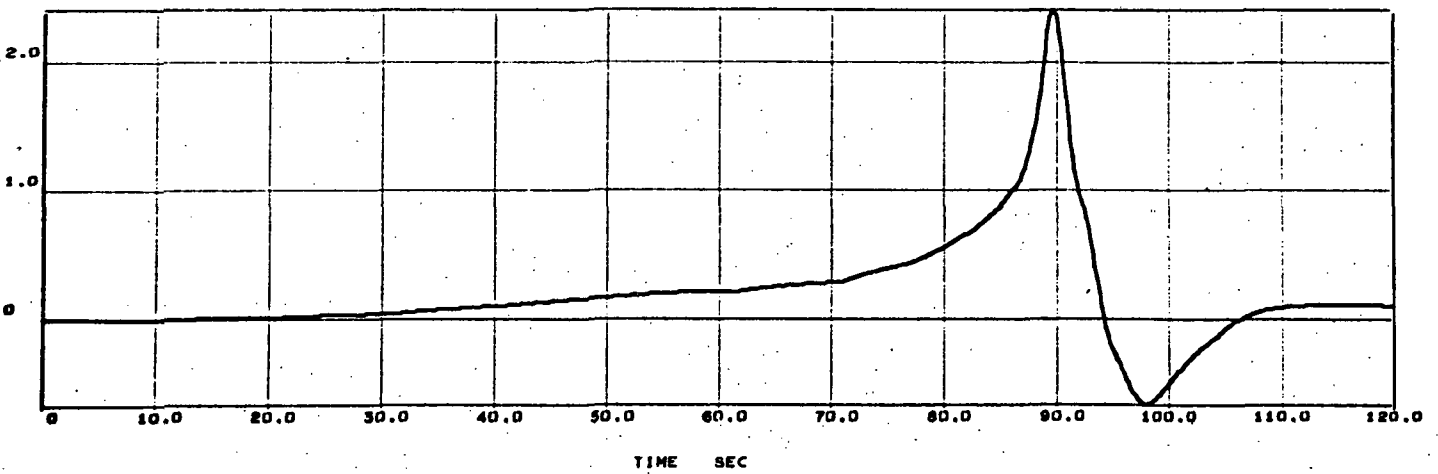
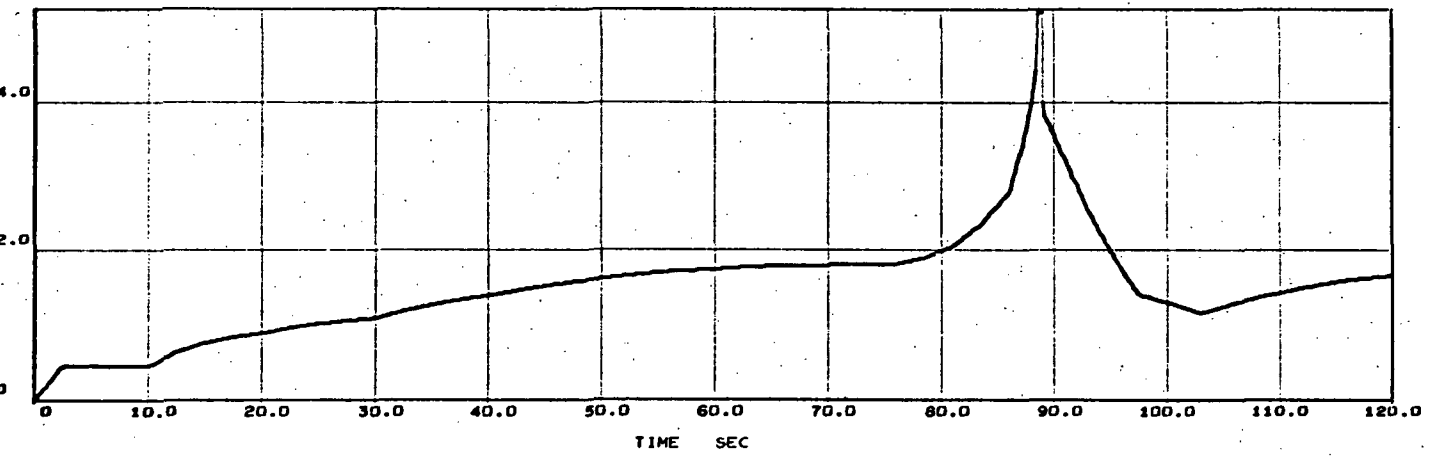
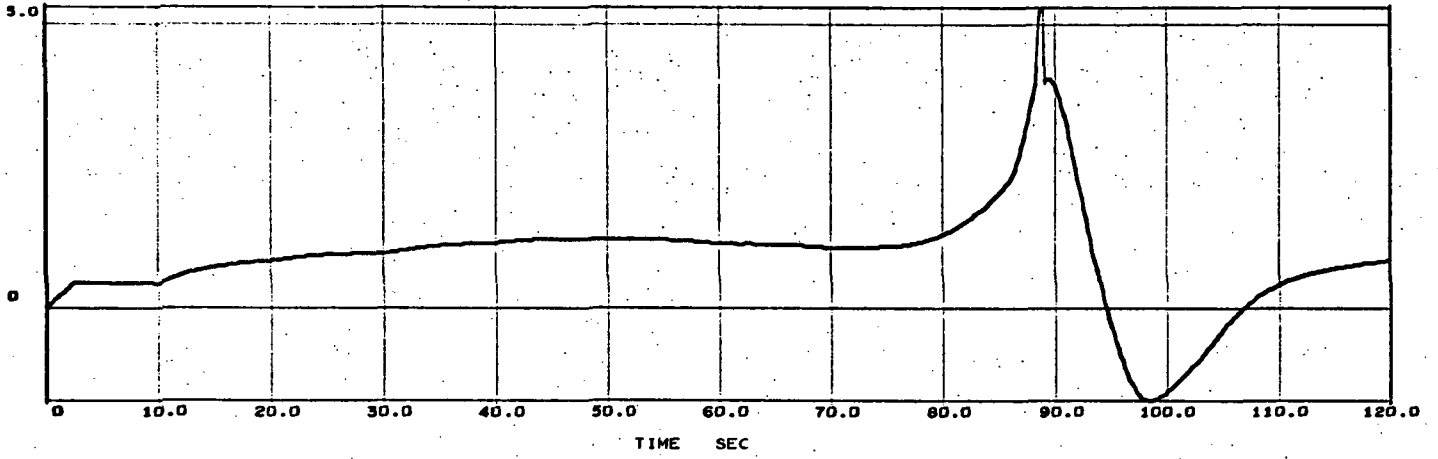
$\alpha_w$  6 Response

INT-21 ASCENT SIMULATION



$\alpha_w$  6 Response

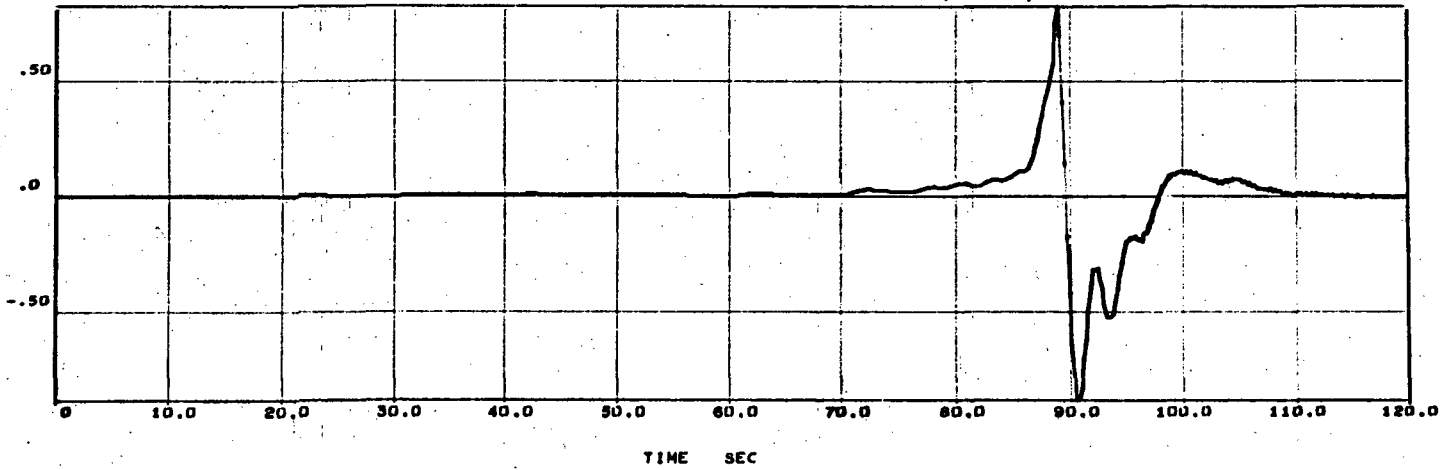
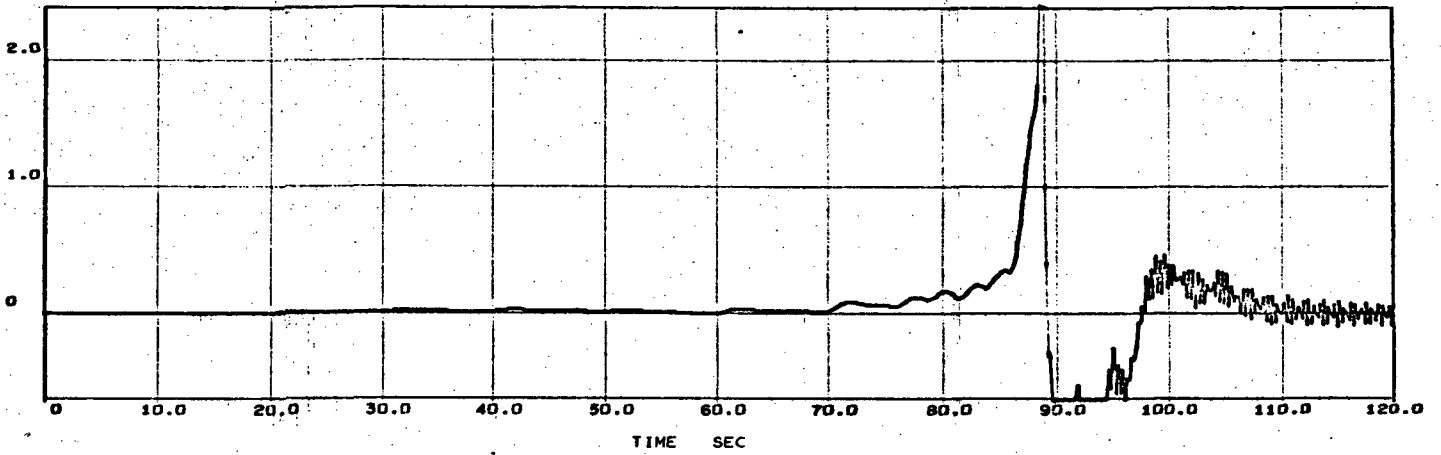
INT-21 ASCENT SIMULATION



$\alpha_w$  Response

D-21

INT-21 ASCENT SIMULATION



$\alpha_w 6$  Response